HIGH SPEED EDDY-CURRENT COUPLINGS AND DYNAMOMETERS

by

PHILIP NORMAN JACKSON, B.Sc.

A Thesis submitted for the degree of

DOCTOR OF PHILOSOPHY

at

THE UNIVERSITY OF ASTON IN BIRMINGHAM

NOVEMBER 1975

SUMMARY

This thesis contains a study of high speed eddy-current couplings and dynamometers.

After a short introductory chapter, which includes a description of the various types of coupling and an appraisal of existing coupling literature, the work is divided into two parts:

i) The derivation and verification of a general temperature theory for assessing the effects of loss member temperature on the performance and design of eddy-current couplings.

ii) Comprehensive testing of a new water cooled high speed eddy-current dynamometer and investigation whether existing coupling theory was valid at high frequencies.

There are no publications dealing specifically with either of these topics. This thesis therefore fills two gaps in eddy-current coupling literature.

Acknowledgements

The work in this thesis was carried out under the supervision of Professor E. J. Davies, Professor in Electrical Engineering, The University of Aston in Birmingham; the author is deeply indebted to Professor Davies for his guidance, encouragement and stimulus.

The author also wishes to thank the following:

Redman Heenan Froude Ltd., who financed the author and the new experimental machine.

The Science Research Council, for their joint financial support.

Dr. M. T. Wright, who was advisor for this work.

Mr. R. C. Ellet, for many discussions.

Dr. A. L. Bowden and Mr. B. James for their advice and interest.

Mr. N. Kerruish and Mr. A Sutton for their advice on analytical problems.

The technical staff of the Electrical Machines Centre, particularly: Mr. B. Harrison, Mr. L. Radford, Mr. J. Lightfoot and Mr. E. Clenton.

His wife, without whom . . . . . .

CONTENTS

Page No.

Page No.

Page No.

Page No.

Page No.

Page No.

Page No.

List of Symbols

a	Constant
b	Constant
c	Constant or specific heat ($Ws/kg^{o}C$)
d_L	Loss member thickness (m)
d_p	Equivalent pipe diameter or hydraulic mean diameter (H.M.D) (m)
e	Induced emf (V)
f	Armature reaction multiplier
g	Airgap length (m)
h	Surface heat transfer coefficient = NuK/L ($W/^{o}Cm^{2}$)
$\bar{h}$	Average surface heat transfer coefficient
j	$\sqrt{-1}$
l	Length (m)
m	Characteristic of magnetising curve
n	Slip speed (rev/min) or number of water channels
n_m	Resultant speed at peak torque (rev/min)
$n_{m,1}$	Speed at peak fundamental torque
p	Pole pairs
r	Power distribution factor or radius (m)
r_{av}	Mean radius of radial current density probe (m)
r_o	Outside radius of drum or cylinder
s	Laplace operator
t	Time (s) or temperature (^{o}C)
t_1	Inlet temperature (^{o}C)
t_2	Outlet temperature
t_b	Mean bulk temperature

v	Velocity (m/s)
x	Cartesian co-ordinate or real part of complex number
y	Cartesian co-ordinate or imaginary part of complex number
z	Cartesian co-ordinate or complex number (x +jy)
A	Area (m^2) or a constant
A_a	Active region surface area (m^2)
B	Flux density (T) or a constant
B_g	Standstill airgap flux density (T)
B_I	Inner region flux density in the new dynamometer
B_o	Outer region flux density in the new dynamometer
C.I.F.	Cauchy's integral formula
D	Drum inside diameter (m)
D_o	Drum or cylinder outside diameter
E	Electric field (V/m) or emissivity
F	Ampere-turns (mmf) (AT)
F_g	Applied mmf per tooth or pole
Fø	Flux component of mmf (resultant mmf)
Fr	Armature reaction mmf
Fr'	Equivalent field produced armature reaction mmf (fFr)
Fr_1	Fundamental armature reaction mmf
H	Magnetic field strength (AT/m)
I	Rotational inertia (kg m^2)
I_f	Field current (A)
J	Current density (A/m^2)
K	Pole arc/pole pitch ratio or a constant
K	Thermal conductivity ($W/^oCm$)

K_B	Stephan-Boltzman constant (5.67×10^{-8} S.I. units)
L	Length (m) of characteristic dimension in heat transfer equations
L_A	Length of active rigion
L_D	Axial length of drum
L_T	Apparent length of loss member in which eddy-currents flow
Lp	Distance between current density probe centres
N	Slip speed (rev/s)
P	Power (W)
P_A	Active region power
P_g	Airgap power loss
P_n	nth root of $x'/\beta = \cot(x')$
P_o	Power passing through to loss member backface (W)
P_T	Total power ($T\omega$)
Q	Mass flow rate (kg/s)
R	Mean pitch circle diameter (m)
S	Number of air slots
T	Torque (Nm) or absolute temperature (^oK or ^oC Abs.)
T_h	hth harmonic torque (Nm)
T_m	Resultant peak torque
$T_{m,1}$	Peak fundamental torque
V	Voltage (V)
W	Heat flux or loss density (W/m^2)
W_A	Active region heat flux
W_g	Airgap heat flux
W_o	Heat flux passing through to loss member backface
α	Reciprocal of skin depth (m^{-1}) or material parameter

β	Non-dimensional quantity defined by equation 2.33 or attenuation factor
δ	Skin depth (m) or armature reaction phase angle
θ	Temperature function
θ_m	Mean film temperature (^oC)
λ_1	Fundamental wavelength in the peripheral direction (m)
μ	Permeability or viscocity (Kg/ms)
ρ	Resistivity (Ω m) or density (kg/m^3)
τ	Time constant (s)
$\tau\phi$	Flux time constant
τf	Field time constant
τ_n	Thermal time constants (n = 1, 2, 3 . . .)
τ_T	Torque time constant
ϕ	Flux (Wb)
ϕac_1	Fundamental flux per pole
ϕ_I	Flux passing through inner laminated section of new dynamometer
ϕ_o	Flux passing through outer laminated section of new dynamometer
ω	Angular frequency, $2\pi N$, (rad/s)
Λ	Permeance

Dimensionless 'groups' or 'numbers' used in heat transfer

Gr	Grashof number	$= g L^3 \theta_m \rho^2/\mu^2 T$
Nu	Nusselt number	$= hL/K$
$\bar{Nu}$	Average Nusselt number	$= \bar{h} L/K$
Pr	Prandtl number	$= c\mu/K$
Re	Reynolds number	$= v\rho L/\mu$

Subscripts

av	Mean value
c	Loss member backface coolant
D	Drum machine
g	Airgap quantity or airgap coolant
h	Harmonic order
n	Integer
s	Loss member quantity
3D	Three dimensional

Superscripts

^	Peak value
–	Above a symbol denotes a vector quantity or a transformed quantity

M.K.S. units are used throughout.

Any variations on these symbols are defined in the text.

CHAPTER 1

INTRODUCTION

1.0 Introduction

1.1 Background and Objectives of this Thesis

Recent literature on eddy-current couplings stresses their use as variable speed drives.[12] But, calibrated, stalled eddy-current couplings are also used as dynamometers and the main purpose of this work was to investigate the performance and design of high speed eddy-current dynamometers; more specifically a 75 kW, 14,000 rev/min dynamometer.

Basically an eddy-current dynamometer consists of a rotor, stationary member and a means to measure torque and speed. The power dissipated is proportional to the relative speed between the two members, which means that large amounts of power have to be removed at high input speeds. This power is usually dissipated in a cooled solid iron loss member and it is this cooling that is usually the major design problem for most eddy-current dynamometers. For high speed machines, other major problems exist, e.g. mechanical design and optimum electro-magnetic design, which are related.

As far as the author is aware there is no published work on high speed couplings nor on the effects of loss member temperature on the performance of couplings or their cooling system design.

The objectives of this thesis can be summarised as:

a) To determine the most suitable types of coupling for use in high speed eddy-current dynamometers.

b) To investigate the effects of loss member temperature on the performance of couplings and also establish foundations for their cooling system design.

c) To design and build an experimental machine which can be used to determine whether existing coupling theory is applicable to high speed couplings and to study their behaviour.

1.2 Outline of Thesis

The remainder of this chapter contains a brief description of the existing types of eddy-current coupling and a review of the most important coupling literature.

Chapter 2 contains a theory for predicting loss member surface temperatures and thermal time constants. The effects of these temperatures on coupling performance are analysed in detail. Cooling system design is also considered.

To verify the basic temperature theory an air cooled drum coupling with and without endrings was used; chapter 3 gives the results of the tests and the theoretical correlations.

The arrangement, instrumentation and testing of a new water cooled, high speed, eddy-current dynamometer are discussed in chapters 4 and 5. Davies generalized coupling theory[8] is used extensively throughout chapter 5 for comparisons with the experimental curves. The temperature theory is also applied to the water cooled loss member. In the last part of chapter 5, the transient performance of the new machine is studied.

1.3 The eddy-current coupling

1.3.1 Basic principle of operation

An eddy-current coupling consists of a loss memeber and, usually, an electromagnet field member. The two members are mechanically separated from each other by a small airgap and either one or both are free to rotate.

When the two members rotate relative to each other, eddy-currents are induced in the loss member. The field* set up by these eddy-currents reacts with the inducing airgap flux and a retarding torque is produced which is a function[3,8] of slip speed, field current and machine parameters.

---

* Commonly referred to as the armature reaction field[3] since it changes the flux density distribution across a pole and also reduces, by Lenz's law, the total flux from the pole.

Power losses are associated with the eddy-currents and these must be supplied by the input. The general power balance equation is given by

$$2\pi NT = 2\pi NT\,(1-s) + (\text{slip power})$$

where N = input speed in rev/s

T = torque in Nm

and s = (input speed - output speed)/input speed.

So the eddy-current loss or slip power is given by $2\pi NTs$.

When a coupling is used as a dynamometer or brake, s = 1 and all the input power is dissipated in the loss member, whence it must be removed by efficient cooling.

More comprehensive details of coupling operation can be found in references 2 and 3.

1.3.2 Types of eddy-current coupling

There are two general groups of eddy-current coupling; drum and disc types. Figure 1.1 shows the basic constructional differences between them. Both will operate with any field arrangement that produces a changing pattern of airgap flux density. The most common field arrangements are:

i) Wound synchronous machine poles[10]

ii) Lundell or fully interdigitated poles[3,4]

iii) Inductor or homopolar types[2,8]

iv) Semi-Lundell or partially interdigitated poles[10]

The loss member has two functions; it carries the main flux from pole to pole (so it must be ferromagnetic) and it must allow eddy-currents to be generated freely within it (so it should also have a low resistivity). Hence, for maximum electro-magnetic efficiency, the material must have a high μ/ρ ratio[8]. Pure

iron is usually used for this purpose since it has the most suitable combination of these properties, but this also has a low tensile strength. It is not possible therefore to use all the above combinations of couplings and field arrangements for high speed dynamometers.

Consider drum couplings; the field member obviously cannot be rotated at high speeds due to the winding(s). Only the drum can rotate and because it must be made from a highly permeable, but mechanically weak, material and because the yield strength of iron and steel reduces with temperature[51], the inside diameter, D, is seriously limited. It can be shown[8] that torque increases as $D^{2+}.L_D$, where L_D is the axial length of the drum. If D is restricted to a small value then, to produce a specific torque, L_D may have to be excessively large and whirling speeds may have to be considered. (Torque production is not normally a problem in large couplings say, greater than 75kW but cooling may be since cooling area only increases as $D.L_D$.)

Parasitic airgap machines are also possible and figure 1.2 shows two such couplings with interdigitated and inductor (homopolar) field arrangements. However, these tend to have complex geometry and weak sections on the rotor, as indicated. It is possible to strengthen this type of rotor by changing its geometry; it could then be rotated at high speeds, but as it still has to carry flux, it must be magnetic and so the problem of tensile strength remains. Nevertheless, this consideration is not as critical as for the loss drum since there is no heat produced in the rotor of parasitic types, except under transient conditions.

There are of course other variations of drum couplings, but all have a magnetic rotating member. Drum couplings were therefore rejected as unsuitable for high speed dynamometers of 75 kW and above.

Figure 1.3 shows two disc loss member couplings with salient pole field arrangements. As far as the author is aware there is only one publication[13] dealing with this type of coupling. There is no published data on disc inductor couplings, thus a design for such a machine was developed; its operation and constructional features are discussed in Appendix 4.

It was argued that both disc salient pole and disc inductor couplings were suitable for high speed applications. The advantages and disadvantages of both types are considered in chapter four and the disc inductor coupling was chosen as the most appropriate for use in a 75 kW, 14,000 rev/min dynamometer. The design of the prototype high speed machine is also discussed in chapter 4.

1.4 Survey of literature

1.4.1 Introduction

In most coupling literature the main objectives are to obtain expressions relating torque, slip speed, machine parameters and exciting current. Derivation of these expressions involves analysis of the electro-magnetic fields in and on the surface of the loss member. The problems[10] encountered in a theoretical treatment of these fields are the common ones met in any analysis of the electro-magnetic field in or near a conducting medium in which eddy-currents are present; the analysis only becomes particular to the coupling when the airgap geometry is taken into account.

In all theories the starting point is Maxwell's equations, and these apply to any conducting medium, magnetically linear or not, and they can be expanded in any co-ordinate system. Major complications arise when dealing with magnetically non-linear iron.

1.4.2 Publications

One of the first theoretical treatments of the coupling was given by Rudenburg[1] in 1906. He develops an elegant linear theory based on a homogeneous semi-infinite block in which the axial (y) and radial (z) directions are assumed infinite.

Armature reaction effects were taken into account by defining the resultant on load magnetic field in the loss member as

$$\bar{H} = \bar{H}_o + \bar{H}_r \qquad (1.1)$$

where $\bar{H}_o$ = standstill field set up by excitation member

$\bar{H}_r$ = eddy-current reaction field

and $\bar{H}$ = resultant field.

Since the standstill field $\bar{H}_o$ is irrotational[27, 60] it must therefore satisfy Laplace's equation and for Rudenburg's model this reduces to

$$\frac{\partial^2 \bar{H}_o}{\partial x^2} + \frac{\partial^2 \bar{H}_o}{\partial z^2} = 0 \qquad (1.2)$$

After solving (1.2) he substituted (1.1) into the linear diffusion equation and showed that

$$\frac{\partial^2 \bar{H}_r}{\partial x^2} + \frac{\partial^2 \bar{H}_r}{\partial z^2} = \frac{\mu}{\rho}\left(\frac{\partial \bar{H}_o}{\partial t} + \frac{\partial \bar{H}_r}{\partial t}\right) \qquad (1.3)$$

Rudenburg then goes on to give a solution for (1.3) and derive expressions for the dissipated power (P) in the loss member at high and low speeds. He shows that at low speeds

$$P \propto v^2$$

and at high speeds

$$P \propto v^{1/2}$$

where v is the velocity of the loss member with respect to the field, i.e. the slip speed.

An interesting feature of Rudenburg's theory, and one that almost every other author neglects, was his analysis of the neutral axis movement of the peripheral magnetic field ($H_{r,x}$). At rest this axis coincides with the pole centre line, but as velocity increases Rudenburg shows that it moves away from the centre line. Since the peak fundamental armature reaction mmf, $\hat{F}r_1$, must lead $\hat{H}_{r,x}$ by $\pi/2$ this means the zero of armature reaction also moves with velocity. Rudenburg did not give any experimental results and it was left to Davies[3], fifty-seven years later, to investigate the movement of the armature reaction zero.

Whilst Rudenburg's theory gives a basic understanding of the coupling, it does not yield useful practical results for couplings with ferrous loss members, due undoubtedly to neglect of variable μ. He accounted for the cross pole currents, which he assumed to flow wholly outside the active region, by a geometry multiplier; the effects of these end-region currents on the distribution of the electromagnetic field are commonly called end-effects.

Gibbs[2] gives the first valid treatment of practical couplings. He deals mainly with inductor couplings though, as Davies[3] points out, his results are valid for all couplings, with the correct modifications.

Gibbs assumes a fundamental axial current density only, Jz, and shows that the linear relationship for the surface loss density, W, is given by

$$W = \frac{\rho . J_m^2}{4 \alpha} \qquad (1.4)$$

Where α is the reciprocal of skin depth

ρ loss member resistivity

and Jm the peak fundamental surface current density. He derives expressions connecting current density, fundamental flux, machine parameters and slip speed and then goes on to show that

$$H_m = \frac{J_m}{\sqrt{2}\,\alpha} \qquad (1.5)$$

where Hm is the peak fundamental magnetic field intensity in the peripheral direction. He also shows that the phase displacement, between Hm and Jm is 45^{o}.

By eliminating Jm from equations 1.4 and 1.5 Gibbs introduces a term $\mu^{1/4}$ Hm. He takes numerical values from a typical loss member magnetisation curve and plots $\mu^{1/4}$ Hm against Hm, using this he was then able to find the numerical value of the fundamental a.c. flux necessary to support a given surface loss density W.

Gibbs realised his conceptual model was incorrect since it neglected cross pole currents. To account for these he assumed, like Rudenburg, that they flowed wholly outside the active region and also that they were resistance limited. By using the Schwartz - Christoffel transformation, which assumes Laplace's equation applies to the end-regions, he derives an equivalent end-region resistance which he compares with the active region resistance and produces a resistivity multiplier r. The use of Laplace's equation in the end-regions is logically inconsistent, but experimental and theoretical comparisons show that r gives good results, indicating its use is valid.

Gibbs' analysis is unsatisfactory in that he assumes the standstill airgap flux density is unchanged on load, which is manifestly wrong, and further he adds the fundamental flux and armature reaction components of excitation arithmetically, which is also wrong as they are displaced, in space, by a considerable angle.

Dissatisfaction with these aspects of Gibbs' theory led Davies[3,4] to his work on couplings. After including the peripheral field distribution, Davies follows

Gibbs approach up to equations 1.4 and 1.5. He shows that the loss equation is only valid when $\sqrt{2}.\alpha \gg 2\pi/\lambda$, where λ is the fundamental peripheral wavelength.

Davies, like Gibbs, rearranges his expressions to give

$$\mu^{1/4}.H_m = \left[\frac{8\ W}{\omega\ e}\right]^{1/4} \qquad (1.6)$$

At this point Davies introduces an analytical relationship which he discovered. He found from a log-log plot of $\mu^{1/4}$ H against H, for wrought iron that

$$\mu^{1/4}\ H = 0.97\ H^{0.77} \qquad (1.7)$$

which implies

$$B = 0.9\ H^{0.077} \qquad (1.8)$$

Davies points out that these equations only apply for values of H from 250 At/m to 250,000 At/m and postulates that this is the region where most couplings operate, i.e. above the knee of the B-H curve.

Using (1.7) allowed Davies to derive completely analytical equations for the peak fundamental armature reaction mmf, $\hat{F}r_1$ and fundamental a.c. flux per pole, ϕac_1. By comparing the flux producing capabilities of Fr_1 with the stand-still airgap flux density Davies derives a factor f, which he defines as

$$\hat{F}r_1' = f\ \hat{F}r_1 \qquad (1.8)$$

Where $\hat{F}r_1'$ is an equivalent field produced armature reaction mmf.

He then develops the fundamental performance equation of the coupling

$$Fg^2 = F\phi^2 + Fr'^2 - 2F\phi Fr'.\cos(\delta) \qquad (1.9)$$

where Fg = the applied excitation mmf to overcome armature reaction and set up ϕac_1 for a particular loss density.

$F\phi$ = fundamental flux component of mmf

and δ = 135° if $\sqrt{2}.\alpha \gg 2\pi/\lambda$

After differentiating (1.9), Davies derives expressions for peak fundamental torque, $T_{m,1}$, and speed at peak fundamental torque, $n_{m,1}$, which are both analytical and functions of the machine parameters and excitation mmf.

Substituting the expressions for $T_{m,1}$ and $n_{m,1}$ back into (1.9) Davies produces, perhaps his most important contribution, a generalised torque - slip curve for couplings.

Davies also presents a comprehensive experimental study of a Lundell coupling. He corroborates his theoretical work adequately and in the process developed many experimental techniques which have since been used, extensively by many authors.

To allow for end-effects Davies uses two experimental factors, r_1 and r_2; ϕac_1 is multiplied by r_1 to increase the active region induced voltage which must force the current density through the end-region impedance; r_2 is the factor by which the active region power must be increased to obtain the total dissipated power.

Davies also shows that the torque produced by the airgap flux density harmonics (harmonic torques) is small in the region of peak torque, he therefore limits all his analysis to fundamental quantities. However, even though the harmonic torques contribute little to T_m, the author suggests they may have a considerable effect on n_m, e.g. assume that the harmonic torques obey Davies generalised curve and also that a fifth and seventh harmonic torque, each of 0.16 $T_{m,1}$ and both acting at $6n_{m,1}$, are present plus the fundamental. By adding the harmonic torques to the fundamental, using the generalised curve, it can be shown that the resultant peak torque is 1.18 $T_{m,1}$, but the resultant speed at peak torque is 3.5 $n_{m,1}$.

In a later paper[8] Davies extended his theoretical approach to include the general expression

$$\mu^{1/4} H = k_1 H^m \tag{1.10}$$

or

$$B = a H^b \tag{1.11}$$

These equations extend Davies theory to cover any loss member material that obeys (1.11). He gives general equations for $T_{m,1}$, $n_{m,1}$, $\hat{Fr}_1$ and ϕac_1 in terms of the machine parameters, excitation and material parameter m. He also develops generalised loss, flux and armature reaction curves.

In the same paper he describes experimental tests on an inductor coupling. A theoretical comparison of inductor and Lundell couplings is also given.

James'[9] work is basically an experimental investigation of couplings with and without endrings. He shows that Davies generalised curves obey both types of coupling, indicating Gibbs' premise, that end-effects can be accounted for by a constant multiplier, is probably valid.

For his endring coupling, James demonstrated that there was a considerable flux density variation over the active region in the axial direction, suggesting the existence of active region cross pole currents which the endrings were supposed to eliminate.

Using linear theory, James estimates up to 40% harmonic torque for his endring coupling, which would suggest that Davies theory is not applicable to endring couplings yet, as already stated, James showed that it was. His value of harmonic torques must therefore be too high.

James deals with end-effects using the same model as Gibbs. He derives a loss multiplier based on the end-region scalar potential and shows that it gives better results than Gibbs' resistivity multiplier. However, it suffers from the same logical inconsistencies as Gibbs' end-effect treatment.

Both Gibbs and Davies theory are subject to the same strictures:

a) They both combine a non-linear relationship for μ with the results of linear analysis. This cannot be justified mathematically but seems to give good results in practice.

b) Equation 1.5 is fundamental to both their theories and so as Davies states ... 'once the value of μ at Hm is found, it applies for the whole sinusoidal excersion of the flux density for all points in the drum. This can only be justified by the results that it gives in practice.' In other words both neglect the spatial variation of permeability.

Bowden[14], whilst not dealing specifically with couplings, gives an excellent non-linear two dimensional theory of electro-magnetic fields in solid iron. The results of which, are easily adapted to coupling theory using Davies'[8] methods for dealing with the airgap geometry.

From Maxwells equations, Bowden shows that

$$\nabla^2 \bar{H} = - \frac{1}{\rho} \cdot \frac{\partial \bar{B}}{\partial t} \qquad (1.12)$$

This equation is the general diffusion equation, it applies to all media, linear or non-linear, and only assumes that Ohm's law is valid, i.e. $E = \rho J$.

Bowden substitutes (1.11) into (1.12) then, in common with Davies, he assumes the peripheral magnetic field, H_x, is much greater than the radial component, H_y. He goes on to obtain a solution for the resulting non-linear differential equation in which both the spatial and time variation of μ is implicitly accounted for. Bowden's solution for the attenuation of the magnetic field as it penetrates the iron is given by

$$\hat{H}_x(y,t) = \hat{H}_x(o,t) \left[1 - \alpha_n \cdot y\right]^{\beta_n} \qquad (1.13)$$

where $\hat{H}_x(y,t)$ = the peak value of the peripheral magnetic field at any depth y.

$\hat{H}_x(o,t)$ = peak value of the peripheral magnetic field at the surface.

$1/\alpha_n$ = limiting depth of penetration or skin depth

and β_n = the attenuation factor. (Both α_n and β_n are functions of the material parameter b in equation 1.11).

From the Maxwell equation

$$\text{curl } \bar{H} = \bar{J}$$

Bowden derives the general expression for current density and hence the electric field. Then, using Poynting theorem, he obtains the dissipated power in the loss member. He also derives expressions for fundamental flux and peak fundamental armature reaction mmf. Bowdens theory predicts a phase displacement of 36^o between the peak fundamental axial current density and the peripheral magnetic field strength at the surface.

Bowden's theory however, only accounts for the fundamental saturation harmonic and so his theory, in its published form, is limited to deriving the fundamental electro-magnetic relationships only.

To account for end-effects, Bowden equates a linear two dimensional theory to his theory and obtains an equivalent non-linear permeability μ_e. He then substitutes μ_e into a linear three dimensional analysis[10] and obtains a power distribution factor R_L. Whilst this end-effect solution is an improvement on most other attempts, it still has its limitations, since the value of μ_e chosen is assumed to apply to all points in the loss member.

Gonnen and Stricker[7] are the only other authors to include the spatial variation of permeability. They use the equation

$$\mu = \mu_s e^{\lambda y}$$

where μ_s is the surface permeability ($y = o$) and λ is approximately equal to the reciprocal of the skin depth, $1/\delta$. Their solution to Maxwell's equations is based on Hankel functions and therefore the parameters that govern coupling operation are obscured in their final expressions.

They account for end-effects using a resistivity multiplier, similar to Gibb's; they also estimate up to 40% increase in torque due to the excitation mmf harmonics.

Malti and Ramakumar[5] give a linear three dimensional solution for an inductor coupling. They include armature reaction effects in a similar manner to Rudenburg (equation 1.1) except they use flux densities and define their basic relationship as

$$\bar{B} = \bar{B}_1 + \bar{B}_2 \qquad (1.14)$$

where $\bar{B}_1$ = the standstill flux density

$\bar{B}_2$ = armature reaction flux density

and $\bar{B}$ = the resultant.

Following Rudenburg, their basic equation is given by

$$\nabla^2 \bar{B}_2 = \frac{\mu}{e} \cdot \left(\frac{\partial \bar{B}_1}{\partial t} + \frac{\partial \bar{B}_2}{\partial t} \right) \qquad (1.15)$$

Malti et al resort to a crude type of Carter's coefficient to determine the effects of airgap geometry. They introduce an equivalent smooth airgap by multiplying the actual airgap length by the ratio of pole pitch to pole arc, $1/K_2$ (including fringing effects) and then, account for the rate of change of airgap permeance by multiplying $\partial \bar{B}_2 / \partial t$ by K_2, which is effectively an average value.

To solve (1.15) they assume the eddy-current distribution in the loss member is 'laminar', i.e. the currents flow in layers, and means that only two

components of current density exist. This assumption is only strictly correct when the eddy-current reaction is negligible, which in practical couplings is not correct.

After deriving the two components of current density they obtain what they claim is the three dimensional power loss in the loss member, and hence an expression for torque. Their analysis implicitly accounts for armature reaction, end-effects and harmonic torques but neglects variable μ.

They give theoretical and experimental torque-slip curves for an inductor coupling which, they claim, show the correctness of their theory. At low excitations their claim seems valid but at high excitations there is little evidence to suggest that their theory is correct. Undoubtedly their poor correlation at high excitations is due to neglect of variable permeability.

They also say that 'by solving their problem in three dimensions', which is a misnomer since they assume laminar conditions, 'the region between the set of north and south poles need not be treated separately'. This is wrong because the eddy-currents in this middle region, in their coupling, are effectively separate and for theoretical purposes their type of inductor coupling should be treated as two separate machines, as will be shown in chapter 5. In addition they also neglect to say how they determine the apparent length of loss member, i.e. the length in which all the eddy-currents are assumed to flow. This is a particularly vexing problem in a three dimensional analysis. (See chapter 2, section 2.15.1).

Wright[10] gives a three dimensional treatment of the copper faced coupling. By assuming the backing iron is linear he derives expressions for the loss in the copper and iron. Using the expressions he shows that the influence of the backing iron on the performance of most practical copper faced couplings is negligible and that the main purpose of the iron is to carry the pole flux.

From the loss equations, he follows Davies' basic methods and derives expressions for T_m and n_m in terms of the machines parameters and excitation. Wright then shows that not one but a family of generalised torque-slip curves are necessary to describe the behaviour of all copper faced couplings. These curves are functions of a dimensionless parameter G which, for a given machine is proportional to

$$G \propto \frac{1}{\sqrt{d(g+d)}}$$

where d = depth of copper

g = physical airgap length

and (g + d) = magnetic airgap.

Wright also develops an excellent theory for the transient performance of couplings. This theory is based on transient solution of the two dimensional diffusion equation using Laplace transforms and the convolution theorem for the resulting inversion. End-effects are neglected.

He corroborates the theory using test results from a copper endring coupling. Wright also shows that his endring coupling obeys Davies steady state theory.

Naturally, there are many other publications dealing with eddy-current couplings, but most do not include at least one or more of the four considerations which are generally thought to be the most important:

i) Armature reaction,

ii) Variable μ,

iii) End-effects,

iv) Harmonic torques.

No author has dealt successfully with all these topics.

There is also, of course, related literature on solid rotor induction motors but these have not been discussed because their airgap geometry is different from a couplings.

Gibbs[2] is the only author to consider, although only briefly, loss member cooling.

A more detailed discussion than this of the problems involved in coupling analysis is given in reference 10.

CHAPTER 2

THE EFFECTS OF LOSS MEMBER TEMPERATURE ON THE PERFORMANCE AND DESIGN OF EDDY-CURRENT COUPLINGS AND DYNAMOMETERS.

2.0 The effects of loss member temperature on the performance and design of eddy-current couplings and dynamometers

2.1 Introduction

There were two main reasons for this work on temperature effects in eddy-current couplings:

a) Both T_m and n_m were known[4, 9, 10] to fluctuate considerably with the temperature of the loss member. This is due to both physical and electrical changes in the coupling. Hence, for assessment of the movement in the torque-speed curves and satisfactory design of the cooling system, the parameters which determine the loss member temperature must be found.

b) Since the loss member temperature is critical in large couplings, it would be useful if thermal ratings and optimum operating times could be given under certain conditions. For this, the thermal time constant and the parameters that control it must be known.

There is little information in the literature on coupling cooling systems or the effects of temperature upon their performance. At present, cooling system design is based on previous test results and a few semi-empirical equations. It is therefore desirable to put this in a more precise basis.

An analysis is presented which shows the effects of the fundamental design parameters on the loss member temperature and thermal time constant. It is also shown that most of the common cooling methods can be incorporated into this theory by using a general equation for the Nusselt number.

2.2 Loss member temperature and its effect on T_m and n_m

Davies[4, 8], James[9] and Wright[10] all observed that the torque-speed curve of a practical coupling would be changed by the temperature of the loss member. However, their particular experimental work was carried out quickly and the loss

member temperature was not allowed to rise appreciably so they did not consider this effect in any detail. Gibbs[2] also discusses this problem.

Temperature effects in the two general groups of coupling, drum and disc types, are discussed in the following sections.

2.2.1 Temperature effects in drum couplings

It can be shown[8] that

$$T_m \propto 1/g \qquad (2.1)$$

and

$$n_m \propto \rho\, g^2 \qquad (2.2)$$

Both ρ and g are functions of loss member temperature as are the constants of proportionality for both these equations. These constants are functions of the loss member B-H curve[3,14] which in turn is a function of loss member temperature. Bozorth[31] shows that the effects of material temperature on magnetisation curves is small over the limited temperature range being considered here. Therefore, to a first order approximation, all the terms in T_m and n_m that are derived from the B-H curve may be considered independent of temperature.

To observe the effects of drum expansion, tests were carried out by the author which showed that the airgap length could change by up to 50% in small couplings. From equation 2.1 this means the peak torque will change by inverse proportion; a worked example is given later to illustrate drum expansion more clearly. The results of the tests, which were carried out on Davies[3] and James[9] couplings, are given in chapter 3.

The resistivity, ρ, of the drum is a direct function of temperature and the electrical characteristics of the coupling are changed significantly if it varies. At high frequencies the value of resistivity to be used in any calculations is based

on the temperature of the skin depth which, for all practical purposes, can be assumed the same as the active surface. During normal operation ρ can increase by two to three times over its ambient value.

Consider a typical air-cooled coupling[3] with a 'cold' drum inside diameter, D, of 0.159m, a 'cold' airgap length, g, of 2.54×10^{-4}m, an active surface temperature of 150°C, a back face temperature of 115°C and ambient of 15°C. Also assume that the drum radial thickness is small compared with its diameter and that the field member does not expand.

From figure 2.1, which shows the resistivity of 'Armco'* iron plotted against temperature,

$$\rho\,(150^{\circ}C) \simeq 2\,\rho\,(15^{\circ}C)$$

Calculation of drum expansion is based on the back face temperature of the loss (Fig 1.1) member. The coefficient of thermal expansion, α, for iron and steel is approximately 12×10^{-6} per $^{\circ}$K. Hence, using the well known equation

$$L_h = L\,(1 + \alpha t)$$

where t is the temperature difference between ambient and the drum back face temperature, $L = \pi D$ and $L_h = \pi D_h$ the peripheral lengths of the loss drum cold and hot respectively. Substituting the appropriate values yields

$$D_h = D(1.0012) = 0.15919\text{m}$$

Subtracting the original 'cold' drum diameter from this gives the change in diameter as 1.9×10^{-4}m, which is double the change in airgap length, i.e. 0.95×10^{-4}m per airgap. Whence

$$g_h(\text{hot}) = 1.4g$$

---

* Armco or pure iron is usually used for coupling loss members because of its high μ/ρ ratio.

putting the values of ρ (150°C) and g_h (hot) into expressions 2.1 and 2.2 it can be shown that

$$\frac{T_m(\text{hot})}{T_m(\text{ambient})} = 0.715$$

and

$$\frac{n_m(\text{hot})}{n_m(\text{ambient})} = 3.92$$

These are pessimistic values nevertheless, the effects of loss member temperature are clearly demonstrated. The overall effect of drum temperature on the torque-slip curves, at constant excitation, is shown pictorially on figure 2.2

2.2.2 Temperature effects in disc couplings

The same basic arguements apply to disc couplings except that the loss member thickness is usually small compared to the disc diameter. Consequently, the expansion in the axial direction is negligible. Expansion in the radial direction is unimportant. This means that the airgap length, g, does not change and so peak torque is a constant and not a function of temperature. However, ρ still changes and so

$$n_m \propto \rho \qquad (2.3)$$

If ρ doubles, torque at a particular speed only falls by about 20%. This can be shown using Davies generalised torque-slip curve[8]. The above observations will be verified by experiment later.

2.3 Parameters affecting loss member temperature

The loss member temperature may be affected by:

a) W_o, active region surface heat flux or loss density in watts/m^2; which is a function[4, 8] of p, D, L_A, g, K(K') and excitation (Fg).

b) Physical properties of loss member, specific heat (c_s), material density (ρ_s), and thermal conductivity (K_s).

c) Loss member thickness (d_L).

d) Coolant inlet temperature ($t_{1.c}$).

e) Velocity of coolant (v_c).

f) Whether coolant flows in slots or across a flat surface; if in slots, their number (n) and hydraulic mean diameter (d_p).

g) Physical properties of coolant, viscosity (μ_c) density (ρ_c), thermal conductivity (K_c) and specific heat (c_c).

h) Radiation in the airgap.

i) Convection in the airgap.

j) Any low thermal resistance paths; the effect of these on temperature will depend to a large extent on the temperature gradient through the loss member to the coolant.

The value of W_o for an endring machine is usually straightforward but for a coupling with a solid iron loss member it is modified by electrical end-effects. Heat losses may also have to be taken into account in both; these are discussed later.

A theory covering all these factors is extremely complicated so a) to g) have been included, h) and i) can be taken into account, approximately, after the active region surface temperature has been found and j) is considered a second order effect.

2.4 Thermal time constant

The time for a coupling to reach steady state temperature conditions when running at constant speed and constant torque depends on similar factors to those listed in section 2.3. Air cooled couplings tend to have very large thermal time constants compared to water cooled couplings. In turn, both these are usually large compared to the electrical time constants.[10,11]

It would be very useful commercially if couplings could be given short time and continuously rated dissipation capacities. A typical example of this would be an eddy-current brake which operates for a short time over a lengthy duty cycle.

Choosing the size of such a coupling could be based on the short time rating and so its selection is optimised for this particular application. At present the choice of a coupling for this type of duty would almost certainly be founded on the designer's previous experience and would probably tend to be too large.

2.5 Transient theory of loss member temperature

The theory is based on solution of the diffusion or heat flow equation with two 'radiation'* boundary conditions[45]. The general form of the diffusion equation for most heat flow problems can be shown to be[45,46,48]

$$\nabla^2 \theta = \frac{c_s \rho_s}{K_s} \cdot \frac{\partial \theta}{\partial t} \qquad (2.4)$$

At first sight, this equation does not seem valid since no term has been included to account for heat generated within the surface of the loss member, which there obviously is in a coupling. However, we are only interested in the effects of high loss member temperatures on the performance of the coupling and for a given excitation, the highest temperatures occur at maximum slip speed. Hence, the eddy-current skin depth, δ, in most practical couplings is very small and so the loss skin depth, which is $\delta/2$, is even smaller; this is easily shown for both

---

* The term 'radiation' boundary condition is classical notation, but as Carslaw and Jaeger[45] point out, it is a little misleading and the clumsier but more accurate description is 'linear heat transfer into a medium at a temperature t'.

linear[10] and non-linear[14] electro-magnetic theories using the well known relationship

$$P = \int \varrho \cdot \bar{J}^2$$

All the heat is therefore generated within a thin surface skin of negligible thermal capacity and so it may be assumed that the coupling has a loss member of thickness $d_L - \delta/2$ with a heat flux into its surface. Equation 2.4 is now directly applicable to the problem. This mathematical simplification considerably reduces the labour involved in solving the equations. Nevertheless, the problem is still complex because of the two 'radiation' boundary conditions.

Many authors[32, 33] have solved this problem assuming an infinite block and using one of these boundary conditions at the surface, but this is clearly not applicable to couplings with a finite loss member thickness and a cooling fluid passing over the back face.

The main difficulties in the solution arise in the inversion of the final transformed equations and determining the value of surface heat flux to use in the equations. A numerical technique was used to invert the equations and a general method is developed using a table of typical values. Extreme care has to be exercised when finding the value of surface heat flux. Not only do electrical end-effects have to be taken into account but also the heat flux losses. Both of these are discussed in detail later.

The term $c_s \varrho_s / K_s$ in equation 2.4 is sometimes replaced by $1/k$, where k is called Kelvin's diffusivity constant and it is analagous to μ/ϱ encountered in electrical problems on diffusion. For iron, μ is a variable and depends on B and H, similarly c_s/K_s is a variable but depends on the temperature of the iron.

Figure 2.3 shows specific heat, c_s, and thermal conductivity, K_s, plotted against temperature for a low carbon steel such as mild steel or 'Armco' iron.

It can be seen that both c_s and K_s vary considerably with temperature. An equation of the type $y = m.t + c$ could be fitted to both graphs over the range $0 - 600^{o}C$* if desired and then substituted into equation 2.4.

The problem however is analytically intractable and numerical methods have to be used to solve the equations. Moreover, the design parameters that control the loss member temperature would be obscured in the numerical solution a compromise must therefore be made.

It has been found from experimental data that the temperature range we are interested in for most couplings is 0 to $300^{o}C$. The variation of c_s/K_s over this range is shown on figure 2.4; if an average value of c_s/K_s is taken then its maximum possible error is $\pm$ 20%, and for most practical purposes $c_s \cdot \rho_s/K_s$ may be assumed constant. With experience it is possible to estimate coupling temperatures therefore; more accurate values of c_s/K_s can be obtained.

VARIATION OF SPECIFIC HEAT / THERMAL CONDUCTIVITY WITH TEMPERATURE.

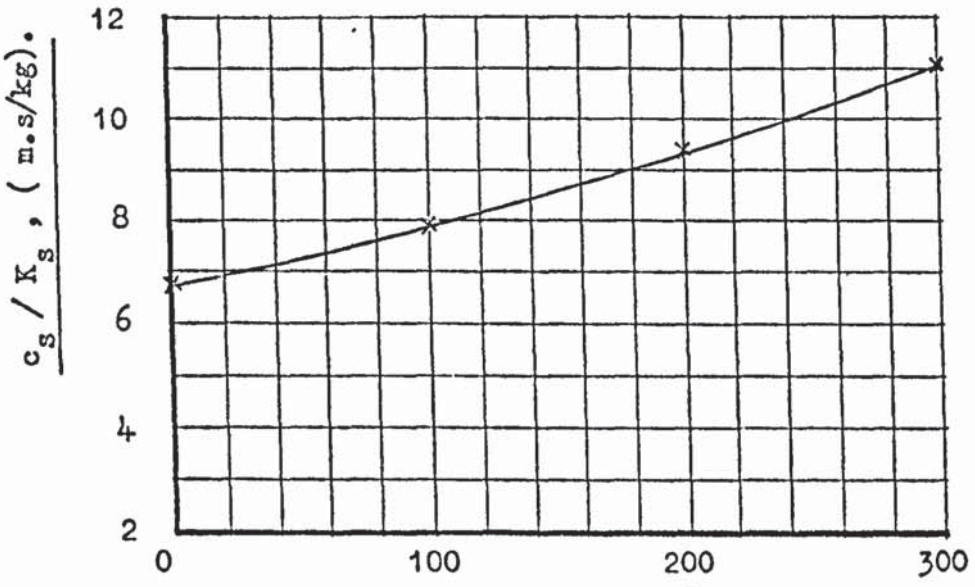

Figure 2.4

---

* Above approximately $600^{o}C$ the electrical equations cease to be strictly valid because of the "Onset" of the Curie point[31].

2.6 Simplifying Assumptions

Equation 2.4 gave the general form of the diffusion equation. This can be expanded in any co-ordinate system and the two most commonly used in coupling theory are polar and cartesian co-ordinates.

For drum couplings if d_L the drum thickness is small compared to D the drum inside diameter there is little error[3] in using cartesian co-ordinates. The complete cartesian form of the diffusion equation is given by

$$\frac{\partial^2\theta}{\partial x^2} + \frac{\partial^2\theta}{\partial y^2} + \frac{\partial^2\theta}{\partial z^2} = \frac{c_s \rho_s}{K_s} \cdot \frac{\partial \theta}{\partial t} \qquad (2.6)$$

This equation has been found to give good results for drum couplings even for small machines such as the one used by Davies[4,8].

By considering the temperature gradients in a drum coupling equation 2.6 can be simplified. Because of symmetry, the gradient in the peripheral direction is zero and so

$$\frac{\partial \theta}{\partial x} = 0 \qquad (2.7)$$

In most practical cases the temperature gradient through the loss member is large compared to the temperature gradient in the axial direction. Hence

$$\frac{\partial \theta}{\partial y} \gg \frac{\partial \theta}{\partial z} \simeq 0 \qquad (2.8)$$

This approximation is not strictly correct for small 'naturally' cooled couplings where the loss member rotates in still air; but even for these good results have been obtained, as will be shown later.

Substituting 2.7 and 2.8 into equation 2.6 gives the approximate differential equation to the temperature distribution in a drum coupling

$$\frac{\partial^2\theta}{\partial y^2} = \frac{c_s \rho_s}{K_s} \cdot \frac{\partial \theta}{\partial t} \qquad (2.9)$$

For disc couplings polar co-ordinates must be used and the polar form of the diffusion equation is

$$\frac{1}{r}\cdot\frac{\partial^2\theta}{\partial \phi^2} + \frac{\partial^2\theta}{\partial z^2} + \frac{\partial^2\theta}{\partial r^2} + \frac{1}{r}\cdot\frac{\partial\theta}{\partial r} = \frac{c_s \rho_s}{K_s} \cdot \frac{\partial \theta}{\partial t} \qquad (2.10)$$

Using similar argu ments, for the temperature gradients, to those applied to drum couplings it can be shown that

$$\frac{\partial \theta}{\partial \phi} = 0 \qquad (2.11)$$

and

$$\frac{\partial \theta}{\partial z} \gg \frac{\partial \theta}{\partial r} \simeq 0 \qquad (2.12)$$

Putting these relationships into equation 2.10 reveals that Bessel's equation is not involved in the solution and the resulting differential equation for disc couplings is given by

$$\frac{\partial^2\theta}{\partial z^2} = \frac{c_s \rho_s}{K_s} \cdot \frac{\partial \theta}{\partial t} \qquad (2.13)$$

Equations 2.9 and 2.13 have the same form, so the same solution can now be used for both disc and drum couplings.

2.7 Summary of Assumptions

The theory is based on the following assumptions:

a) The temperature throughout the skin depth is the same as the surface temperature.

b) A value of active region surface less density W_o can be defined and is assumed to pass entirely into the loss member at the surface. In practice W_o is not necessarily the same as W_T, the total loss density, because of heat losses.

c) The temperature gradient through the loss member is large and any low thermal resistance paths do not modify the temperature distribution greatly.

d) At high slip speeds all the heat is generated within the loss skin depth which has a negligible thermal capacity.

e) The material properties c_s, ρ_s and K_s are all assumed constant, based on the discussion in section 2.5.

f) Airgap heat transfer, i.e. radiation and conduction, are neglected for the time being.

g) The loss member temperature differential equation is the same for both disc and drum couplings.

h) All the heat flux that passes in at the surface is carried away by the back face coolant, i.e. there are no heat losses in the loss member.

i) Thermal time constants are much greater than the electrical time constants[10,11]; this means the thermal system does not detect any small electrical changes.

2.8 Solution of the loss member temperature differential equation

The following analysis is based on drum couplings for clarity, but is equally applicable to disc couplings; consider equation 2.9

$$\frac{\partial^2 \theta}{\partial y^2} = \alpha_s^2 \cdot \frac{\partial \theta}{\partial t} \qquad (2.14)$$

where $$\alpha_s^2 = c_s \cdot \rho_s / K_s \qquad (2.15)$$

Taking Laplace transforms with respect to time gives

$$\frac{\partial^2 \bar{\theta}(y,s)}{\partial y^2} - \alpha_s^2 s\, \bar{\theta}(y,s) = -\alpha_s^2\, \theta(y,o) \qquad (2.16)$$

$\theta(y, o)$ is the temperature of the loss member at any depth at $t = o$. If the loss member is the same temperature throughout them $\theta(d, o) = \theta(o, o) = \theta(y, o) \triangleq t_{1,c}$, where $t_{1,c}$ is the temperature of the back face coolant at the inlet to the coupling; it may also be the ambient temperature.

The transformed equation 2.16 is a standard second order differential equation which has two solutions, a particular integral and complementary function. These can be solved using classical methods and the complete general solution can be shown to be

$$\bar{\theta}(y,s) = A.\cosh(\alpha_s y s^{1/2}) + B.\sinh(\alpha_s y s^{1/2}) + t_{1,c}/s \qquad (2.17)$$

Appropriate boundary conditions must be applied to this to obtain a particular solution for couplings.

2.9 Boundary conditions

The developed analytical model is shown on figure 2.5. At the surface y = o the 'radiation'[45] boundary condition is given by

$$W_o = - K_s \cdot \frac{\partial \theta(y,t)}{\partial y} \qquad (2.18)$$

The negative sign shows that the flow of heat is in the direction of decreasing temperature.

Taking Laplace transforms

$$\frac{\partial \bar{\theta}(y,s)}{\partial y} = - \frac{W_o}{s \cdot K_s} \qquad (2.19)$$

Assuming no heat is lost in the loss member, then the heat flux W_o that passes in at the surface y = o must be carried away by the coolant on the back face at $y = d_L$. The general boundary condition for heat flow from a solid to a fluid can be shown[45] to be

$$K_s \cdot \frac{\partial \theta(y,t)}{\partial y} = - h_c \cdot \theta_m \qquad (2.20)$$

where h_c = Nu K_c/L, the surface heat transfer coefficient on the loss member back face.

L is the characteristic dimension; for drum couplings the outside diameter, D_o, will be taken.

Nu, Nusselt number

θ_m, mean film temperature and is the difference between the back face temperature $\theta(d, t)$ and the coolant. Usually the arithmetic* mean film temperature is used

---

* There are two methods of caluclating θ_m - the logarithmic mean and arithmetic mean - both are discussed in reference 46.

$$\theta_m = \left[\frac{\theta_1 + \theta_2}{2}\right] \tag{2.21}$$

and $$\theta_1 = (\theta(d,t) - t_{1,c}) \tag{2.22}$$

$$\theta_2 = (\theta(d,t) - t_{2,c}) \tag{2.23}$$

Substituting θ_1 and θ_2 into equation 2.21 and rearranging yields

$$\theta_m = \left[\theta(d,t) - (t_{1,c} + t_{2,c})/2\right] \tag{2.24}$$

The name given to the term $(t_{1,c} + t_{2,c})/2$ is the mean bulk temperature, $t_{b,c}$, of the cooling fluid and it is this temperature that is usually used when evaluating the physical properties of the cooling medium.

Putting equation 2.24 into 2.20 gives the general result

$$\frac{\partial \theta(y,t)}{\partial y} + \frac{h_c}{K_s} \cdot \theta(y,t) = \frac{h_c \cdot t_{b,c}}{K_s} \tag{2.25}$$

Taking Laplace transforms

$$\frac{\partial \bar{\theta}(y,s)}{\partial y} + \frac{h_c}{K_s} \cdot \bar{\theta}(y,s) = \frac{h_c \cdot t_{b,c}}{s\, K_s} \tag{2.26}$$

Equations 2.19 and 2.26 can now be applied directly to the general solution, equation 2.17, to find the constants A and B.

The equation for the back face heat transfer coefficient, h_c, depends upon the type of coupling and the geometry of the cooling system. Convection is analytically very complex and empirical equations must be used in the solution. Nonetheless, a general form[48] of the Nusselt number, Nu, exists, which applies for all the important configurations encountered in couplings, i.e.

$$Nu = a\, Re^{b}\, Pr^{c} \tag{2.27}$$

where Re is the Reynolds number, Pr the Prandtl number and a, b and c are constants which are dependent upon the coupling and cooling system; they are determined experimentally and a review of them is given in Appendix 1. Under certain conditions the Reynolds number must be replaced by a term which includes a function of both the Reynolds and Grashof number; this is also discussed.

2.10 Particular solution using boundary conditions

Applying the boundary conditions given by equations 2.19 and 2.26 to the general solution, equation 2.17, and putting y = o and y = d_L respectively it can be shown that

$$\bar{\theta}(y,s) = \frac{\left[\frac{W_o}{sK_s}\left[\cosh(\alpha_s d_L s^{1/2}) + \frac{h_c \cdot \sinh(\alpha_s d_L s^{1/2})}{s^{1/2} K_s \alpha_s}\right] + \frac{h_c(t_{2,c}+t_{1,c})}{2sK_s}\right]\cosh(\alpha_s y s^{1/2})}{\left[\alpha_s s^{1/2} \cdot \sinh(\alpha_s d_L s^{1/2}) + \frac{h_c}{K_s} \cdot \cosh(\alpha_s d_L s^{1/2})\right]}$$

$$- \frac{W_o \cdot \sinh(\alpha_s y s^{1/2})}{\alpha_s K_s s^{3/2}} + \frac{t_{1,c}}{2} \qquad (2.28)$$

This equation is the general solution to the transient temperature distribution in terms of the Laplace operator s and co-ordinate dimension y, which is the depth into the loss member from the active surface.

$\bar{\theta}(y,s)$ must now be inverted to the time domain and as can be seen the general expression is extremely complicated. Various parts can be inverted using standard Laplace transform tables; the others have to be inverted either numerically or using Cauchy's integral formula[57, 58, 59] (C.I.F.), or a combination of both.

To use C.I.F. the numerator of the relevant parts must be analytic and the zeros of the denominator must be found. If these conditions are fulfilled, then $\bar{\theta}(y,s)$ as a whole can be shown to satisfy Jordan's Lemma[58,59] and as

$$|s| \longrightarrow \infty$$

then

$$F(s) \longrightarrow 0$$

Cauchy's integral formula is given by

$$\theta(y,t) = \frac{1}{2\pi j} \oint_J \frac{\text{Numerator}}{\text{Denominator}} . e^{st} . ds \Bigg|_{s \to 0} \qquad (2.29)$$

This technique of inversion is straightforward and widely used; the major problem inverting equation 2.28 is finding the zeros of the denominator term

$$\left[\alpha_s s^{1/2} . \sinh(\alpha_s d_L s^{1/2}) + \frac{h_c}{K_s} . \cosh(\alpha_s d_L s^{1/2})\right] \qquad (2.30)$$

No simple analytical solution is available for this expression and a general method must be employed to find its roots, i.e. what values of s make the equation zero.

2.11 Denominator zeros of $\bar{\theta}(y,s)$

It is convenient to rewrite equation 2.30 in terms of the harmonic functions sine and cosine.

Hence, rearranging

$$-\frac{K_s \alpha_s s^{1/2}}{h_c} = \coth(\alpha_s d_L s^{1/2})$$

Putting s = -s and expanding both in terms of exponentials it can be shown that

$$z = \cot(\beta z) \qquad (2.31)$$

where

$$z = \frac{K_s \alpha_s s^{1/2}}{h_c} \qquad (2.32)$$

and β is a non-dimensional quantity defined by

$$\beta = \frac{h_c d_L}{K_s} \qquad (2.33)$$

In general the expression 2.31 has three solutions:

a) z real

b) z imaginary

c) z complex in x + jy form.

To find the real or imaginary roots is relatively simple but to find the complex roots considerable analysis is necessary. (See section 2.11.3).

2.11.1 Real roots of the denominator of $\bar{\theta}(y,s)$

Putting z = x into equation 2.31

$$x = \cot(\beta x)$$

The roots of this are found simply by plotting the function with different values of β; for this particular solution it is convenient for graph plotting to change the form of the equation slightly.

Let $\beta x = x'$ this gives

$$\frac{x'}{\beta} = \cot(x') = f_x \qquad (2.34)$$

Figure 2.6 shows this plotted. The slope of the straight line is $1/\beta$ and depends on the loss member thickness d_L, heat transfer coefficient h_c and the loss member thermal conductivity K_s. It can be seen from this graph that there are an infinite number of positive and negative roots; the negative roots are equal in absolute value to the positive ones and also there are no repeated roots. The roots occur when

$$x' = \pm p_n = \alpha_s d_L s^{1/2}$$

Rearranging gives

$$s = -\frac{p_n^2}{\alpha_s^2 d_L^2} \qquad (2.35)$$

This shows that the roots of the denominator of $\bar{\theta}(y,s)$ all lie on the negative real axis when z is real.

If equation 2.34 is rearranged as

$$x' \tan(x') = \beta \qquad (2.36)$$

it becomes a well known Transcendental Equation[45] and its first six roots for various values of β are given in table 2.1. To obtain the roots for β values not given in the table the plotting technique described above must be used.

2.11.2 Imaginary roots of the denominator of $\bar{\theta}(y,s)$

Substituting $z = jy$ into equation 2.31 yields

$$jy = \cot(j\beta y)$$

rewriting cot. in terms of exponentials it can be shown that

$$-y = \coth(\beta y) = f_y \qquad (2.37)$$

Figure 2.7 shows this plotted and as can be seen the negative sloping straight line will never cross the coth (βy) curves. This means that equation 2.37 has no imaginary roots which is to be expected since the temperature response is known to approach a limiting value.

2.11.3 Complex roots of the denominator of $\bar{\theta}(y,s)$

Expanding equation 2.31 in terms of exponentials and simplifying gives

$$e^{2j\beta z} = \left[\frac{z+j}{z-j}\right]$$

TABLE 2.1

The first six roots , P_n , of the Transcendental Equation

$$x' \tan(x') = \beta$$

β	P_1	P_2	P_3	P_4	P_5	P_6
0	0	3·1416	6·2832	9·4248	12·5664	15·7080
0·001	0·0316	3·1419	6·2833	9·4249	12·5665	15·7080
0·002	0·0447	3·1422	6·2835	9·4250	12·5665	15·7081
0·004	0·0632	3·1429	6·2838	9·4252	12·5667	15·7082
0·006	0·0774	3·1435	6·2841	9·4254	12·5668	15·7083
0·008	0·0893	3·1441	6·2845	9·4256	12·5670	15·7085
0·01	0·0998	3·1448	6·2848	9·4258	12·5672	15·7086
0·02	0·1410	3·1479	6·2864	9·4269	12·5680	15·7092
0·04	0·1987	3·1543	6·2895	9·4290	12·5696	15·7105
0·06	0·2425	3·1606	6·2927	9·4311	12·5711	15·7118
0·08	0·2791	3·1668	6·2959	9·4333	12·5727	15·7131
0·1	0·3111	3·1731	6·2991	9·4354	12·5743	15·7143
0·2	0·4328	3·2039	6·3148	9·4459	12·5823	15·7207
0·3	0·5218	3·2341	6·3305	9·4565	12·5902	15·7270
0·4	0·5932	3·2636	6·3461	9·4670	12·5981	15·7334
0·5	0·6533	3·2923	6·3616	9·4775	12·6060	15·7397
0·6	0·7051	3·3204	6·3770	9·4879	12·6139	15·7460
0·7	0·7506	3·3477	6·3923	9·4983	12·6218	15·7524
0·8	0·7910	3·3744	6·4074	9·5087	12·6296	15·7587
0·9	0·8274	3·4003	6·4224	9·5190	12·6375	15·7650
1·0	0·8603	3·4256	6·4373	9·5293	12·6453	15·7713
1·5	0·9882	3·5422	6·5097	9·5801	12·6841	15·8026
2·0	1·0769	3·6436	6·5783	9·6296	12·7223	15·8336
3·0	1·1925	3·8088	6·7040	9·7240	12·7966	15·8945
4·0	1·2646	3·9352	6·8140	9·8119	12·8678	15·9536
5·0	1·3138	4·0336	6·9096	9·8928	12·9352	16·0107
6·0	1·3496	4·1116	6·9924	9·9667	12·9988	16·0654
7·0	1·3766	4·1746	7·0640	10·0339	13·0584	16·1177
8·0	1·3978	4·2264	7·1263	10·0949	13·1141	16·1675
9·0	1·4149	4·2694	7·1806	10·1502	13·1660	16·2147
10·0	1·4289	4·3058	7·2281	10·2003	13·2142	16·2594
15·0	1·4729	4·4255	7·3959	10·3898	13·4078	16·4474
20·0	1·4961	4·4915	7·4954	10·5117	13·5420	16·5864
30·0	1·5202	4·5615	7·6057	10·6543	13·7085	16·7691
40·0	1·5325	4·5979	7·6647	10·7334	13·8048	16·8794
50·0	1·5400	4·6202	7·7012	10·7832	13·8666	16·9519
60·0	1·5451	4·6353	7·7259	10·8172	13·9094	17·0026
80·0	1·5514	4·6543	7·7573	10·8606	13·9644	17·0686
100·0	1·5552	4·6658	7·7764	10·8871	13·9981	17·1093
∞	1·5708	4·7124	7·8540	10·9956	14·1372	17·2788

Putting z = (x+jy) and separating the modulus and argu ment produces:

Modulus

$$e^{-4\beta y} = \left[\frac{x^2 + (y+1)^2}{x^2 - (y-1)^2}\right] = f_{z,m} \qquad (2.38)$$

Argument

$$2\beta x = \text{Arg.}\left[\frac{z+j}{z-j}\right] = f_{z,a} \qquad (2.39)$$

To show whether equation 2.31 has any complex roots only the modulus equation 2.38 need be considered. Figure 2.8 shows curves of $f_{z,m}$ and $e^{-4\beta y}$ plotted against y for constant values of x. The only intersection of the two functions occurs at y = o which effectively proves that the only roots of the denominator are real; in fact this is now obvious since β is always positive because h_c, d_L and K_s are real physical quantities.

If the two sets of curves had crossed at any point other than y = o this would have shown that z = cot (β z) had complex roots. To find these another set of curves similar to figure 2.8 would have had to be constructed using the argument equation 2.39. From these two graphs a third one with two sets of curves could then be drawn with ordinates x and y. The complex roots of the equation are then found where the x - y curves cross.

It was previously suspected that the denominator would not have any complex roots since the transient temperature response of a coupling is known not to contain the oscillations of overshoots which are normally associated with complex roots.

2.12 Inversion of $\bar{\theta}(y,s)$

The general expression for $\bar{\theta}(y,s)$ is given by equation 2.28, since it is so complex it must be expanded and inverted term by term using C.I.F.[57, 58, 59].

Letting

$$\left[\alpha_s s^{1/2}.\sinh(\alpha_s d_L s^{1/2}) + \frac{h_c}{K_s}.\cosh(\alpha_s d_L s^{1/2})\right] = De \qquad (2.40)$$

and expanding the general equation gives

$$\bar{\theta}(y,s) = \frac{t_{1,c}}{s} - \frac{W_o.\sinh(\alpha_s y s^{1/2})}{\alpha_s K_s s^{3/2}} + \frac{W_o.\cosh(\alpha_s d_L s^{1/2})\cosh(\alpha_s y s^{1/2})}{s K_s De}$$

$$+ \frac{W_o.h_c.\sinh(\alpha_s d_L s^{1/2}).\cosh(\alpha_s y s^{1/2})}{\alpha_s K_s^2 De.s^{3/2}}$$

$$+ \frac{h_c.(t_{2,c}-t_{1,c}).\cosh(\alpha_s y s^{1/2})}{2s\,De.K_s} \qquad (2.41)$$

There is no difficulty inverting the terms which do not contain De. Inversion of the others however is complicated and the method of 'Residues' must be used in conjunction with C.I.F. Appendix 2 gives details of the 'Residue' method and the inversion of each term.

2.13 The general solution

Adding all the individually inverted terms of equation 2.41, which are given in Appendix 2, gives the general solution for $\theta(y,t)$.

$$\theta(y,t) = t_{1,c} + \frac{W_o.y}{K_s}$$

$$+ \sum_{n=1,2,3}^{\infty} \frac{W_o}{h_c}\left[1 - \frac{2\beta.\cos(P_n).\cos(P_n.y/d_L)}{P_n^2 K_s D_n} e^{-t/\tau_n}\right]$$

$$+ \sum_{n=1,2,3}^{\infty} \frac{W_o d_L}{K_s}\left[1 - \frac{2\beta.\sin(P_n).\cos(P_n y/d_L)}{P_n^3 D_n} e^{-t/\tau_n}\right]$$

$$+ \sum_{n=1,2,3}^{\infty} \frac{(t_{2,c} - t_{1,c})}{2} \left[1 - \frac{2\beta \cos(P_n y/d_L)}{P_n^2 D_n} e^{-t/\tau_n} \right] \quad (2.42)$$

where $$D_n = \left[\cos(P_n) + \frac{(1+\beta).\sin(P_n)}{P_n} \right]$$

and $$\tau_n = \alpha_s^2 d_L^2 / P_n^2$$

This solution gives the temperature distribution in time and one dimension in space y which is the depth into the loss member from the active surface. It can be applied to any coupling for a particular loss density or heat flux W_o and known method of cooling.

The general equation for h_c can be substituted into $\theta(y,t)$ if desired; this is given by

$$h_c = \frac{Nu.K_c}{L} = \frac{a\ Re^{b}.Pr^{c}.K_c}{L}$$

For brevity h_c will not be substituted at present and its general form is only given here to show that the solution is completely general even though empirical equations must be used for heat transfer problems.

The design parameters that control the loss member temperature are easily identified in equation 2.42. By putting y = o and y = d_L respectively, the temperature distribution and response at the active surface and back face are easily found. For a drum coupling it is then relatively simple to calculate the effects of drum expansion and temperature - dependent active surface resistivity on the torque - speed curves. Care must be taken however, when calculating drum expansion effects because W_o is a function of torque which changes and so an iterative calculation must be used for large expansions; this is discussed in chapter 3.

Parameters controlling the loss member thermal time constants are also easily found and are seen to be

$$\tau_n = c_s \rho_s d_L^2 / K_s P_n^2 \qquad (2.43)$$

where P_n is a function of the back face cooling medium and the loss member's material constants.

For most applications it will be shown later that only the first one or two terms of equation 2.42 need be considered since

$$e^{-P_{n+1}^2} / e^{-P_n^2} \quad \simeq \quad \text{very small (see table 2.1)}$$

and

$$|\text{Term } (n+1)| \; / \; |\text{Term } (n)| \qquad \text{also small usually}$$

Using these approximations permits the equation to be reduced to a simple form in most cases. Nevertheless, it must be stressed that these comments are only included for guidance and the complete general solution must be applied and simplified according to each individual application. In the next section, the solution is adapted to air cooled drum couplings and in chapter 5 to a water cooled disc inductor coupling.

2.14 Air cooled drum coupling simplification

In section 2.11.1 a general method for finding values of P_n was detailed. Basically this involved plotting a graph of the function

$$\frac{x'}{\beta} = \cot(x')$$

Figure 2.6 shows a typical plot of this equation where the slope of the straight line is $1/\beta$. For air cooling, β tends to be very small and so the slope is very large. This can be verified from the definition of β

$$\beta = \frac{h_c . d_L}{K_s} = \frac{Nu . d_L}{L} . \left[\frac{K_c}{K_s}\right]$$

or more generally for drum couplings

$$\beta = a\, Re^{b}\, Pr^{c} . \left[\frac{d_L}{D_o}\right] . \left[\frac{K_c}{K_s}\right] \qquad (2.44)$$

where D_o is the drum outside diameter and it is the characteristic heat transfer dimension chosen for drum couplings in this thesis. The terms K_c/K_s and d_L/D_o are usually very small; since air is the coolant in this case then K_c (air) $<< K_s$ and for most practical couplings $d_L << D_o$. The ratio K_c/K_s varies with temperature but over the limited temperature range being considered here this is relatively small as was shown previously. (see page 25)

If β is small, then $1/\beta$ is large and P_n tends to be independent of the value of slope$_\lambda$ (Fig 2.6). The Reynolds number in equation 2.44 is dependent upon the cooling fluid velocity, so β is also velocity dependent and the slope is a variable. However, since d_L/D_o and K_c/K_s are both small, quite large changes in velocity and hence β do not significantly change the values of P_n; this can be seen from figure 2.6 and table 2.1.

For small values of β, large values of slope, P_1 is also small[45] and roots higher than P_1 approximate to $(n-1)\pi$. Putting y = o and using these approximations and those given in section 2.13 it can be shown that the active surface temperature response $\theta(o, t)$ for an air cooled coupling is given by

$$\theta(o,t) = t_{1,c} + \frac{W_o}{h_c}\left[1 - \frac{2\beta . \cos(P_1)\, e^{-t/\tau_1}}{P_1^2 D_1}\right]$$

$$+ \frac{W_o d_L}{K_s}\left[1 - \frac{2\beta . \sin(P_1)\, e^{-t/\tau_1}}{P_1^3 D_1}\right]$$

$$+ \frac{(t_{2,c} - t_{1,c})}{2} \left[1 - \frac{2\beta\, e^{-t/\tau_1}}{P_1^2 D_1} \right] \qquad (2.45)$$

This can be simplified further, as P_1 is small then

$\sin(P_1)/P_1 \triangleq 1$, $\cos(P_1) \triangleq 1$ also remembering that β is small and noting that $(t_{2,c} - t_{1,c}) \triangleq 0$ for a cylinder rotating in an infinite quiescent fluid (see Appendix 1). Furthermore, it can be shown from table 2.1 that $\beta/P_1^2 \triangleq 1$; this only applies for air cooled coupling when β is small. Using these approximations equation 2.45 reduces to

$$\theta(o,t) = t_{1,c} + \left[\frac{W_o d_L}{K_s} + \frac{W_o}{h_c} \right] (1 - e^{-t/\tau_1})$$

multiplying top and bottom by h_c and taking W_o outside the bracket gives

$$\theta(o,t) = t_{1,c} + \frac{W_o}{h_c} \left[1 + \frac{h_c d_L}{K_s} \right] (1 - e^{-t/\tau_1})$$

but $h_c d_L / K_s = \beta$ which is small so the equation now becomes

$$\theta(o,t) = A + B\,(1 - e^{-t/\tau_1}) \qquad (2.46)$$

where $A = t_{1,c}$ and $B = W_o/h_c$

The above equation shows that the active surface temperature - time response of an air cooled coupling can be approximated to a simple exponential. This elegant result is rather surprising in view of the complicated general solution that was obtained. Nevertheless, equation 2.46 will be corroborated later by experimental results taken from an air cooled drum coupling.

As P_1 is insensitive to changes in β and provided average values of c_s and K_s are taken, calculation of the thermal time constant τ_1 is straightforward and good results have been obtained. Surface temperature prediction however is not simple and consideration of the complicated problems of electrical end-effects[2] and airgap heat losses may be involved when determining W_o.

2.15 Active region heat flux for couplings with and without endrings.

Before the theory of previous sections can be used for predicting loss member temperatures, a value of W_o must be obtained for use in the equations. Care must be exercised when determining this quantity and it must, by necessity, be based upon the size and type of coupling and to a large extent the designer's experience.

For an endring coupling the total heat flux developed in the active region, W_A, is found simply from

$$W_A = T\omega/\pi DL_A$$

It should be stressed that in general Wo does not equal W_A since airgap heat losses reduce the latter. The power balance equation for an endring coupling is given by

$$P_T = P_o + P_g + P_L \qquad (2.47)$$

where P_T = $T\omega$, the total power and also the active region power P_A for an endring coupling.

P_o = power that passes through to the loss member's back face and $W_o = P_o/\pi DL_A$

P_g = total airgap power loss by rediation and convection

P_L = loss along ribs and any low thermal resistance paths.

In most practical couplings $P_g > P_L$ and both are usually negligible and so it may be reasonably assumed that

$$W_A \triangleq W_o$$

But, if it is found in practice that P_g is not small, then an approximate value for it can be calculated using the laminar flow and radiation equations which are discussed later.

For a solid iron coupling, electrical end-effects[2] must be taken into account. To determine the active region heat flux (W_A) the distribution of dissipated power

between the active and end regions must be found.

Many authors have attempted to solve the problem of end-effects in couplings, but with little success. Part of a solution which has been found to give good results is presented here. It is based on modification of a linear three dimensional theory[10].

A power distribution factor 'r' will be defined as

$$r = \frac{P_{3D}(T)}{P_{3D}(A)} = \frac{P_T}{P_A} \qquad (2.48)$$

A solid drum coupling is sometimes referred to as a three dimensional coupling and $P_{3D}(T) = P_T$ the total power $(T\omega)$. Hence

$$W_A = \frac{P_{3D}(T)}{r\pi D L_A} = \frac{T\omega}{r\pi D L_A} \qquad (2.49)$$

Equation 2.49 gives the loss density (or heat flux) in the active region of a solid drum coupling which, may then have to be reduced by the heat flux losses before an effective value of W_o can be found.

2.15.1 The power distribution factor 'r'

The total dissipated loss in a coupling with end-effects, derived from a three dimensional theory[4], is

$$P_{3D}(T) = \int_{-L_T/2}^{L_T/2} \int_{0}^{\infty} \int_{0}^{\rho\lambda_1} e \left(J_{3D}\right)^2 \partial x \partial y \partial z \partial t \qquad (2.50)$$

where L_T is the total length of loss member available for eddy-currents to flow on.

Similarly, the total loss in the active region only, for a coupling with end-effects is given by

$$P_{3D}(A) = \int_{-L_A/2}^{L_A/2} \int_{0}^{\infty} \int_{0}^{\rho\lambda_1} e \left(J_{3D}\right)^2 \partial x \partial y \partial z \partial t \qquad (2.51)$$

It has been shown in reference 4 that only two components of current density exist in a three dimensional coupling theory

$$J_x(x,y,z,t) = Re\left[A.\sin(\pi z/L_T).e^{-\beta y}.e^{j(2\pi x/\lambda_1 - \omega t - \gamma y)}\right] \quad (2.52)$$

and

$$J_z(x,y,z,t) = Re\left[B.\cos(\pi z/L_T).e^{-\beta y}.e^{j(2\pi x/\lambda_1 - \omega t - \gamma y)}\right] \quad (2.53)$$

where $$B/A = 2L_T/\lambda_1 \quad (2.54)$$

It can be seen from equations 2.50 and 2.51 that the only difference between the integrations is in the z direction, therefore only the z components need be considered.

From equation 2.50

$$P_{3D}(T) = e\int_{-L_T/2}^{L_T/2}\left[f(x,y,t).B^2.\cos^2(\pi z/L_T) - f(x,y,t)A^2.\sin^2(\pi z/L_T)\right]\partial z$$

Expanding and integrating

$$P_{3D}(T) \propto \left[\frac{(B^2-A^2)}{2}z\right]_{-L_T/2}^{L_T/2} + \left[\frac{(B^2+A^2)}{4}.\frac{L_T}{\pi}.\sin(2\pi z/L_T)\right]_{-L_T/2}^{L_T/2}$$

Substituting equation 2.54 and putting in the limits yields

$$P_{3D}(T) \propto A^2\left[(4L_T^2/\lambda_1^2 - 1)\frac{L_T}{2} + \left[(4L_T^2/\lambda_1^2 + 1)\frac{L_T}{4\pi}.\sin(2\pi z/L_T)\right]\right]_{-L_T/2}^{L_T/2} \quad (2.55)$$

Similarly for $P_{3D}(A)$

$$P_{3D}(A) \propto A^2\left[(4L_T^2/\lambda_1^2 - 1)\frac{L_A}{2} + \left[(4L_T^2/\lambda_1^2 + 1)\frac{L_T}{4\pi}.\sin(2\pi z/L_T)\right]\right]_{-L_A/2}^{L_A/2} \quad (2.56)$$

Ratioing equations 2.55 and 2.56 gives the power distribution factor 'r'

$$r = \frac{1}{\frac{L_A}{L_T} + \left[\frac{(2L_T/\lambda_1)^2 + 1}{(2L_T/\lambda_1)^2 - 1}\right]\frac{\sin(\pi L_A/L_T)}{\pi}} \qquad (2.57)$$

where λ_1 = $\pi D/p$ fundamental wavelength, p = pole pairs.

L_A = active length

L_T = apparent length of loss member.

Equation 2.57 only applies for $L_T/L_A > 2$; lower values than this are physically impossible in solid iron couplings.

For a solid drum coupling, L_T is not the total length of the drum in the axial direction (L_D). It is the surface length of drum available for eddy-currents to flow on and includes the ends of length d_L and the back face. Selection of a value for L_T presents a problem if the loss member depth (d_L) is small. This is because eddy-currents in the active surface influence those on the back face and restrict their flow[3]. In this situation L_T is given approximately by the axial length of drum L_D plus 2 d_L and does not include the back face. When d_L is relatively large compared with the skin depth (δ) then L_T is given by $2L_T$ plus $2d_L$.

2.16 Airgap heat transfer including its effect on the general solution

In most commercial couplings airgap heat losses are usually small compared with the dissipated power in the loss member. Under certain conditions or for special applications this may not be true and for completeness it is necessary to show how the general solution is modified.

There is little useful information in the literature about convective heat transfer and turbulent fluid flow in the airgaps of electrical machines. So, for simplicity, only laminar flow will be assumed here. This does not of course

include radiation losses which may or may not be small depending on the temperature difference between field and loss member and also the emissivities of the surfaces.

The only difference to the previous theory is in the boundary condition at the active surface. The heat flux distribution at y = o, neglecting radiation, is given by

$$W_A = W_o + W_g \tag{2.58}$$

where W_A for an endring coupling is given by $T\omega/\pi DL_A$

W_o heat flux passing through to back face

W_g airgap heat flux

For laminar flow[45] W_g is given by

$$W_g = -K_g \cdot \frac{\partial \theta(y,t)}{\partial y} \tag{2.59}$$

where K_g is the thermal conductivity of the airgap coolant and the negative sign shows that heat flow is in the direction of decreasing temperature which, in this case, is in either direction from the surface y = o.

The equation for W_o is the same as that given previously by equation 2.18. Substituting this and equation 2.59 into 2.58 gives

$$W_A = -(K_s + K_g) \cdot \frac{\partial \theta(y,t)}{\partial y} \tag{2.60}$$

This equation is now the new boundary condition at y = o and takes into account laminar flow in the airgap. Comparing equation 2.60 with equation 2.18, it is apparent that the two boundary conditions have the same form. Therefore the solutions must also be similar and so, by replacing W_o with W_A and K_s by $(K_s + K_g)$ in the general solution, the effects of airgap heat transfer become obvious.

The thermal conductivity for steel and air are obtained from figure 2.3 and reference 46 respectively.

$$K_s(0^oC) = 67 \ (W/m^oC)$$

and $$K_g(0^oC) = 0.0242 \ (W/m^oC)$$

These values show that K_s changes little when K_g is added to it and so airgap heat losses are small for purely laminar flow.

It should be pointed out that laminar flow gives the minimum value for airgap losses and in a practical coupling it is unlikely that the airgap coolant flow is laminar. Equation 2.59 could have been replaced by the general boundary condition

$$W_g = - h_g \theta_{m,g}$$

where h_g is the airgap surface heat transfer coefficient and $\theta_{m,g}$ the mean film temperature. However, there is little point in pursuing this substitution as there is no suitable data available, to the author's knowledge, for h_g.

The above analysis is not conclusive and no general decision can be made whether or not airgap heat transfer is negligible. Nevertheless, it will be shown later from experimental measurements that in both air cooled drum couplings and a water cooled disc coupling airgap losses are small.

Radiation losses in the airgap and from the back face are also usually small but this depends on the temperature difference between the loss member and its surroundings. The airgap radiation heat flux, $W_{R,g}$, can be calculated approximately from the equation for concentric cylinders[46] or parallel planes which is given by

$$W_{R,g} = K_B \cdot \left[\frac{E_1 E_2}{E_1 + E_2 - E_1 E_2} \right] \cdot (T_1^4 - T_2^4) \qquad (2.61)$$

This equation is based on the Stephan-Boltzman law where $K_B = 5.67 \times 10^{-8}$ (S.I. units), E_1, T_1 and E_2, T_2 are the emissivites and temperatures of the loss member

and pole teeth respectively, both temperatures being the absolute values in ^{o}C Abs. The back face radiation heat flux $W_{R,B}$ can also be calculated if necessary, using the isolated surface[46] radiation equation.

2.17 Conclusions

A basic theory for predicting eddy-current coupling loss member temperatures and thermal time constants has been derived. The design parameters that control these quantities are also clearly identified. One of the main objectives of the theory was to form the basis of a method for designing coupling cooling systems and provide foundations for further work. It is considered that this has been achieved.

There is, as far as the author is aware, no relevant information on radiation and convection losses in the airgaps of electrical machines. The literature on rates of heat transfer from rotating members is also limited and sketchy. A review of this is given in Appendix 1.

An approximate method is detailed for finding values of W_o in solid iron couplings. Further research however, is necessary on heat losses and electrical end-effects before a general method can be formed. On the other hand, the procedure for obtaining thermal time constants is simple and shown to be relatively insensitive to variations in β. This is corroborated experimentally in the next chapter.

CHAPTER 3

TEMPERATURE EFFECTS IN AIR COOLED DRUM COUPLINGS WITH AND WITHOUT ENDRINGS

3.0 Temperature effects in air cooled drum couplings with and without endrings

3.1 Introduction

To verify the theory of chapter 2 it was decided to follow previous practice [9,10] and to examine experimentally similar drum couplings with and without endrings; this would also show the thermal differences, if any, caused by electrical end-effects.

Two groups of tests were carried out with each drum:

a) Using Davies'[3] x-y plotter technique, the steady state torque-speed curves and the corresponding temperature rise of the active surface were measured.

b) With the coupling running at maximum slip speed and constant excitation, the fall off in torque with time and the temperature-time response of the active surface were measured using two x-y plotters simultaneously.

The thermal time constants for both drums are derived from the temperature-time curves, and compared with the theoretical thermal time constants.

In the last part of the chapter the measured surface temperatures for both the endring and solid iron drums are compared with the theoretical values. A breakdown of the heat transfer distribution in the endring coupling is also included.

3.2 The experimental coupling

The experimental machine used in this research was that used by Davies[3,4] and James[9] and comprehensive details of it can be found in their work. The most important parameters of the endring drum, solid iron drum and the pole member are given in table 3.1

Table 3.1

Pole member

outside diameter	=	158.5 mm
radial airgap, g	=	0.254 mm
number of poles, 2p	=	12
fundamental wavelength, λ_1	=	83.5 mm
axial length of pole	=	25.4 mm
pole arc/pole pitch, K	=	0.69
winding turns	=	2600

Copper endring drum

inside diameter, D	=	159 mm
outside diameter, D_o	=	171 mm
thickness of drum, d_L	=	12 mm
active length, L_A	=	25.4 mm
axial length of drum, L_D	=	63.5 mm
resistivity of iron, ρ	=	$11.2 \times 10^{-8}\ \Omega m$

Solid iron drum

inside diameter, D	=	159 mm
outside diameter, D_o	=	171.5 mm
thickness of drum, d_L	=	12.5 mm
axial length of drum, L_D	=	82.5 mm
resistivity of iron, ρ	=	$11.2 \times 10^{-8}\ \Omega m$

3.3 Instrumentation

Torque was measured by means of a torque arm fitted with strain gauges[3,9]. The coupling was driven by a 3.75 kW induction motor - coupling unit[12] with a tachometer fitted on the output shaft.

To measure the surface temperatures identical groups of thermocouples were fastened in both drums. Five couples were fitted to each drum, four on the active surface and one on the outside surface opposite the centre of the active region. Figure 3.1 shows their positions and identifying letters. A thermocouple was also attached to a pole of the field member.

Position of thermocouples in both drums

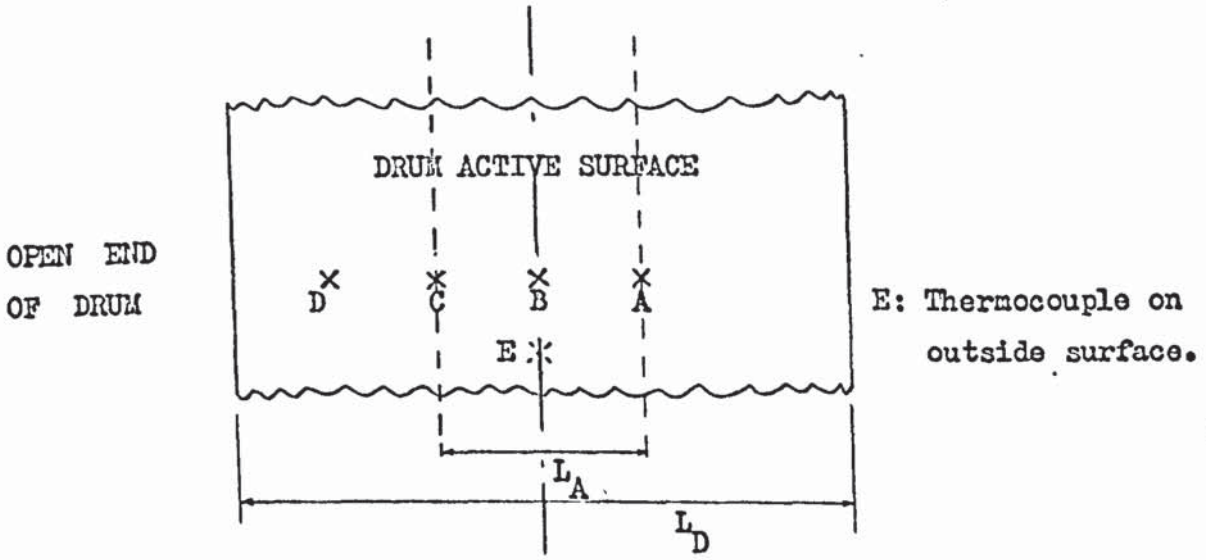

Figure 3.1

Since the experimental machine has a rotating drum, all the thermocouple leads had to be brought out through silver slip rings. These were connected between the drive unit and the experimental coupling. To get the leads to the rings a small slot was cut along the main shafts which supported the drums. A raised tagboard positioned on the outside surface was used to make intermediate connections of the thermocouple leads. The purpose of the tagboard was to allow easy replacement and inclusion of other thermocouples as necessary. Figure 3.2 shows the endring drum and its supporting shaft with the raised tagboard and slot clearly visible.

3.4 Preliminary investigation

The experimental coupling has no special provision for cooling the loss memb. and it relies entirely on the rotation of the drum in free air. The mechanisms of heat transfer in this situation are complex and there is little information on it; see Appendix 1.

Temperatures from all the thermocouples in both drums were noted during this preliminary investigation. It was observed that, over the limited test range, the temperature of the field member did not rise appreciably. In the axial direction, over the active region, there was little difference between the temperatures. Towards the open end of the drums however, the temperatures, measured using thermocouple D, started to fall. This was expected since cool air has more access to these regions. Nevertheless, these temperatures were only 10% to 20% less than those in the active regions. The temperatures of the outside surfaces were also found to be 10% to 20% less than in the active regions. This is a small temperature gradient through the drums but, since they are cooled naturally by rotation in free air, this was also expected.

Based on these preliminary tests it was decided that only the temperatures given by thermocouple B would be recorded since these were clearly representative of the temperatures across the active regions. Further, the back face temperature - time curves were not recorded,since torque - time curves would show more effectively the effects of drum expansion.

3.5 Torque - slip curves

Figures 3.3 and 3.4 show the measured torque - slip curves, at various excitations for the experimental coupling when fitted with the endring and solid iron drum respectively. Both sets of curves were taken using Davies' x-y plotter technique[3].

Surface temperature against time curves were also taken simultaneously with the torque-slip curves. These curves have not been included for space reasons but show that the active region temperature does not rise appreciably during the time taken to obtain a torque-slip curve using the x-y plotter method.

Therefore, any theoretical calculations involving the 'cold' torque-slip curves should be based on a value of the iron resistivity, ρ , taken at ambient temperature. At very high excitations however, some modification may be necessary to the value of ρ.

3.6 Drum couplings operating under normal conditions

The information obtained from theoretical comparisons with the 'cold' torque - slip curves is extremely useful for the basic design of couplings but is of little use when trying to predict the performance of practical couplings operating under normal running conditions.

It was shown in chapter 2 that the loss member temperature was directly proportional to W_o, the surface heat flux or loss density. The highest temperatures therefore occur at the maximum value of W_o. It can be shown, from Davies'[8] generalised loss curve, that this condition is produced at maximum slip speed and maximum excitation. So, as we are mainly interested in the worst temperature conditions,all the experimental results presented in this section were taken at maximum slip and various excitations.

3.6.1 Surface temperature against time curves

The measured temperature - time curves for the endring and solid iron drum are shown on figures 3.5 and 3.6. Each set of curves was taken at the maximum slip speed of 1450 rev/min and various excitations.

Both figures show that the rate of rise of temperature increases rapidly with excitation and also that the curves appear to be exponential as was predicted in chapter 2.

Whilst these curves were taken, the slip speed was monitored and found to remain approximately constant for most of the tests. It was noted that, for excitations greater than 0.3 A, the slip speed started to fall, e.g. for 0.5A, the speed had reduced to 1430 rev/min.

All the curves shown on both figures start from 30^{o}C. This was not the ambient temperature, which was 25^{o}C. After each test the excitation was removed and the machine left running to cool the drum. Even so, it took a considerable time to reduce the drum temperature to 30^{o}C and so it was not possible, due to lack of time, to start each test from ambient temperature.

3.6.2 Variation of torque with time at maximum slip speed and different excitations

As most practical couplings have solid iron loss members, torque - time curves were taken for the solid drum only; these curves are shown on figure 3.7, they were taken simultaneously with the temperature - time curves.

In chapter 2, it was predicted that since both ρ and g were functions of the drum temperature, the torque would fall dramatically as loss density W_o increased. This is exactly what the torque - time curves show.

A typical calculation of the change in ρ, g, T_m and n_m for the experimental machine was given in section 2.2.1.

3.7 Measured thermal time constants

In section 2.14, it was shown that the theoretical equation to the active region surface temperature, θ (o, t), for an air cooled drum coupling approximated to a law of the type

$$\theta(o, t) = A + B(1 - e^{-t/\tau_1}) \qquad (3.1)$$

where A is the ambient temperature ($t_{1,c}$) and B the temperature difference between the active surface final value and ambient.

Rearranging equation 3.1 and taking logs gives

$$-t/\tau_1 = \log_e\left[\frac{A+B-\theta(o,t)}{B}\right] = \log_e F(\theta) \qquad (3.2)$$

The equation can now be applied to the measured surface temperature responses, given on figures 3.5 and 3.6, and the thermal time constant τ_1 evaluated.

3.7.1 Thermal time constant - copper endring drum

Table 3.1 gives values of A, B, t, $\theta(o,t)$ and $F(\theta)$ taken from figure 3.5

Table 3.1

Excitation: 0.2A

$\theta(o,t)$ (^oC)	t (s)	$F(\theta)$
40	16	0.882
50	48	0.765
60	92	0.647
70	154	0.53
80	240	0.412
90	354	0.294
100	526	0.176

$A = 30^oC$

$B = 85^oC$

Figure 3.8 shows $F(\theta)$ plotted against t on log-linear paper. The excellent linearity of the points shows that the approximate solution for $\theta(o,t)$ is valid. It can be seen that the line through the points does not pass through $F(\theta) = 1$; this is because of the neglected terms in the general solution.

The thermal time constant is given by the reciprocal of the slope and its value is

$$\tau_1 = 299 \text{ s}$$

Substituting the values of A, B and τ_1, into equation 3.1 gives the measured relationship between the active region surface temperature and time

$$\theta(o,t) = 30 + 85\ (1 - e^{-t/299}) \qquad (3.3)$$

This equation will be compared with the theoretical response later.

3.7.2 Thermal time constant - solid iron drum

The following data, given in tables 3.2 and 3.3, is taken from the measured surface temperature-time response curves for the solid iron drum which are shown on figure 3.6

Table 3.2

Excitation: 0.2A

$\theta(o,t)$ (^oC)	t (s)	$F(\theta)$	
40	26	0.867	$A = 30^oC$
50	67	0.733	$B = 75^oC$
60	118	0.6	
70	190	0.467	
80	290	0.333	
90	420	0.2	

also

Table 3.3

Excitation: 0.15A

$\theta(o,t)$ (^oC)	t (s)	$F(\theta)$	
40	70	0.768	$A = 30^oC$
50	190	0.535	$B = 43^oC$
60	380	0.302	
65	520	0.185	
70	780	0.07	

Values of $F(\theta)$ from both tables are plotted against time (t) on figures 3.9 and 3.10. The points are again linear, verifying that the approximate equation for $\theta(o, t)$ also applies to solid iron drum couplings.

The thermal time constants are again found from the reciprocal of the slopes and are from the two figures respectively.

$$\tau_1 = 285s \quad \text{(Excitation: 0.2A)}$$

and

$$\tau_1 = 320s \quad \text{(Excitation: 0.15A)}$$

The difference in the two values of τ_1 is attributed to variation of the temperature dependent material constants c_s and K_s. A comprehensive analysis of changes in thermal time constants with temperature is given in chapter 5 for a water cooled loss member.

3.8 Comparison of measured and theoretical thermal time constants

The theoretical definition of the thermal time constant was given in chapter 2 as

$$\tau_1 = c_s \rho_s d_L^2 / K_s P_1^2 \qquad (3.4)$$

where P_1 is a function of the non-dimensional quality β which in turn is a function of h_c, d_L and K_s.

Before τ_1 can be calculated, values for both h_c and then β must be determined The back face heat transfer coefficient (h_c) for a drum or cylinder rotating in free air is obtained from the appropriate Nusselt number equation; Appendix 1, equation A1.3.

Whence

$$\bar{Nu}_D = 0.19(Re_D^2 + Gr_D)^{0.35} \qquad (3.5)$$

This equation only applies for $Re_D > 5 \times 10^4$ where Re_D is the Reynolds number and its definition is

$$Re_D = D_o^2 \omega \rho_c / \mu_c \qquad (3.6)$$

Substituting into equation 3.6, using a maximum speed of 1450 rev/min, gives

$$Re_D = 2.845 \times 10^5$$

For the experimental coupling it can also be shown that

$$Re_D^2 \gg Gr_D$$

Thus, using this approximation and the definition of $\bar{Nu}_D$ in equation 3.5 gives, after rearranging

$$h_c = 0.19 (Re_D)^{0.7} K_c / D_o \qquad (3.7)$$

Substituting for K_c, D_o and Re_D yields

$$h_c = 200 \text{ W/m}^{2o}\text{C}$$

The value of β can now be calculated from

$$\beta = h_c d_L / K_s \qquad (3.8)$$

Loss member thickness d_L is slightly different for both drums; from table 3.1

copper endring drum, d_L = 12 mm

and solid iron drum, d_L = 12.5 mm

K_s is taken at 100°C and its value from figure 2.3 is 61 W/m°C. The value of β using d_L = 12.0 mm is found from equation 3.8

Hence,

$$\beta = 0.0$$

Since P_1 is insensitive to small variations in β, this value will be used for both drums. The root P_1 corresponding to $\beta \simeq 0.04$ is obtained from table 2.1

$$P_1 = 0.199$$

Taking values of c_s and K_s at 100°C and substituting them, P_1 and d_L into equation 3.4 it can be shown that

Copper endring coupling (d_L = 12 mm)

$$\tau_1 = 272\text{s} \quad \text{(compare 299s experimentally)}$$

Solid iron coupling (d_L = 12.5 mm)

τ_1 = 292s (compare 285s to 320s experimentally)

Because of the complex nature of heat transfer in couplings and accepting there may be errors in the experimental values of τ_1 this correspondence is excellent.

3.9 Comparison of the measured and theoretical loss member temperatures

From section 2.14 the approximate theoretical equation for the active region surface temperature $\theta(o, t)$ was shown to be

$$\theta(o, t) = t_{1,c} + (W_o/h_c)(1 - e^{-t/\tau_1}) \qquad (3.9)$$

Before this equation can be used for predicting drum temperatures, a value of the heat flux (W_o) passing through the loss member must be determined. In chapter 2 it was pointed out that airgap heat losses may have to be taken into account in endring couplings and in solid iron couplings end-effects as well. In the following sections the heat losses in the endring coupling and end-effects in the solid iron coupling are both analysed in detail. Their effect on temperature prediction is also demonstrated.

3.9.1 Heat transfer distribution in the air cooled endring coupling

3.9.1.1 Heat flux W_o passing through the loss member

The following data was taken from the endring coupling at a speed of 1450 rev/min and an excitation of 0.2A:

measured torque, T = 5.0 Nm

active region surface temperature

$\theta(o, \infty)$ = 115°C

back face temperature, $\theta(d_L, \infty)$ = 105°C

field pole temperature approximately

ambient, θ_{AMB} = 25°C

The total power P_T is fround from

$$P_T = T\omega$$

$$= 785 \text{ W}$$

Consider now the general expression, from chapter 2, for W_o in the loss member

$$W_o = - K_s \cdot \frac{\partial \theta}{\partial y} \qquad (3.10)$$

The quantity $\partial\theta/\partial y$ can be replaced by

$$\left(\frac{\theta(o, \infty) - \theta(d_L, \infty)}{d_L} \right)$$

and the value of $K_s(100^oC)$ is taken as $61 W/m^oC$. Therefore, it can be shown

$$W_o = 5.05 \times 10^4 \text{ W/m}^2$$

But

$$P_o = W_o A_a$$

where $A_a = \pi D L_a$ the active region surface area $= 1.27 \times 10^{-2} m^2$

So, $P_o = 640$ W

Neglecting rib losses, the airgap power loss, P_g, is calculated from the power balance equation

$$P_g = P_T - P_o$$

$$= 145 \text{ W}$$

So 19% of the total power is removed via the airgap by radiation and convection.

As a cross check on this value of P_g, its individual components of airgap radiation (P_{Rg}) and convection ($P_{c,g}$) are calculated later.

3.9.1.2 Heat transfer from the loss drum outside surface

The numerical value of the back face heat transfer coefficient (h_c) for a cylinder rotating in free air was given in section 3.8 as

$$h_c = 200 \text{ W/m}^{2o}C$$

Multiplying h_c by the appropriate drum outside surface area and the temperature difference between the back face and ambient will give the power removed by convection ($P_{c,B}$) from the drum outside surface. For heat transfer calculations in air cooled endring couplings, the surface area of the two copper endrings must be added to that of the iron, as the thermal conductivity of copper is considerably greater than that for the iron and so the thermal time constant for the endrings is much smaller than the active regions (τ_1). Hence, heat is distributed quickly over the entire back face which becomes an approximate isothermal surface.

The outside surface area of the endring drum, A_E, is calculated from $\pi D_o L_D$, whence

$$A_E = 3.41 \times 10^{-2} \text{ m}^2$$

Using h_c, A_E and a temperature difference of 80°C (from section 3.8) gives

$$P_{c,B} = 550 \text{ W}$$

There is a difference of 90W between $P_{c,B}$ and P_o (3.9.1.1) indicating that either h_c was inaccurate (A_E is not considered a source of error, since it must be increased to bring $P_{c,B}$ up to P_o and clearly this is not reasonable) or the difference is removed by rib losses and back face radiation heat transfer or a combination of both.

The outside surface is classed as an isolated surface and the relevant radiation equation is given in reference 46 as

$$W_{R,B} = 5.67.10^{-8} E_B \left[T_B^4 - T_{AMB}^4 \right] \qquad (3.11)$$

where E_B is the emissivity of the back face and T_B and T_{AMB} the back face and ambient temperatures in °C Abs.

Selection of a value for E_B is nebulous as the condition of the drum surface is open to conjecture. The presence of iron and copper on the same surface complicates the problem and so the method is necessarily approximate but it does give an

idea of the magnitudes involved. From references 46 and 48 the emissivities for oxidised iron and dull copper are both approximately 0.8. So, putting $T_B = (273 + \theta(d_L, \infty)) = 378^oC$ Abs., $T_{AMB} = (273 + \theta_{AMB}) = 298^oC$ Abs. and $E_B = 0.8$ into equation 3.11 yields

$$W_{R,B} = 561 \text{ W/m}^2$$

which, when multiplied by A_E, gives the outside surface radiation loss

$$P_{R,B} \triangleq 20 \text{ W}$$

This calculation of back face radiation loss is rough but does show that when the loss member temperature is high radiation heat transfer may not be negligible. The other 70W which has not been accounted for is put down to inaccuracy in the empical equation (A1.3) from which h_c was derived and rib loss, i.e. where the drum is welded to the main shaft, see reference 3 for a sectional view of the experimental machine.

3.9.1.3 Airgap heat transfer

In section 3.9.1.1 it was shown that airgap power loss, P_g, was 145 watts. As a cross check on this value the component parts of P_g were calculated.

Since there is no relevant data on convective heat transfer in the airgaps of couplings an approximate value for heat transfer via the air, $P_{c,g}$, is calculated based on the assumption that laminar conditions exist in the airgap. This premise is considered reasonable because there is no air-flow through the experimental machines airgap as only one end of the drum is open; see figure 3.2.

The general expression for laminar flow[45,46] (conduction) is given by

$$W_{c,g} = - K_g \cdot \frac{\partial \theta}{\partial y} \qquad (3.12)$$

where K_g is the thermal conductivity of air, taken in this case at the average value between $\theta(o, \infty)$ and θ_{AMB}, i.e. 70°C; its numerical value from reference 46 is 0.0284 W/m°C. The term $\partial\theta/\partial y$ in equation 3.12 is replaced with

$$\frac{\partial \theta}{\partial y} = \left(\frac{\theta(o,\infty) - \theta_{AMB}}{g} \right)$$

From section 3.9.1.1 $(\theta(o, \infty)-\theta_{AMB}) = 90^{o}C$ and g the airgap length from table 3.1 is 2.54×10^{-4}m.

Thus,

$$W_{c,g} = 1.01 \times 10^{4} \text{ W/m}^2$$

In an endring coupling, the eddy-current loss is dissipated almost entirely in the active region and so the surface area of the endrings is not involved in airgap heat transfer calculations. Therefore, multiplying $W_{c,g}$ by A_a (1.27×10^{-2}m^2), the active region surface area, gives

$$P_{c,g} = 128 \text{ W}$$

Airgap radiation heat transfer, $P_{R,g}$, is calculated from equation 2.61

$$W_{R,g} = 5.67 \times 10^{-8} \left[\frac{E_1 E_2}{E_1 + E_2 - E_1 E_2} \right] \left[T_1^4 - T_2^4 \right] \qquad (3.13)$$

where E_1 and E_2 are the emissivities of the drum iron and pole teeth respectively and their value from reference 46, assuming oxidised iron conditions, is 0.8, $T_1 = (\theta(o, \infty) + 273) = 388^{o}C$ Abs. and $T_2 = T_{AMB} = (\theta_{AMB} + 273) = 298^{o}C$ Abs.

Hence, substituting these values into equation 3.13

$$W_{R,g} = 469 \text{ W/m}^2$$

and so multiplying by A_a yields

$$P_{R,g} \triangleq 6.0 \text{ W}$$

The total airgap power loss (P_g) is then found by adding $P_{c,g}$ and $P_{R,g}$

$$P_g = 134 \text{ W}$$

This value compares well with that obtained using the power balance equation; from section 3.9.1.1

$$P_g = 145\ W$$

3.9.2 Analytical values of the temperatures in the endring coupling

It was stated in section 3.9.1.2 that the thermal time constant of the copper endrings was much smaller than that for the active region, τ_1. Consequently, the temperatures throughout the endring drum tend to equalise before the active region final temperature is reached. To calculate numerical values of the surface temperatures therefore, the value of W_o has to be based on the complete surface area of the endring drum, $A_E = 34.1 \times 10^{-2} m^2$.

The active region surface temperature, $\theta(o, \infty)$, and the back face temperature, $\theta(d_L, \infty)$, will be calculated first, neglecting airgap power loss, P_g, and then taking it into account.

From chapter 2 the theoretical equations were shown to be

$$\theta(o, \infty) = t_{1,c} + W_o/h_c \qquad (3.14)$$

and

$$\theta(d_L, \infty) = t_{1,c} + W_o/h_c - W_o d_L/K_s \qquad (3.15)$$

The value of $K_s(100^oC)$ is taken as 61 W/m^oC and h_c (from section 3.8) as 200 $W/m^{2o}C$. At 0.2A and 1450 rev/min the total power, P_T, dissipated in the endring drum is 785 W.

So, neglecting airgap heat losses

$$W_o = P_T/A_E$$
$$= 2.3 \times 10^4\ W/m^2$$

Substituting W_o, h_c and K_s into equations 3.14 and 3.15 and knowing $t_{1,c} = 30^oC$ and $d_L = 12$ mm gives

$$\theta(o, \infty) = 145^oC$$

and $$\theta(d_L, \infty) = 140^oC$$

The airgap power transfer, P_g, will now be taken into account to show how these values are modified. From section 3.9.1.1 the value of P_g was given as 145W. Thus,

$$P_o = P_T - P_g$$
$$= 640 \text{ W}$$

The value of W_o becomes

$$W_o = P_o/A_E$$
$$= 1.875 \times 10^4 \text{ W/m}^2$$

Putting the new value of W_o into equations 3.14 and 3.15 yields

$$\theta(o, \infty) = 124^oC \quad \text{(compare } 115^oC \text{ measured)}$$

similarly

$$\theta(d_L, \infty) = 120^oC \quad \text{(compare } 105^oC \text{ measured)}$$

Using the above values of $\theta(o, \infty)$ the theoretical equation for the active region surface temperature - time response can be shown, from previous sections, to be

a) <u>Neglecting airgap heat losses, P_g.</u>

$$\theta(o, t) = 30 + 115\,(1 - e^{-t/272})$$

and

b) <u>Taking into account, P_g.</u>

$$\theta(o, t) = 30 + 94\,(1 - e^{-t/272})$$

The measured relationship was given in section 3.3 as

$$\theta(o, t) = 30 + 85\,(1 - e^{-t/299})$$

After P_g is taken into account, the correlation is good. This seems to indicate that the theory of chapter 2 needs to be made more precise by introducing airgap losses into the initial equations. However, it should be noted that the air-cooled coupling

is a special case in which the back face coolant is the same as that in the airgap. In contrast,most large commercial couplings have water cooled loss members and so their airgap heat transfer is negligible since h_c(water) $\gg$ h_g(air). It will be shown in chapter 5 that P_g is less than 10% of P_T in a water cooled eddy-current dynamometer.

3.9.3 Prediction of temperatures in the solid iron coupling

An approximate method for finding the active region dissipated power, P_A, and hence the active region heat flux, W_A, in couplings with end-effects was given in section 2.15. This involved the power distribution factor 'r' where

$$r = P_T/P_A \qquad (3.16)$$

where

$$r = \frac{1}{\frac{L_A}{L_T} + \left[\frac{(2L_A/\lambda_1)^2+1}{(2L_A/\lambda_1)^2-1}\right] \cdot \frac{\sin(\pi L_A/L_T)}{\pi}} \qquad (3.17)$$

From table 3.1 (solid drum)

L_D = 82.5 mm

L_A = 25.4 mm

d_L = 12.5 mm

λ_1 = 83.5 mm

L_T = $2L_D + d_L$ (only one end of drum open)

= 177.5 mm

Substituting these values into equation 3.17 gives

r = 3.33

From figures 3.4 and 3.5 at 1450 rev/min and 0.2A excitation,

measured torque, T = 5.2 Nm

active region surface temperature,

$\theta(o, \infty)$ = 105^oC

initial temperature of drum, $t_{1,c}$ = $30^{o}C$

An excitation of 0.2A was chosen because torque fall off was small, see figure 3.7.

The total power dissipated in the solid drum is found from

$$P_T = T\omega$$

$$= 790\ W$$

and so using r = 3.33 and equation 3.16

$$P_A = 237\ W$$

Hence,

$$W_A = P_A / \pi D L_A$$

$$= 1.87 \times 10^4\ W/m^2$$

Neglecting airgap losses and assuming there are no heat losses in the drum then

$$W_o \triangleq W_A$$

From chapter 2, the theoretical equation for the active region surface temperature, $\theta(o, \infty)$, is given by

$$\theta(o, \infty) = t_{1,c} + W_o/h_c$$

Substituting $t_{1.c} = 30^{o}C$, $h_c = 200\ W/m^2\ ^{o}C$ (from section 3.8) and the above value of W_A into this equation produces

$$\theta(o, \infty) = 123.5^{o}C \qquad \text{(compare } 105^{o}C \text{ measured)}$$

The predicted value is high because the airgap losses, which would reduce W_A, have been neglected. They may be taken into account, if necessary, using the same methods as given for the endring coupling.

The complete theoretical surface temperature response can be shown to be

$$\theta(o, t) = 30 + 93.5\ (1 - e^{-t/292})$$

compared with the measured response, at 0.2A, which is

$$\theta(o,t) = 30 + 75\ (1 - e^{-t/285})$$

This is again good correspondence and it could be improved if airgap losses were taken into account.

3.10 Conclusions

It would appear from the experimental results that similar couplings with and without endrings running at slip speeds higher than n_m have approximately the same thermal time constant, τ_1. The small difference between the experimental values of τ_1 for the two drums can be attributed to;

a) the solid drum being slightly thicker than the endring drum and

b) the difference in material constants c_s and K_s caused by the different power distributions and hence different temperatures in the two drums.

The correlation between the measured and theoretical thermal time constants is excellent, with errors ranging from 3% to 11%. The theoretical method for predicting τ_1 is precise because β is small for air-cooled couplings and so relatively large errors in its value have little effect on P_1, as table 2.1 shows.

Various surface temperatures in the endring coupling are calculated with and without taking into account the airgap power loss, P_g. These predicted temperatures are shown to compare reasonably well with the measured values when P_g is neglected and very accurately when it is allowed for. A comprehensive experimental breakdown of P_g is given and it is shown that 19% of the total power dissipated in the endring drum is removed via the airgap.

The active region surface temperature in the solid iron coupling was also calculated, the main purpose being to investigate the approximate method, given in chapter 2, for dealing with electrical end-effects. Airgap heat losses were neglected but the agreement between measured and theoretical temperatures was still good, indicating that the method is satisfactory.

In general the work in this chapter has shown that the theory given in chapter 2 forms a good basis for design purposes.

CHAPTER 4

THE HIGH SPEED EDDY-CURRENT DYNAMOMETER

4.0 The high speed eddy-current dynamometer

4.1 Introduction

The new high speed dynamometer is described in this chapter. Before dealing with its design and instrumentation the factors which influenced the choice of coupling are considered. These include rotational inertia, speed, power rating and cooling of the loss member. Many of these quantities had preferred values defined by Redman, Heenan, Froudes high speed eddy-current dynamometer specification. Consequently, the final design of the new machine was constrained by these requirements.

For space reasons, detailed design work on the magnetic circuit, electrical design, whirling speeds, stress analysis of the disc and cooling system have been omitted since much of it is well documented in standard texts, details of which can be found in the list of references.

The last sections of this chapter deal with the high speed drive system and instrumentation of the new machine.

4.2 Eddy-current couplings for use in high speed dynamometers.

The four basic types of coupling discussed in section 1.3 were all considered for use in high speed dynamometers and, in particular, for a 75 kW, 14000 rev/min machine.

It was decided that only two of these types were suitable for this application:

a) Disc loss member with salient pole field system

b) Stationary loss member with inductor (homopolar) field system.

Drum couplings were dismissed as unsatisfactory. The main reasons were that discs are capable of much higher speeds than cylinders, at high speeds their axial length is a problem, they are difficult to cool efficiently, drum expansion

causes loss of performance (see chapter 3) and parasitic airgap inductor and lundell type usually have weak mechanical sections because of their complex geometry and so are not usually capable of high speeds.

4.2.1 Disc loss member with salient pole field system (d.s.p. coupling)

The major problem with this type of coupling (shown on figure 1.3) is cooling of the rotating loss member. One solution is to spray water onto the disc, but the drag created would retard the transient response and the coupling would have a high minimum torque which is undesirable in dynamometers. An alternative would be to have a hollow disc and pass water along the rotating shaft. The technology involved however is formidable and so it is not considered practicable.

In addition, there are related electro-magnetic and mechanical problems to consider. For effective electro-magnetic operation the loss member material must have a high permeability/resistivity ratio[4, 8, 12]; high permeability for magnetic efficiency and low resistivity for electrical efficiency. Pure iron and mild steel both have these properties but are not suitable because of their low tensile strength. A steel with a high tensile strength must therefore be used and in general these have low permeability/resistivity ratios. This means there will be more leakage flux and the mmf would have to be increased to force flux through the disc.

The stress analysis of the disc is extremely complicated, not only must the high centrifugal forces be taken into account, but also the significant reduction[51] of disc material yield strength with temperature, heat being generated in the disc by the eddy-currents.

Axial magnetic pull is an inherent problem with single sided disc couplings[13] but it can be eliminated in double sided types provided the flux densities on each side of the disc are equal.

The main advantages of this type are its high torque at low speeds and it can be designed to have a very fast transient response[10,11].

4.2.2 Stationary loss member with inductor (homopolar) field system

Since there was no published information about disc inductor couplings a design for such a machine was developed. Its main constructional features are shown on figure 4.1, more comprehensive details of its characteristics and operation can be found in Appendix 4*.

This machine has a stationary loss member and a stationary field member which also incorporates an annular excitation coil. The loss member can now be indirectly water cooled and made from pure iron with its necessary high permeability/resistivity ratio.

The rotating member is shown on figure 4.2; its only function is to produce a permeance variation which modulates the airgap flux. No heat is produced directly in it but it does absorb radiated heat from the loss member which is dissipated naturally by the rotation.

It has negligible zero excitation torque (minimum torque) and the rotating parts have low inertia, which is one of the factors governing transient response.

The main problems are associated with the rotating permeance member. Ideally the disc material should be non-magnetic, have a low density, high resistivity and good tensile strength. High resistivity is required because metals are conductors and under transient conditions eddy-currents will flow in the disc delaying the flux changes in the machine.

Mechanical and electrical design of the disc are related; the optimum size of insert would normally be dictated by electro-magnetic considerations but this

---

* Appendix 4 is a copy of the provisional patent application which protects the main constructional features of the new machine.

may be modified by strength considerations in high speed couplings. If the slots in which the inserts fit are too large then the disc will be mechanically weak; if they are too small, electrical operation of the coupling will suffer to some extent. It will be seen later that these problems are easily solved with existing materials and technology and that a disc capable of very high speeds can be produced.

Axial magnetic pull on the disc is not a problem provided the flux densities on each side of it are approximately the same. There is nevertheless a large attractive force between the stationary field and stationary loss member but this is relatively unimportant since both can be fixed rigidly in the axial direction.

Torque-time response will not be as fast as the d.s.p. coupling since inductor couplings inherently carry more flux[4,8]. Nevertheless, this can be by laminating most of the magnetic circuit and designing for low saturation levels.

After considering the advantages and disadvantages of the various couplings, it was decided that this type was the most suitable for a 75 kW, 14000 rev/min machine and in the next sections details of such a machine are given.

4.3 Design

4.3.1 General arrangement and design of experimental high speed dynamometer

Figure 4.1 shows the mechanical arrangement of the experimental high speed dynamometer. The main body is overhung to avoid disturbing the high speed bearings and to facilitate easy removal of the loss member and rotating permeance member. The main body is supported by two trunnion bearings and it would rotate if it were not prevented by a locked torque arm. This provides a simple and accurate method of measuring the reaction torque of the dynamometer. Figure 4.3 shows a close up of the actual experimental machine and the above features are easily identified.

The high speed shaft and disc are supported by two pairs of precision angular contact ball bearings, mounted back to back to eliminate axial shaft movement which is normally a problem with disc machines. No shaft movement was experienced in the experimental machine.

Because of the high speeds involved,it was necessary to calculate the first critical speed of the shaft assembly. A numerical technique was used which took into account the weight of the disc at one end of the shaft, the drive coupling at the other, shaft diameter and distance of bearings apart;the value is given in table 4.1 (p 81)

Adjustment of the two airgaps is provided by jacking screws which move the field member and loss member independently with respect to the disc. As the disc rotates, each point on the loss member and field member opposite the ring of high permeability inserts sees a fluctuating permeance which modulates the unidirectional airgap flux. Eddy-currents are therefore induced in these surfaces adjacent to the airgap. To prevent eddy-currents flowing in the two sections of the field they were laminated as shown on figure 4.1. This phenomenon is useful in a commercial dynamometer since,by replacing the laminated sections with cooled solid iron,the torque is effectively doubled.

The experimental dynamometer was designed with only one loss member so that the eddy-currents were concentrated in one place and easily monitored. Cooling of the loss member is provided by water flowing in channels which are arranged edge-on to the flux.

Under steady state conditions,eddy-currents are not induced in the disc because each point on it sees a constant permeance in both airgaps. Nevertheless it does absorb radiated heat from the loss member and field coil. Air passages were therefore provided and when the disc rotates it acts as a natural pump,forcing

cooling air across itself.

To minimise leakage fluxes the field former was made from an aluminium casting and the shaft from non-magnetic stainless steel.

All the important dimensions and details of the experimental dynamometer are given in table 4.1

4.3.2 The rotor (permeance modulation member)

Figure 4.4 shows the rotor for the experimental machine. The main disc was manufactured from Titanium because it was the most suitable material for this application. Other materials, such as non-magnetic stainless steel, could have been used for the disc but in general would have a higher density, lower tensile strength and lower resistivity than Titanium and are therefore less attractive.

The high permeability inserts (or slugs) were manufactured from mild steel. They are secured in the slots in the Titanium disc with a high temperature adhesive and by peening at four points on each side.

Design of the disc was complicated by conflicting mechanical and electrical requirements which were briefly discussed in section 4.2.2. The basic method was to calculate the required size of insert for satisfactory electro-magnetic operation and then analyse the stresses[51,55,56] produced in the disc at the desired maximum speed. This proceeded on a trial and error basis until a satisfactory compromise between electrical and mechnical operation was obtained.

The yield stress for Titanium quoted by the manufacturers varies from 900 N/mm^2 (58 ton/in^2) to 1300 N/mm^2 (84 ton/in^2). It was considered that this was not accurate enough for design purposes and a number of standard test pieces to fit a Hounsfield tensometer were prepared from the same Titanium sheet as used for the disc. The average value of yield stress obtained and other details of the disc are given in table 4.1.

After the disc was assembled,it was dynamically balanced with the excess weight being removed by linishing across the diameter.

4.3.3 Electro-magnetic design

The original specification for the dynamometer stated that it must be capable of maintaining 75 kW from 2000 rev/min up to 14000 rev/min. It was decided, partly for reasons discussed in section 4.3.1 and partly for instrumentation and drive limitations, that the experimental machine was to be potentially capable of the full rating, but for experimental purposes it was to produce only a quarter of 75 kW. The reduced rating was achieved by using only one loss member and increasing the two airgaps from their designed value of 0.5 mm to 1 mm. These measures then allowed the dynamometer, after simple modification, to meet the original specification if necessary.

The slug width/slug pitch ratio which is the same as tooth width/tooth pitch ratio (K′) in normal inductor couplings was chosen as 0.45. Davies[8] has shown that this is the value for inductor couplings, which uses the fundamental flux most effectively. It is known* however that much smaller values of K′ could have been used with only a small reduction in torque. This is particularly useful for future reference,since reducing this ratio would increase the mechanical strength of the disc. Nevertheless 0.45 was chosen so that the experimental dynamometer could be designed by dimensional ratioing from Davies[8] inductor coupling which also had the same tooth width/tooth pitch ratio.

Dimensional ratioing is a technique widely used in coupling design and accurate estimates of the peak torque and speed at peak torque for one machine can be obtained from another. This was not straightforward since Davies[8] inductor coupling was a

---

* From unpublished work belonging to E. J. Davies, Professor of Electrical Engineering at the University of Aston in Birmingham

drum type machine and the basic equations had to be interpreted for disc machines.

Figure 4.2 shows inner and outer pitch circle diameters these are the mean diameters of the two rings of inserts. In Appendix 3 they are shown to be equivalent to the diameter D in normal machine terms. The length of insert is also shown to be equivalent to the active length, L_A, in a normal machine

The inner and outer regions were analysed as two separate machines. Having chosen K' and established equivalent D and L_A values for the inner and outer regions Davies[4,8] dimensional equations were used to determine the other machine parameters.

A number of different combinations of D, L_A and p were tried for the equivalent inner and outer machines, where p is the number of inserts. Airgap length g was chosen as small as mechanically possible taking into account the high speeds involved.

It was initially assumed that the flux density in the outer airgaps was approximately the same as in the inner airgaps. This is shown in chapter 5 to be slightly inaccurate because of the leakage fluxes around the outside of the field member.

Values of peak torque and speed at peak torque were estimated for the two regions and Davies[4] normalised torque-slip curve was used to obtain the torque-slip curve for each. These were then added to obtain the resultant curve.

It was found that by choosing different numbers of inserts for the inner and outer regions and varying their pitch circle diameters as well as length that the torque-slip curves could be tailored. The actual choice of p, D and L_A is too involved and lengthy for publication here since it involved simultaneous analysis of the stresses in the disc and consideration of the leakage flux paths.

The magnetic circuit was designed for low flux density levels to ensure that approximately all the excitation mmf was used in forcing flux across the two airgaps

and through the disc. Figure 4.5 shows the field member. It can be seen that it has substantial sections; the laminations are also clearly seen.

The permeance of the main and leakage flux paths were calculated using well known methods[25] and an equivalent magnetic circuit was used to estimate the distribution of flux in the machine. Considering the complex geometry of the dynamometer and the straight line approximations made when calculating the permeance of the various flux paths, the theoretical and measured flux distributions are very close, as will be shown in chapter 5.

The total mmf to be supplied by the field coil was estimated using the methods detailed in Gibbs[2] classical paper. Knowing the mmf required from the coil the depth of slot, number of turns and wire diameter were calculated using standard d.c. coil theory[29]. The coil was wound with 760 turns of 1.25 mm diameter wire, enamel insulated. It is rated at 6A which gives a total mmf of 4560 AT and it has a cold d.c. resistance of 8.9 Ω. Fibre wedges were used to secure the coil in the slot.

The axial thickness of the rotor was made at least fifteen times greater than the airgap width. It can be shown[2] that the non-magnetic region between the inserts then approximates to an infinitely deep slot when seen by the loss member and so a maximum permeance variation is achieved.

During preliminary tests the loss member and backing plate were found to flex in diaphragm fashion , producing a non-linear airgap. The reason was found to be the water manifolds which create weak sections and, since there is a large axial magnetic pull between the stationary loss member and field member, this produced the deflection. This was eliminated by fitting a heavy strengthening plate.

4.3.4 The loss member and its cooling system

Figure 4.6 shows the loss member which is made from hydrogen annealed pure iron ('Armco'). The cooling water channels are also clearly shown. There are

48 in the outer ring of a 1/16 inch square section and 24 in the inner ring of $\frac{1}{4}$ inch square section. These slot sizes were chosen to correspond with the milling machine cutters that were available.

The reason for the different number and size of water channels in the two regions of the loss member was to obtain an equal temperature distribution in the radial direction and so minimise distortion. The initial unequal temperature is caused by the different power developed in the inner and outer regions.

Standard theory[46,48] of pipes in parallel was used to design the cooling system. An equivalent hydraulic mean diameter was found for each slot and from this the slot dimensions were calculated.

The water inlet pressure was specified to be no greater than 2 bar with a throughput not exceeding 40 litres per kWH at an output temperature of approximately 40°C; the water output temperature is fixed to minimise scaling. The only variables therefore were the number of slots, their surface area and the water velocity through them, assuming of course that the power to be removed has a defined maximum value.

After machining, the loss member was 'sheradized' to prevent rusting and build up of deposits. The active surface was reground after this process to ensure that the torque-slip characteristics were not changed[2].

4.3.5 Details of experimental high speed dynamometer

The most important details and parameters of the experimental machine are given in table 4.1.

Table 4.1

Details of experimental high speed dynamometer

Rotating permeance member (disc)		
tooth width/tooth pitch ratio, inner and outer regions	=	0.45
number of inserts in outer ring	=	18
length of outer inserts	=	32 mm
number of inserts in inner ring	=	9
length of inner inserts	=	58 mm
Disc material - Titanium - measured maximum yield stress	=	1100 N/mm^2 (70 $tons/in^2$)
Insert material - mild steel		
Width of disc	=	15 mm
Weight of disc and inserts	=	9.5 kg
Rotational inertia of disc only (approximate)	=	0.158 kg m^2
Axial airgaps:		
a) designed value	=	0.5 mm
b) value used in experimental work	=	1.0 mm
first critical speed of disc and shaft	=	34,400 rev/min
mean pitch circle diameter - outer	=	312 mm
mean pitch circle diameter - inner	=	170 mm
Field member and excitation coil		
spiral laminations, thickness	=	1 mm
slot size: axial length	=	60 mm
radial length	=	23 mm
winding turns	=	760

diameter of coil wire (enamel insulated) = 1.25 mm

winding resistance (cold) = 8.9 Ω

rated coil current = 6A

Loss member and cooling system

resistivity of pure iron ('Armco') = 11.2×10^{-8} Ω m

thickness of loss member = 16 mm

cooling channels a) outer = 48 channels x 1/16 inch square section

b) inner = 24 channels x $\frac{1}{4}$ inch square section

4.4 The high speed drive system

Figure 4.7 shows the general arrangement of the experimental apparatus. The main drive was provided by a 4 pole, 75 kW induction motor driving through a 75 kW water cooled drum inductor coupling. The low speed end of the gearbox was connected to the drive coupling by a sliding shaft and two universal joints. The high speed end was connected to the experimental dynamometer by a splined shaft.

A schematic diagram of the experimental apparatus and high speed drive system is shown on figure 4.8. The dynamometer (A) was run up smoothly with the drive coupling (C) and induction motor (D). Using a coupling as the gearbox drive also allowed closed loop control of the output shaft speed to be easily arranged[12]. Feedback for the control system was provided by a d.c. tachogenerator (E).

The dynamometer excitation was taken from a 150V, 6A stabilised d.c. power supply (G).

4.5 Instrumentation

4.5.1 Torque measurement

An electrical signal proportional to torque was provided by means of four strain gauges fixed on the dynamometer torque arm. The gauges, two in compression and two in tension, were connected in a full bridge circuit with a potentiometer for zeroing the output under no load conditions. The connections are shown in figure 4.9. Each gauge was rated at 0.3 watts and had an unstrained resistance of 500 ohms.

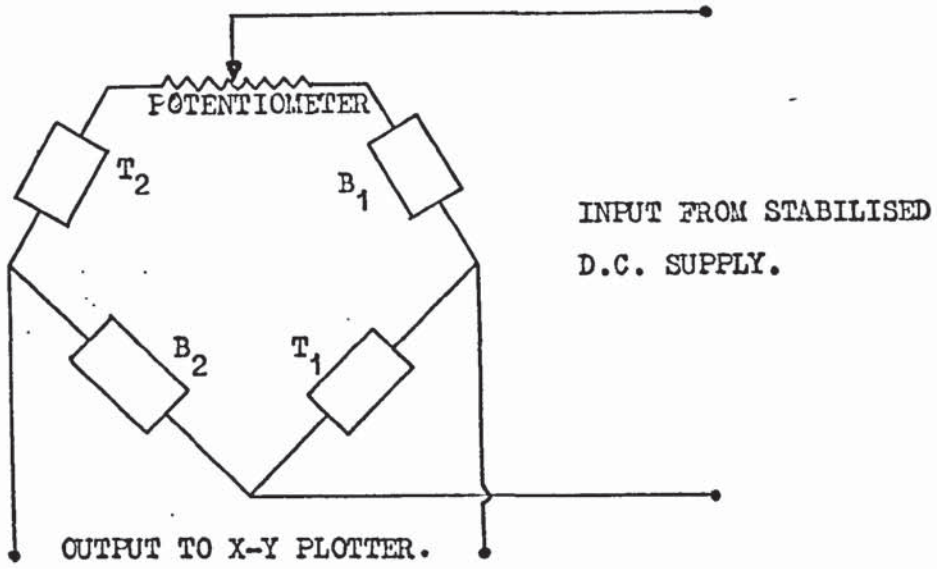

T = Top gauges on torque arm.
B = Bottom gauges on torque arm.

Figure 4.9

The torque arm was made from 13 mm square bar ($\frac{1}{2}$ inch square stock size) and its effective length was 0.5 m from the centre line of the shaft to the support pivot screw. Detailed design of torque arms can be found in reference 3.

Counter balance was provided by another arm fitted with a sliding weight fixed diametrically opposite the torque arm.

Calibration of the strain gauges was carried out using a supported spring balance attached to the pivot screw at the end of the torque arm. Load was then applied by means of the counter balance arm and the bridge input voltage adjusted until the required deflection was obtained on the high input impedance x-y plotter.

4.5.2 Speed measurement

A permanent magnet d.c. tachogenerator, driven by a toothed belt from the drive coupling output shaft, was used to obtain an electrical signal proportional to speed. The same signal was used in the speed feedback loop of the drive couplings

control system. Care was therefore taken not to short circuit the tachogenerator leads, otherwise the control system would have detected a zero speed condition and applied full excitation to the drive coupling which would have responded by accelerating to full speed.

The tachogenerator had an output of 0.1 V/rev/min.

4.5.3 Flux measurement

4.5.3.1 Arrangement of search coils on stationary field member

Figure 4.10 shows the search coil arrangement on the stationary field member. Search coil 3 measures the shaft leakage flux, 4 and 5 measure the flux entering and leaving the inner and outer laminations respectively and 6, 7 and 8 measure the leakage flux around the outside of the field former.

The search coils comprise a single turn of 40 S.W.G. copper wire (LEWMEX) fastened with Permabond 101 contact adhesive.

Each pair of search coil leads were twisted together to avoid pick up and terminated in multicore sockets which were connected to a 50 way rotary switch by screened multicore cable and plugs. The rotary switch allowed selection of any search coil to the output terminals.

4.5.3.2 Full pitch search coils

Figure 4.11 shows two full pitch search coils on the loss member surface, one spanning the outer active region the other the inner active region. Full pitch search coils in inductor couplings embrace half a tooth (slug) pitch in the peripheral direction and not a tooth pitch as would normally be expected. This is because of the homopolar field. The flux progresses through a complete cycle between teeth and a search coil embracing a tooth pitch would therefore have zero net induced emf.

These particular search coils were used to obtain the mean standstill flux density under a tooth and slot.

Both search coils consisted of a single turn of 40 S.W.G. Lewmex wire fastened with Permabond contact adhesive.

The leads were also brought out in the same manner as the search coils in the previous section.

4.5.3.3 Flux meters

The steady state flux was measured using a 'Norma' ballistic flux meter. This instrument was critically damped by connecting a decade resistance box in series with the search coils. The box was then adjusted until the terminal resistance was 30 ohms. In all the steady state flux tests the method of field reversals[3] was used.

The transient flux response was measured using a 'Hirst' integrating flux meter with output terminals giving the integrated search coil voltage directly. The instrument had a high input impedance and so the search coil resistance did not introduce any errors. The flux meter also had a drift compensation which was found to be poor, so all transient flux tests were carried out quickly after zeroing the instruments.

The output was fed to a storage oscilloscope fitted with a polaroid camera for recording the traces.

A magnetic standard was used to check the calibration of both flux meters.

4.5.4 Loss member surface temperature

4.5.4.1 Thermocouple array on loss member surface

The loss member was provided with thermocouples to measure its thermal time constant and the temperature distribution across it. Figure 4.11 shows the positions of the couples on the loss member surface.

Standard manufactured thermocouples could not be used because their lead diameters were too large for the machine airgap, typical diameters varied from 0.5 mm to 1.0 mm.

Special thermocouples were therefore made with an overall diameter of 0.3 mm, their leads consisted of 40 S.W.G. copper wire (LEWMEX) and 42 S.W.G. nickel-copper (CONSTANTAN) wire insulated with a double layer of rayon. The thermal junction was made by removing a small amount of insulation from the end of each lead then tightly twisting them together; they were then bonded by soldering.

Each lead was carefully twisted together along its entire length to eliminate pick up. The ends were then brought out via multicore cable and terminals to the same rotary switch as used for thesearch coils in section 4.5.3. Permabond was used to stick the couples to the loss member.

4.5.4.2 Temperature measurement

A Pitman Veritell-D digital pyrometer was used to measure the temperatures. It was designed for use with copper-constantan thermocouples only and had a temperature range of 0 - 400°C with an indicator accuracy of 0.25% range $\pm$ 1 digit at room temperature. Cold junction compensation was fitted as standard. The input impedance was not less than 1 megohm and the thermocouple lead resistance may be as high as 100 ohms without effect on accuracy.

Initial zeroing of the digital pyrometer was performed using a standard copper-constantan thermocouple immersed in melting ice. The zero was also checked periodically during the experimental tests.

The instrument was connected directly to the rotary switch terminals so that any of the loss member thermocouples could be switched in to it. Also connected to the rotary switch and in parallel with the digital pyrometer was a high input impedance x-y plotter which was used to record surface temperature against speed and time.

4.5.5 Surface current density

4.5.5.1 Position of current density probes on loss member surface

Figure 4.12 shows the matrix of current density probes on the loss member surface. Probes Z_1 to Z_{11} all have 1 cm centres and measure the distribution of

radial current density, probes X_1 to X_{11} also have 1 cm centres and measure the distribution of peripheral current density in the radial direction. Probes Z_{12} and Z_{13} span the two active regions and measure the mean radial current density; the results from these two probes were used to construct the peripheral airgap flux density waves.

Each current density probe consists of a pair of twisted leads each of 42 S.W.G. nickel-copper (CONSTANTAN) wire insulated with a double layer of rayon. The ends of each probe lead were physically attached to the loss member surface using a spot welding technique[14] which had been found to give good results in practice.

The leads were terminated in the same manner as the search coils in section 4.5.3 and then brought out to the rotary switch. Permabond 101 was again used to fasten the leads to the loss member surface.

4.5.5.2 Current density measurement.

A current density probe does not measure directly what its name implies, it only measures the voltage V between two points. However, knowing the distance Lp between the probe centres and the resistivity, ρ, of the surface the magnitude of current density can be estimated from Ohms law equation 4.1:

$$J = \frac{V}{\rho \, Lp} \qquad (4.1)$$

Equation 4.1 is innaccurate if the temperatures between the two probe contacts are radically different this is obvious since ρ is a function of temperature.

Even though the probe does not measure the magnitude of current density, the time varying voltage and surface current density do have the same general shape provided the value of ρ at the two contact points is approximately the same. The output from the current density probes was fed to a storage oscilloscope and the traces recorded using a polaroid camera.

4.6 Conclusions

In this chapter the new experimental high speed dynamometer has been described along with its instrumentation. Most of its design features are superior to the original Redman, Heenan, Froude specification and it is thought that the new machine is satisfactory for a 75 kW, 14,000 rev/min dynamometer. Ultimately however it will be judged on its dynamic performance which is analysed in chapter 5.

CHAPTER 5

THE HIGH SPEED DYNAMOMETER - EXPERIMENTAL RESULTS

5.0 The high speed dynamometer - experimental results

5.1 Introduction

In this chapter the experimental work on the high speed dynamometer is discussed. The main objectives of the work were:

a) to investigate the performance of the new machine and confirm that it is suitable for a 75 kW, 14000 rev/min dynamometer,

b) establish whether or not existing coupling theory[4,8] could be used with confidence to design high speed machines and

c) study the behaviour of a water cooled loss member and the effects of surface temperature on the performance of a disc type coupling.

To verify that the experimental machine obeyed general coupling theory measurements of torque, slip speed, fundamental flux per pole and peak fundamental armature reaction mmf were obtained and compared with the numerous generalised curves. The relationships between these quantities are also determined and compared with the theoretical exponents derived by Davies[3].

The measured surface temperatures and thermal time constants are analysed and the results compared with predicted values which were derived using the theory of chapter 2.

In the last part of the chapter the new machine's transient response is studied.

5.2 Standstill magnetisation curves

Before commencing general testing, the standstill saturation curves were measured and compared with the design curves. Figure 5.1 shows the curves of measured and calculated fluxes leaving ($\emptyset_I$) and entering ($\emptyset_o$) the laminated sections of the field member.

The calculated curves are based on an equivalent magnetic circuit with the branches representing the reluctance of the various flux paths. Correlation between measured and calculated curves is very good considering the straight line approximations made when estimating many of the reluctance values.

Figure 5.2 shows a half section of the dynamometer and a table of the measured and calculated flux distribution at standstill; where 1 and 2 are total fluxes entering and leaving the loss member active regions, 3 is shaft leakage flux, 4 and 5 fluxes leaving and entering the laminated sections of the field member and 6, 7, 8 the leakage fluxes around the outside of the field member.

DISTRIBUTION OF FLUX AT STANDSTILL , EXCITATION : 4 A.

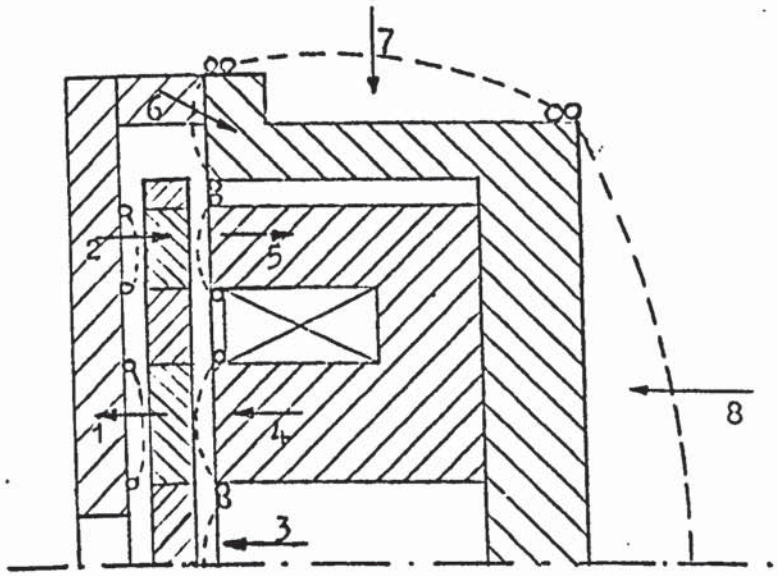

	Measured (mWb)	Calculated (mWb)
1 :	15.3	16.5
2 :	10.8	11.1
3 :	0.53	neglected
4 :	17.5	17.5
5 :	13.1	12.1
6 :	2.65	2.08
7 :	0.31	0.72
8 :	2.04	2.6

Figure 5.2

(3, 6, 7, 8 are leakage fluxes)

The measured leakage fluxes are seen to be high. In a practical machine they could be substantially reduced by closing the two airgaps to their design value, 0.5 mm, and replacing the mild steel spacer between the loss member and field former with a non-magnetic one. These modifications would tend to equalise the fluxes ϕ_I and ϕ_o which is desirable for performance reasons.

5.3 Torque-slip curves

Figure 5.3 shows the family of torque-slip curves for the experimental machine. They were obtained by setting the field current at standstill and maintaining it constant with a constant current power supply, then increasing the speed of the drive coupling. The speed and torque signals were fed to an x-y recorder which plotted the torque-slip curves automatically as speed increased. Other researchers[3,9,10] used this method to obtain the curves quickly and limit the temperature rise of the loss member.

To verify that temperature rise was negligible,various loss member surface temperature against slip curves were taken simultaneously with the torque-slip curves using another x-y plotter. The curves are not included for space reasons but do show that loss member surface temperature does not increase appreciably whilst a torque-slip curve is taken.

Because the loss member is water cooled,its temperature falls rapidly to the water inlet temperature after the excitation is removed. The value of resistivity (ρ) to be used for any theoretical comparisons with the torque-slip curves may therefore be taken at the water inlet temperature.

The power developed by the machine at 2000 rev/min had to be at least a quarter of 75 kW to meet the dynamometer specification (see chapter 4). Torque corresponding to this power level at 2000 rev/min is 90 Nm; figure 5.3 shows that this is easily exceeded when rated excitation, 6A, is applied.

In later sections the torque slip curves are plotted on log-log paper and compared with Davies[3,8] generalised torque-slip curve.

5.4 Variation of main fluxes with excitation at various slip speeds

The search coils described in section 4.5.3.1 were used to check the variations of the main fluxes with speed and excitation. Flux measurements were carried out using the method of reversals[3]. At high speeds, the excitation had to be kept low because of drive limitations.

Figure 5.4 shows total flux (ϕ_I) leaving the inner laminated section of the field through search coil 4 and figure 5.5 the total flux (ϕ_o) entering the outer laminated section of the field through search coil 5. Both quantities are plotted against excitation at various slip speeds.

A comparison of the two figures reveals immediately that ϕ_I is considerably larger than ϕ_o. In section 5.2 it has been shown that this difference was caused by the high leakage fluxes around the outside of the loss member. The standstill leakage fluxes are plotted against excitation on figure 5.6.

The curves on both figures 5.4 and 5.5 are not as divergent with speed as in Lundell[3,9] or salient pole couplings[10]. Their general form is understandable if the operation of inductor couplings is considered in simplified form. For a given field current, a flux exists in the machine at standstill whose value is dictated by the magnetic circuit. Figure 5.7 shows the idealised standstill airgap flux density wave, Bg, in an inductor coupling; it is unidirectional because of the homopolar field.

IDEALISED STANDSTILL AIRGAP FLUX DENSITY WAVE IN AN INDUCTOR COUPLING.

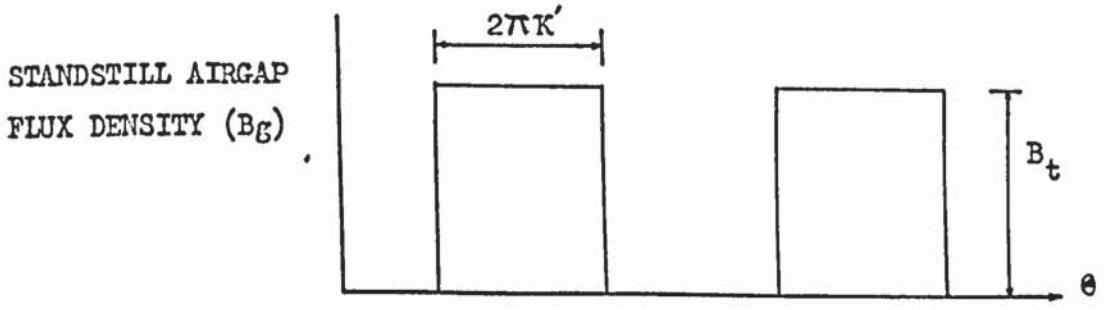

Figure 5.7

The Fourier series for Bg is given by

$$B_g = B_t \left[K' + \sum_{h=1,2}^{\infty} \frac{\sin(hK'\pi).\cos(h\theta)}{h} \right] \qquad (5.1)$$

Equation 5.1 shows that Bg contains a mean level plus all the odd and even harmonics. The fundamental component is the major torque producer whilst the mean level contributes nothing and only saturates the magnetic circuit.

With a tooth width/tooth pitch ratio (K') of 0.45,it can be shown from equation 5.1 that the mean level and fundamental have similar magnitudes. This means, approximately, that only half the flux in the machine is used usefully.

When the airgap flux density moves relative to the loss member, the fundamental component generates eddy-currents in that member; these in turn produce an armature reaction flux. The armature reaction flux subtracts from the fundamental flux (Lenz's law) and so less is available to generate losses, but the mean level is unaffected. Eventually a balance is reached when the mmf needed to set up fundamental flux, overcome armature reaction flux and establish the mean level equals the applied field mmf.

As speed rises the fundamental flux will fall, because less is needed to generate losses, and the armature reaction flux will rise, the mean level remaining approximately the same. This now means that the reduction in total flux will be much less than in Lundell[3,9] or salient pole[10] couplings; it is in fact roughly half their reduction. This is exactly what figures 5.4 and 5.5 show. The wave forms of airgap flux density will obviously change with speed and excitation and they will be discussed later.

5.5 Torque variation with excitation and total flux $\emptyset_I$ at various slip speeds

Figure 5.8 shows torque plotted against excitation and total flux ($\emptyset_I$) at various slip speeds. The slopes for both flux and excitation are nearly the same which verifies that the flux - excitation curve is approximately linear over a wide range of frequencies as figure 5.4 shows.

No conclusions concerning general coupling theory[4,8] can be drawn from these curves since the situation is obscured by the torque, which is the resultant of two different torque-slip curves, and total flux which includes all the harmonics and a mean level. Nevertheless, the relationship between torque (outer) and fundamental flux for the outer region can be computed and compared with theory; this is done in later sections.

Even though no specific conclusions can be drawn from figure 5.8 it is suspected that general trends will be obeyed.

It can be shown[3] theoretically that:

$$T \propto (I_f)^{1.54} \quad \text{(at speeds in excess of } n_m) \quad (5.2)$$

and

$$T \propto (I_f)^{2.85} \quad \text{(at speeds much lower than } n_m) \quad (5.3)$$

a third relationship is also known[4,8]

$$T \propto (I_f)^{2} \quad \text{(at } n_m) \quad (5.4)$$

The equations show that as speed increases the exponent of I_f decreases, figure 5.8 shows this tendency.

At 6000 rev/min (approaching peak torque), Slope of (a) = 2.06 (compare 2.0)

At 500 rev/min (low speed) , Slope of (g) = 2.36 (compare 2.85)

The comparisons are approximate, but do show that the experimental machine tends to obey the general relationship between torque and excitation. This observation is extremely significant because the maximum frequency of eddy-currents in Davies[3] coupling was 150 Hz. The loss member eddy-current frequencies in the experimental dynamometer at 6000 rev/min were 1.8 kHz and 0.9 kHz in the outer and inner regions respectively; that is to say twelve and six times higher than the eddy-current frequency in Davies[3] coupling.

The indication is that the governing factor in coupling operation is the actual speed with respect to the speed at peak torque (n/n_m) and not eddy-current frequency which appears to be arbitrary. This is investigated in detail later.

5.6 Surface current density

5.6.1 Oscillograms of current density across the loss member surface

In section 4.5.5.1 and figure 4.12 the matrix of current density probes on the surface of the loss member was described.

The purpose of the 1 cm centre probes was to:

a) enable a general investigation to be carried out of the current density distribution across the double region loss member,

b) determine whether or not the different frequency eddy-currents in the two regions influenced each other and hence confirm or otherwise the assumption that the machine could be treated as two separate couplings for design purposes, and

c) check if the signals from probes Z_{12} and Z_{13} will be representative of the mean radial current density across the two active regions.

Probes X_1 to X_{11} and Z_1 to Z_{11} were not all positioned on the same radial line as shown on figure 4.18. Initially only probes at the inner and outer edges of the two active regions were included; the others were added as the work progressed and for space reasons were distributed around the loss member. Their phase relationships are therefore arbitrary, but their magnitudes are related and can be compared.

Figures 5.9 to 5.14 show the oscillograms of the current density waves taken from the 1 cm probes at various slip speeds and excitations. It was intended to take six sets of oscillograms with 2A and 4A excitation at 2000, 4000 and 6000 rev/min, but the drive motor overloaded at 4A, 6000 rev/min so a set at 3A, 6000 rev/min were taken instead. The figures show that the wave shapes from each

probe are similar, even though excitation and slip speed change. A close inspection however reveals that their magnitudes are different (see section 5.6.2).

Probes X_1, Z_1, X_7, Z_7, X_{11}, Z_{11} measure the current density in the three end regions[2] of the machine. The oscillograms from probes X_1, Z_1, X_{11} and Z_{11} show that the waves become sinusoidal when the eddy-currents are outside the influence of the inducing airgap flux density. In a later section their peak to peak magnitudes are plotted against slip speed at various excitations. Davies[3] also observed that the end region current density waves were sinusoidal in a drum type coupling.

The reasons for the waves becoming sinusoidal are not fully understood nor are end-effects* in general. One theory is that because the wavelengths of the airgap flux density harmonics in the peripheral direction are much less than the length of the active region, the machine appears infinitely long to these same harmonics. It is known[14] that machines satisfying the wavelength condition for the fundamental tend to have negligible end-effect. Therefore, it can be argued that the same criterion also applies to the harmonics, and since Gibbs[2] has shown the equivalence of the airgap flux density wave in the peripheral direction, By(x), and the time distributed radial current density, Jz(t), at the surface of the loss member then a full solution for the fundamental current density may adequately account for end effects.

The oscillograms from probes X_7 and Z_7 also show a tendency for the waves to become sinusoidal. They are not as clearly defined as the waves in the other two end regions but do show that the lower frequency of the inner eddy-currents is apparently dominant. To obtain more information about the eddy-current interaction between the two regions requires a much finer mesh of probes. Neverthe-

---

* End-effects refer to the influence of all eddy currents outside the active region.

less, an insight to the problem is provided by the oscillograms from probes Z_{10}, Z_8 and Z_6. They show that the waves from Z_{10} and Z_8 are the same frequency and approximately the same magnitude, and that the wave from Z_6 has the same general shape, but is half their frequency.

If the two regions had a major influence on each other, the wave from Z_8 would be different to that from Z_{10} because the latter is at the outer edge and not influenced by the inner region. While this does not prove conclusively that the two regions can be treated separately and hence as two independent machines, it is thought the assumption is reasonable for design purposes.

It can be shown[10] theoretically that the peripheral and radial current density components should be zero and maximum respectively at the centre of the active region. The oscillograms show this is true for the outer region, but not for the inner region which has a pronounced unsymmetrical distribution. This may be due to current crowding caused by the hole in the centre of the loss member. The oscillograms from probes X_2 and Z_2 show clearly that the eddy-currents are turning round dramatically before they reach the middle. Interestingly enough the active region swept area above and below probe X_5 is approximately the same; however, the unsymmetrical distribution needs further investigation.

The source of the ripple on some of the oscillograms, particularly X_2 and Z_2, is not known, but it is thought to be produced by either bad probe contacts on the loss member surface or much more likely the wires from the probe contacts are not laid exactly in line therefore introducing a $d\phi/dt$ voltage into the probe signal.

5.6.2 Current density distribution across the two active regions.

The oscillograms on figures 5.9 to 5.14 show that the current density distribution across the outer active region is symmetrical, but across the inner

active region it is unsymmetrical. To illustrate this more clearly the quantities defined on figure 5.15 were measured from the active region oscillograms, at various slip speeds and excitations, and their actual current density magnitudes were calculated as detailed in section 4.5.5.2.

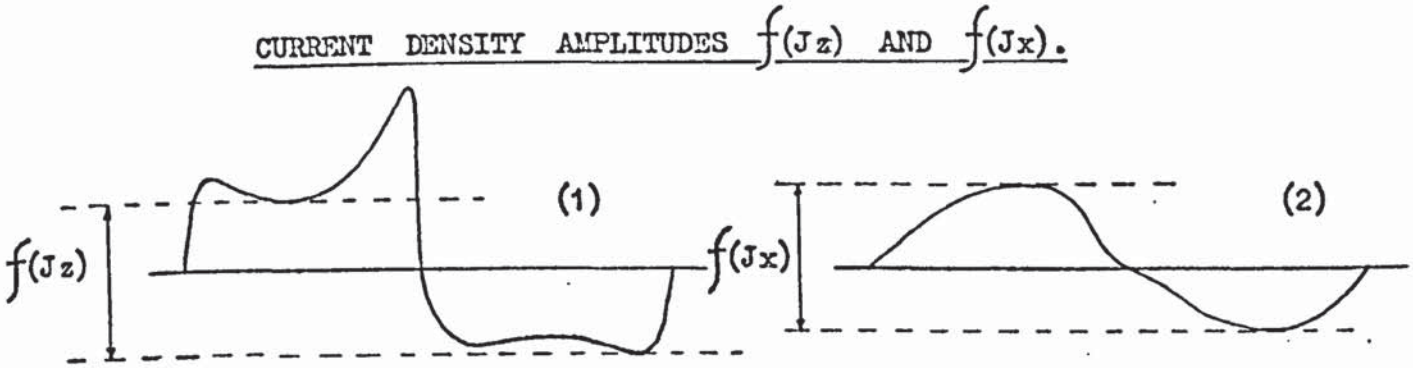

General shapes of radial current density wave (1) and peripheral current density wave (2).

Figure 5.15

The results are plotted on figures 5.16 to 5.19 and show, at the same speed and excitation, that the peak radial current density magnitudes are approximately the same in both regions, which is surprising in view of their different parameters. The explanation is found by comparing the ratio of the measured magnitudes with that calculated using the well known equation:

$$\bar{e} = \bar{B} \wedge \bar{v} . l \qquad (5.5)$$

where B = airgap flux density (T)

v = the relative velocity between rotor and loss member given by $2\pi r_{av}.N$ (m/s); N is slip speed (rev/s) and r_{av} the mean radius of the current density probe (m).

l = length of probe Lp (m)

e = the emf across the probe terminals (V).

Consider the magnitudes from probes Z_9 and Z_5 at 2A, 6000 rev/min; from figures 5.16 and 5.17, the ratio of Jz_9/Jz_5 can be shown to be 1.08.

From figures 5.4 and 5.5 the ratio of $\emptyset_o/\emptyset_I$ (proportional to B_o/B_I) at 2A, 6000 rev/min is 0.7. The mean radius of probe Z_9 is 156 mm and for Z_5 97 mm. Substituting these figures into equation 5.5 and remembering the probes are the same length:

$$\frac{Jz_9}{Jz_5} \propto \frac{e(\text{outer})}{e(\text{inner}} = 0.7 \times \frac{156}{97} = 1.12 \quad \text{(compare measured 1.08)}$$

This simple analysis shows that the uneven flux distribution between inner and outer produces approximately the same peak current density magnitudes in the two regions of the loss member. It can be shown that the analysis also applies to the other probes.

5.6.3 End region current density

The peak to peak values of the oscillograms from probes X_1, Z_1, X_{11} and Z_{11} were measured and their magnitudes calculated as described in section 4.5.5.2. Figure 5.20 shows the components plotted against frequency at various excitations. The radial magnitudes in both end regions are seen to be approximately the same, which is not too surprising considering the results of section 5.6.2. What is surprising, however, is that the radial and peripheral magnitudes in both end regions, at the same speed and excitation, are also approximately the same. It would be interesting to see if this equal distribution pattern is repeated further out in the end regions.

Figure 5.20 also indicates that the magnitudes are approximately proportional to both speed and excitation over the range covered. The linear relationship between the magnitudes and excitation is to be expected, since figures 5.4 and 5.5 show that the machine is unsaturated at 4A, 6000 rev/min. Even though straight lines have

been drawn through the experimental points it is suspected that they do in fact lie on curves flattening out at higher frequencies. This is also implied by the straight lines themselves as they do not pass through the origin at zero slip speed, which of course they should.

5.6.4 Oscillograms of the mean radial surface current density in the active regions

To determine whether the new machine obeys general coupling theory[8] estimates must be made of the peak fundamental armature reaction mmf ($\hat{F}r_1$) and fundamental flux per pole ($\emptyset ac_1$). Both these quantities are derived from the peripheral airgap flux density waves which are usually[3] obtained from search coils spaced across a tooth or pole. Normal methods could not be used because it was not possible to measure the signals from search coils attached to the high speed rotor.

The alternative was to measure the active region radial current density and then construct the airgap flux density wave using equation 5.6

$$Ez.dt = By.dx \qquad (5.6)$$

This equation was given by Gibbs[2] and shows that the time varying radial current density is proportional to the space distributed peripheral airgap flux density at the surface of the loss member.

The two full length active region probes (see section 4.5.5) Z_{12} and Z_{13} were used to obtain oscillograms of the radial current density. In a previous section, it was shown that the current density magnitudes varied across the active regions, particularly the inner, where it falls appreciably towards the middle. The two probes therefore measure the mean radial current density.

Figures 5.21 to 5.24 show the oscillograms from probes Z_{12} and Z_{13}. The waves are the normal[3] peaky type expected in couplings and the demagnetising effect of the armature reaction at the higher speeds can clearly be seen. Figure 5.24 shows the oscillograms taken from probe Z_{13} at low slip speeds. The waves at 500 rev/min are poor quality due to lack of sensitivity of the control system at

low speeds and to the oscilloscope which was set on its lowest range for these pictures. They show that the armature reaction is very small at 500 rev/min, which corresponds to an eddy-current frequency in the outer region of 150 Hz. The significance is that in Davies[3] coupling at 150 Hz the armature reaction was completely dominant, but at this frequency his coupling was operating well above the peak torque point the experimental dynamometer was not.

In section 5.6.3 it was shown that the current density distribution across the outer active region was symmetrical, but across the inner region unsymmetrical. Because of the labour involved, it was decided to analyse the oscillograms from probes Z_{13} only. It was argued that if general coupling theory[8] could be shown to apply for the outer region then it must also apply to the inner region, since the outer region eddy-current frequency was double that of the inner. In the next section, the results from probes Z_{13} are used to derive the on-load peripheral airgap flux density wave in the outer active region.

5.7 Airgap flux density

5.7.1 Derivation of the peripheral airgap flux density distribution in the outer region

The current density oscillograms from probes Z_{13} were replotted on a much larger scale and their zero line, see figure 5.25 later in text, found by counting squares; they were also converted to flux density using equation 5.7 which is derived from (5.5)

$$B(\text{outer}) = \frac{e}{Lp.v} \quad (T) \qquad (5.7)$$

where e = probe voltage

Lp = length of probe (equals the length of the outer active region, $L_A = 3.2 \times 10^{-2}$ m)

v = mean velocity of rotor with respect to the outer region

$= 2\pi.r_{av}.N$

r_{av} = mean radius of outer region = 0.156 m

N = rotor slip speed (rev/s)

The areas above and below the zero line are equal by Kirchoff's law, since they represent the current that flows under a tooth in one direction and back under a neighbouring slot in the opposite direction. Unfortunately the flux density waves produced solely from the oscillograms, by replotting and using equation 5.7, are not the complete peripheral airgap flux density waves; a mean d.c. level must be added before they are useful. The loss member in a homopolar coupling reacts only to the space varying components of airgap flux density and so the current density oscillograms are simply facsimilies of these changing quantities and do not show the d.c. flux density level.;

The full pitch search coils, discussed in section 4.5.3.2, were used to measure the standstill tooth and slot flux densities. It will be obvious from the nature of the experimental machine that the flux linking the two search coils depends on their position with respect to the inserts in the rotor. The flux was measured using the method of reversals[3] and the rotor was moved until maximum and minimum readings were obtained. These readings are not the exact tooth and slot fluxes because considerable fringing takes place as the flux crosses the airgap. Nevertheless, they are compatible with the oscillograms since they were both measured in the same plane, at the surface of the loss member.

The minimum reading, $\phi_{F.P.}$ (min), is a measure of the slot flux, ϕ_s, and when it is divided by the area of the full pitch search coil, $A_{F.P.}$, the mean slot flux density, B_s, is obtained. The maximum reading, $\phi_{F.P.}$ (max) is not the tooth flux, ϕ_t, because the tooth width/tooth pitch ratio is 0.45 and the full pitch coils have a pitch of 0.5. So, the maximum reading includes a fraction of the slot flux as well as the tooth flux. Equation 5.8 was therefore used to calculate slot

flux from the measured maximum values; the value of ϕ_t is approximate because fringing is neglected.

$$\phi_t = \left[\phi_{F.P.}(\max) - 0.1\,\phi_{F.P.}(\min)\right] \qquad (5.8)$$

Mean slot flux density, B_t, was then found by dividing ϕ_t by the area of the inserts, A_t. The areas of the inserts and search coils in the two regions are given below.

$$A_{F.P.}(\text{outer}) = 8.64 \times 10^{-4}\,m^2$$

$$A_{F.P.}(\text{inner}) = 17.20 \times 10^{-4}\,m^2$$

$$A_t \quad (\text{outer}) = 7.79 \times 10^{-4}\,m^2$$

$$A_t \quad (\text{inner}) = 15.55 \times 10^{-4}\,m^2$$

Table 5.1 gives the measured maximum and minimum standstill fluxes from the full pitch search coils and the corresponding tooth and slot flux densities at various excitations.

Table 5.1

Excitation (A)	Standstill flux from full pitch search coils, $\phi_{F.P.}$ (mWb)				Mean standstill airgap flux density. (T)			
	OUTER		INNER		OUTER		INNER	
	max.	min.	max.	min.	B_t	B_s	B_t	B_s
2	0.246	0.0466	0.727	0.13	0.31	0.054	0.469	0.0756
3	0.37	0.0713	1.06	0.2	0.466	0.083	0.684	0.1163
4	0.493	0.092	1.415	0.25	0.621	0.106	0.912	0.145

The d.c. flux density levels were introduced by assuming the slot magnetisation was negligible at 500 rev/min, figure 5.24 shows that armature reaction is small at this speed. B_s was then drawn tangentially to the lowest point on the replotted 500 rev/min waves, see figure 5.25, and hence B_t scaled from this reference point.

CONSTRUCTION OF PERIPHERAL AIRGAP FLUX DENSITY WAVES.

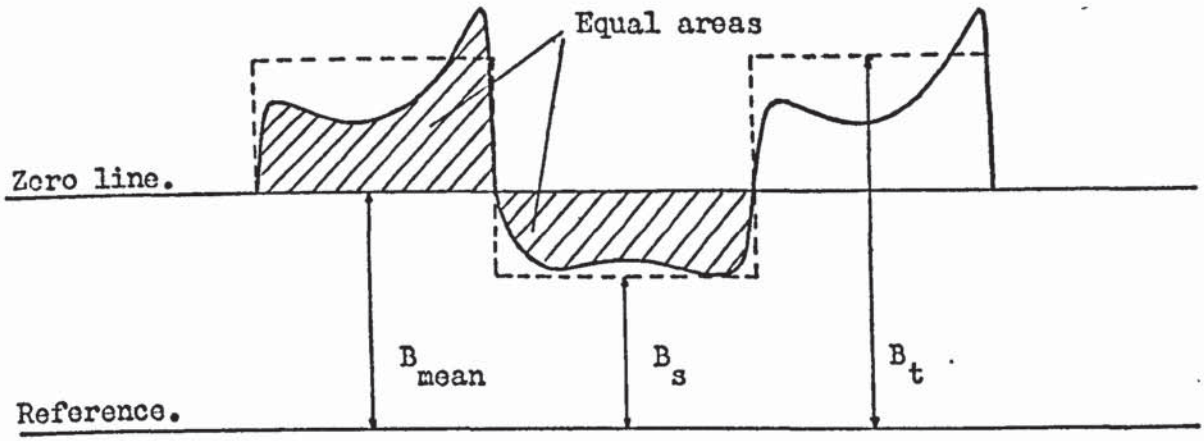

Figure 5.25

Knowing where the zero line of the 500 rev/min wave was, by counting squares, B_{mean} was then measured. This value was then added to the zero line of other replotted oscillograms at the same excitation, but higher slip speeds. The reference level was therefore established for each replotted wave and so B_t and B_s were then measured from it.

Figures 5.26 to 5.28 show the constructed peripheral airgap flux density waves at the surface of the loss member in the outer region; armature reaction effects are evident in all the waves. It can be seen that, as the speed increases at a given excitation, the resultant flux falls as the armature reaction produced flux rises.

The phase angle of armature reaction[3] is also seen to change and in common with the results from Davies[8] inductor coupling it is greater than 60^{o}, whereas that for a Lundell[4] coupling, over a similar speed range, approached 53^{o}. The discrepancy originates from the slightly different mechanisms that produce the

alternating flux components and the pole arc/pole pitch ratio which is different[8] in Lundell and inductor couplings. The angle increases with speed because the armature reaction produced flux must move, by Lenz's law, to oppose the applied flux. This is similar to armature reaction in synchronous machines which, in the limit, progresses to the quadrature axis therefore magnetising the quadrature axis and demagnetising the direct axis. Similarly in couplings the armature reaction magnetises the slot and demagnetises the tooth.

The armature reaction phase angles were not analysed in detail because of the approximate method used to obtain B_t and B_s. A small error in these quantities will change the phase angles considerably as the figures show. Two other quantities were derived from these curves:

a) The fundamental and harmonic components of airgap flux density were obtained by Fourier analysis.

b) The magnitudes of the peak fundamental armature reaction mmf, $\hat{Fr}_1$ were estimated.

These quantities are used later in checking Davies[8] general eddy-current coupling theory.

The applied mmf was not distributed equally between the four active regions because of the leakage paths which produce different flux densities in each airgap, see section 5.2. For this reason, the AT/tooth values shown on figures 5.26 to 5.28 were estimated approximately by assuming that there is negligible mmf loss in the magnetic circuit, and that the flux density in the active and parasitic airgaps was the same, i.e. neglecting leakage flux between the two regions. This implies that all the applied mmf was used in forcing flux across the two airgaps and also distributed in the ratio of the measured standstill flux density in each active region.

5.7.2 Fourier analysis of the airgap flux density waves

Each of the on-load airgap flux density waves shown on figures 5.26 to 5.28 were analysed up to the 17th harmonic using a computer program. This required a minimum of 36 points for each wave, so they were divided into 36×10^{o} intervals.

The Fourier analysis of the flux density waves is summarised in tables 5.2, 5.3, 5.4, 5.5 and 5.6.

Table 5.2 shows that the fundamental component of airgap flux density decreases with slip speed. This was expected[8] and these results are analysed in detail later.

It can be seen from table 5.3 that the mean flux density remains approximately constant over the speed range, as it should, and also doubles with excitation. This is a valuable check and gives confidence in the method used to construct the airgap flux density waves, particularly the inclusion of the mean standstill levels using the full pitch search coils.

In tables 5.4 to 5.6 the harmonic content of the waves is seen to be high. All the odd and even harmonics are present with the 3rd, 5th, 7th and 9th dominant. At low speeds, the even harmonics are negligible. This is explained by assuming the airgap flux density wave, at low speeds, approximates to the idealised standstill wave shown on figure 5.7. The assumption is reasonable because armature reaction effects are small at low speeds. Equation 5.1 gave the Fourier series for the idealised wave and the coefficient of the harmonic components was given by

$$\left|Bg_h\right| = \frac{\sin(hK'\pi)}{h} \qquad (5.9)$$

With a tooth width/tooth pitch ratio (K') of 0.45 it can be shown from equation 5.9 that there are practically no even harmonics. As slip speed increases the airgap flux density waves become peaky because of armature reaction and hence their even harmonic content increases as the tables indicate.

Table 5.2

Peak values of the fundamental component of the peripheral airgap flux density waves expressed in Tesla

Slip speed (rev/min) / Excitation (A)	500	2000	4000	6000
2	0.135	0.106	0.095	0.09
3	0.184	0.148	0.134	0.127
4	0.246	0.195	0.172	0.161

Table 5.3

Mean flux density of the peripheral airgap flux density waves expressed in Tesla

Slip speed (rev/min) / Excitation (A)	500	2000	4000	6000
2	0.165	0.161	0.16	0.16
3	0.24	0.235	0.237	0.237
4	0.315	0.301	0.296	0.295

Table 5.4

Mean level and harmonic content of the peripheral airgap flux density waves expressed as a per unit of the fundamental

EXCITATION : 2A

h \ n	500	2000	4000	6000
0	1.23	1.52	1.67	1.78
1	1.0	1.0	1.0	1.0
2	0.058	0.187	0.241	0.291
3	0.395	0.454	0.473	0.497
4	0.043	0.087	0.118	0.146
5	0.224	0.258	0.276	0.290
6	0.050	0.058	0.081	0.098
7	0.144	0.161	0.179	0.190
8	0.053	0.055	0.075	0.085
9	0.095	0.106	0.121	0.134
10	0.058	0.059	0.077	0.086
11	0.064	0.075	0.088	0.101
12	0.059	0.064	0.076	0.086
13	0.041	0.055	0.067	0.080
14	0.062	0.066	0.078	0.088
15	0.025	0.042	0.057	0.068
16	0.064	0.065	0.077	0.086
17	0.013	0.036	0.050	0.061

n = slip speed, rev/min

h = harmonic order

Table 5.5

Mean level and harmonic content of the peripheral airgap flux density waves expressed as a per unit of the fundamental

EXCITATION : 3A

h \ n	500	2000	4000	6000
0	1.3	1.585	1.76	1.87
1	1.0	1.0	1.0	1.0
2	0.103	0.218	0.257	0.304
3	0.415	0.484	0.509	0.519
4	0.051	0.098	0.123	0.155
5	0.224	0.270	0.295	0.302
6	0.050	0.064	0.083	0.097
7	0.140	0.164	0.184	0.197
8	0.056	0.072	0.087	0.094
9	0.097	0.112	0.127	0.147
10	0.061	0.077	0.092	0.098
11	0.070	0.080	0.096	0.115
12	0.067	0.080	0.094	0.099
13	0.049	0.054	0.074	0.089
14	0.070	0.077	0.093	0.099
15	0.033	0.039	0.058	0.075
16	0.073	0.073	0.090	0.098
17	0.016	0.025	0.046	0.065

n = slip speed, rev/min

h = harmonic order

Table 5.6

Mean level and harmonic content of the peripheral airgap flux density waves expressed as a per unit of the fundamental

EXCITATION : 4A

h \ n	500	2000	4000	6000
0	1.28	1.55	1.73	1.84
1	1.0	1.0	1.0	1.0
2	0.101	0.229	0.278	0.321
3	0.414	0.487	0.521	0.536
4	0.057	0.096	0.133	0.162
5	0.229	0.277	0.305	0.320
6	0.060	0.077	0.101	0.117
7	0.142	0.172	0.197	0.208
8	0.066	0.082	0.102	0.111
9	0.093	0.113	0.136	0.147
10	0.067	0.086	0.106	0.112
11	0.063	0.081	0.097	0.109
12	0.069	0.086	0.104	0.111
13	0.040	0.058	0.072	0.084
14	0.071	0.085	0.103	0.108
15	0.023	0.044	0.056	0.066
16	0.070	0.083	0.100	0.105
17	0.011	0.035	0.045	0.057

n = slip speed, rev/min

h = harmonic order

5.7.3 Harmonic torques

In this thesis, "harmonic torques" refer to the components of torque produced by the airgap flux density harmonics. These torques add directly to the fundamental torque because airgap flux density harmonics are space harmonics and travel at the same speed as the fundamental flux density.

Since this subject is controversial and its analysis complex it will not be discussed in detail here. It is clear however, from other authors'[8,9,10] work that in the region of peak torque the contribution by all the harmonics to the total torque is between 9% and 36%. These figures were both based on Davies[8] fundamental flux equation and also that the hth harmonic poles are h times the fundamental poles and the flux/pole is 1/h for the same peak flux density. The general equation used was

$$\frac{T_h}{T_1} \propto \frac{1}{h^{1/4m-2}} \left[\frac{\hat{B}_h}{\hat{B}_1}\right]^{\frac{2m}{2m-1}} \qquad (5.10)$$

The two extreme values of m are 0.75 and 1.0, where m = 0.75 represents fully saturated conditions and m = 1.0 represents linear conditions. Davies[8] produced the 9% value using m = 0.75 which gives

$$\frac{T_h}{T_1} \propto \frac{1}{h} \cdot \left[\frac{\hat{B}_h}{\hat{B}_1}\right]^3$$

Using linear theory, m = 1.0, James[9] estimated the 36% figure, which must be considered an overestimate since he proved that the loss member in his experimental machine was saturated (m < 1). The equation he used was

$$\frac{T_h}{T_1} \propto \frac{1}{h^{1/2}} \cdot \left[\frac{\hat{B}_h}{\hat{B}_1}\right]^2$$

Wright[10] points out that the truth must lie somewhere between the two because Davies approach underestimates the harmonic torques, he himself uses m = 0.77, so the relationship becomes

$$\frac{T_h}{T_1} \propto \frac{1}{h^{0.92}} \cdot \left[\frac{\hat{B}_h}{\hat{B}_1}\right]^{2.85}$$

These remarks and equations apply only to couplings with negligible end-effects. An estimate of the harmonic torques, based on equation 5.10, has not been made for the experimental machine because this had considerable end-effects with the added complications of unsymmetrical end regions plus a congested middle region in which eddy-currents of different frequencies existed.

During his research the author carried out extensive experimental and analytical work on harmonic torques, but due to certain aspects of the theory being incomplete and also lack of space it has not been included. Nevertheless, the following general conclusions were reached.

a) The value of pole arc/pole pitch ratio (tooth wideth/tooth pitch) is critical to the harmonic torque contribution in couplings; Davies has himself verified this* experimentally.

b) The contribution of harmonic torques to the total torque was indeed between 9% and 36% in the region of peak torque, as other authors[8,9,10] have shown.

---

* Whilst working in America for the General Electric Company Davies carried out extensive unpublished work on inductor couplings with different tooth width/tooth pitch ratios. He observed that using K' values from 0.45 to 0.115 the reduction in total torque was approximately 50%. For $K' = 0.115$ the predicted torque, using fundamental flux only, was negligible which indicated that harmonic torques are considerable in couplings with low K' values.

c) Because the harmonic poles are h times the fundamental, the harmonic torques have speeds at peak harmonic torques ($n_{m,h}$) much higher than the fundamental ($n_{m,1}$). Consequently, even though the harmonic torques are small in the region of peak fundamental torque, their nature is such that when added to the fundamental torque-speed curve the resultant speed at peak torque (n_m) can be up to 4 times greater than the predicted $n_{m,1}$. These comments only apply to couplings with negligible end-effects, when these are accounted for n_m can be as much as 8 times $n_{m,1}$, but the resultant peak torque changes little[9]. Most authors claim reasonable success in predicting absolute values of peak torque, yet none have predicted speed at peak torque values with any accuracy.

d) The ratio of harmonic torque to the fundamental increases with slip speed[10]. It is thought that this is only true until the harmonic torques themselves reach their peak torque speeds.

e) Workable solutions for end-effects are available, but accurate calculation of the resultant absolute values of T_m and n_m still cannot be performed because of the more complicated problem of dealing with harmonic torques.

5.8 Fundamental flux per pole for the outer region

Figure 5.29 shows the variation of fundamental flux per pole, ϕac_1, with slip speed for various excitations. The values were calculated from the peak fundamental airgap flux density components given in table 5.2. Fundamental flux per pole is defined as

$$\phi_{ac_1} = \frac{2}{\pi} \cdot \hat{B}_1 \cdot \frac{\lambda_1}{2} \cdot L_A \qquad (5.11)$$

where $\lambda_1 = 2 \cdot \frac{\pi}{p} \cdot r_{av}$ for the experimental machine.

L_A = length of outer active region.

From table 4.1, for outer region, therefore

$$\emptyset ac_1 = 5.5 \times 10^{-4} . \hat{B}_1$$

The values of $\emptyset ac_1$ will be used later when general coupling theory is investigated.

5.9 Peak fundamental armature reaction mmf for the outer region

Davies method[3] was used to estimate the peak fundamental armature reaction mmf, $\hat{F}r_1$, from the airgap flux density waves shown on figures 5.26 to 5.28. The method was developed for Lundell couplings and neglects harmonics higher than the third, which is also assumed to have the same zero as the fundamental armature reaction. It was therefore very approximate even when applied to Lundell couplings and Davies himself states that the numerical values of $\hat{F}r_1$ obtained by the method should be used with caution and not too much faith placed in them.

When applied to the experimental machine the basis of the method is not strictly correct because the armature reaction wave includes all the odd and even harmonics. In the absence of an alternative method however, it was used and errors can be expected in the numerical values of $\hat{F}r_1$. On the other hand their variation with torque and speed is thought to be correct, but this depends on whether the relative contributions of the fundamental and harmonic components to the resultant armature reaction wave remain the same.

One of the objectives of this work was to determine if general coupling theory[8] applied to high speed machines. Hence, measurements of peak fundamental armature reaction mmf were included for the sake of completeness and because no data has been previously published on high speed couplings.

The measured values of $\hat{F}r_1$ are shown on figure 5.30 plotted against slip speed for various excitations. These values are used later when the relationship between torque, slip speed and armature reaction is derived for the outer region and also in checks on Davies[8] normalised armature reaction curve.

5.10 Estimation of torque produced by the outer region

All Davies[8] theoretical equations were derived for Lundell and salient pole couplings and strictly they only apply to any one individual machine. Nevertheless, it was stated previously that when designing inductor couplings it was usual to treat their two regions as separate machines. Davies' equations are therefore taken to apply to each of the two regions in the experimental dynamometer.

In later sections the relationships between fundamental torque, slip speed, peak fundamental armature reaction mmf and fundamental flux per pole will be investigated for the outer region; more specifically the experimental indices are compared with those predicted theoretically[3]. Before this can be attempted however an estimate must be made of the relative torque contributions from the two regions. The numerical value of outer region torque, T (outer), can then be obtained from the measured torque which is the sum of T (outer) and T (inner).

The torque referred to in all Davies equations is the fundamental component, T_1, but fortunately the numerical values of the harmonic torques can be neglected in the speed range up to and including peak torque. This is the speed range covered in this experimental work and so

$$T_1(\text{outer}) \quad \simeq \quad T(\text{outer}) \qquad \text{(see section 5.7.3)}$$

Peak fundamental torque, $T_{m,1}$, and speed at peak fundamental torque, $n_{m,1}$, are related to the coupling parameters by the following equations, which were given by Davies[8] for drum couplings and are modified for disc couplings in Appendix 3.

$$T_{m,1} = \frac{p R L_A}{g} . (F_g)^2 \qquad (5.11)$$

$$n_{m,1} = \frac{e g^2 p^{4m-1}}{R^{4m} (F_g)^{4-4m}} \qquad (5.12)$$

Assuming that these equations apply to each region of the dynamometer and also that airgap length (g) and loss member surface resistivity (ρ) are the same for both regions, then, using table 4.1 and m = 0.77, it can be shown that:

$$\frac{T_{m,1}(\text{outer})}{T_{m,1}(\text{inner})} = 2.07 \frac{\hat{B}_{g_1}(\text{outer})}{\hat{B}_{g_1}(\text{inner})}$$

and

$$\frac{n_{m,1}(\text{outer})}{n_{m,1}(\text{inner})} = 0.653 \frac{\hat{B}_{g_1}(\text{outer})}{\hat{B}_{g_1}(\text{inner})}$$

The quantities $\hat{B}g_1$ are the peak fundamental values of the standstill flux density wave in each airgap. It can be shown that they are proportional to the difference in the mean standstill tooth flux density, B_t, and slot flux density, B_s, in each region so

$$\frac{\hat{B}_{g_1}(\text{outer})}{\hat{B}_{g_1}(\text{inner})} \propto \frac{B_t(\text{outer}) - B_s(\text{outer})}{B_t(\text{inner}) - B_s(\text{inner})} \simeq 0.7 \text{ (from table 5.1)}$$

Substituting the relationship into the above equations gives

$$\frac{T_{m,1}(\text{outer})}{T_{m,1}(\text{inner})} \simeq 1.015$$

also

$$\frac{n_{m,1}(\text{outer})}{n_{m,1}(\text{inner})} \simeq 0.9052$$

Using these values and Davies[3] generalised curve the torque-slip characteristic for each region was plotted on the same log-log graph paper. The two curves

were then added, and the resultant, which represents the measured torque-slip curve, renormalised to allow a direct comparison between it and its two components. It was then a simple exercise to obtain the torque distribution between the inner and outer region at any actual slip speed. Some important values are given in table 5.7 where n/n_m refers to the resultant curve, which incidently is approximately the same as Davies generalised torque-slip curve.

Table 5.7

Theoretical distribution of torque between the outer and inner region

T(outer)/T(inner)	n/n_m (n_m=10,000 rev/min)	Slip speed (rev/min)
1.39	0.05	500
1.20	0.2	2000
1.08	0.4	4000
1.025	0.6	6000

The numerical values of the outer region torque were computed using the above table and the measured torque-slip curves shown on figure 5.3. Table 5.8 gives a summary of T(outer) and the corresponding measured torque at various slip speeds and excitations.

5.11 Relationship between torque, fundamental flux per pole and slip speed for the outer region.

The general theoretical relationship between fundamental torque, slip speed and fundamental flux per pole is obtained from reference 8

$$T_1 \propto \phi_{ac_1}^{\frac{2m}{2m-1}} \cdot n^{\frac{1}{4m-2}} \qquad (5.13)$$

Most authors[3,9.10] use m = 0.77, but as Davies pointed out this value only applies when the saturation level in the skin depth is very high. Nevertheless,

Table 5.8

Measured torque and estimated outer region torque at various slip speeds and excitations

Excitation : 2A

Measured torque T (Nm)	Outer region torque T (outer) (Nm)	Slip speed (rev/min)
5.5	3.2	500
13.0	7.2	2000
16.5	8.25	4000
18.7	9.25	6000

Excitation : 3A

13.8	8.0	500
31.5	17.6	2000
39.0	20.0	4000
42.5	21.25	6000

Excitation : 4A

27.5	16.0	500
58.5	33.0	2000
72.3	38.0	4000
81.0	41.0	6000

putting m = 0.77 into equation 5.13 gives

$$T_1 \propto \text{Øac}_1^{2.85}.n^{0.925}$$

Figure 5.31 shows the outer region torque, from table 5.8, plotted against fundamental flux per pole, from figure 5.29, at various slip speeds. Also shown, by cross plotting, is the variation of T (outer) with slip speed at constant fundamental flux.

The measured index of Øac_1 increases from 2.64 (m = 0.817) at 500 rev/min to 2.78 (m = 0.781) at 6000 rev/min. This can be considered good agreement with the theoretical index of 2.85 (m = 0.77). The index of speed varies from 0.83 (m = 0.8) at 0.05 mWb to 0.85 (m = 0.795) at 0.1 mWb. This is also good correlation with the theoretical value of 0.925 (m = 0.77).

A comparison of the measured indices given here with those from reference 8 reveals that they have an extraordinary similarity. This was not expected even though the experimental machine and Davies inductor coupling were operating over a similar n/n_m range.

At the maximum test speed, the experimental dynamometer had an eddy-current frequency in its outer region of more than six times that in Davies inductor coupling, so the skin depth in this region was at least $1/\sqrt{6}$ times shallower. It was thought therefore that the iron would be operating in the region of the magnetisation curve where m = 0.77 or even 0.75, but as the results show m appears to progress towards the limiting value as slip speed increases.

The inference is that when couplings are operating at low n/n_m values even if their eddy-current frequencies are abnormally high (1.8 kHz in the outer region at 6000 rev/min and hence a very small skin depth) their loss members may not be in a highly saturated condition corresponding to m = 0.77 or 0.75.

The results summarised on figure 5.31 prove that the outer region obeys equation 5.13 and likewise general theory[8] also. This verifies that two region inductor couplings can be treated as separate machines for design purposes as was previously inferred by the current density oscillograms discussed in section 5.6.1.

Considering how T(outer) and $\emptyset ac_1$ were obtained, they are remarkably linear on log-log plots and give confidence in the measurements and in the conclusions which are drawn from them.

5.12 Relationship between torque, slip speed and peak fundamental armature reaction mmf for the outer region

Figure 5.32 shows the measured values of peak fundamental armature reaction mmf ($\hat{F}r_1$), from figure 5.30, plotted against outer region torque, from table 5.8, at various constant slip speeds. Also shown (by cross plotting) is the variation of $\hat{F}r_1$ with slip speed at constant torque. The points are again remarkably linear on log-log plots, considering the doubtful procedure used to obtain $\hat{F}r_1$ which was discussed in section 5.9.

The measured slopes do not have a marked variation as did those given on figure 5.31; the slopes of $\hat{F}r_1$ against T(outer) vary from 0.6 at 2000 rev/min to 0.61 at 6000 rev/min; the slopes of the $\hat{F}r_1$ - speed lines were approximately constant at 0.25. These results can be compared with the theoretical equation[8] relating peak fundamental armature reaction mmf, fundamental torque and slip speed, it is given by

$$\hat{F}r_1 \propto T_1^{1/2m} . n^{1/4m} \qquad (5.14)$$

where $\hat{F}r_1$ in this equation is with respect to the loss member and not as usual[3,9.10] the field member, putting m = 0.77 yields

$$\hat{F}r_1 \propto T^{0.65} n^{0.325} \qquad \text{(theoretical)}$$

This compares reasonably well with the measured indices.

$$\hat{Fr}_1 \propto T^{0.61} n^{0.25} \qquad \text{(from test)}$$

The index for torque is good correspondence with theory, but that for speed is considered poor. This was put down to the method used to obtain $\hat{Fr}_1$ and on reflection it is surprising the measured indices are as close to the theoretical values as they are. These results tend to confirm the conclusions reached in the previous section.

5.13 Generalised curves

It was discussed in section 1.4 that Davies most useful contribution to coupling theory was perhaps the generalised curves he derived for torque, fundamental flux per pole, peak fundamental armature reaction mmf and drum loss. In the following sections his calculated curves, using m = 0.77 are compared with the experimental results. Drum loss is not considered separately since it is a derivative of the torque. It follows therefore that if the generalised torque-slip curve is valid then the loss curve will also be valid.

5.13.1 Generalised torque-slip curve

The measured torque-slip curves are plotted on figure 5.33 at various excitations. Davies[8] generalised curve is superimposed onto each torque-slip curve and the general correspondence is good except at low slip speeds. The measured torque-slip curves from machines of the type under test would not normally fit the generalised curve so well because the characteristics of inner and outer regions would in general be different. However, it has been shown, in section 5.10, for the experimental dynamometer that

$$T_m(\text{outer}) \simeq T_m(\text{inner})$$

and

$$n_m(\text{outer}) \simeq 0.9\, n_m(\text{inner})$$

so that, at high slip speeds, the distribution of torque between the two regions is approximately the same, but at low slip speeds the ratio of T(outer)/T(inner) increases, as table 5.7 shows. At low speeds therefore the measured torque will diverge from the generalised curve. This is exactly what figure 5.33 shows and it is now obvious that the agreement between the measured torque-slip curves and generalised curve was a coincidence.

The generalised curve strictly applies to any one individual machine and to test it fairly in this case it must be compared with the torque produced by either of the two regions and not the sum of both as was measured. On figure 5.34 the estimated outer region torque (from table 5.8) is compared with the generalised curve and the overall correlation is now excellent even at low slip speeds. This was expected since the approximation[4] $\sqrt{\Sigma} \propto \gg 2\pi/\lambda_1$ was thought to be valid (at 500 rev/min the outer region eddy-current frequency was 150 Hz) even though the actual n/n_m value was low.

A comparison of figures 5.33 and 5.34 reveals that the resultant speed at peak torque is considerably greater than the outer region speed at peak torque. This will be utilised in the next section when the other generalised curves are compared with the experimental results.

5.13.2 Fundamental flux per pole and peak fundamental armature reaction mmf generalised curves

Figure 5.35 shows the measured values of $\emptyset ac_1$ and $\hat{F}r_1$ plotted on log-log paper at various excitations. Davies generalised curves for both quantities are also shown; they were not fitted to the experimental points like the torque-slip curves, but drawn in at the predicted outer region speed at peak torque values. These were obtained from figure 5.34 at the appropriate excitations for each set of experimental points.

The agreement of the $\emptyset ac_1$ experimental points with the fundamental flux generalised curve is very good. On the other hand the $\hat{F}r_1$ points are a poor fit to the armature reaction generalised curve. The error is thought to be due to the inaccurate method used to determine the $\hat{F}r_1$ values.

Since the generalised torque and flux curves have been shown to be valid, for the experimental machine, it follows that the armature reaction generalised curve also applies because it is implicit in both of the others[8]. It is apparent therefore that a more accurate method of estimating peak fundamental armature reaction mmf for inductor couplings must be found.

5.14 Peak torque and speed at peak torque by dimensional ratioing

It was stated in chapter 4 that the experimental dynamometer was designed by assuming it could be treated as two separate disc machines. The peak torque and speed at peak torque were then derived for each machine by dimensional ratioing from Davies[8] drum inductor coupling. The accuracy of the ratioing technique when applied to high speed couplings will now be investigated.

The peak torque and speed at peak torque equations for disc and drum machines are obtained from Appendix 3. By ratioing them and assuming the resistivities are the same it can be shown that

$$\frac{T_{m,1}(\text{dynamometer})}{T_{m,1}(\text{Davies inductor})} = \left[\frac{g_i}{g_d}\right].\left[\frac{P_d \cdot L_{A,d} \cdot R_d}{P_i \cdot L_{A,i} \cdot D_i}\right].\left[\frac{F_{g_d}}{F_{g_i}}\right]^2 \qquad (5.15)$$

and

$$\frac{n_{m,1}(d)}{n_{m,1}(i)} = \left[\frac{g_d}{g_i}\right]^2.\left[\frac{P_d}{P_i}\right]^{4m-1}.\left[\frac{D_i}{R_d}\right]^{4m}.\left[\frac{F_{g_i}}{F_{g_d}}\right]^{4-4m} \qquad (5.16)$$

where the suffix 'd' refers to the experimental dynamometer and 'i' to Davies inductor coupling.

With an excitation of 0.25A (325 AT/tooth) Davies inductor coupling produces, from one region only, a peak torque of 7.75 Nm at a speed of 4000 rev/min. Substituting these values and the appropriate machine parameters, from reference 8 and table 4.1, into equations 5.15 and 5.16 yields

$$T_{m,1}(d) = 11.7 \left(\frac{Fg_d}{325}\right)^2$$

also $$n_{m,1}(d) = 12,300 \left(\frac{325}{Fg_d}\right)^{0.92}$$

where m is taken as 0.77

Table 5.9 gives values of $T_{m,1}(d)$ and $n_{m,1}(d)$ for various excitations, also tabulated are the estimated values of these quantities from figure 5.34.

Table 5.9

Comparison of the estimated outer region peak torque and speed at peak torque with those obtained by dimensional ratioing

Excitation		Estimated values from figure 5.34		By dimensional ratioing	
I_f (A)	Fg_d(approx) (AT/tooth)	$T_{m,1}(d)$ (Nm)	$n_{m,1}(d)$ (rev/min)	$T_{m,1}(d)$ (Nm)	$n_{m,1}(d)$ (rev/min)
2	310	9.5	8500	10.6	12300
3	465	21.75	7500	23.9	8850
4	620	41.0	6800	42.6	6750

The peak torques compare reasonably well, but the speed at peak torques have poor correspondence which is undoubtedly due to the different end-effects and harmonic torques in the experimental machine and Davies inductor coupling. Their harmonic torques are different because the dynamometers airgap flux density is

richer in harmonics than Davies machine at the same AT/tooth.

James[9] has shown that similar couplings with and without end-effects have approximately the same peak torques, yet entirely different speedsat peak torque. It follows therefore that similar machines with different end-effects also have corresponding peak torques, but not the same speedsat peak torque . This is the main reason for the good correlation in peak torques and poor agreement in speedsat peak torque .

Even though dimensional ratioing does not give accurate n_m values for the dynamometer this does not detract from its usefulness. The nature of the generalised torque-slip curve is such that in the speed range $0.5 < n/n_m < 3$ the torque is still within 10% of the T_m value. When designing a coupling its peak torque must be predicted accurately whereas its speed at peak torque need not be too precise and table 5.9 shows that dimensional ratioing is adequate for obtaining peak torque values.

In conclusion this section has shown that normal methods can be used with confidence to design high speed couplings.

5.15 Loss member surface temperature

5.15.1 Variation of surface temperature with time at various slip speeds and excitations

Figures 5.36 to 5.38 show the loss member surface temperature - time response curves at different excitations and speeds. Each figure contains corresponding results from thermocouples 3 and 5 - only the results from these two were recorded, since a preliminary investigation, using all the thermocouples shown on figure 4.11, revealed that the temperatures across the two active regions were reasonably uniform. It was originally intended to use the couples in the centres of the two active regions, T/C 5 and T/C 2, but the latter was damaged during initial testing. The temperatures from thermocouple 7 were also noted and found to be

lower than those from thermocouple 5, e.g. at 2.5A, 4000 rev/min, T/C 7 gave 34°C compared to 39°C from T/C 5.

An inspection of the curves reveals that the temperatures of the two regions are only slightly different, which gives confidence in the cooling system design. The responses also appear to be exponential and they will be proved so later when the thermal time constants for the two regions are derived.

The curves were all taken with a cooling water throughput of 27 litres/minute (0.46 kg/s). This was set by adjusting the cooling system outlet valve and then recording the time taken for the outlet water to fill a calibrated container.

5.15.2 Torque variation with time at different slip speeds and excitations

In chapter 2 it was discussed that the loss member temperatures in disc couplings would only have a limited effect on the torque. This is verified by figure 5.39 which shows measured torque - time curves at various slip speeds and excitations; they were taken simultaneously with the temperature - time curves and correspond to a temperature range up to 60°C.

The constancy of the dynamometer torque with temperature is extremely valuable when predicting surface temperatures since the loss density is also constant at a particular speed. In contrast, the loss density in drum couplings is not constant because of their considerable torque reduction as temperature increases (see chapter 3) and so, in general, their loss member temperature prediction must be based on an iterative use of the relevant equations.

5.15.3 Heat transfer distribution in water cooled couplings

It was assumed in the theory of chapter 2 that airgap heat transfer was negligible. Before the equations given there could be applied to the dynamometer it was therefore necessary to verify this assumption and the simplest method was to use the power balance equation.

$$P_T = P_{c,B} + P_g \quad (5.17)$$

where P_T = total power = $T.\omega$ (5.18)

$P_{c,B}$ = power removed by back face coolant

$$= Q_c \cdot c_c \cdot (t_{2,c} - t_{1,c}) \quad (5.19)$$

P_g = total airgap heat transfer by radiation and convection

$$\triangleq Q_g \cdot c_g \cdot (t_{2,g} - t_{1,g}) \quad (5.20)$$

and T = total measured torque (Nm)

ω = mechanical angular velocity, $2\pi N$ (rad/s)

Q_c = water mass flow rate (kg/s)

c_c = specific heat of water (Ws/kg^{o}C)

$t_{2,c}$ = water outlet temperature (^{o}C)

$t_{1,c}$ = water inlet temperature (^{o}C)

Q_g = air mass flow rate in the airgap (kg/s)

c_g = specific heat of air taken at mean bulk temperature, $t_{b,g}$ (Ws/kg^{o}C)

$t_{2,g}$ = air outlet temperature from the airgap (^{o}C)

$t_{1,g}$ = air inlet temperature to the airgap, ambient (^{o}C)

The quantity P_g was calculated first from the difference between P_T and $P_{c,B}$ and then as a cross check from equation 5.20.

Table 5.10 gives measured values of T, $t_{1,c}$ and $t_{2,c}$ along with the calculated values of P_T, $P_{c,B}$ and $(P_T - P_{c,B})$. The specific heat of water was taken as 4190 Ws/kg^{o}C and Q_c, from section 5.15.1, was 0.46 kg/s (27 litres/minute). The table shows that the airgap losses are a small percentage of the total losses and so confirming they may be neglected for theoretical purposes.

To calculate P_g directly, the components of equation 5.20 must be obtained. The temperatures $t_{2,g}$ and $t_{1,g}$ were measured with thermocouples placed in the air

Table 5.10

Excitation : 3A

Slip speed rev/min	T (Nm)	$t_{1,c}$ (^{o}C)	$t_{2,c}$ (^{o}C)	P_T (W)	$P_{c,B}$ (W)	$P_g=(P_T-P_{c,B})$ (W)	(P_g/P_T)x100 (%)
2000	25	10	12.5	5230	4810	420	8%
4000	38	10	17.25	15800	14000	1800	11%

inlet and outlet passages; the specific heat of air, c_c, was taken at the mean bulk temperature ($t_{b,g}$) and is, from reference 46, 1006 Ws/kg^{o}C. The quantity Q_g was estimated from the following equation.

$$Q_g = S.A.\rho.v$$

where S = number of air outlet slots = 12

A = area of each air slot = $3.226 \times 10^{-4} m^2$

ρ = density of air[46] (taken at $t_{b,g}$) = 1.215 kg/m^3

v = air velocity in outlet passages

The air velocity was derived from measurements taken with a pitot-static tube which was positioned in the air outlet passages. As the tube was traversed across a slot, a considerable variation in pressure head was observed and so only the maximum readings were recorded. Figure 5.40 shows the computed maximum slot velocities plotted against slip speed.

Values of v, Q_g, $t_{2,g}$ and $t_{1,g}$ are given in table 5.11 for an excitation of 3A at 2000 and 4000 rev/min

Table 5.11

Excitation: 3A

Slip speed (rev/min)	v (m/s)	Q_g (kg/s)	$t_{2,g}$ (^{o}C)	$t_{1,g}$ (^{o}C)
2000	25.9	12.2×10^{-2}	23.5	21
4000	50.8	24×10^{-2}	25.0	21

MEASURED AIR VELOCITY - SLIP SPEED.

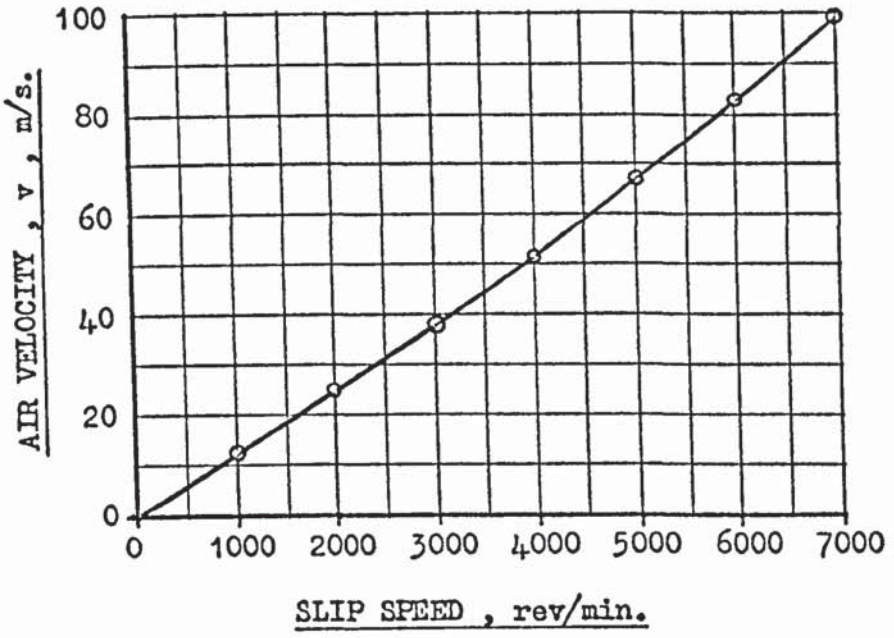

Figure 5.40

By substituting the appropriate values from table 5.11 into equation 5.20 it can be shown that at 2000 rev/min

P_g = 305 W (compare 420 W from table 5.10)

and at 4000 rev/min

P'_g = 1000 W (compare 1800 W from table 5.10)

It is appreciated that these values are very 'approximate', nevertheless, they do provide a valuable check on those given previously.

From the above results it can be concluded that, in general, airgap heat transfer can be neglected in water cooled couplings provided their surface temperatures are not excessively high. This decision could also have been reached knowing that $h_c \gg h_g$ for water cooling since K(water) $\gg$ K(air), where h_c and h_g are the surface heat transfer coefficients and K thermal conductivity.

5.15.4 The general theoretical equation for the loss member surface temperature

By putting y = o into the general solution, equation 2.42, it can be shown that the active surface temperature, $\theta(o, t)$, in couplings is given by

$$\theta(o,t) = t_{1,c}$$

$$+ \sum_{n=1,2,3}^{\infty} \frac{W_o}{h_c}\left[1 - \frac{2\beta.\cos(P_n)\, e^{-t/\tau_n}}{P_n^2.D_n}\right]$$

$$+ \sum_{n=1,2,3}^{\infty} \frac{W_o d_L}{K_s}\left[1 - \frac{2\beta.\sin(P_n)\, e^{-t/\tau_n}}{P_n^3 D_n}\right]$$

$$+ \sum_{n=1,2,3}^{\infty} \left(\frac{t_{2,c} - t_{1,c}}{2}\right)\left[1 - \frac{2\beta \cdot e^{-t/\tau_n}}{P_n^2 D_n}\right] \qquad (5.21)$$

where

$$D_n = \left[\cos(P_n) + \frac{(1+\beta).\sin(P_n)}{P_n}\right]$$

$$\tau_n = \alpha_s^2 d_L^2 / P_n^2 \qquad (5.22)$$

$$\beta = h_c.d_L / K_s \qquad (5.23)$$

This equation applies to any one machine and for consistency with previous sections it will be adapted to the outer region only.

The most important parameter is the non-dimensional quantity β since P_n, D_n and τ_n are all functions of it. So before the solution can be simplified the numerical value of β for the outer region must be obtained. Its components are h_c, the surface heat transfer coefficient on the back face, d_L and K_s which are the thickness and thermal conductivity of the loss member respectively.

In the dynamometer h_c is not uniform over the back face because the cooling water flows in channels. However, if these are evenly distributed and not spaced too far apart little error is introduced by using the standard heat transfer equations for pipes. For a single pipe the empirical equation for the Nusselt number is given in Appendix 1 as

$$\bar{Nu} = 0.023\, Re^{0.8} Pr^{0.4} \qquad (5.24)$$

or

$$\bar{Nu} = h_c d_p / K_c \qquad (5.25)$$

where d_p is the hydraulic mean diameter[46] of a single water channel and K_c the cooling water's thermal conductivity taken at its mean bulk temperature. The equation for $\bar{Nu}$ applies for both water and air when $Re > 10^4$.

Reynolds number for the outer region can be found from

$$Re = \rho_c v_c d_p / \mu_c \qquad (5.26)$$

where

$$v_c = 4Q_c / n \pi d_p^2 \rho_c \qquad (5.27)$$

and ρ_c, μ_c are the density and viscosity of water taken at the mean bulk temperature $t_{b,c} = (t_{2,c} - t_{1,c})/2$ and n the number of water channels in the outer region.

The numerical values of the above quantities are found from section 5.15.3, table 4.1 and reference 46.

Q_c = 0.46 kg/s

n = 48

d'_p (outer) = 1.59×10^{-3} m

$t_{b,c} \triangleq 14^{\circ}C$

ρ_c = 992 kg/m^3

μ_c = 1.13×10^{-3} mkg/s

K_c = 0.588 W/m$^{\circ}$C

Pr = 7.95

Substituting the appropriate values into equations 5.26 and 5.27 it can be shown that

$$Re\,(\text{outer region}) = 6,800$$

For water in pipes the transition period[46] from laminar to fully turbulent flow is in the range $2\,100 < Re < 10,000$ and so the above value of Reynolds number only approximately satisfies equation 5.24. Re is low because the cooling water flow rate was 27 litres/minute (0.46 kg/s) and not the designed value of 50 litres/minute. The low flow rate was caused by a combination of the gear box oil cooler, which was supplied in parallel with the loss member, and the small section water supply pipe.

Rearranging equations 5.24 and 5.25 in terms of h_c then substituting the appropriate values of Re, Pr, d_p and K_c yields

$$h_c\,(\text{outer region}) = 21,400\ W/m^{2o}C$$

The numerical value of β can now be obtained from equation 5.23; taking the value of d_L, the depth of the loss member from the airgap surface to the bottom of the outer region slots, as 1.6×10^{-2} m and K_s, the loss member thermal conductivity, as 63 $W/m^{o}C$ which is the average value between $o^{o}C$ and $100^{o}C$ from figure 2.3.

Hence,

$$\beta'\,(\text{outer region}) = 5.4$$ (compare $\beta = 0.04$: for an air cooled drum coupling)

The roots P_n corresponding to this value of β are obtained from table 2.1 and the first four are approximately

$$P_1 = 1.318$$

$$P_2 = 4.03$$

$$P_3 = 6.91$$

$$P_4 = 9.89 \triangleq 3\pi$$

Roots higher than P_4 can be approximated by $(n-1)\pi$.

Except for W_o all the terms in the general solution, equation 5.21, are now known for the water cooled dynamometer, but before these are substituted and the equation simplified theoretical values of the thermal time constants will be calculated.

5.15.4.1 Outer region theoretical thermal time constants

The analytical equation for the thermal time constants was given previously as

$$\tau_n = \alpha_s^2 d_L^2 / P_n^2 \qquad (5.28)$$

where $\alpha_s^2 = c_s \cdot \rho_s / K_s$

c_s and K_s are obtained from figure 2.3 and their average value between 0 and 100°C was taken. The numerical value of these and the other components of τ_n are summarized below.

$c_s = 485\ Ws/kg^oC$

$\rho_s = 7800\ kg/m^3$

$K_s = 63\ W/m^oC$

$d_L = 1.6 \times 10^{-2} m$

Substituting these and the values of P_n into equation 5.28 yields the thermal time constants of the exponential terms in the general solution; the first few values are given in table 5.12.

Table 5.12

Theoretical thermal time constants for the outer region

n	P_n	τ_n(s)
1	1.318	10.1
2	4.03	0.9
3	6.91	0.3
4	9.89	0.146

These values of τ_n will be used in the next section when the general solution is simplified. τ_1 will also be compared later with the measured thermal time constant of the outer region.

5.15.4.2 Approximate solution for the loss member surface temperature $\theta(o,t)$

By substituting the values of P_n, τ_n and β into equation 5.21 it can be shown that

$$\theta(o,t) = t_{1,c}$$

$$+ \frac{W_o}{h_c}\left[1 - 0.337\,e^{-t/10.1} - 0.238\,e^{-t/0.9} - 0.108\,e^{-t/0.3} \cdots\cdots\right]$$

$$+ \frac{W_o d_L}{K_s}\left[1 - 0.99\,e^{-t/10.1} - 0.072\,e^{-t/0.9} - 0.0147\,e^{-t/0.3} \cdots\cdots\right]$$

$$+ \left(\frac{t_{2,c} - t_{1,c}}{2}\right)\left[1 - 1.3\,e^{-t/10.1} + 0.372\,e^{-t/0.9} - 0.172\,e^{-t/0.3} \cdots\cdots\right]$$

All the exponential terms, except the fundamental, are negligible after approximately 2 seconds, but many of them have a significant magnitude at t = o.

From table 5.10 it can be shown that $(t_{2,c} - t_{1,c})/2$ is only $3.5^{o}C$ at an excitation of 3A and slip speed of 4000 rev/min, so this term will be neglected. The term W_o/h_c can also be shown to be small since $1/h_c \ll d_L/K_s$ and so it too is neglected. The only remaining exponential terms have the coefficient $W_o d_L/K_s$ and the above equation shows that these all have a very small magnitude except the fundamental. The general solution therefore, reduces to the simple exponential form

$$\theta(o,t) = t_{1,c} + W_o d_L/K_s(1 - 0.99\,e^{-t/10.1}) \qquad (5.29)$$

It must be stressed that this equation only applies to the water cooled dynamometer and not to any other water cooled couplings; the particular solution for

those must be derived individually from the general solution. In its present form equation 5.29 is slightly inconsistent since, at t = o, it says that

$$\theta(o,o) = t_{1,c} + W_o d_L / K_s (1 - 0.99)$$

which of course is not correct because at t = o, $\theta(o,o)$ should equal $t_{1,c}$. The inconsistency is due to the neglected terms; taking these into account the solution is modified to

$$\theta(o,t) = A + B(1 - e^{-t/\tau_1}) \qquad (5.30)$$

where $A = t_{1,c}$

and $B = W_o d_L / K_s$

The simple form of the approximate solution is extremely surprising (as was that for the air cooled coupling in chapter 3) in view of the formidable general solution and the complicated nature of heat transfer. Nevertheless, in the next section it is shown to be correct.

5.15.5 Comparison of measured and theoretical thermal time constants

Having shown that the surface temperature has a simple exponential time response, the thermal time constants can be derived from the measured temperature-time responses shown on figures 5.36 to 5.38. Hence, rearranging equation 5.30 and taking logs produces

$$-t/\tau_1 = \log_e \left[\frac{B - [\Theta(o,t) - A]}{B} \right] = \log_e F(\Theta)$$

which is the equation of a straight line.

Table 5.13 gives values of A, B, t and $\theta(o,t)$; these quantities were taken from the measured responses at various excitations and slip speeds; the temperature function, $F(\theta)$, is also computed and included. From each set of results given in the table, $F(\theta)$ and t were taken and plotted on log-linear graph paper. These plots are shown on figures 5.41 and 5.42. The linearity of the points indicates that the approximate solution is correct. The straight lines do not pass

through the point $F(\theta) = 1.0$ because of the neglected terms in the general solution.

Taking the reciprocal of the slopes gives the measured thermal time constants. For the outer region at 3A, 2000 rev/min , τ_1 is 14.8s at 4A, 2000 rev/min it is 14.5s and at 3A, 4000 rev/min it has increased to 15.4s. The measured time constant for the inner region at 3A, 2000 rev/min is 12.8s; it is different from the outer region τ_1 because h_c and d_L for the two regions are not the same.

The variation of measured thermal time constant was expected and is best explained using the theoretical equation for τ_1. From section 5.15.4.1 τ_1 was defined as

$$\tau_1 = c_s \rho_s d_L^2 / K_s P_1^2 \qquad (5.31)$$

Both c_s and K_s are functions of loss member temperature, which in turn is a function of excitation and slip speed; as these change, temperature also changes and hence so do the material constants. To a small extent the term P_1^2 is also temperature dependent since it is obtained using the non-dimensional quantity β which is a function of K_s, but table 2.1 shows P_1 changes little for quite large changes in β.

As slip speed or excitation or both increase, the loss member temperature also increases. Figure 2.3 shows that c_s increases with temperature whilst K_s decreases, and so the general trend of τ_1 is to increase with temperature. To determine the maximum change in thermal time constant over a typical temperature range of say 0 to 300°C, which encompasses the operating temperature of the majority of commercial couplings, values of c_s and K_s were taken from figure 2.3 at these limiting values.

Hence,
$c_s(0^\circ C) = 452$ Ws/kg°C
$c_s(300^\circ C) = 559$ Ws/kg°C
$K_s(0^\circ C) = 67.1$ W/m°C
$K_s(300^\circ C) = 49.5$ W/m°C

Table 5.13

Measured values of A, B, t and $\theta(o, t)$

time (s)	Surface temperature $\theta(o, t)$ (^{o}C)	$F(\theta) = \left[\frac{B - (\theta(o, t) - A)}{B}\right]$	
0	10	1.0	From T/C5
10	20.5	0.422	Excitation: 3A
20	24	0.232	Slip speed: 2000 rev/min
30	26	0.122	$A = 10^{o}C$
40	27	0.069	$B = 18.25^{o}C$
50	27.5	0.042	
0	10	1.0	T/C5
10	29	0.442	4A
20	36	0.235	2000 rev/min
30	40	0.117	$A = 10^{o}C$
40	41.75	0.066	$B = 34^{o}C$
50	42.75	0.0375	
0	10	1.0	T/C5
10	35	0.447	3A
20	44	0.248	4000 rev/min
30	49	0.138	$A = 10^{o}C$
40	51.75	0.076	$B = 45.2^{o}C$
50	53.3	-	

Table 5.13 (cont'd)

0	10	1.0	T/C3
10	23	0.48	3A
20	29.5	0.22	2000 rev/min
30	32.5	0.1	A = 10°C
40	33.75	0.05	B = 25°C
50	34.75	-	

Substituting these values into equation 5.31 and ratioing gives

$$\frac{\tau_1\,(300^\circ C)}{\tau_1\,(0^\circ C)} = 1.62$$

This simple analysis shows that τ_1 increases with temperature; it also emphasises that care must be taken when selecting values of c_s and K_s for theoretical calculations. For this purpose it is usual to take average values over the temperature range of the coupling under investigation.

The difference between the theoretical value of τ_1 (outer) and the measured value was put down to the low Reynolds number of 6,800, which does not satisfy exactly the conditions defined for the particular Nusselt number used, and the use of pipe equations for the slotted water cooled loss member. In the region between two slots the pipe equations do not apply; nevertheless, if they are reasonably close together, this error is thought to be small. A general equation for $\bar{Nu}$ in the range $2100 < Re < 10,000$ is not available because this range corresponds to the transition period between laminar and fully turbulent flow so the equation for $Re > 10,000$ was used for convenience.[46]

Figure 5.43 shows the experimental and theoretical surface temperature - time responses. An average of the measured thermal time constants was taken for the experimental response; the value used was 14.9 seconds.

Considering the approximations and the methods used in the derivation of both the theoretical and measured thermal time constants, the correspondence between the two responses is considered good.

SURFACE TEMPERATURE - TIME RESPONSE.

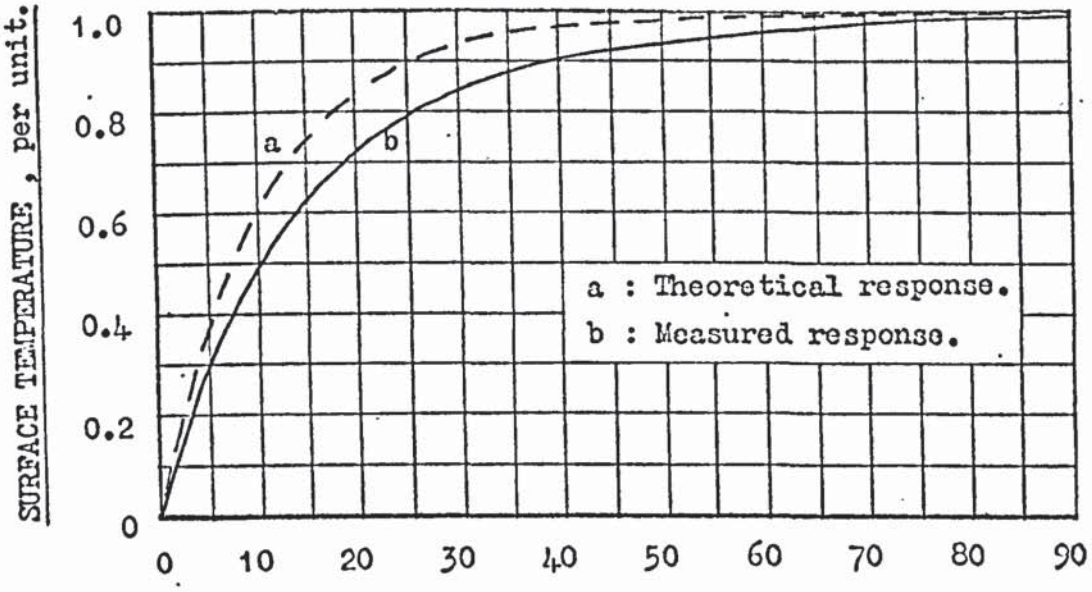

Figure 5.43

5.15.6 Prediction of the outer region surface temperature

Before the approximate solution, given in section 5.15.4.2, can be used to predict surface temperatures, the quantity W_o must be determined. This was defined in chapter 2 as the heat flux passing through the loss member in the active region only. If airgap heat transfer is small, as it is in this case, then W_o is found by dividing the power dissipated in the active region, P_A, by the area of the active region, A_a. In a coupling with a solid iron loss member the total power, P_T, is not all dissipated in the active region, as was discussed in chapter 2, and so its distribution between the active and end regions must therefore be obtained before W_o can be found.

To determine P_A in couplings with solid iron loss members involves consideration of the complicated problem of electrical end-effects[2], which few authors

have dealt with satisfactorily. In chapter 2 an approximate solution was given for the power distribution in a coupling with end-effects. The relationship between total power and active region power was defined as

$$P_A = P_T/r \qquad (5.32)$$

where r is a geometrical factor derived from a linear three dimensional theory[10], given by

$$r = \frac{1}{\frac{L_A}{L_T} + \left[\frac{4(L_T/\lambda_1)^2 + 1}{4(L_T/\lambda_1)^2 - 1}\right] \cdot \frac{\sin(\pi L_A/L_T)}{\pi}} \qquad (5.33)$$

This equation only applies for $L_T/L_A > 2$, but values less than this are physically impossible in a solid iron machine. The main problem when using this equation is to determine the length L_T in which all the eddy-currents flow. For the experimental dynamometer it was argued that these currents would only flow outwards to the inner edge of the spacer between the loss member and field member, see figure 4.1, and inwards to the centre of the middle region. The arguments behind this assumption were that the high resistance 'sheradized' skin on the spacer would prevent eddy-currents flowing on it and the considerable leakage flux through it would stop the currents passing to the outside edge of the loss member. The innermost limit of L_T was defined from the oscillograms shown on figures 5.9 to 5.14. The values of L_A, L_T and λ_1 for the outer region of the dynamometer are:

$$L_A = 3.2 \times 10^{-2} \text{m}$$

$$L_T = 8.0 \times 10^{-2} \text{m}$$

$$\lambda_1 = 5.45 \times 10^{-2} \text{m}$$

Substituting these values into equation 5.33 produces

$$r(\text{outer}) \simeq 1.3$$

Table 5.14 gives various values of T(outer) (from figure 5.34), outer region total power (P_T), active region power (P_A) (calculated using equation 5.32) and active region heat flux or loss density (W_o). The area of the outer active region, A_a, was taken as $3.142 \times 10^{-2} m^2$

Table 5.14

Excitation 3A

Slip speed (rev/min)	T(outer) (Nm)	P_T (W)	$P_A = P_T/1.3$ (W)	W_o (kW/m^2)
2000	17	3500	2700	86
4000	21	8800	6780	216

The values of W_o given in the table can now be used in the approximate theoretical equation for predicting surface temperatures in the outer region.

At 3A, 4000 rev/min

From equation 5.29 the term containing W_o was given as

$$B = W_o d_L / K_s$$

Substituting the appropriate values into this gives

$$B = \frac{216,000 \cdot 1.6 \cdot 10^{-2}}{63} = 55^{\circ}C$$

Putting $B = 55^{\circ}C$, $t_{1,c} = 10^{\circ}C$ and $\tau_1 = 10.1s$ into equation 5.30 yields the approximate theoretical equation for the loss member surface temperature in the outer region.

$$\theta(o,t) = 10 + 55 (1 - e^{-t/10.1}) \quad \text{(theoretical)}$$

The measured response is obtained from figure 5.37(a)

$$\theta(o,t) = 10 + 45 (1 - e^{-t/15.4}) \quad \text{(measured)}$$

Similarly at 3A, 2000 rev/min

$$B = \frac{86,000 \cdot 1.6 \cdot 10^{-2}}{63} = 22^{\circ}C$$

substituting into equation 5.30

$$\theta(o,t) = 10 + 22\,(1 - e^{-t/10.1}) \qquad \text{(theoretical)}$$

and from figure 5.36(a) the measured response

$$\theta(o,t) = 10 + 18.5\,(1 - e^{-t/14.8}) \qquad \text{(measured)}$$

The correlation between the measured and theoretical surface temperatures is good and hence the general analytical method is satisfactory for design purposes. The deviation is due to neglecting the airgap heat transfer, hence W_o is high, and the values of active region power (P_A) are not exact since the solution for the power distribution factor, r, was approximate. The use of the factor r (p67) however, does appear to give reasonable answers.

5.16 Transient response

The following transient work was included so that the torque-time response of the dynamometer could be found and also because there was no previously published data on inductor coupling response.

In previous sections, it was shown that the experimental machine could be thought of as two separate couplings each with end-effects and each having different characteristics. So, Wright's transient theory[10] could not be used for predicting the dynamometer's torque response as it was developed specifically for single couplings without end-effects.

It was also not possible to measure the torque-time response accurately since, under transient conditions, the torque arm vibrated and the signal from the strain gauges fluctuated violently. An alternative was to employ the transient torque measuring equipment used by Wright[10], but due to lack of space this could not be fitted to the apparatus.

The torque-time response was therefore calculated from the general torque-flux relationship which was given by Davies[3] as

$$T \propto (\emptyset)^x \qquad (5.34)$$

where $2 < x < 3$; the two limits of x correspond to linear and fully saturated theory respectively.

The flux $\emptyset$ in equation 5.34 is strictly the fundamental flux, $\emptyset ac_1$, since the equation was developed from fundamental quantities for single region couplings. However, as the time response of fundamental flux and total flux are clearly the same then the per unit torque-time response can be calculated from the total flux response using the above relationship; it should also be noted that $\emptyset ac_1$ and total flux are not proportional. The exponent x is known to be a variable and so the torque response was only calculated for the two limits, the actual response lying somewhere between the two extremes.

5.16.1 Excitation current and flux response at standstill and various slip speeds

Figure 5.44 shows oscillograms of the standstill flux responses from search coils 1, 2 and 4. They were obtained by feeding the integrated search coil voltages into a storage oscilloscope. Also shown is the excitation current, I_f, response which was recorded simultaneously with the flux responses. It was derived by measuring the voltage across a calibrated resistance (whose value was negligible compared with the field coil resistance) connected in series with the coil. Before the oscillograms were taken the magnitude of the flux and current were adjusted, via the oscilloscopes input amplifiers, until they were the same. These particular oscillograms were taken to verify that the flux response was the same at various sections in the dynamometer, and also to show that the inherent high leakage flux of the inductor coupling had no effect on flux response.

The time responses of I_f and $\emptyset_I$, the total flux leaving the inner laminated section of the field member, at standstill and various slip speeds are shown on figure 5.45. These oscillograms show that the field time constant, τ_f, remains constant as slip speed increases, whereas the flux time constant, $\tau_\emptyset$, reduces from approximately 0.44 seconds at standstill to 0.37 seconds at 6000 rev/min;

these values are checked later in section 5.16.2.

The reason for the reduction in τ_ϕ with speed can be qualitatively explained in terms of the skin depth. As slip speed increases, the depth to which flux penetrates the loss member, and hence the permeance of the flux path, reduces. So the self inductance of the loss member, which depends on this permeance, also reduces with slip speed. The resistance of the loss member however, will increase with slip speed, because of the reduction in area of the eddy-current paths. The loss member time constant, which may be taken as the ratio of loss member inductance and resistance, will therefore reduce with increasing slip speed. This time constant is a measure of loss member damping and so as slip speed increases the effect of the loss member on response becomes negligible and the flux response approaches the excitation response.

In a salient pole coupling with a laminated field member[10], the current and flux response are identical at high speeds. Unfortunately this can never occur in the experimental dynamometer, as figure 5.45 shows, since it has other solid iron paths, notably in the rotor and field member, through which the flux has to pass. Hence, its flux response will always lag the current response, unless all the solid iron paths are replaced with laminations.

5.16.2 Verification that ϕ_I has an exponential response and evaluation of its time constant at various slip speeds

The time response of ϕ_I, shown on figure 5.45, appears to be exponential, but this must be verified since it is crucial for prediction of the torque-time response. Assuming therefore that ϕ_I obeys the law

$$\phi_I = \hat{\phi}_I (1 - e^{-t/\tau_\phi}) \qquad (5.35)$$

rearranging and taking logs gives

$$-t/\tau_\phi = \log_e(1 - \phi_I/\hat{\phi}_I) = \log_e F(\phi) \qquad (5.36)$$

Values of t and $\emptyset_I$ were taken from figure 5.45 at various slip speeds and then using equation 5.36 they were plotted on log-linear paper. The results are shown on figure 5.46 and the linearity of the points verifies that $\emptyset_I$ obeys equation 5.35. The flux time constants were derived in exactly the same way as the thermal constants in section 5.15.5 and they are summarised on the figure.

5.16.3 Torque-time response at various slip speeds

Knowing the relationship between flux and the time, the torque-time response can then be calculated. Substituting equation 5.35 into equation 5.34, using the limits of x and expanding, gives two equations relating per unit torque and time. where

$$T = (1 - 2e^{-t/\tau\emptyset} + e^{-2t/\tau\emptyset}) \qquad (x = 2)$$

and

$$T = (1 - 3e^{-t/\tau\emptyset} + 3e^{-2t/\tau\emptyset} - e^{-3t/\tau\emptyset}) \qquad (x = 3)$$

These functions represent the boundaries of the torque-time response. They are both plotted on figure 5.47 at various slip speeds and, naturally, the measured values of $\tau\emptyset$ were taken at the same slip speeds. Also plotted for comparison are the flux $\emptyset_I$ - time responses, from figure 5.42, and the magnitude reltationship between the above two functions for the same flux. It can be seen that the torque response for a 'linear' machine (x = 2) will be much faster than a 'fully saturated' machine (x = 3).

Table 5.15 compares values of the torque time constant, τ_T, when x = 2 and 3 with the flux time constant $\tau\emptyset$. The values of τ_T were taken when per unit torque, $T = 0.632 = (1 - e^{-1})$.

Table 5.15

Comparison of flux and torque time constants

Slip speed (rev/min)	τ_ϕ (s)	τ_T (s)	
		x = 2	x = 3
2000	0.42	0.66	0.83
4000	0.39	0.62	0.77
6000	0.37	0.59	0.73

The torque time constants are large compared with a laminated salient pole coupling[10] operating over a similar n/n_m range (e.g. 0.11s), but compare well with a solid iron partially interdigitated coupling[10] (e.g. 0.85s). The actual value of τ_T for the experimental machine will lie somewhere between the two extremes given in the table.

Considering its physical size and rating, nominally 75 kW at 2000 rev/min, the dynamometer has a relatively fast torque-time response compared with other inductor couplings* of similar size and rating.

5.17 Conclusions

The extensive testing of the new high speed dynamometer has been described in detail. The results show that it produces adequate torque for its intended application and that its overall design specification has been met. It has also been shown to obey general coupling theory[8] even though its loss member eddy-current frequencies are six to twelve times higher than those in any previously published coupling work. This indicates that eddy-current frequency has little effect on coupling performance and the governing factor in their operation is their actual slip speed with respect to speed at peak torque.

---

* From Redman, Heenan, Froude Technical Library.

Generally, the tests show that the experimental data agrees well with Davies[3] theory. The main deviations were in the measured values of armature reaction mmf, which was expected considering the method of measuring $\hat{F}r_1$; this has always been in some doubt, especially when used with inductor couplings.

The usual methods of designing couplings have also been shown to be valid for high speed machines, in particular, the extremely powerful technique of dimensional ratioing.

A detailed investigation of the eddy-current distribution in a double region loss member with unsymmetrical end-effects is also discussed. This work was useful in verifying that inductor couplings may be designed by treating them as two separate machines.

The theory given in chapter 2 for predicting surface temperatures and thermal time constants has been shown to apply to a water cooled loss member. A comprehensive analysis of airgap heat transfer is also given and shows that it may be neglected in water cooled couplings even when there is a forced air flow through the airgap.

In the last part of the chapter a brief study of the transient performance of the dynamometer is given and values of the torque time constant were calculated from the measured flux time constants.

CHAPTER 6

OVERALL CONCLUSIONS AND SUGGESTIONS FOR FURTHER WORK

6.0 Overall conclusions and suggestions for further work

6.1 Overall conclusions

A theory has been given in chapter 2 for predicting loss member surface temperatures and thermal time constants of eddy-current couplings. The relationship between both these and the parameters of the coupling are also given.

The theory was verified by comparisons with experimental results taken from air-cooled couplings with and without endrings. Additional verification was given in chapter 5 where it was shown that the theory was also applicable to the high speed water cooled dynamometer. In general, the comparisons show that the accuracy with which surface temperatures and thermal time constants can be predicted, using the theory, are adequate for design purposes. It is also thought that the theory, with modifications, may be applied to other related problems, e.g. electro-heat.

The experimental results from the new high speed dynamometer indicate that it behaves like a normal inductor coupling even though its eddy-current frequencies are extremely high, and so existing coupling theory is shown to be applicable to high speed couplings.

The tests on the new machine also show that its performance is superior to the original Redman, Heenan, Froude design specification, which was for 75 kW at 2000 rev/min and an inertia of 0.17 kgm^2, giving a torque/inertia (T/I) ratio of

$$T/I \text{ (spec.)} = \frac{360}{0.17} = 2120 \text{ (N/kgm)}$$

From figure 5.8, the projected torque for the new machine is 480 Nm at 2000 rev/min and from table 4.1 its inertia is 0.158 kgm^2, hence

$$T/I \text{ (new m/c)} = \frac{480}{0.158} = 3040 \text{ (N/kgm)}$$

so that $\frac{T/I \text{ (new m/c)}}{T/I \text{ (spec.)}} = 1.45$

This comparison shows that the new dynamometer has a T/I ratio considerably higher than the original specification. It is also expected that the alternative, and perhaps more commercial, high speed design given in Appendix 4 will have a still higher T/I ratio.

Other important features of the new dynamometer are its simple modular construction, stationary 'indirectly' water cooled loss member (i.e. dry airgap), stationary field member and negligible minimum power level.

It is considered therefore, that the new machine is suitable for a 75 kW, 14000 rev/min dynamometer.

6.2 Suggestions for further work

The theory of chapter 2 could be extended to cover higher temperatures by substituting $y = m.t + c$ for the temperature dependent material properties c_s/K_s, where m and c are constants, y equals c_s/K_s and t is the loss member temperature. In the process the fundamental design parameters may be obscured, but this is the price of advancement. An analysis of the Curie wave* penetration could also be included. This would be useful for electro-heat problems in which surface hardening or even melting times may be required for a particular loss density (or heat flux).

Further work should also include a study of airgap heat transfer at high loss-member temperatures. The radiation losses were small in the couplings discussed in this thesis, but since these losses vary as T^4 then at high loss-member temperatures say, 300°C plus they may be substantial. Detailed information is also required on airgap convection losses; research on this would involve experimental

---

* This is the penetration of the Curie temperature[31] (approx. 600°C) into the loss member.

determination of surface heat transfer coefficients for the most common airgap configurations, perhaps expressed in the form of the general Nusselt number equation, i.e.

$$Nu = a \cdot Re^{b} \cdot Pr^{c}$$

Part of this thesis has dealt with high speed couplings and dynamometers and consequently high frequency eddy-currents in the loss member. However, because the speed at peak torque, n_m, of the experimental machine was also very high (as figure 5.3 shows) there remains at least one outstanding area of coupling operation which has not been investigated i.e. at very high n_m values, say 20 to 40 n_m.

Typical values of n_m for endring couplings[9,10] are 150 to 300 rev/min. Therefore, to study high n_m operation, experimental apparatus capable of at least 10,000 rev/min would be required.

It was shown from the tests on the new dynamometer that a more accurate method of estimating peak fundamental armature reaction mmf ($\hat{Fr}_1$) must be found. A possible approach would be to construct the complete Fr wave from tooth and slot flux measurements and then analyse the wave.

Other areas of further work are:

i) Comparison of the performance of an inductor coupling fitted with a solid iron, endring and copper faced loss member.

ii) Investigation of end-effects and current density distribution in disc couplings.

iii) Prediction of torque produced by the airgap flux density harmonies (harmonic torque) and their effect on the fundamental torque-slip curves.

APPENDICES

Appendix 1

A1 Heat transfer equations

A1.1 Cylinder rotating in an infinite quiescent fluid

The following equations apply to drum type eddy-current couplings rotating in free air and the characteristic dimension chosen is the drum outside diameter D_o.

If $Re_D (\rho_c D_o \omega / \mu_c) < (Gr_D/Pr)^{1/2}$ free convection dominates[37] and the average Nusselt number $(\bar{h}_c D_o / K_c)$ for a 'long cylinder' is given[38] by

$$\bar{Nu}_D = 0.456 (Gr_D Pr)^{0.25} \qquad A1.1$$

This equation applies for stationary cylinders or cylinders rotating very slowly.

In the range where both free and forced convection, or only the latter, are significant the relationship is[40]

$$\bar{Nu}_D = 0.18 \ (0.5Re_D^{\ 2} + Gr_D) \ Pr^{\ 0.315} \qquad A1.2$$

This is the general case for a cylinder rotating at an angular speed $\omega (2\pi N)$ and it is valid for air up to Re_D values of 5×10^4. Dropkin and Carmi[39] extended this up to Re_D values of 4×10^5 and also obtained data at high Grashof numbers. They correlated their results for air with the empirical relationship

$$\bar{Nu}_D = 0.19 (Re_D^{\ 2} + Gr_D)^{0.35} \qquad A1.3$$

At very high speeds, if $Re_D^{\ 2} \gg Gr_D$, equation A1.3 reduces to

$$\bar{Nu}_D = 0.19 \ Re_D^{\ 0.7} \qquad A1.4$$

For air, the Prandtl number is approximately a constant over a very wide range of temperatures. Therefore it may be taken into the constants.

Analytical solutions based on a modified Reynolds analogy have been given by Kays and Bjorklund[40] and Mayhew[43].

Transition phenomena in flow over rotating cylinders have been discussed by Richardson[42], also the influence of free convection on the flow has been investigated by Etemad[38].

A1.2 Cylinder rotating in a forced flow fluid

A forced air cooled drum coupling is basically a cylinder rotating in a forced flow fluid. The air is usually passed to the coupling through a duct with its free stream velocity defined as u_∞ .

The problem of convection from a rotating cylinder with air flow perpendicular to the axis of rotation has been studied experimentally by Kays and Bjorklund[40]. They found four distinct flow regions with transitions between them depending on the ratio of the free stream velocity u_∞ to the rotational speed of the cylinder ωr_o, where r_o is the outside radius of the cylinder. Over the limited range of variables covered in their experiments, their results were correlated by the empirical relationship

$$\bar{Nu}_D = 0.18 \left(0.5\, Re_D^{\,2} + Re_\infty^{\,2} + Gr_D\right) Pr^{0.315} \qquad \text{A1.5}$$

where $Re_\infty = u_\infty D_o \rho_c / \mu_c$

This equation should not be used when the value of the terms inside the square brackets exceeds 10^9. If u_∞ is zero, as in the case of an infinite quiescent fluid, then equation A1.5 reduces to A1.2.

In all equations the physical properties are to be taken at the arith metic mean film temperature or mean between temperature at the outside surface of the cylinder and the temperature of the surrounding medium.

A1.3 Gas and fluid flow through slots and pipes

Heat transfer for gases and fluids flowing in slots and pipes has been studied in great detail and is extremely well documented.[46,47,48] A common method of cooling both disc and drum couplings is to cut slots in the back face of the loss member and pass the cooling fluid, usually water, through them. If the hydraulic mean diameter[46] (H.M.D.) of the slot is taken as the characteristic dimension, then all the equations for circular pipes can be used to calculate the heat transfer.

The Nusselt number for forced convection of fluids and gases flowing through pipes is given by Fishenden and Saunders[46] and McAdams[48] as

$$\bar{Nu}_D = 0.023\, Re^{0.8} Pr^{0.4} \qquad A1.6$$

This equation applies for both water and air when $Re > 10^4$. The characteristic dimension is d_p the diameter of the pipe or the H.M.D. of the slot.

Because Pr varies little from gas to gas, or with temperature for any given gas, equation A1.6 reduces to

$$\bar{Nu}_D = 0.020\, Re^{0.8} \qquad A1.7$$

In both the above equations the physical constants are taken at the mean bulk temperature $t_{b,c}$ of the fluid, i.e. at the mean of the inlet and outlet temperatures of the coolant.

A1.4 Gas and fluid flow over plane surfaces

Disc couplings with slotless loss members may be treated as plane surfaces for heat transfer calculations. The characteristic dimension L is the length of plate in the direction of flow.

Experiments with air and water[46] agree well in the turbulent region, which in this case corresponds to $Re > 2 \times 10^4$, with the expression

$$\bar{Nu}_D = 0.036\, Re^{0.8} Pr^{0.33} \qquad A1.8$$

For air, and other gases with similar Prandtl number, this becomes

$$\bar{Nu}_D = 0.032\, Re^{0.8} \qquad A1.9$$

In these equations the physical constants are taken at the mean film temperature θ_m.

A1.5 General form of the Nusselt number

An inspection of the equations given in this Appendix reveals that they all have the same general form, which is

$$\bar{Nu}_D = a\, Re^b\, Pr^c \qquad A1.10$$

This is useful and means that all of the common cooling system configurations encountered in couplings may be expressed by one general equation and hence, only one general theory also with appropriate values of a, b and c being substituted for a particular type of coupling.

It should also be pointed out that in most of the equations given in this Appendix, Reynolds number could be substituted for in terms of the mass flow rate, inlet and outlet temperatures of coolant and the total power which is to be carried away by the coolant. However, this depends on what information is available and the constraints on the cooling system design.

Appendix 2

A2 Inversion of $\bar{\theta}(y,s)$

A2.1 $\bar{\theta}(y,s)$ terms not containing De

Consider the two terms in equation 2.41 which do not contain De. Inversion of $t_{1,c}/s$ is trivial and is found from standard tables

$$\mathcal{L}^{-1}\left[\frac{t_{1,c}}{s}\right] = t_{1,c} \qquad \text{A2.1}$$

The other term is inverted using C.I.F. directly and noting that the denominator zero occurs when s = o.

Hence,

$$\mathcal{L}^{-1}\left[\frac{W_o.\sinh(\alpha_s y s^{1/2})}{K_s.\alpha_s.s^{3/2}}\right] = \frac{1}{2\pi j}\oint_J \left[\frac{W_o.\sinh(\alpha_s y s^{1/2}).e^{st}.ds}{s^{1/2}.K_s.\alpha_s}\right]\Bigg|_{s\to o}$$

$$\underset{\text{C.I.F.}}{=} \frac{W_o.y}{K_s} \qquad \text{A2.2}$$

NOTE: As $s\to o$ the term $\sinh(\alpha_s y s^{1/2})/s^{1/2} \to \alpha_s y s^{1/2}/s^{1/2} = \alpha y$

A2.2 $\bar{\theta}(y,s)$ terms containing De

A2.2.1 Introduction of 'Residue' method

Consider now the term

$$\mathcal{L}^{-1}\left[\frac{W_o.\cosh(\alpha_s d_L s^{1/2}).\cosh(\alpha_s y s^{1/2})}{s\,K_s.De}\right] \qquad \text{A2.3}$$

It has been shown in section 2.11.1 that De has zeros when

$$s = -\frac{P_n^2}{\alpha^2 d_L^2}$$

where P_n is not an integer and depends on h_c, d_L and K_s. The denominator of the above term therefore is zero for these values of s and also when s = o.

Using C.I.F. therefore

$$\mathcal{L}^{-1}\left[\left[A2.3\right]\right] = \frac{1}{2\pi j}\oint_J \left[\frac{W_o.\cosh(\alpha_s d_L s^{1/2}).\cosh(\alpha_s y s^{1/2}).e^{st}.ds}{K_s\, De\; s}\right]\Bigg|_{s\to 0}$$

$$+ \frac{1}{2\pi j}\oint_J \left[\frac{(W_o/s\,K_s).\cosh(\alpha_s d_L s^{1/2}).\cosh(\alpha_s y s^{1/2}).e^{st}.ds}{De/(s+P_n^2/\alpha_s^2 d_L^2)\;(s+P_n^2/\alpha_s^2 d_L^2)}\right]\Bigg|_{s\to P_n^2/\alpha_s^2 d_L^2} \qquad \text{A2.4}$$

where $De/(s+P_n^2/\alpha_s^2 d_L^2)$ is called the 'Residue' and comes from introduction of the redundant term containing the factors of De.

A2.2.2 Evaluation of 'Residue'

Before C.I.F. can be applied to equation A2.4 the 'Residue' must be evaluated as $s\to -P_n^2/\alpha_s^2 d_L^2$. So, substituting for De from equation 2.40 and using L-hopitals rule

$$\lim_{s\to -P_n^2/\alpha_s^2 d_L^2}\left[\frac{\alpha_s s^{1/2}.\sinh(\alpha_s d_L s^{1/2}) + (h_c/K_s).\cosh(\alpha_s d_L s^{1/2})}{(s+P_n^2/\alpha_s^2 d_L^2)}\right]$$

evaluating this gives the 'Residue'

$$\sum_{n=1,2,3}^{\infty} \frac{\alpha_s^2 d_L^2}{2} \cdot [D_n] \qquad \text{A2.5}$$

where $$D_n = \left[\cos(P_n) + \frac{(1+\beta).\sin(P_n)}{P_n}\right] \qquad \text{A2.6}$$

and $$\beta = \frac{h_c d_L}{K_s}$$

A2.2.3 Inversion of the terms containing De

Substituting the 'Residue' into equation A2.4 and using C.I.F. it can be shown that

$$\left[\left[A2.3\right]^{-1}\right]_{C.I.F.} = \sum_{n=1,2,3}^{\infty} \frac{W_o}{h_c}\left[1 - \frac{2\beta.\cos(P_n).\cos(P_n y/d_L)}{P_n^2.K_s.D_n} e^{-t/\tau_n}\right] \qquad \text{A2.7}$$

where $\tau_n = \alpha_s^2 d_L^2 / P_n^2$ and represents the thermal time constants.

The remaining terms which contain De are evaluated in the same manner as detailed above and it can be shown that the 'Residue', equation A2.5, is common to them all.

Appendix 3

Dimensional equations for disc and drum couplings

The simplest and most accurate method of designing eddy-current couplings is by dimensional ratioing from other similar couplings. Davies[3] derived drum coupling equations which are reproduced here for comparison with the equivalent disc coupling equations

DRUM COUPLINGS

$$T_{m,1} \propto \frac{\rho D L_A}{g} . (F_g)^2 \qquad \text{A3.1}$$

and

$$n_{m,1} \propto \frac{\rho g^2 P^{4m-1}}{D^{4m} (F_g)^{4-4m}} \qquad \text{A3.2}$$

Before the new high speed disc inductor coupling could be designed similar equations to those above had to be obtained. Cartesian co-ordinates were used since it can be shown[13] that curvature effects are small in disc couplings. End-effects were also neglected as they usually cancel when ratioing. Hence, only a fundamental component of radial current density is assumed and, as this premise is consistent with Davies analysis, all his initial equations apply to disc couplings with small modifications.

From reference 3 the basic equation for ϕac_1 was given as

$$\phi_{ac_1} = \frac{4\sqrt{2}}{\omega . Hm} . L_A . W \qquad \text{A3.3}$$

where

$$K_1 (Hm)^{1/m} = \sqrt[4]{\frac{8 W^2}{\rho \omega}} \qquad \text{A3.4}$$

These equations apply to both disc and drum couplings where L_A is the length of the active region.

Figure A3.1 shows the ideal pole shape for a disc coupling

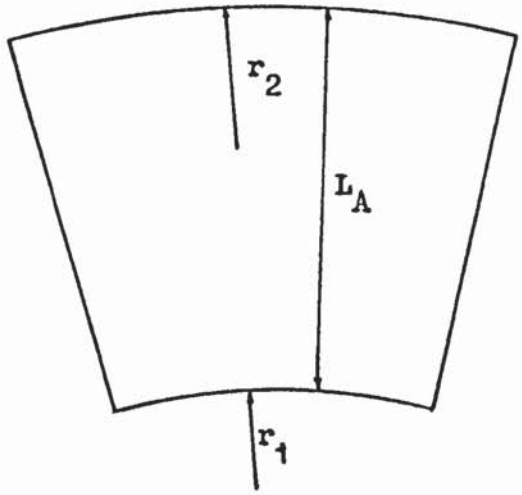

Figure A3.1

given that $L_A = (r_2 - r_1)$ and the active region swept area, $A_a = \pi (r_2^2 - r_1^2) = \pi (r_2 + r_1)(r_2 - r_1)$

The term W in equation A3.3 is the loss density in the active region it is defined

$$W = \frac{T\omega}{pA_a}$$

putting $\omega = 2\pi Np$ and A_a into this equation yields

$$W = \frac{2\,T\,n}{(r_2+r_1)(r_2-r_1)} \qquad \text{A3.5}$$

but $(r_2 - r_1) = L_A$ and the quantity $(r_2 + r_1)$ will be defined as R.

Rearranging equation A3.4 in terms of Hm and substituting it, ω and W in equation A3.3 it can be shown that

$$\phi_{ac_1} = K_2 \cdot \left[\frac{\rho^{1/4m} \, L_A^{1/2m}}{R^{\frac{2m-1}{2m}} \, p^{\frac{4m-1}{4m}}} \right] \cdot \frac{T_1^{(2m-1)/2m}}{n^{1/4m}} \qquad \text{A3.6}$$

where $K_2 = 2^{5/2} \cdot \frac{\pi^{1/4m}}{\pi} \cdot \left[\frac{K_1}{2} \right]^{1/m}$

This equation is identical to that given by Davies[4] for drum couplings. The quantity R is directly comparable to the inside diameter, D, of a drum coupling and is in fact the mean pitch circle diameter of the teeth or poles in a disc coupling.

It can be shown[3] that the general relationship between T, p, ϕac_1 and $\hat{F}r_1$ is

$$T_1 = K_3 \, p^2 . \phi ac_1 . \hat{F}r_1$$

where $K_3 = \pi$

There is no reference in this equation to machine geometry and so by substituting for ϕac_1 and rearranging, the relationship between $\hat{F}r_1$ and disc coupling parameters can be shown to be

$$\hat{F}r_1 = \frac{T_1^{1/2m} \, n^{1/4m}}{K_2 . K_3 . \rho^2 . M} \qquad \text{A3.7}$$

M is defined as $\left[\rho^{1/4m} \cdot L_A^{1/2m} / R^{(2m-1)/2m} \cdot \rho^{(4m-1)/4m} \right]$ and is directly analagous to a similar quantity defined by Davies[4].

Equations A3.6 and A3.7 can now be combined into the performance equation[3] of the eddy-current coupling

$$Fg^2 = K_a(\hat{F}r_1')^2 + K_b(\hat{F}\phi)^2 - K_c 2\hat{F}r_1' \, \hat{F}\phi . \cos(\delta) \qquad \text{A3.7}$$

where Fg = applied mmf per tooth or pole

$\hat{F}r_1'$ = equivalent field produced armature reaction mmf

= $f\hat{F}r_1$; f is the effectiveness of fundamental armature reaction in producing fundamental flux it carries the same definition as given by Davies[4].

δ = a phase angle.

$\hat{F}\phi$ = $\phi ac_1/\Lambda_1$; Λ_1 is derived from the airgap geometry and in terms of disc couplings it is proportional to (RL_A/pg)

$K_{a,b,c}$ = constants

Substituting the relevant relationships into equation A3.7 and following Davies'[3] methods it can be shown that

DISC COUPLINGS

$$T_{m,1} \propto p \frac{R L_A . (Fg)^2}{g} \qquad \text{A3.8}$$

and

$$n_{m,1} \propto \frac{\rho g^2 p^{4m-1}}{R^{4m} (Fg)^{4-4m}} \qquad \text{A3.9}$$

These dimensional equations are identical to those given earlier for drum machines where D is replaced by R; they apply to both inductor and salient pole (or Lundell) couplings. The constants of proportionality are of course different for the two types, but these are not required for designing by dimensional ratioing since they cancel for similar machines; these constants are functions of the machines geometry, i.e. end-effects and tooth width/tooth pitch ratio. The equations apply to any one individual machine or to each region of an inductor coupling.

Strictly the equations given here are for the fundamental peak torque and its speed at peak torque. However, it can be shown* that the dimensional relationships

---

* From unpublished work belonging to the author.

for the harmonic torques are the same as for the fundamental. Therefore, when these fundamental equations are used for dimensional ratioing they do in fact automatically take into account the harmonic torques and this is why this design technique produces such good results.

Appendix 4

PATENT APPLICATION NO. 10790/75

PATENTS ACTS, 1949 & 1961

PROVISIONAL SPECIFICATION

"Eddy Current Dynamometer"

WE, FROUDE ENGINEERING LIMITED, of Gregory's Bank, Worcester, WR3 8AD, a British Company, do hereby declare this invention to be described in the following statement:-

REFERENCES

REFERENCES

1. Rudenburg, R. : 'Energie der Wirblestrom in elektrischen Bremsen und Dynamomaschinen', Sammlung Elektrotechnischer Vortrage, 1906, p 269.

2. Gibbs, W. J. : 'The theory and design of eddy-current slip couplings', BEAMA Journal, 1946, pp 123, 172, 219.

3. Davies, E. J. : 'Two experimental studies in dynamoelectric machinery', part one, Ph.D. thesis, University of Bristol, 1961.

4. Davies, E. J. : 'An experimental and theoretical study of eddy-current couplings and brakes', Trans. I.E.E.E., P.A.S., V82, 1963, p 401.

5. Malti, M. G. and Ramakumar, R. : 'Three dimensional theory of eddy-current couplings', ibid, V82, 1963, p 793.

6. Hansen, A. and Timmler, W. R. : 'Theory of eddy-current couplings - unidirectional flux type', ibid, V82, 1963, p 436.

7. Gonnen, D. and Stricker, S. : 'Analysis of an eddy-current brake', ibid, V84, 1965, p 357.

8. Davies, E. J. : 'General theory of eddy-current couplings and brakes', Proc.I.E.E., V133, 1966, p 825.

9. James, B. : 'Eddy-current couplings with and without endrings', M.Sc. thesis, University of Aston in Birmingham, 1969.

10. Wright, M. T. : 'Steady state and transient performance of eddy-current couplings', Ph.D. thesis, University of Aston in Birmingham, 1972.

11. Davies, E. J., James, B. and Wright, M. T. : 'High performance, low cost, simple eddy-current couplings', I.E.E. Conf. Publ. Oct. 1972.

12. Bloxham, D. A. and Wright, M. T. : 'Eddy-current coupling as an industrial variable speed drive', Proc. I.E.E., V119, (8), 1972, p 1149.

13. Das, A. : 'Face plate eddy-current coupling', M.Sc. thesis, University of Aston in Birmingham, 1973.

14. Bowden, A. L. : 'A study of magnetic non-linearity and finite length effects in solid iron subjected to a travelling mmf wave', Ph.D. thesis, University of Aston in Birmingham, 1973.

15. Davies, E. J., James, B. and Wright, M. T. : 'An experimental verification of the generalised theory of eddy-current couplings', Proc. I.E.E., V122, 1974, p 67.

16. McConnell, H. M. : 'Eddy current phenomena in ferromagnetic materials', A.I.E.E. Trans., V73, (I), 1954, p 226.

17. Maclean, W. : 'Theory of strong electromagnetic waves in massive iron', J. Appl. Phys., V25, (10), 1954, p 1267.

18. Agarwal, P. D. : 'Eddy current losses in solid and laminated iron', Trans. I.E.E.E., V78, (1), 1959, p 169.

19. Bondi, M. A. and Mukherji, K. C. : 'An analysis of tooth-ripple phenomena in smooth laminated pole shoes', Proc. I.E.E., V104C, 1957, p 349.

20. Panasenkov, M. A. : 'Surface effect in solid ferromagnetic bodies taking non-linearity into account', Elektrichestvo, 1958, No. 9, 1-7.

21. Postnikov, I. M. : 'Eddy currents in synchronous and asynchronous machines with unlaminated rotors', Elecktrichestvo, 1958, No. 10, 7-14.

22. Angst, G. : 'Polyphase induction motor with solid rotor; effects of saturation and finite length', Trans. I.E.E.E., V80, 1962, p 9021.

23. Lasocinski, J. : 'Electromagnetic field in the airgap of a finite length machine with solid ferromagnetic rotor', Rozprawy Elektrotech., V12, 1966, pp 69-92.

24. Hensman, G. O. and Norris, W. T. : 'Universal loss chart for the calculation of eddy-current losses in thick steel plates', Proc. I.E.E., V118, (1), 1971, p 277.

25. Pohl, R. : 'The magnetic leakage of salient poles', J.I.E.E., V52, 1913, p 70.

26. Fitzgerald, A. E. and Kingsley, J. R. : 'Electric machinery', second edition, McGraw Hill Book Co. Ltd., 1961.

27. Lammeraner, J. and Stafl, M. : 'Eddy currents', Iliffe Books Ltd. London, 1966.

28. Carter, G. W. : 'The electromagnetic field in its engineering aspects', second edition, Longmans Ltd., 1967.

29. Clayton, A. E. and Hancock, N. N. : 'The performance and design of direct current machines', third edition, Pitman Press, 1959.

30. Seely, S. : 'Electromechanical energy conversion', McGraw Hill Book Co. Ltd., 1962.

31. Bozorth, R. M. : 'Ferromagnetism', D. Van Nastrand Company.

32. Dreyfus, L. A. : 'High frequency heating and temperature distribution in surface hardening of steel', Acta Polytechnica electrical engineering series, V4, No. 5, 1952.

33. Kasper, R. J. : 'Transient temperature distribution in round and slab type loads heated by electric induction', Trans. A.S.M.E., February 1971, p 110.

34. Brown, G. H., Hoyler, C. N. and Bierwith, M.S. : 'Theory and application of radio frequency heating', D. Van Nostrand Company Inc., 1947.

35. Burke, P. E. and Alden, R. T. H. : 'Current density probes', Trans. I.E.E.E., V88, (2), 1969, p 181.

36. Luke, G. E. : 'Cooling of electrical machines', Trans. A.I.E.E., V42, 1923, p 641.

37. Anderson, J. T. and Saunders, O. A. : 'Convection from an isolated heated horizontal cylinder rotating about its axis', Proc. Roy. Soc., V217, 1953, p 555.

38. Etemad, G. A. : 'Free convection heat transfer from a rotating horizontal cylinder to ambient air with interferometric study of flow', Trans. A.S.M.E., V77, 1955, p 1283.

39. Dropkin, D. and Carmi, A. : 'Natural convection heat transfer from a horizontal cylinder rotating in air', ibid, V79, 1957, p 741.

40. Kays, W. and Bjorklund, : 'Heat transfer from a rotating cylinder with and without crossflow', ibid, V80, 1958, p 70.

41. Gazley, C. : 'Heat transfer characteristics of the rotational and axial flow between concentric cylinders', ibid, V80, 1958, p 79.

42. Richardson, P. D. : 'Transition on a heated horizontal rotating cylinder', Journal of Heat Transfer, V83, 1961, p 386.

43. Mayhew, Y. R. and Rodgers, G. F. C. : 'Thermodynamic and transport properties of fluids - S.I. units', second edition, Basil Blackwell Ltd. Oxford, 1967.

44. Hartnett, J. P. and Irvine, F. T. : 'Advances in heat transfer', chapter by F. Kreith, V5, Academic Press, 1968.

45. Carslaw, H. S. and Jaeger, J. C. : 'Conduction of heat in solids', Oxford University press, second edition, 1959.

46. Fishenden, M. and Saunders, O. A. : 'An introduction to heat transfer', Oxford University press, 1950.

47. Ede, A. J. : 'An introduction to heat transfer principles and calculations', Pergamon Press, 1967.

48. McAdams, W. H. : 'Heat transmission', third edition, McGraw Hill Book Co. Ltd., 1958.

49. Walshaw, A. C. and Jobson, D. A. : 'Mechanics of fluids', Longmans, 1962.

50. Ryder, G. H. : 'Strength of materials', Macmillan and Co. Ltd., third edition in S.I. units, 1969.

51. Timoshenko, S. : 'Strength of materials', D. Van Nostrand Company, V2, third edition, 1956.

52. Smithells, C. J. : 'Metals reference book', Butterworths, London, 1967.

53. Jackson, W. J. : 'The effect of heat treatment on the magnetic properties of carbon steel castings', J. Iron and Steel Inst., 1960, p 29.

54. Rauscher, J. W., Kelly, R. E. and Cole, J. D. : 'An asymptotic solution for the laminar flow of a thin film on a rotating disc', Trans. A.S.M.E., March 1973, p 43.

55. Edmunds, H. G. : 'Stress concentration at holes in rotating discs', The Engineer, 1954, pp 618 - 620.

56. Heyman, J. : 'Plastic design of rotating discs', Proc. I. Mech. E., 1958, p 531.

57. McCollem, P. A. and Brown, B. : 'Laplace transforms and theorems', Holt, Rinehart and Winston, 1965.

58. Thomson, W. T., : 'Laplace transformation', Longmans, Green and Co. Ltd., 1957.

59. Carslaw, H. S. and Jaeger, J. C. : 'Operational methods in applied mathematics', Oxford University press, second edition, 1947.

60. Pipes, L. A. and Harvill, L. R. : 'Applied mathematics for engineers and physicists', McGraw Hill Book Co. Ltd., third edition, 1970.

61. Mclachlan, N. W. : 'Ordinary non-linear differential equations in engineering and physical sciences', Oxford University Press, second edition, 1956.

62. Weinberger, H. F. : 'A first course in partial differential equations', Open University set book, Xerox press, 1972.

63. Bateman, H. : 'Tables of integral transforms', McGraw Hill Book Co. Ltd., 2 volumes, 1954.

64. Roberts, G. E. and Kaufman, H. : 'Tables of Laplace transforms', W. B. Saunders Co. Ltd., 1966.

FIGURES FOR CHAPTER 1.

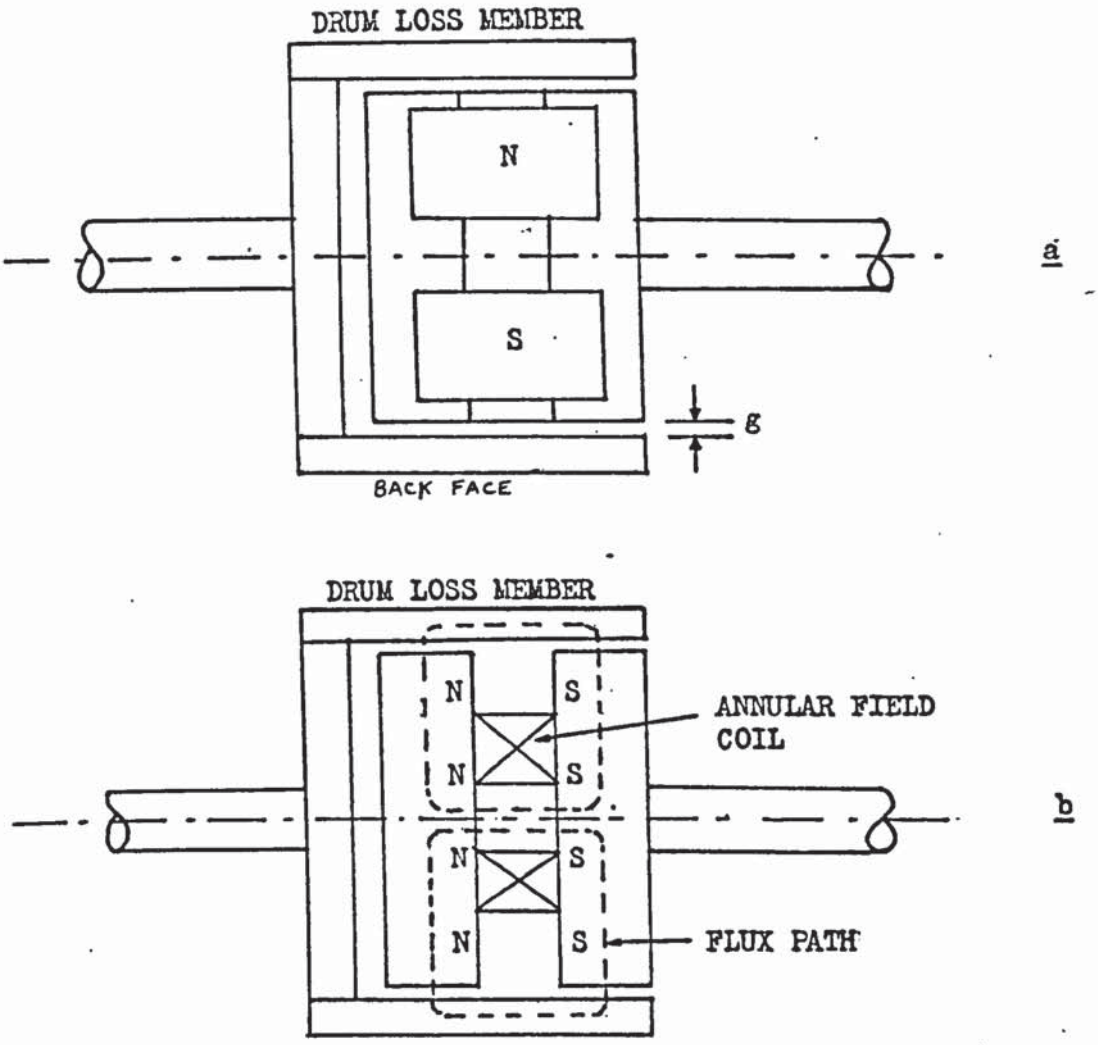

BASIC CONSTRUCTION OF DRUM TYPE SALIENT POLE/LUNDELL COUPLINGS (a) AND INDUCTOR COUPLINGS (b).

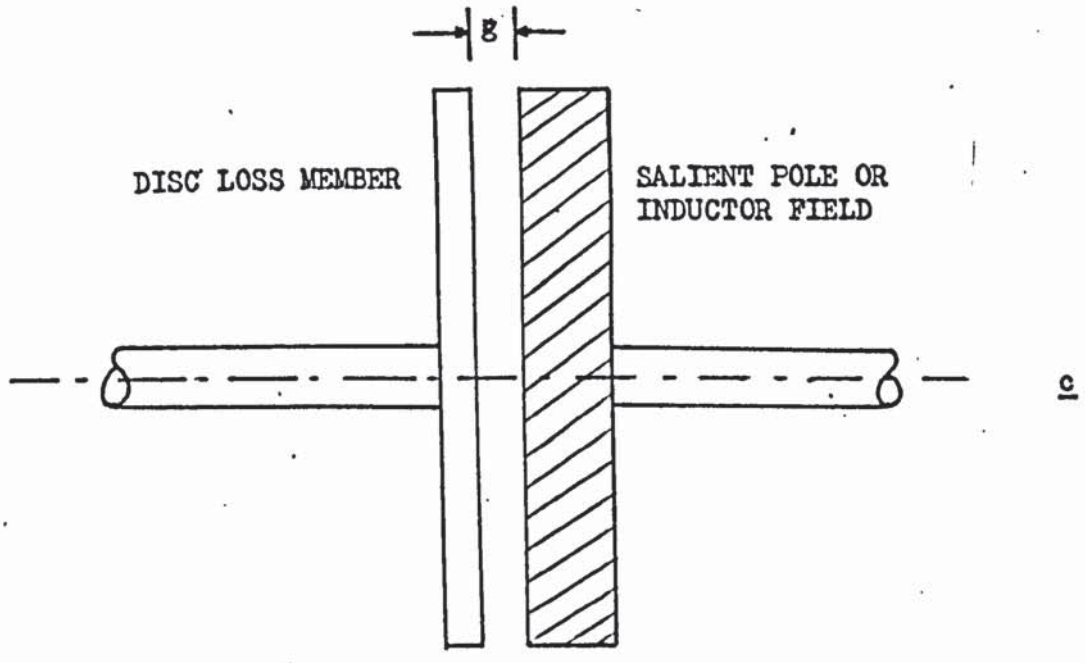

BASIC CONSTRUCTION OF DISC TYPE COUPLINGS.

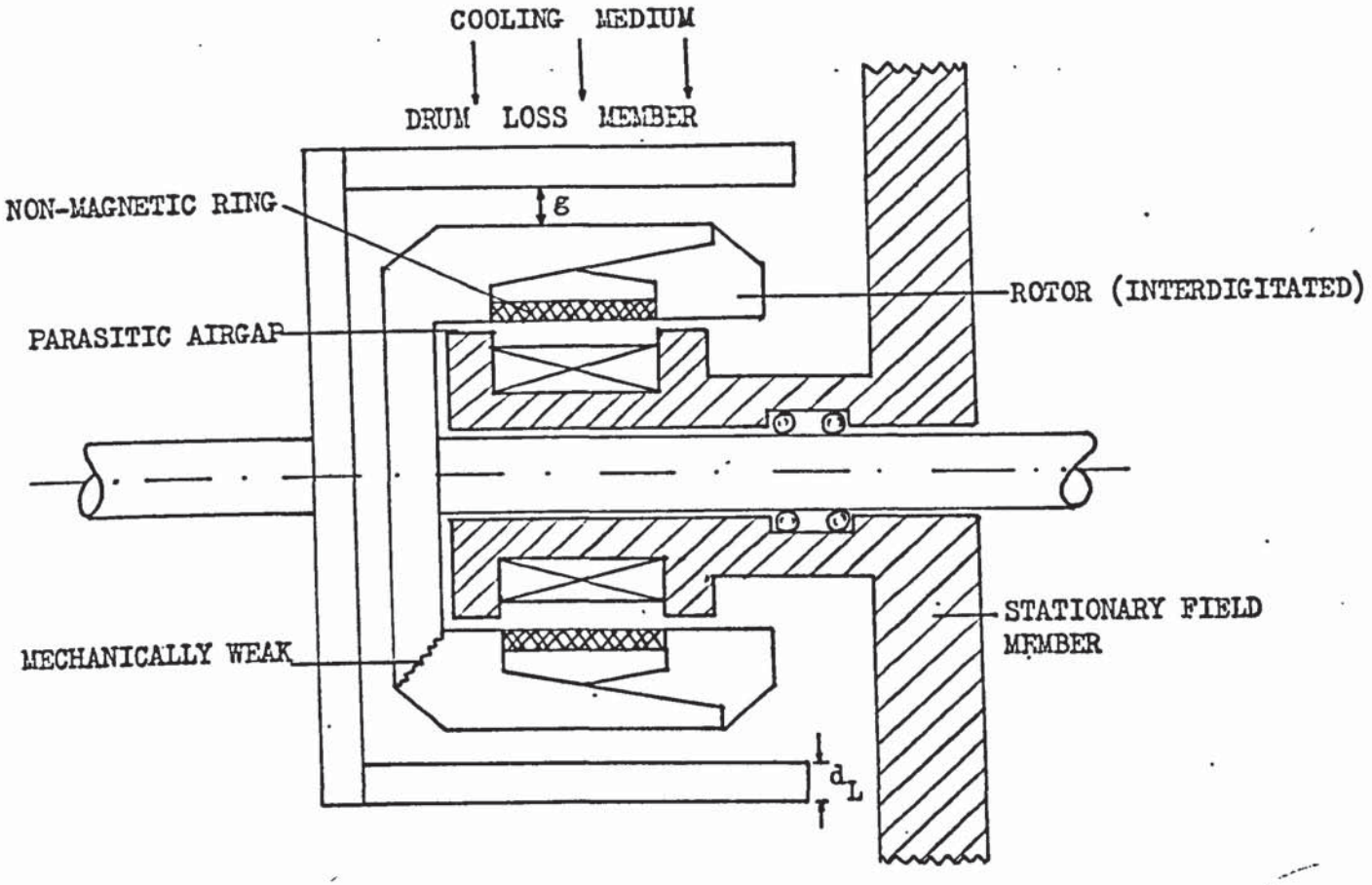

DRUM TYPE LUNDELL COUPLING WITH PARASITIC AIRGAP

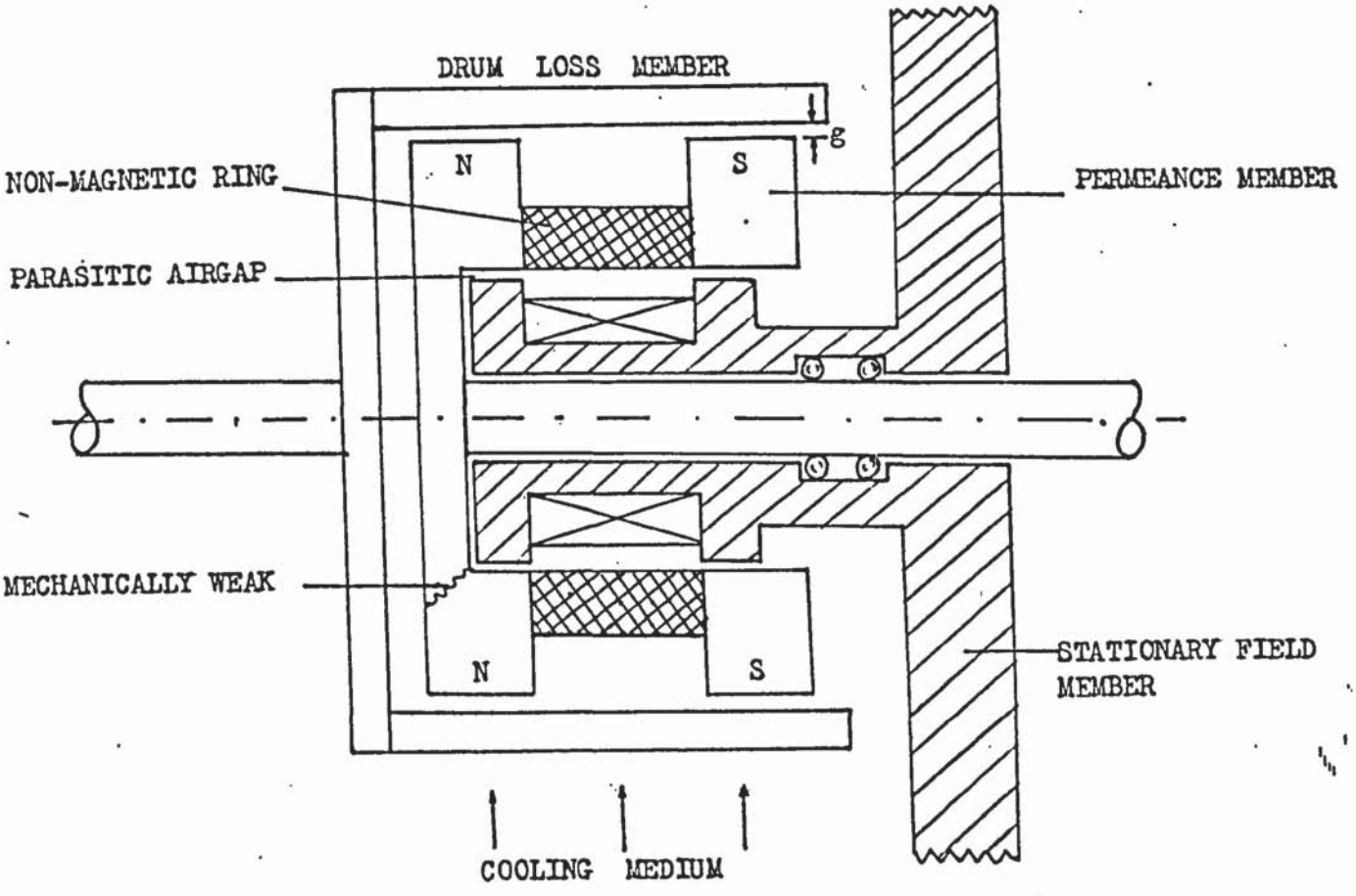

DRUM TYPE INDUCTOR COUPLING WITH PARASITIC AIRGAP

Figure 1.2

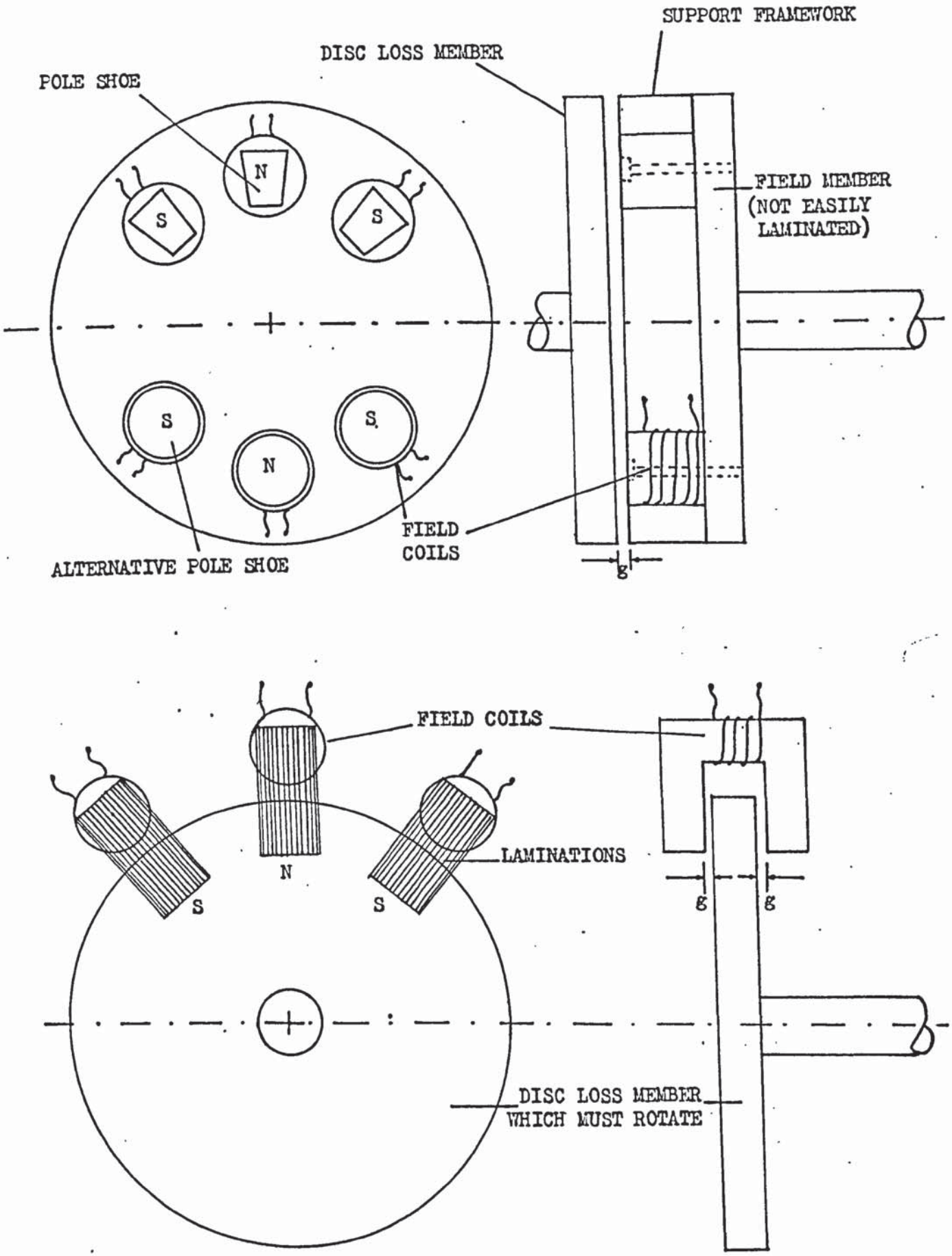

TWO BASIC CONSTRUCTIONS OF DISC TYPE SALIENT POLE COUPLINGS.

Figure 1.3

FIGURES FOR CHAPTER 2.

THE RESISTIVITY OF 'ARMCO' INGOT IRON PLOTTED AGAINST TEMPERATURE.

(NOTE: Curve taken from 'ARMCO' sales brochure.)

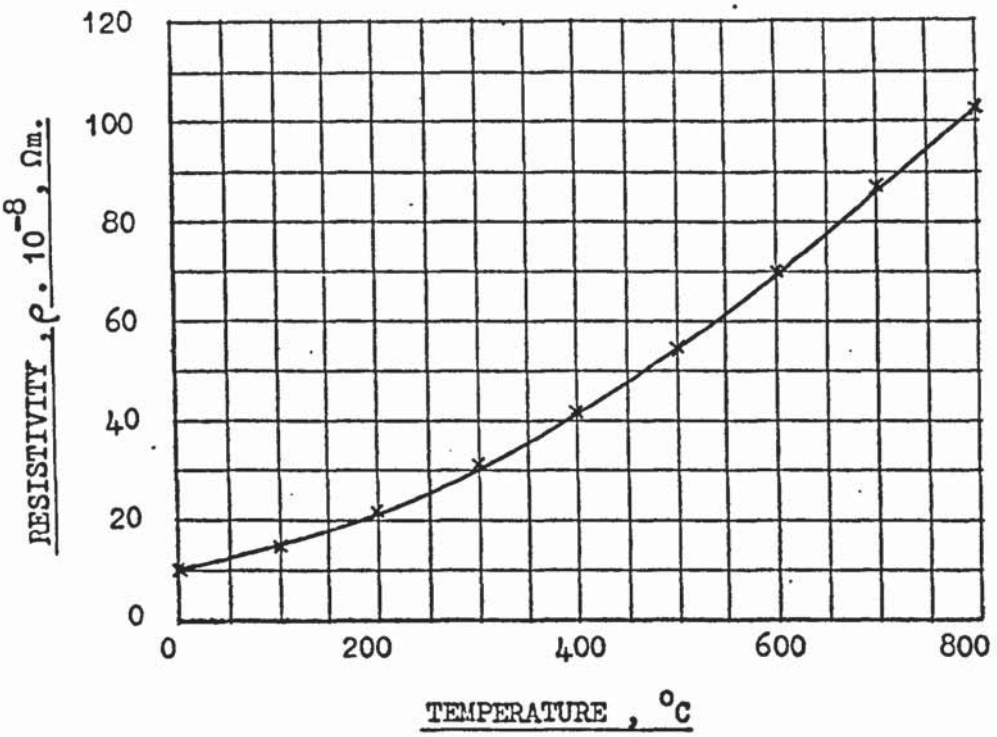

Figure 2.1

THE EFFECTS OF DRUM TEMPERATURE ON THE TORQUE - SPEED CURVES.

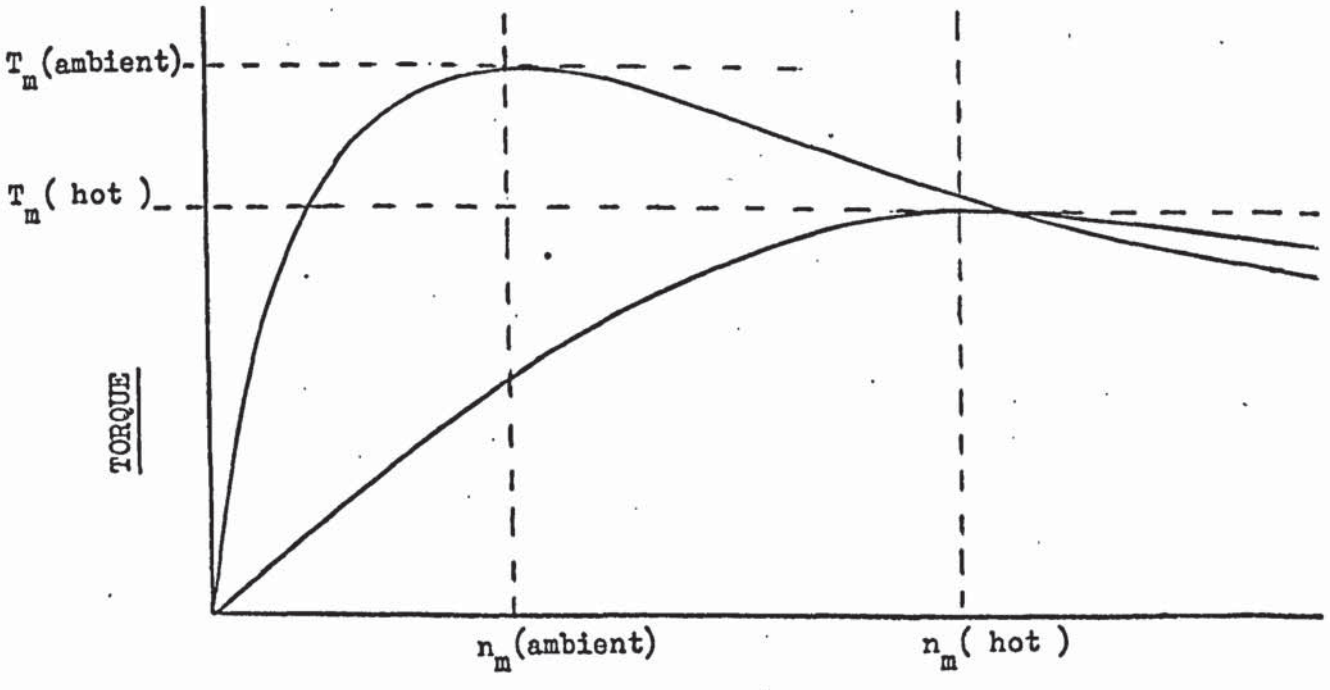

Figure 2.2

THE VARIATION OF SPECIFIC HEAT AND THERMAL CONDUCTIVITY WITH TEMPERATURE FOR A TYPICAL LOW CARBON STEEL SUCH AS 'ARMCO'.

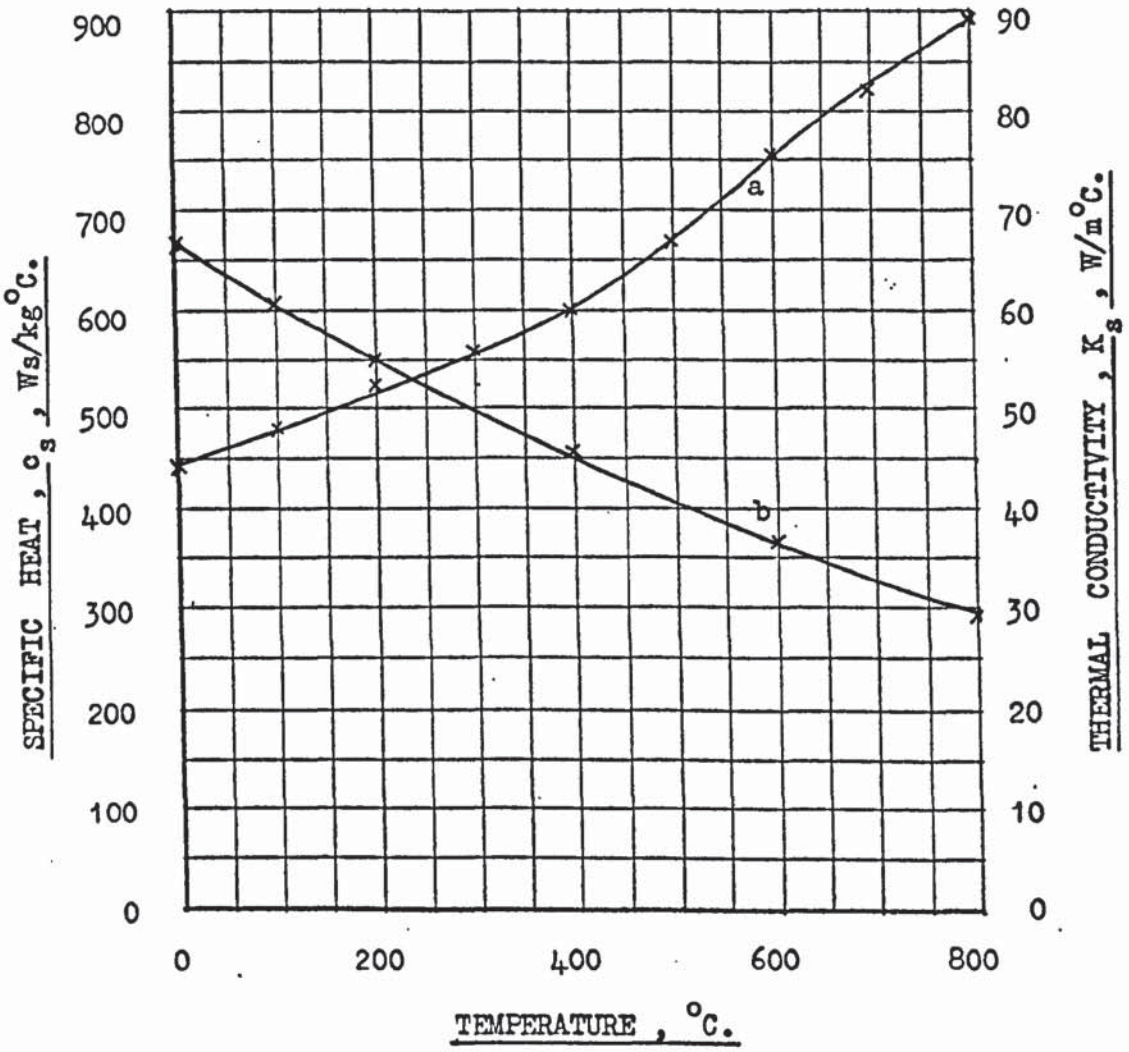

a : Specific heat , c_s , - temperature.

b : Thermal conductivity , K_s , - temperature.

NOTE : Both curves are from reference 52 , typical analysis 0.06% C, 0.4% MN.

Figure 2.3

THE DEVELOPED ANALYTICAL MODEL.

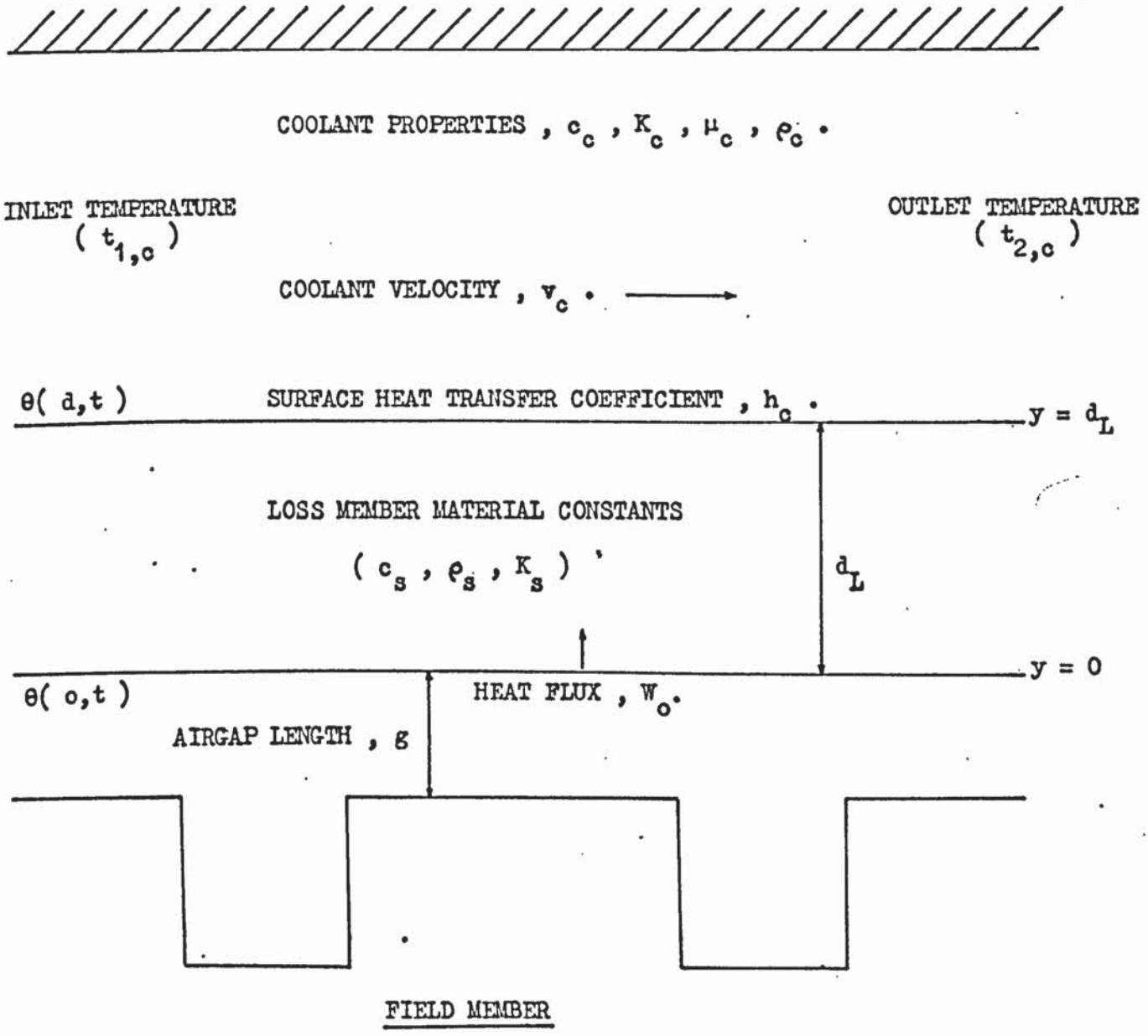

Figure 2.5

ROOTS OF $x'/\beta = \cot(x') = f_{x'}$

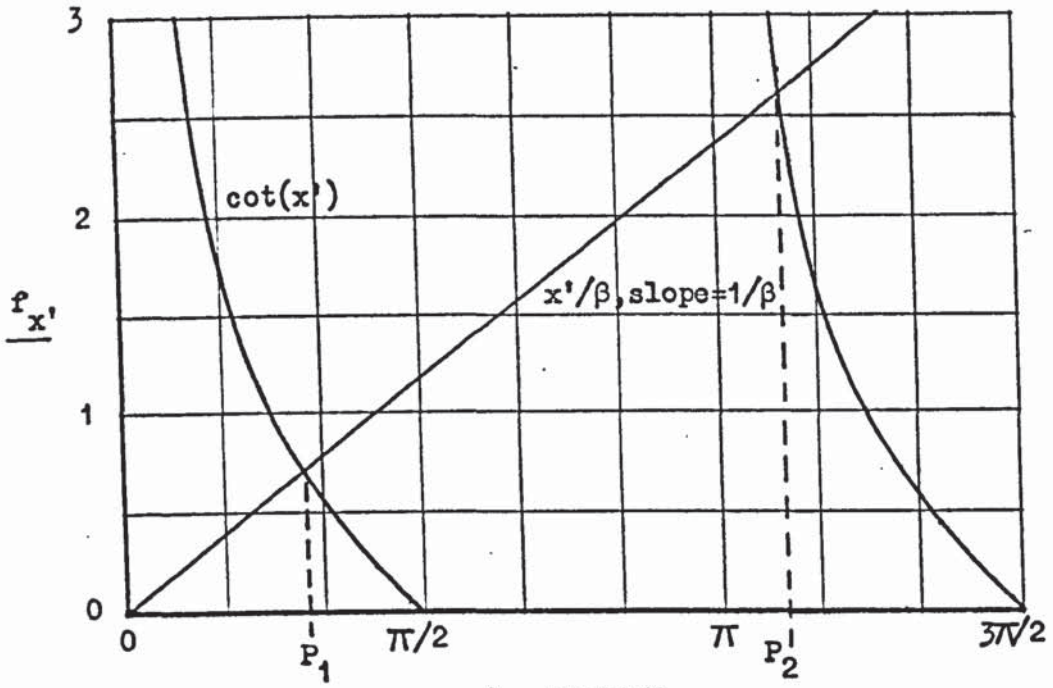

Figure 2.6

ROOTS OF $-y = \coth(\beta y) = f_y$

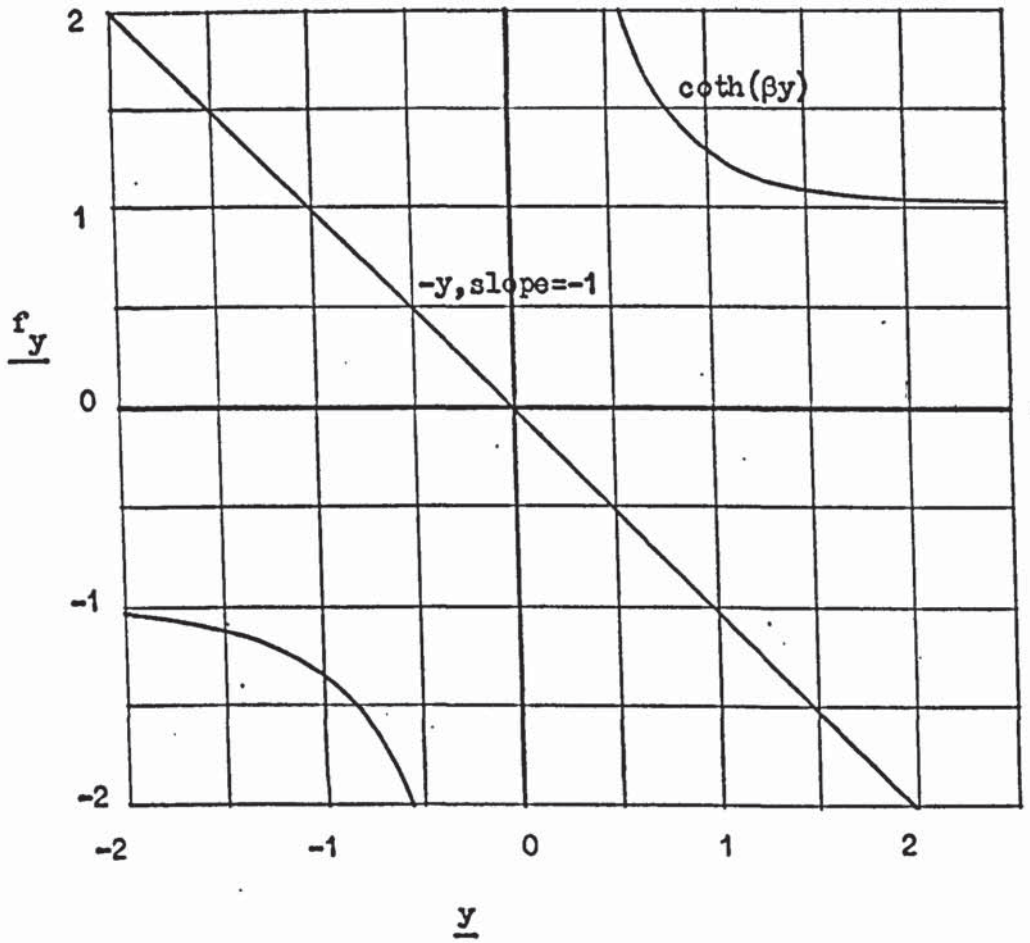

Figure 2.7

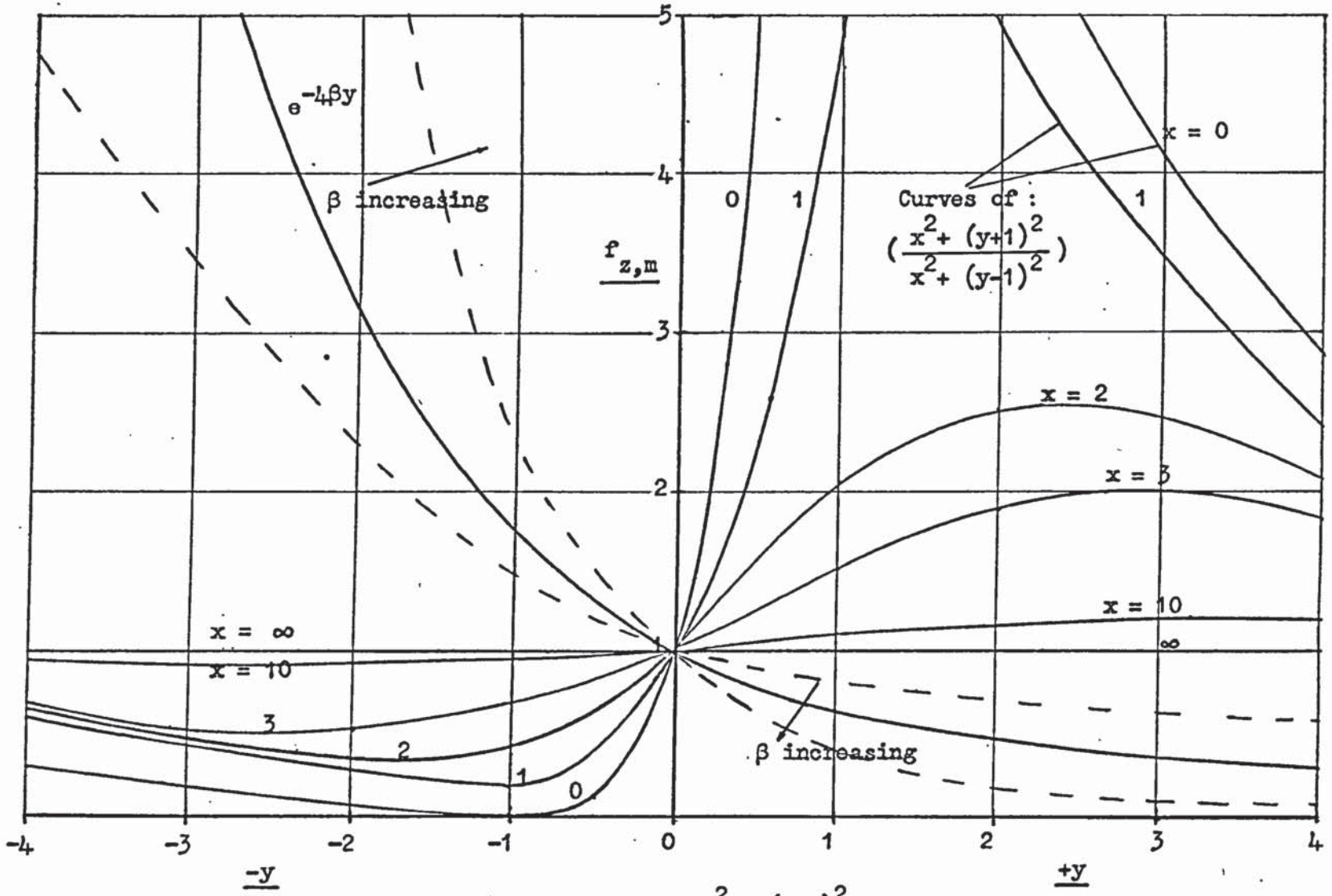

CURVES OF $e^{-4\beta y} = \left(\frac{x^2+(y+1)^2}{x^2+(y-1)^2}\right) = f_{z,m}$

Figure 2.8

FIGURES FOR CHAPTER 3.

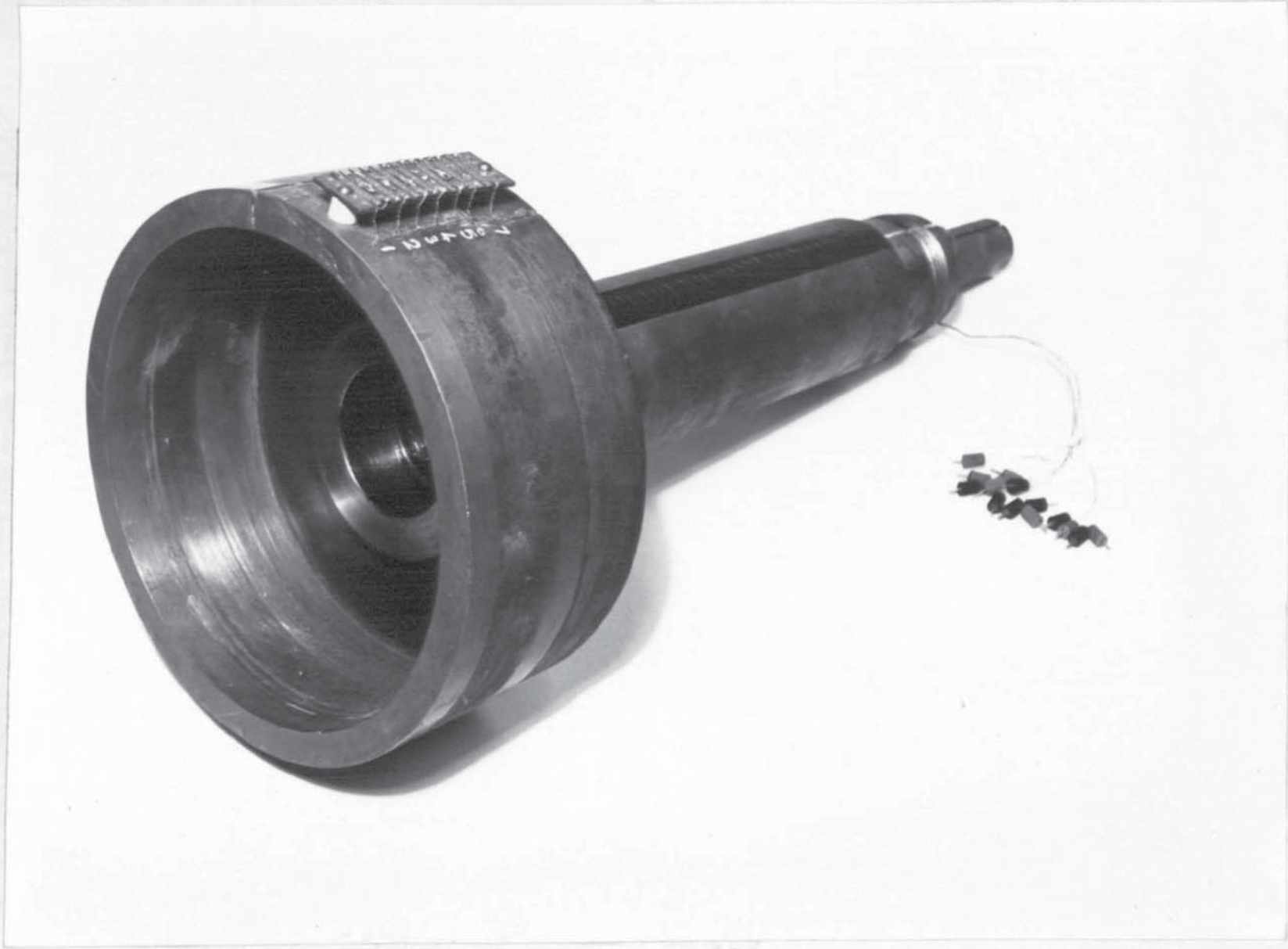

THE COPPER ENDRING DRUM

Figure 3.2

EXPERIMENTAL TORQUE - SLIP CURVES OF THE ENDRING DRUM COUPLING.

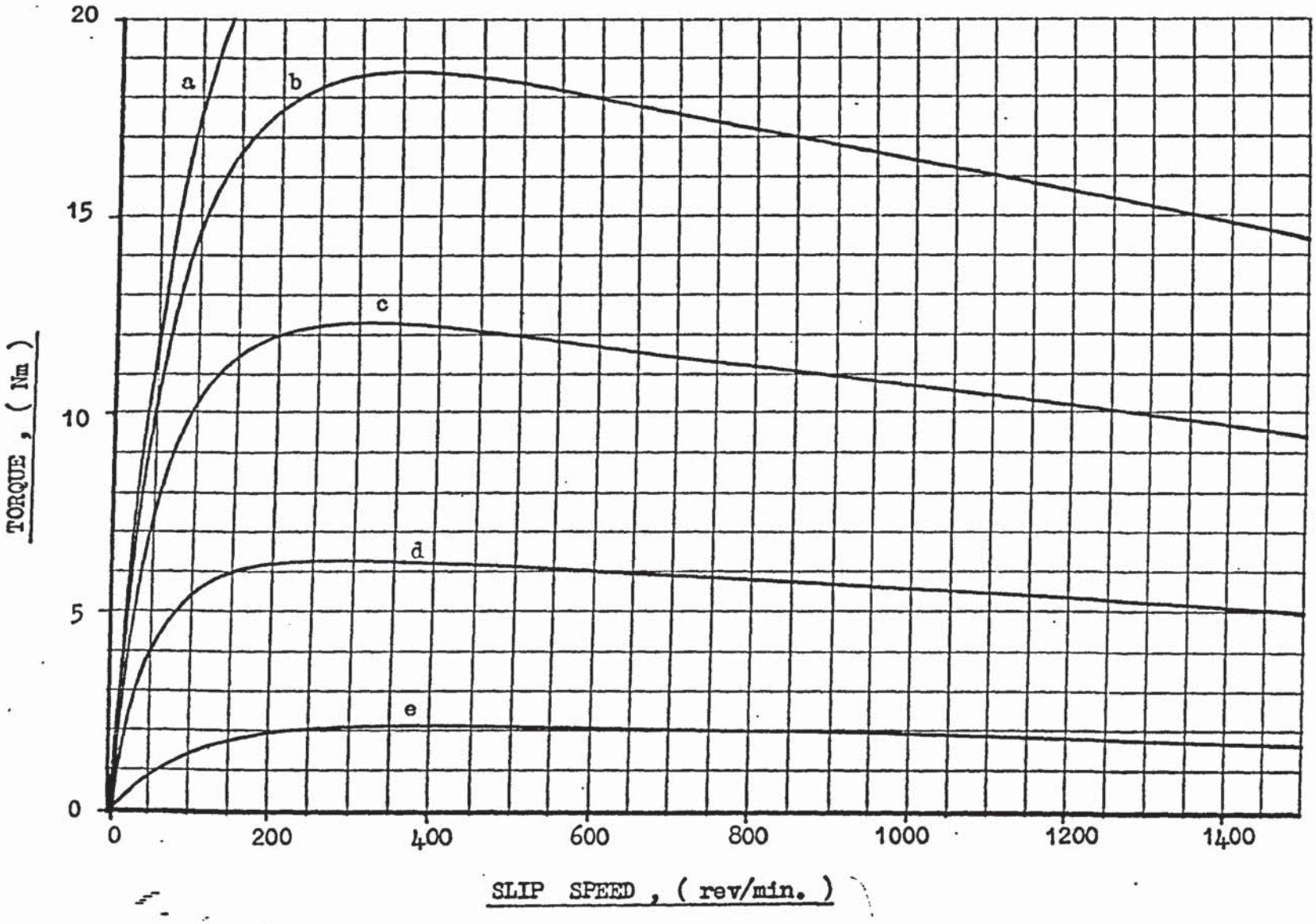

EXCITATION :

a : 0.5A

b : 0.4A

c : 0.3A

d : 0.2A

e : 0.1A

Figure 3.3

EXPERIMENTAL TORQUE - SLIP CURVES OF THE SOLID DRUM COUPLING.

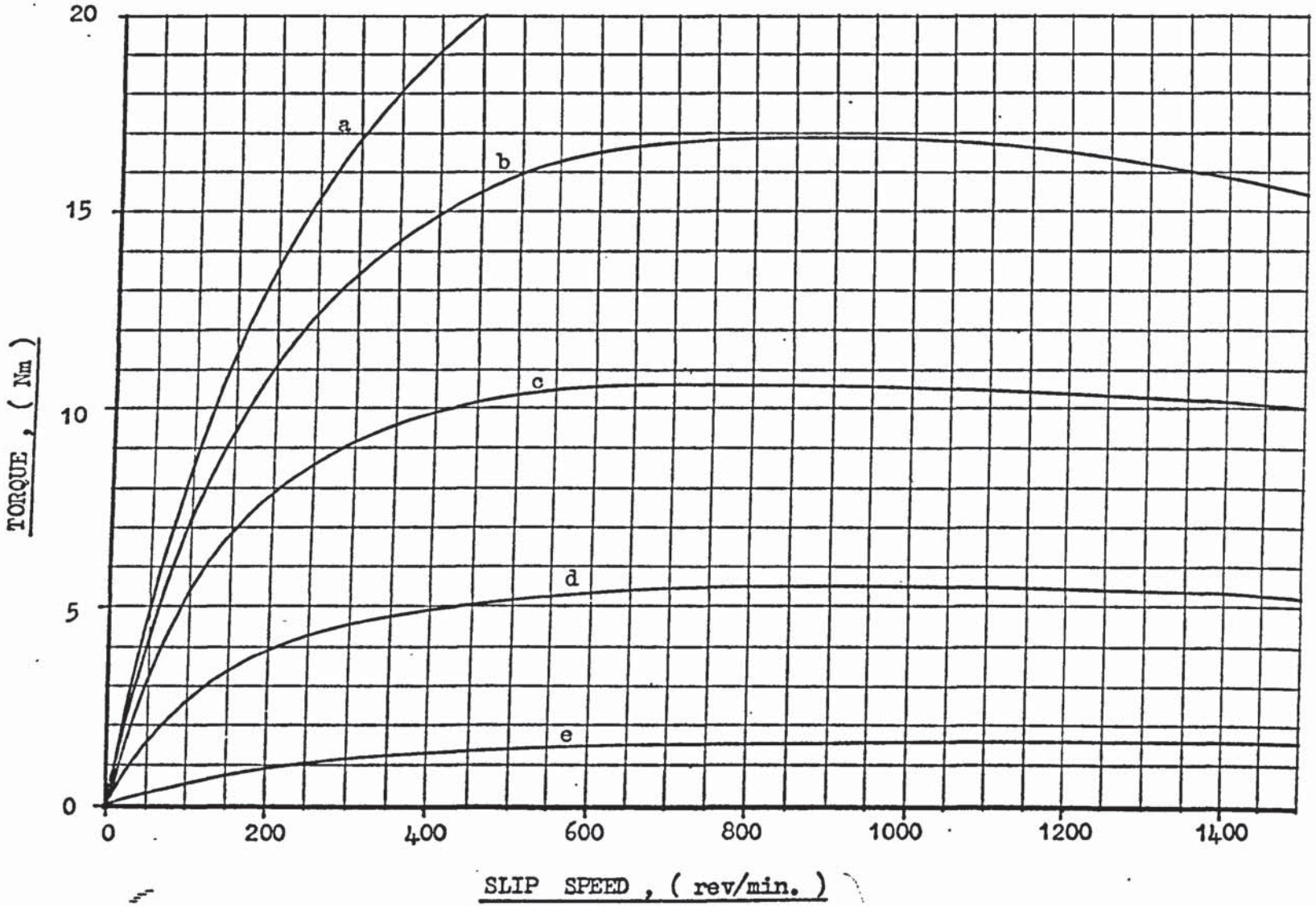

EXCITATION :

a : 0.5A

b : 0.4A

c : 0.3A

d : 0.2A

e : 0.1A

Figure 3.4

SURFACE TEMPERATURE AGAINST TIME CURVES TAKEN FROM THE ENDRING DRUM AT CONSTANT SLIP SPEED AND VARIOUS EXCITATIONS.

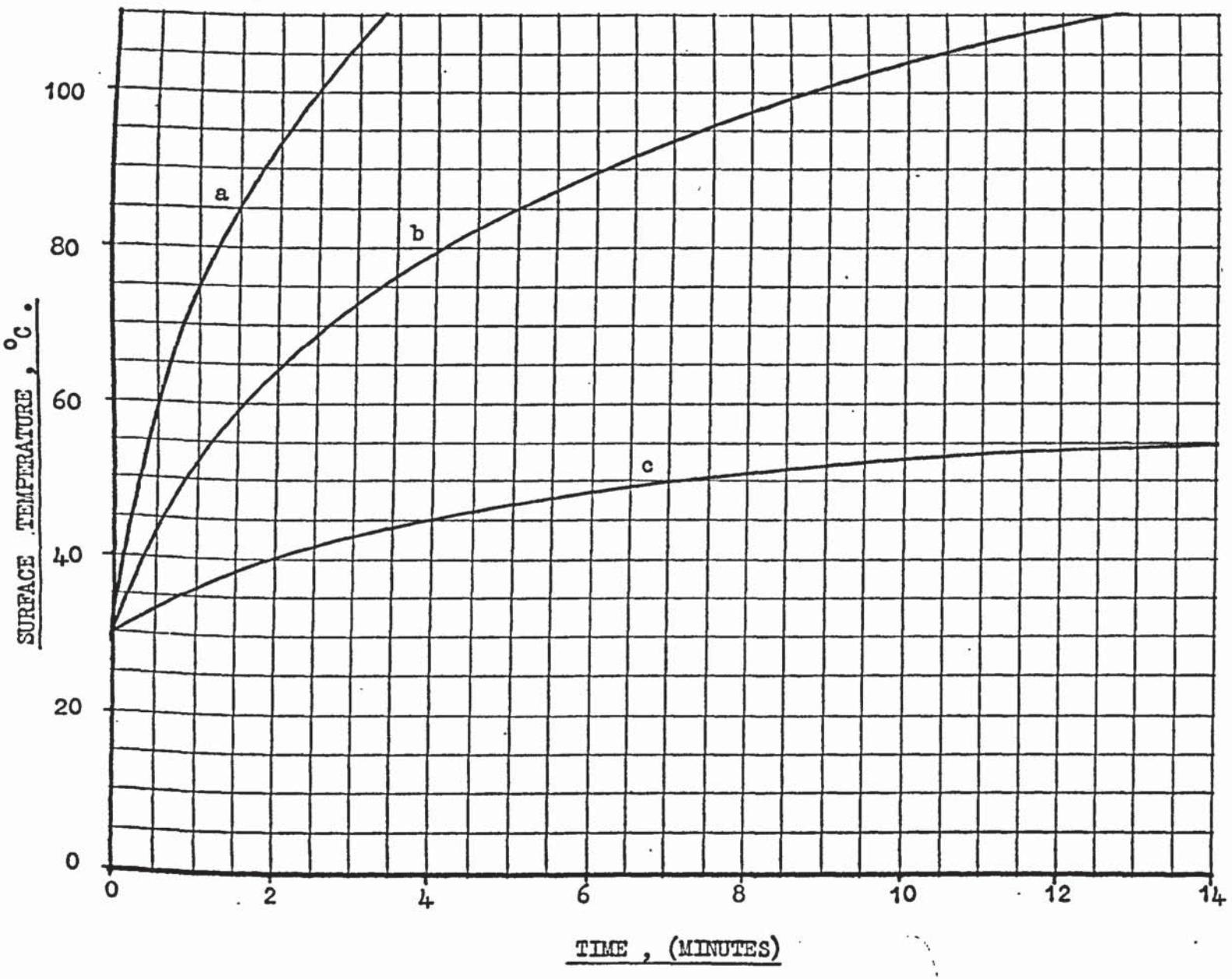

EXCITATION	:	SLIP SPEED
a	: 0.3A	, 1445 rev/min.
b	0.2A	, 1450 rev/min.
c	0.1A	, 1450 rev/min.

NOTE : All curves taken with thermocouple B.

Figure 3.5

SURFACE TEMPERATURE AGAINST TIME CURVES TAKEN FROM THE SOLID DRUM AT CONSTANT SLIP SPEED AND VARIOUS EXCITATIONS.

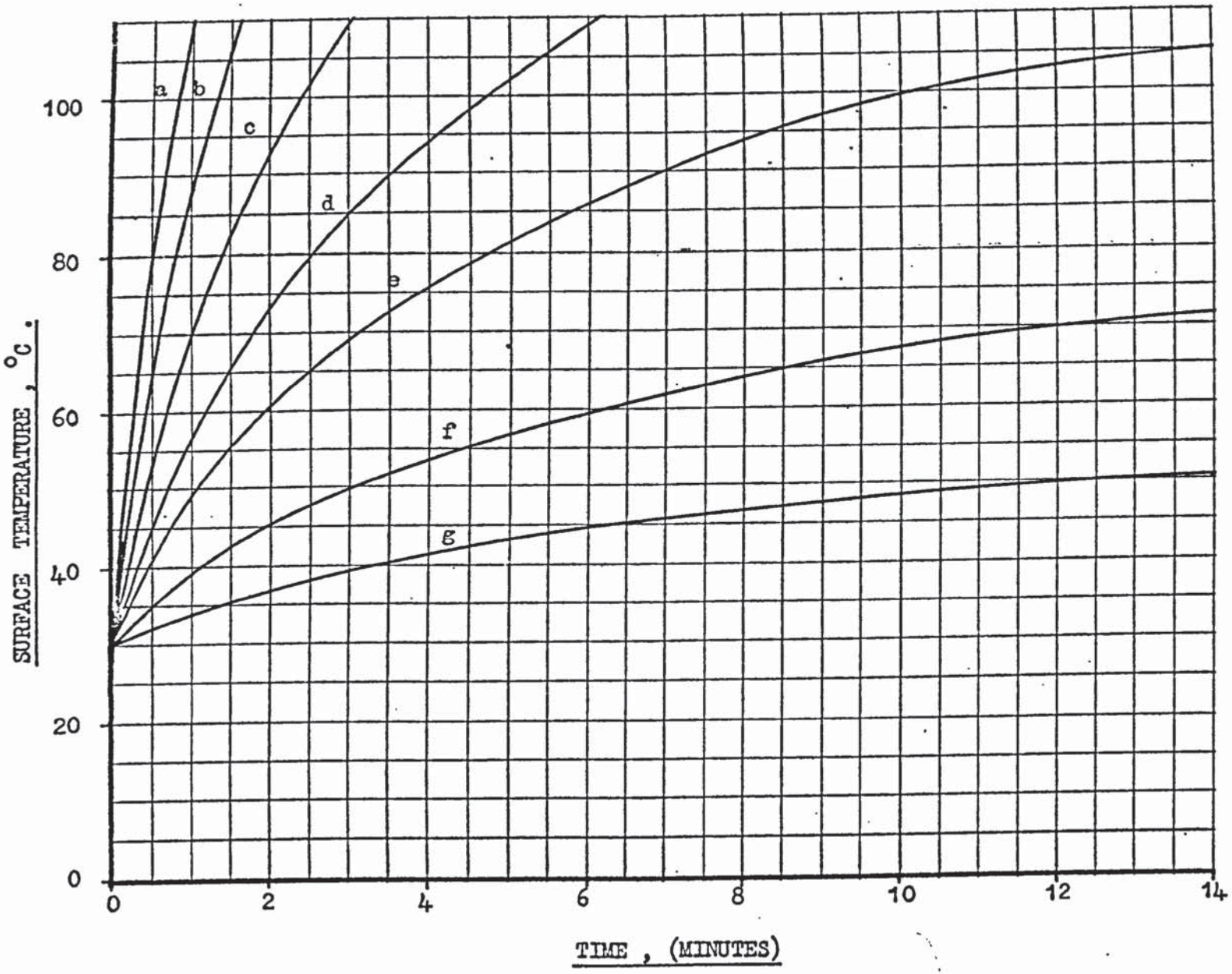

EXCITATION :	SLIP SPEED
a : 0.5 A	, 1430 rev/min.
b : 0.4 A	, 1440 rev/min.
c : 0.3 A	, 1440 rev/min.
d : 0.25A	, 1445 rev/min.
e : 0.2 A	, 1450 rev/min.
f : 0.15A	, 1450 rev/min.
g : 0.1 A	, 1460 rev/min.

NOTE : All curves taken with thermocouple B.

Figure 3.6

EXPERIMENTAL TORQUE - TIME CURVES FROM THE SOLID DRUM TAKEN AT CONSTANT SLIP SPEED AND VARIOUS EXCITATIONS ; TAKEN SIMULTANEOUSLY WITH THE SURFACE TEMPERATURE - TIME CURVES.

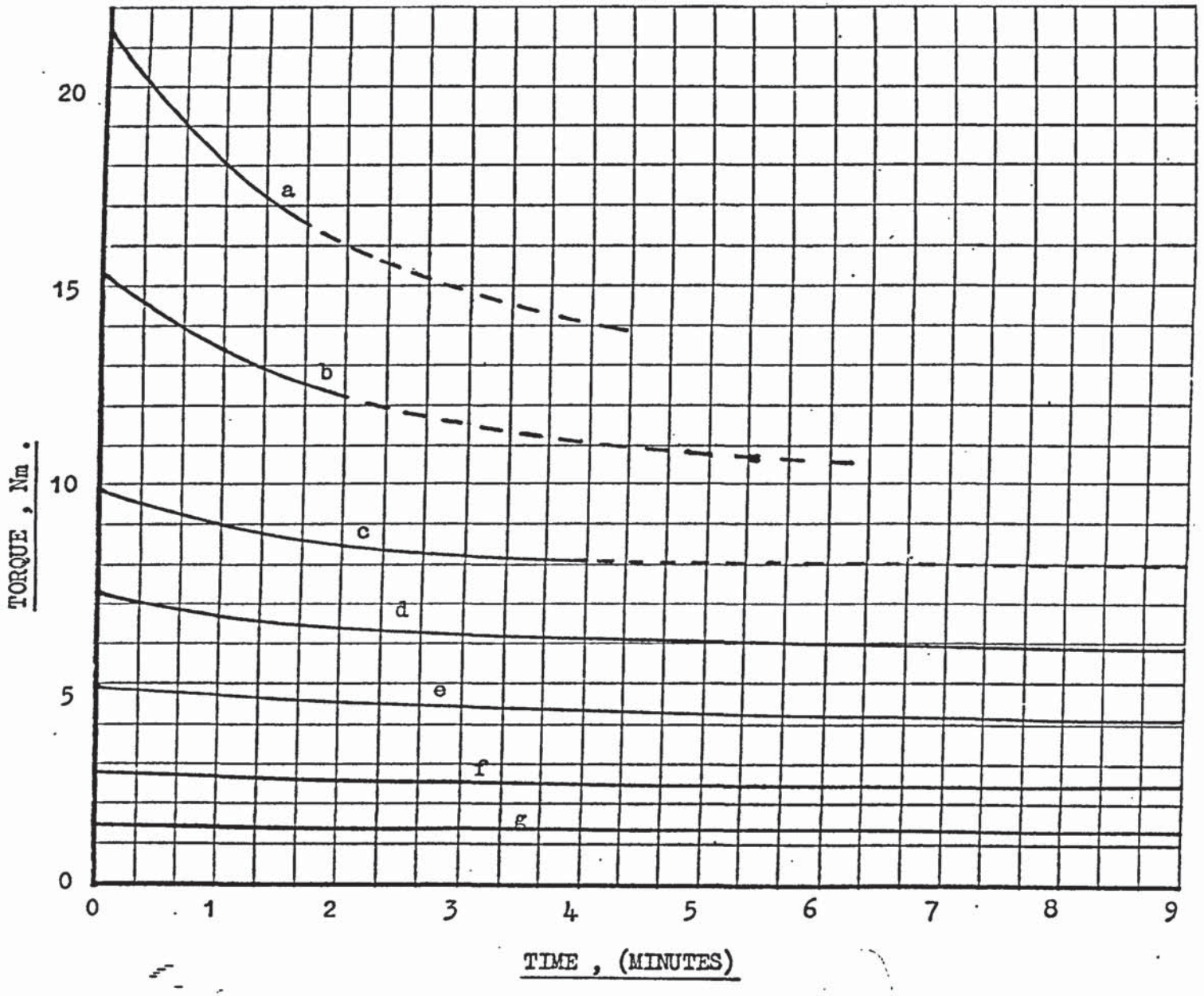

EXCITATION	:	SLIP SPEED
a	: 0.5A	, 1430 rev/min.
b	: 0.4A	, 1440 rev/min.
c	: 0.3A	, 1440 rev/min.
d	: 0.25A	, 1445 rev/min.
e	: 0.2A	, 1450 rev/min.
f	: 0.15A	, 1450 rev/min.
g	: 0.1A	, 1460 rev/min.

Figure 3.7

DERIVATION OF THE ENDRING DRUM THERMAL TIME CONSTANT FROM THE MEASURED SURFACE TEMPERATURE RESPONSE.

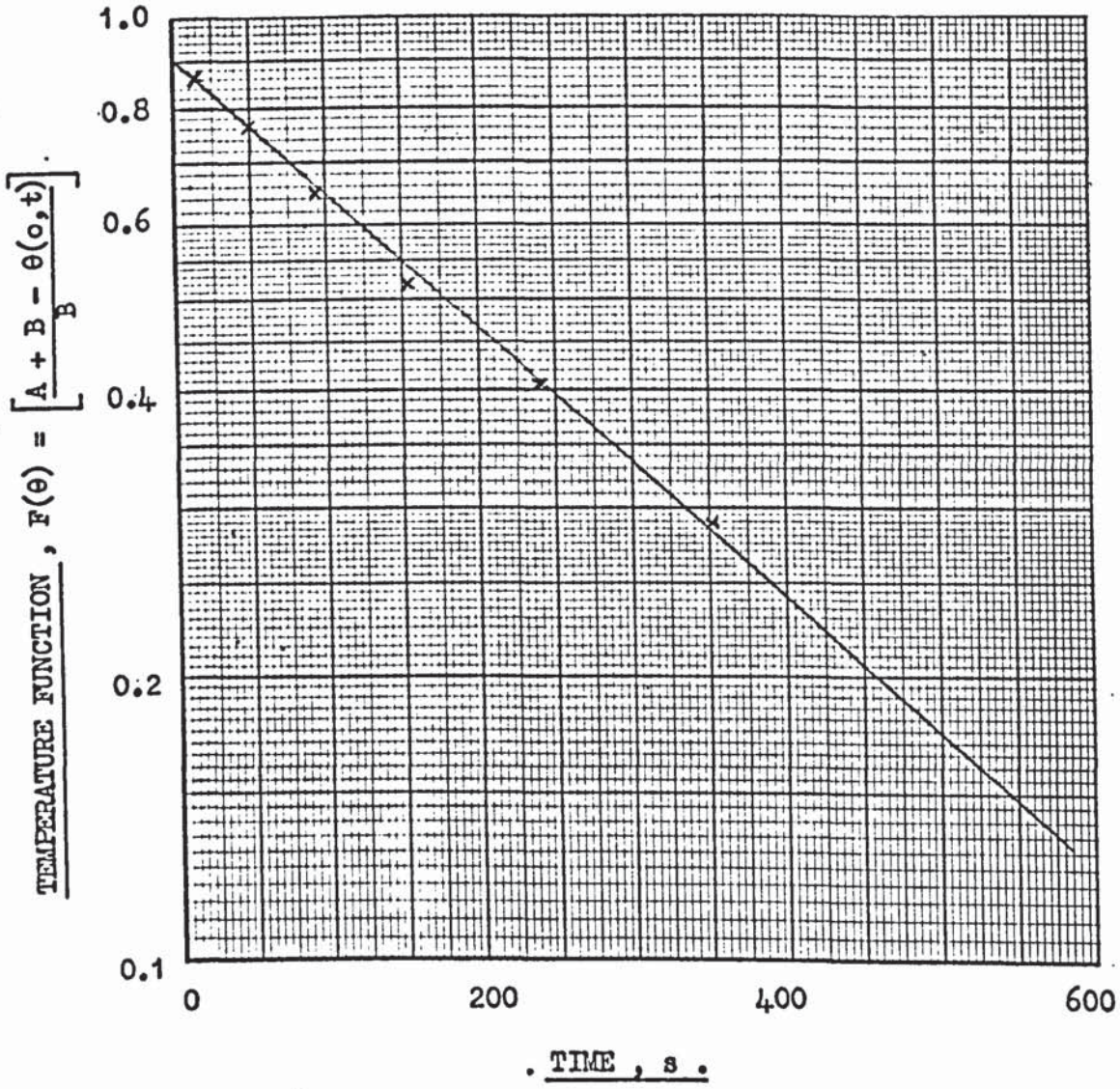

X : Experimental points. (TAKEN FROM FIG 3.5)

Thermal time constant , τ_1 = 299s

Figure 3.8

DERIVATION OF THE SOLID DRUM THERMAL TIME CONSTANT FROM THE MEASURED SURFACE TEMPERATURE RESPONSE.

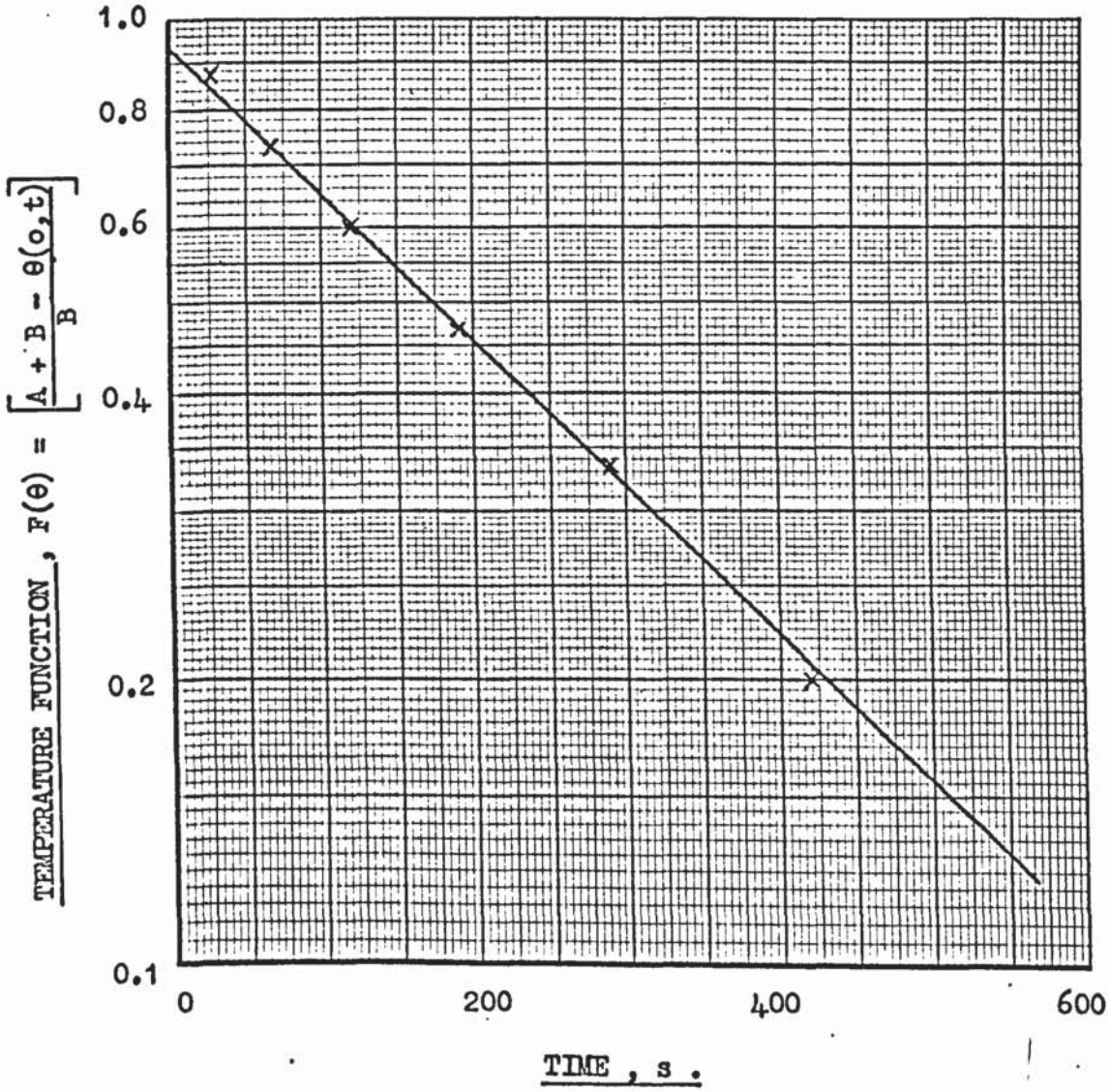

X : Experimental points. (TAKEN FROM FIG 3-6)

Thermal time constant , τ_1 = 285s

Figure 3.9.

DERIVATION OF THE SOLID DRUM THERMAL TIME CONSTANT FROM THE MEASURED SURFACE TEMPERATURE RESPONSE.

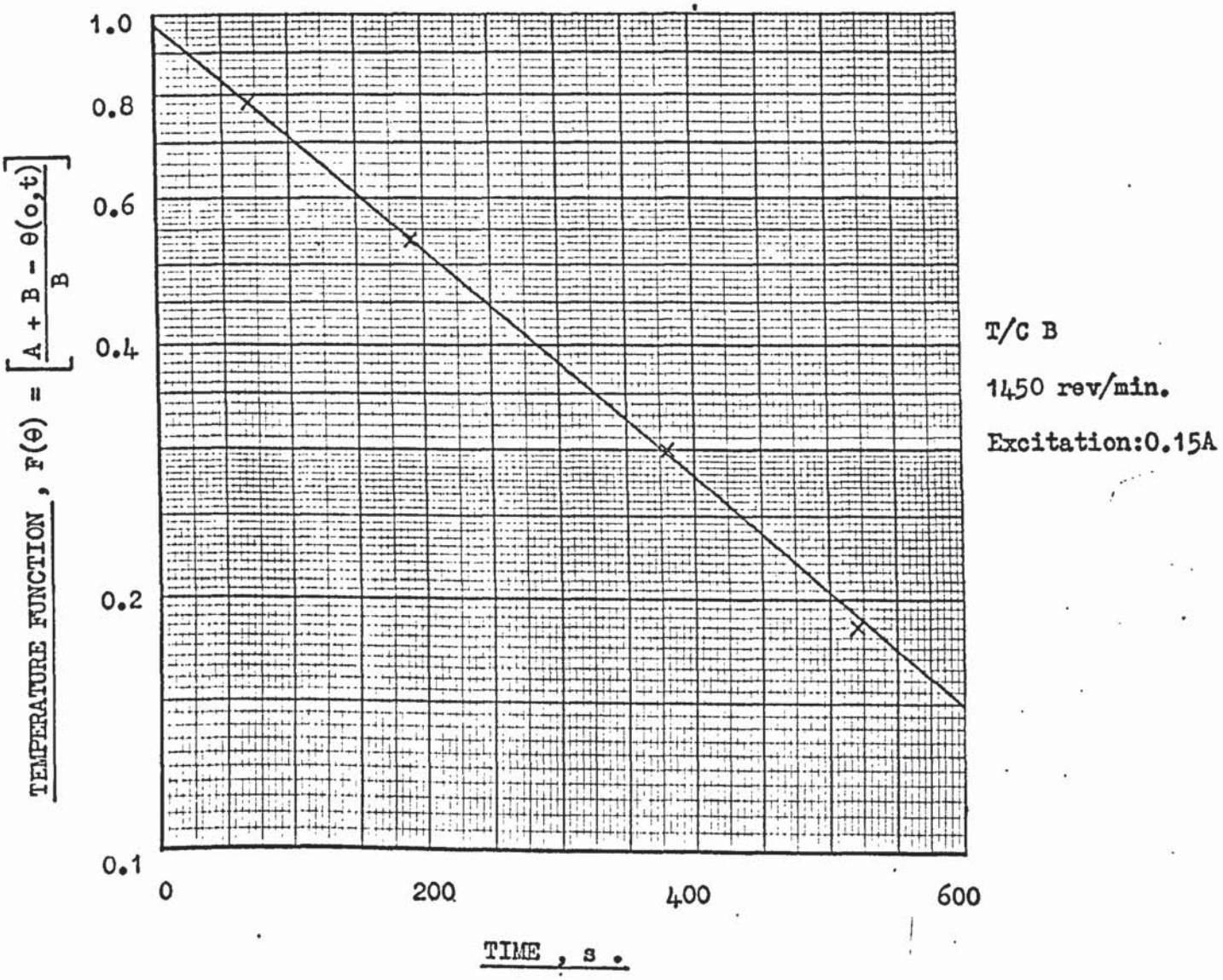

X : Experimental points. (TAKEN FROM FIG 3.6)

Thermal time constant , τ_1 = 320s

Figure 3.10

FIGURES FOR CHAPTER 4.

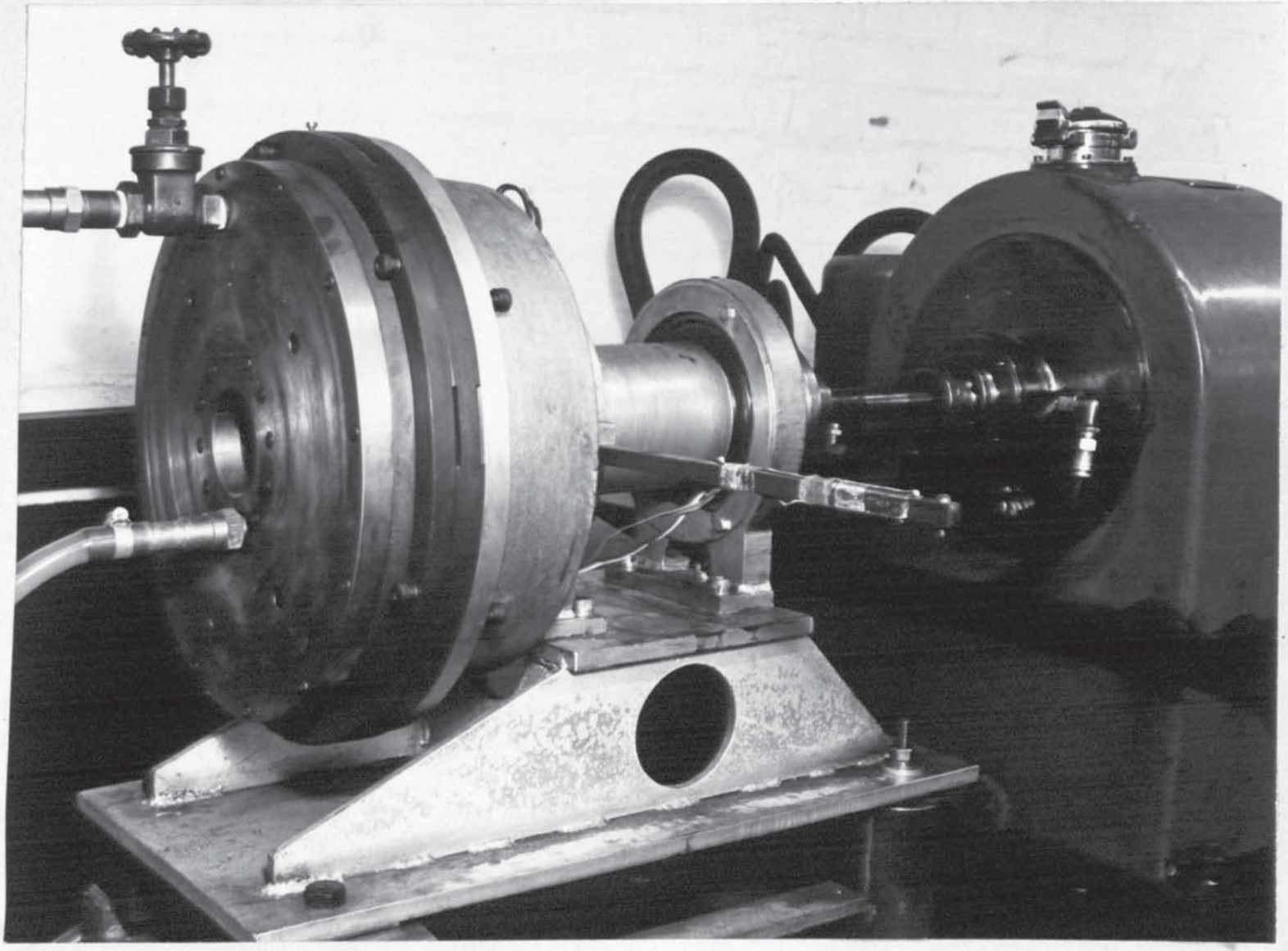

THE WATER COOLED HIGH SPEED EDDY-CURRENT DYNAMOMETER

Figure 4.3

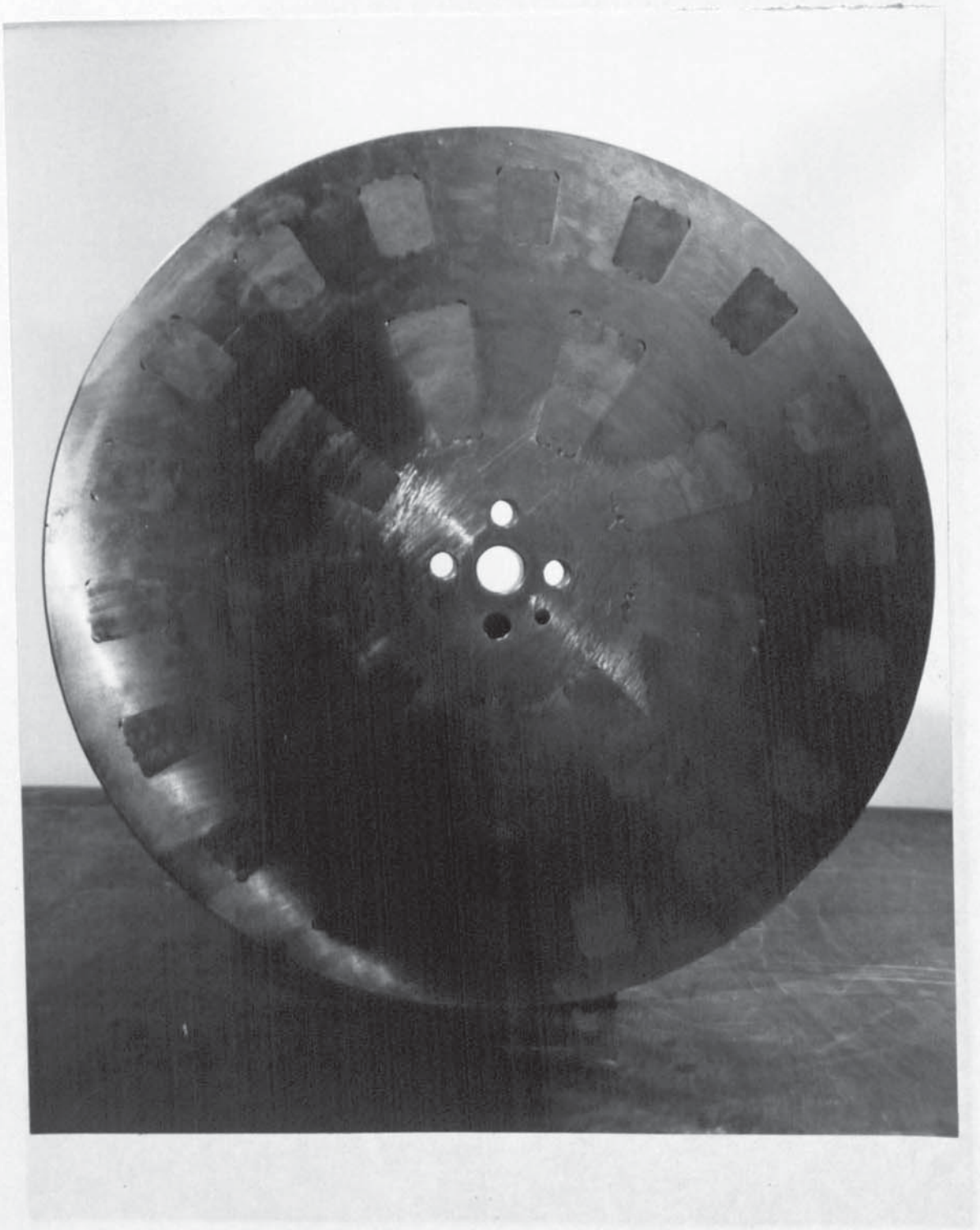

THE ROTOR OR PERMEANCE MEMBER

Figure 4.4

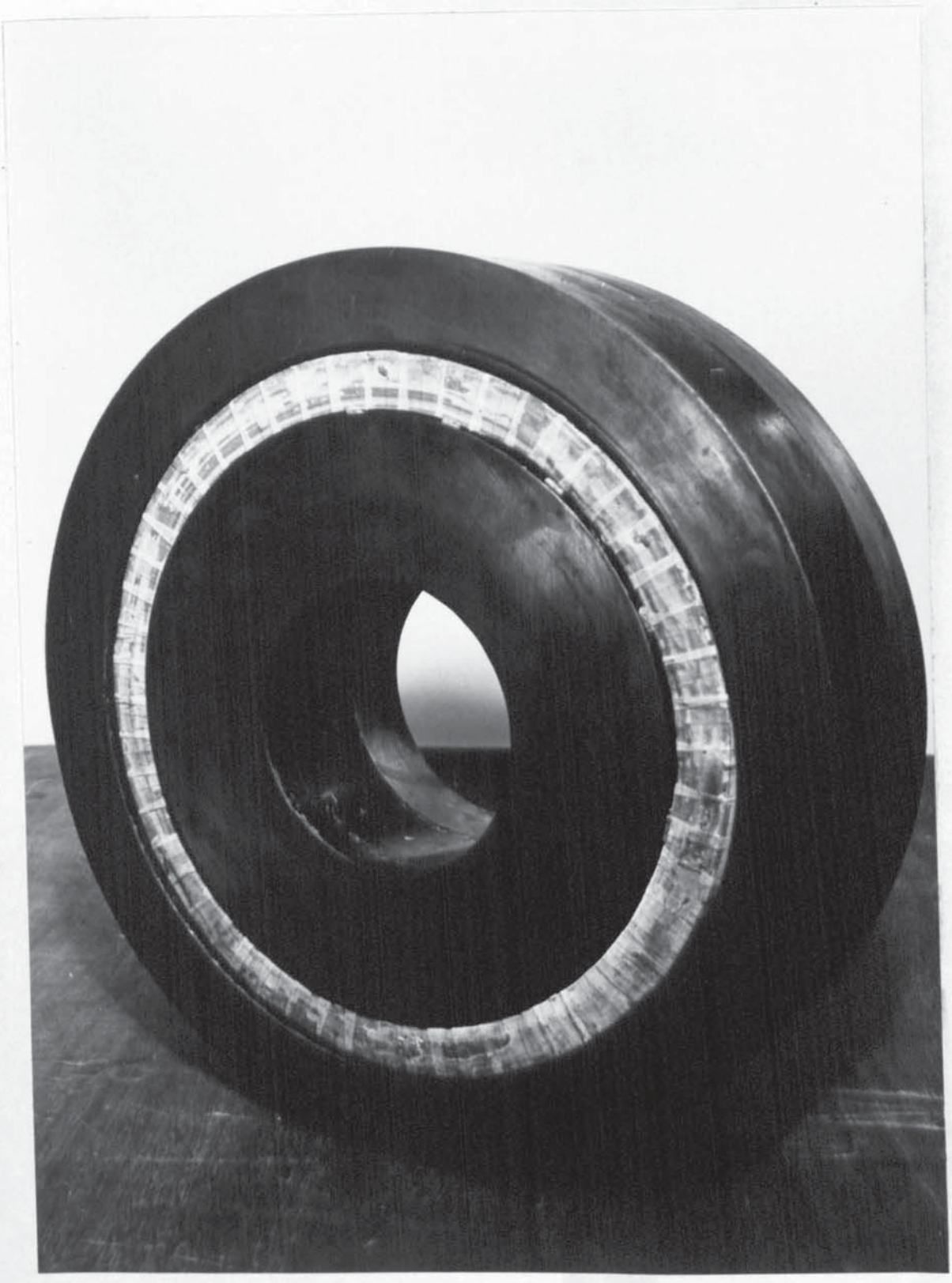

FIELD MEMBER AND EXCITATION COIL

Figure 4.5

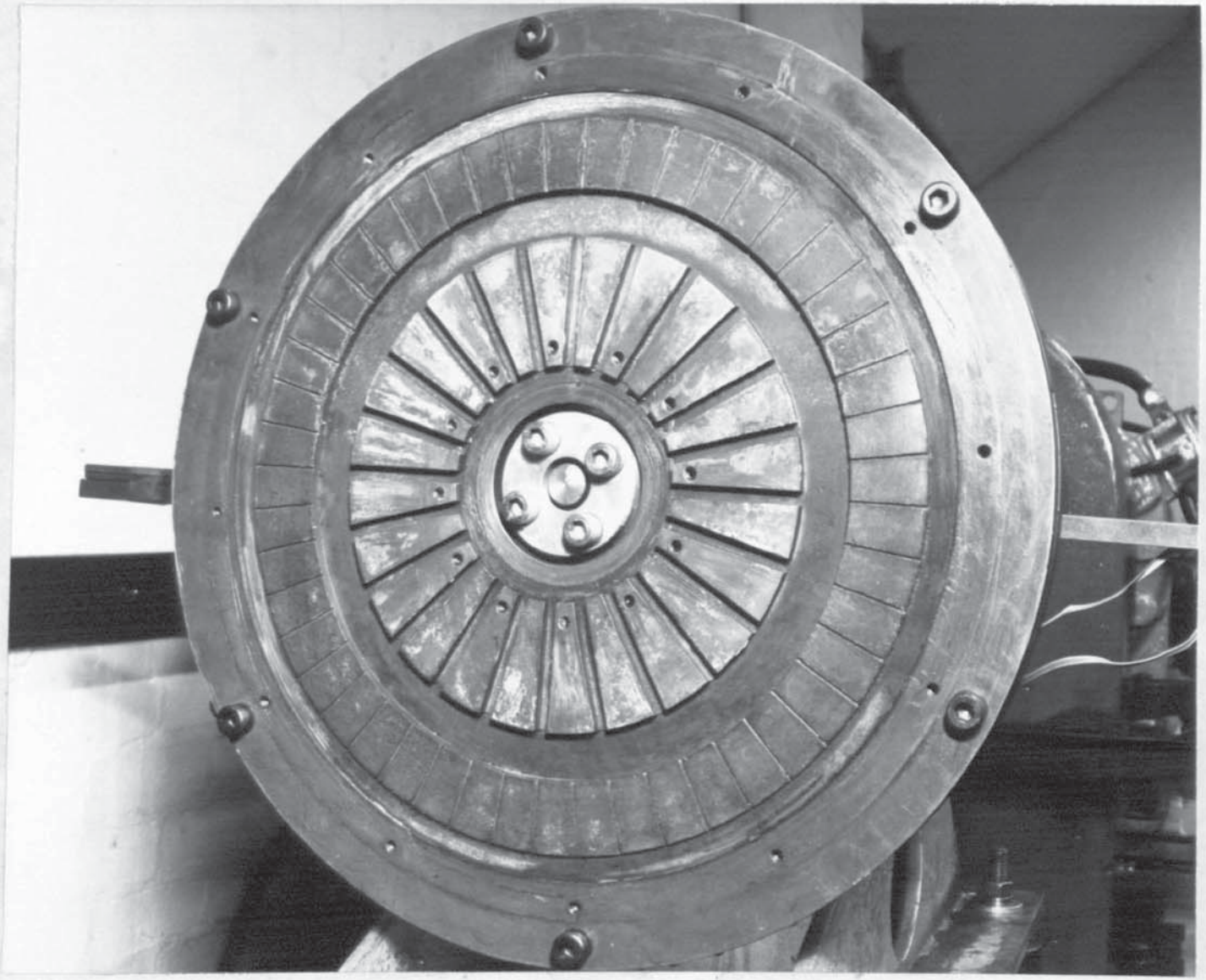

THE LOSS MEMBER COOLING WATER CHANNELS

Figure 4.6

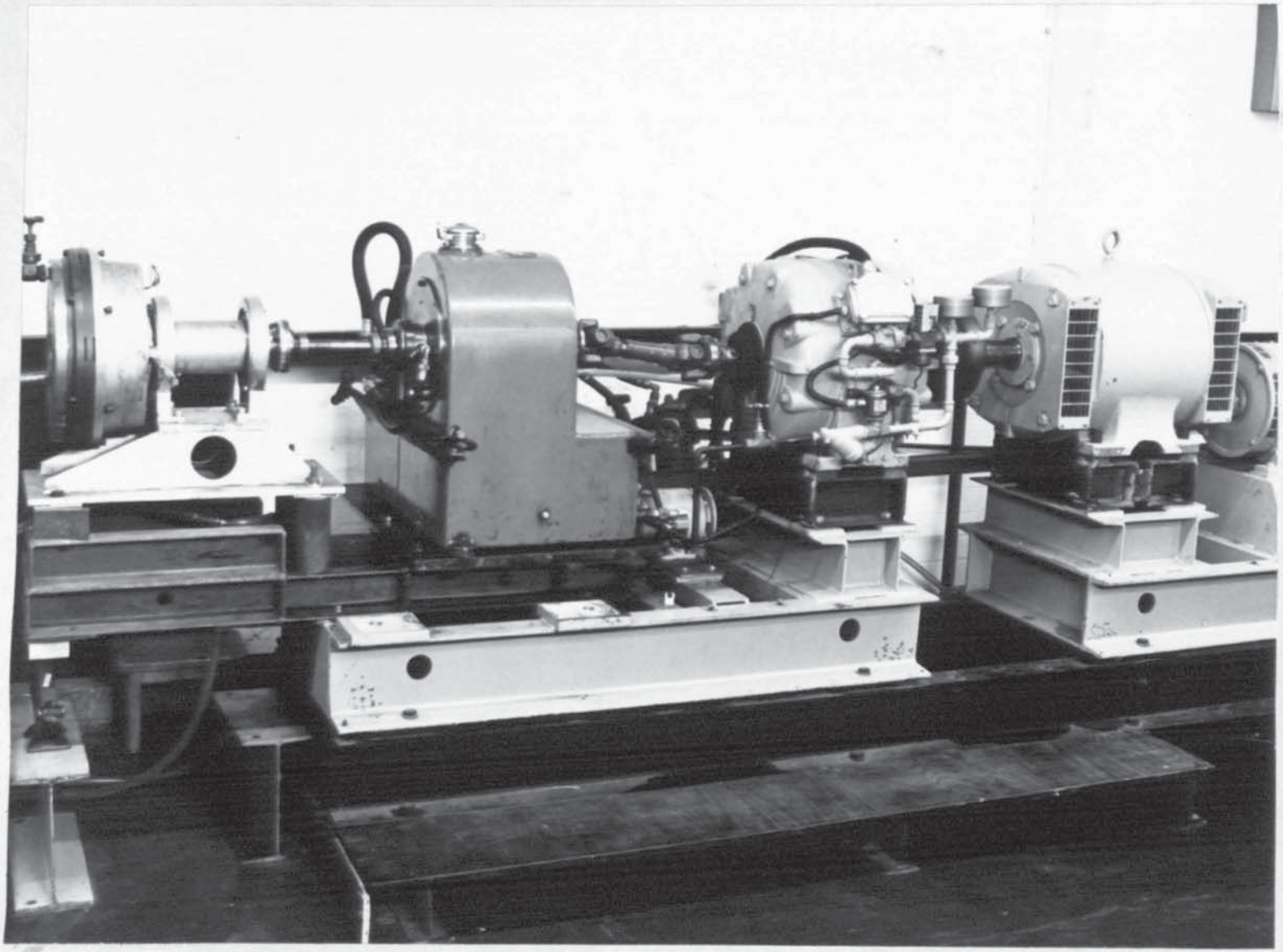

GENERAL LAYOUT OF EXPERIMENTAL APPARATUS

Figure 4.7

SCHEMATIC DIAGRAM OF EXPERIMENTAL APPARATUS.

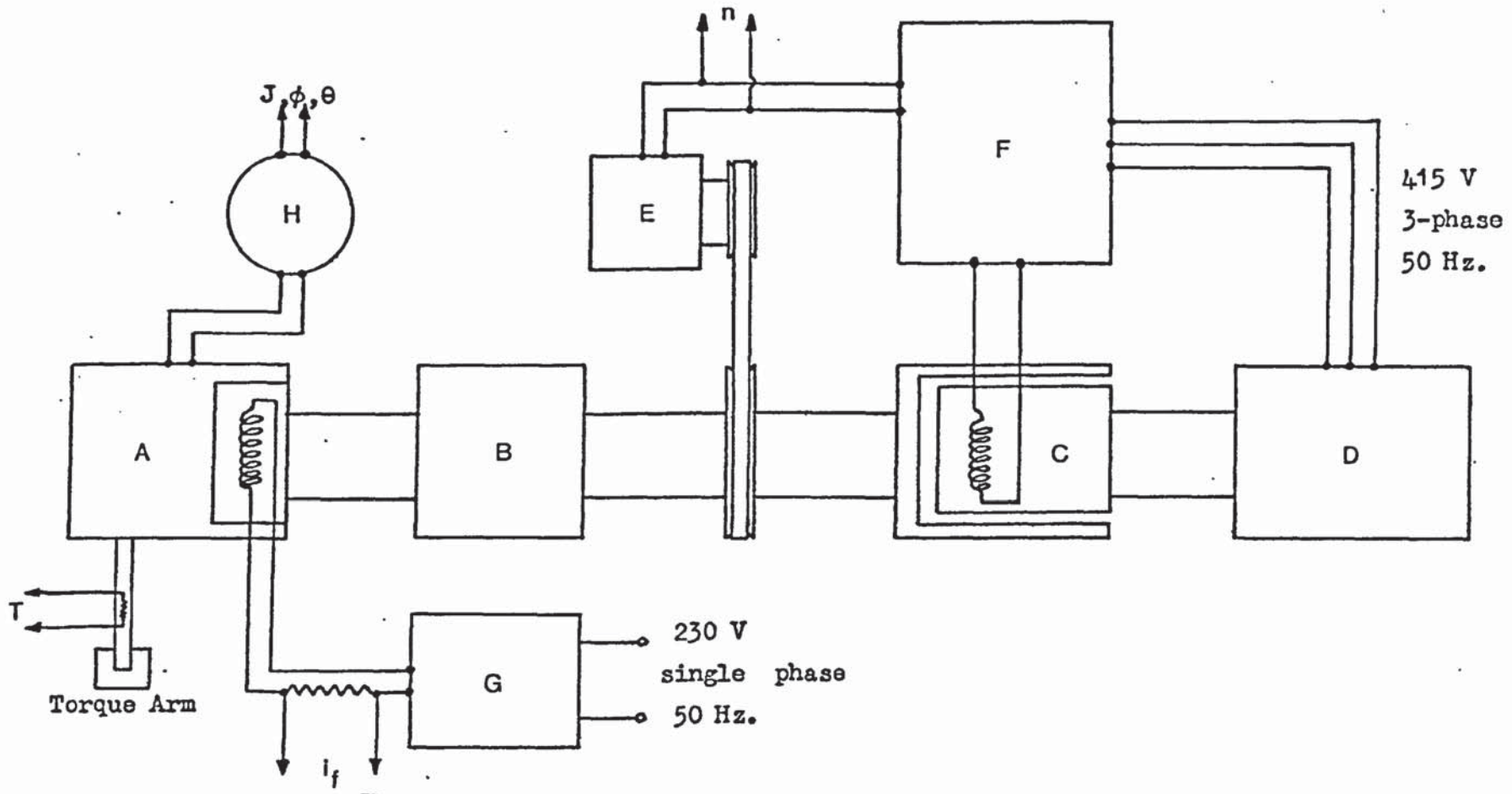

A : High Speed Dynamometer.

B : Gear Box 10:1 Step Up.

C : 75 K.W. Drive Coupling.

D : 4 pole , 75 K.W. Induction Motor.

E : D.C. Tachogenerator.

F : Control Cubicle.

G : Constant current supply for dynamometer field.

H : Rotary switch for search coils.

Figure 4.8

ARRANGEMENT OF SEARCH COILS ON STATIONARY FIELD MEMBER.

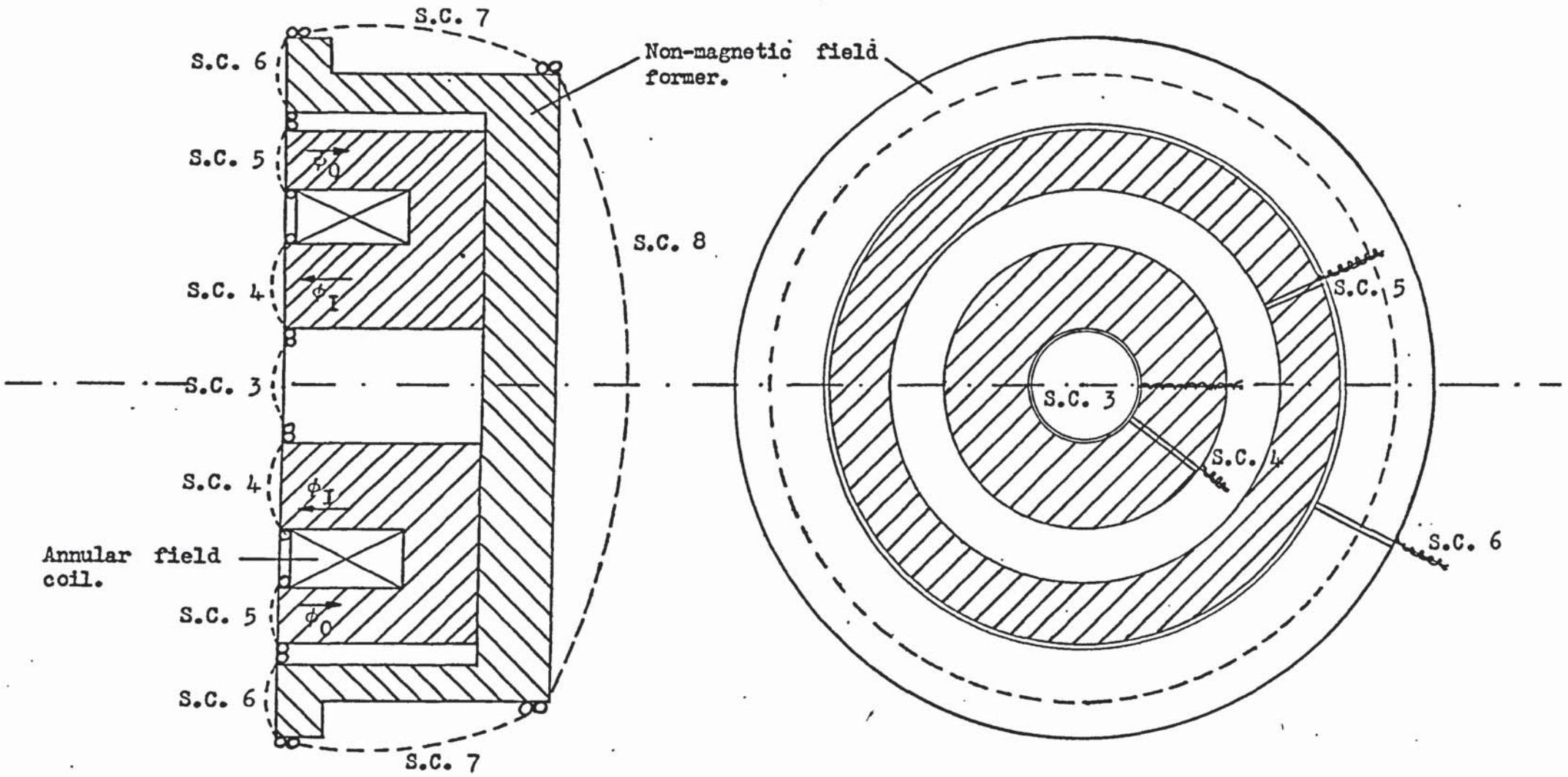

Search coil leads 40 S.W.G. copper wire (Lewmex).

Figure 4.10

ARRANGEMENT OF CURRENT DENSITY PROBES ON STATIONARY WATER COOLED LOSS MEMBER.

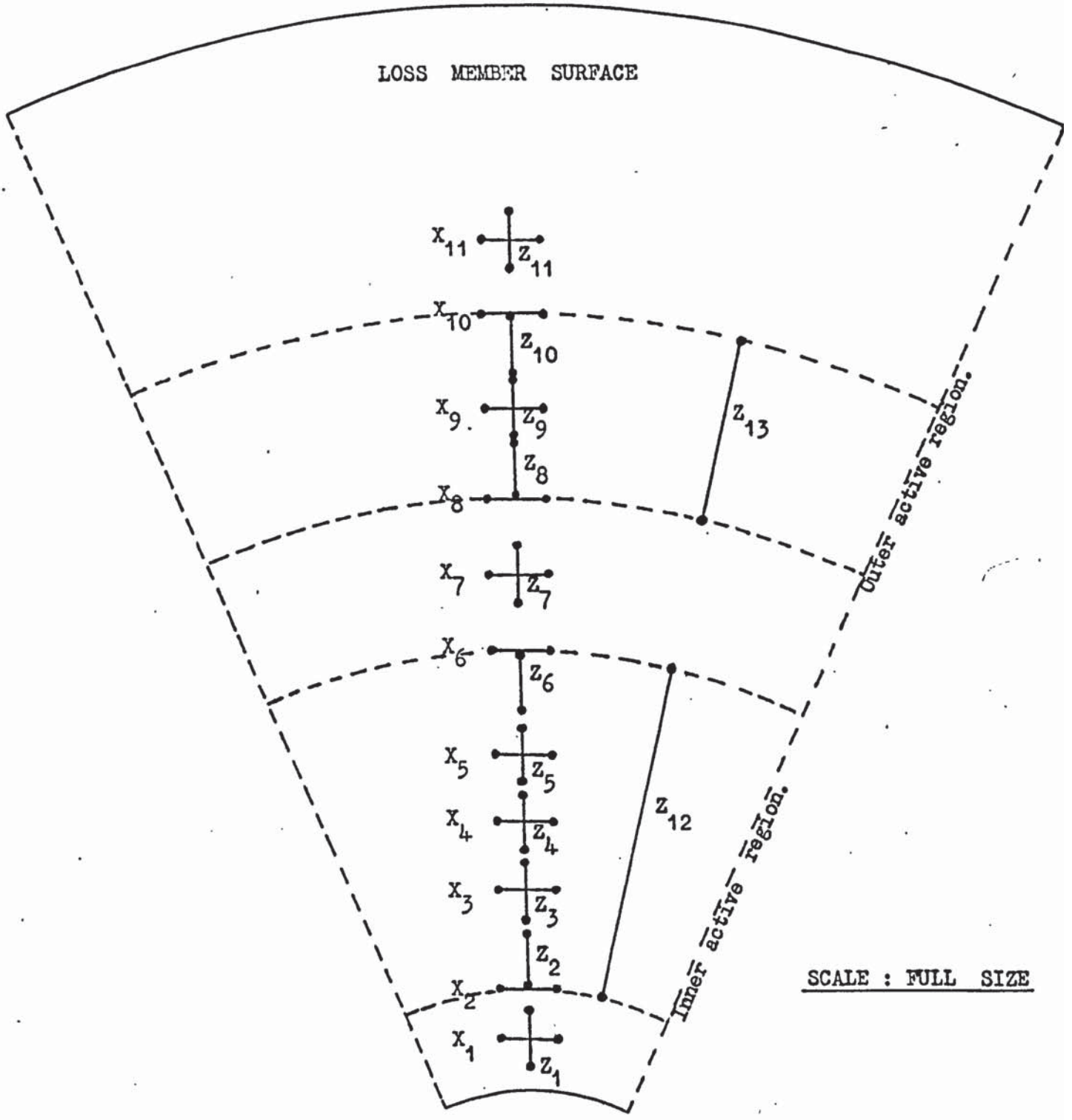

SCALE : FULL SIZE

Z : Radial probes measure Jr (Jz in cartesian coordinates.)

X : Peripheral probes measure Je (Jx in cartesian coordinates.)

Probe leads 42 S.W.G. nickel-copper (CONSTANTAN) wire, rayon covered.

Figure 4.12

FIGURES FOR CHAPTER 5.

STANDSTILL MAGNETISATION CURVES.

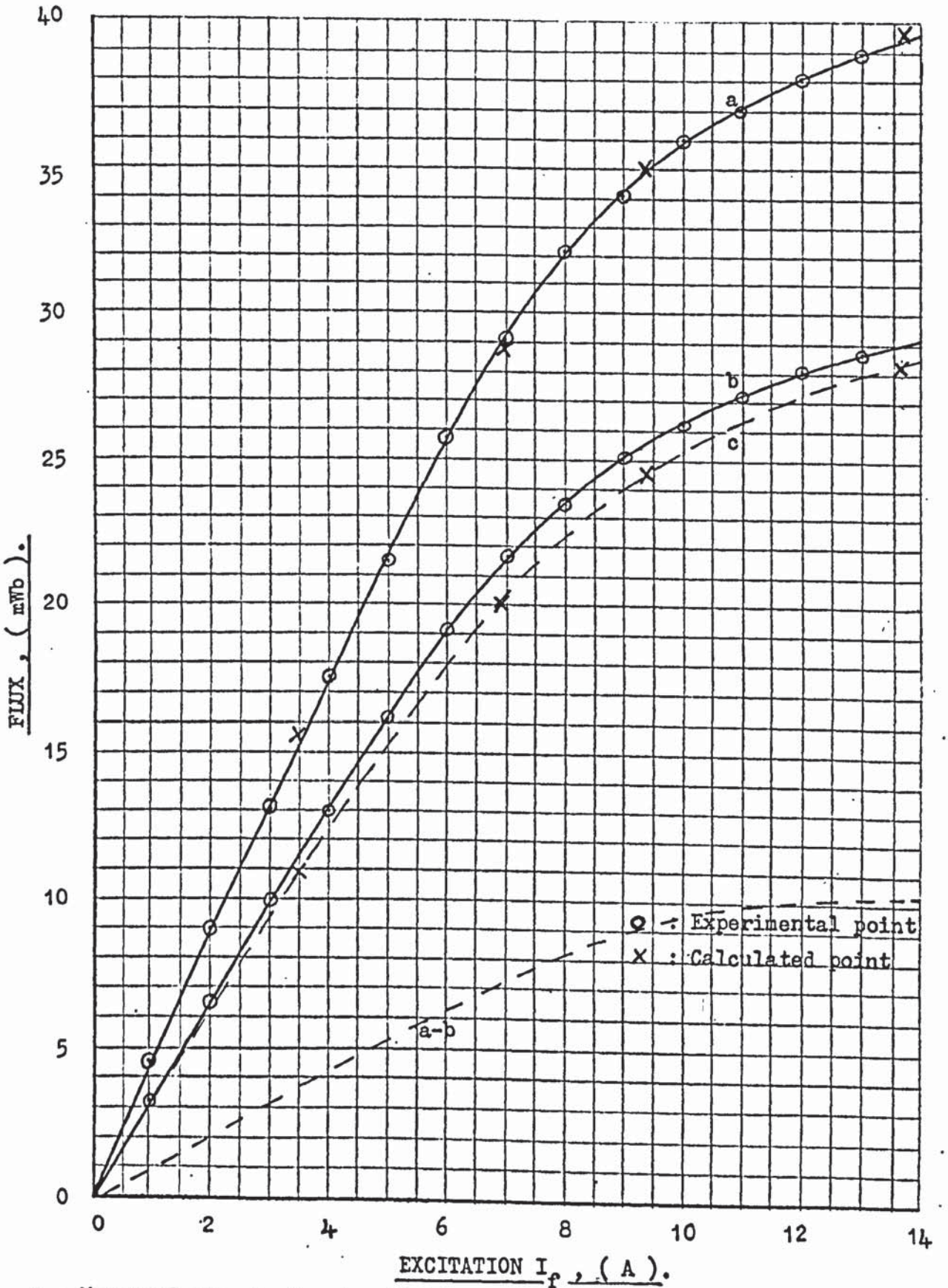

a : Measured flux ϕ_I leaving field member through inner laminated section ; calculated ϕ_I curve is not shown since it follows experimental curve.

b : Measured flux ϕ_o entering field member through outer laminated section.

c : Calculated curve of ϕ_o.

Figure 5.1

EXPERIMENTAL TORQUE - SLIP CURVES OF THE HIGH SPEED DYNAMOMETER.

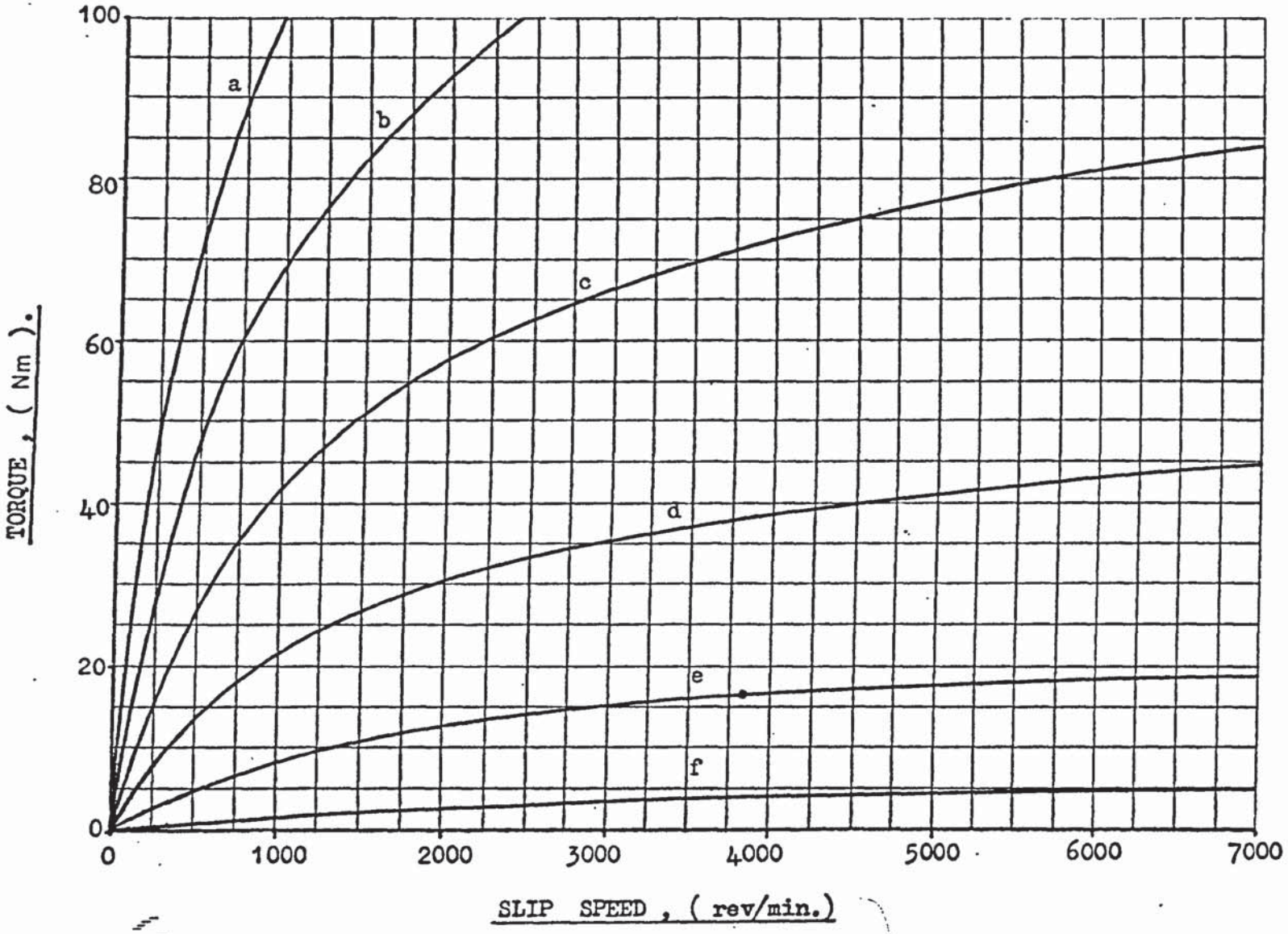

EXCITATION :

a : 6 A
b : 5 A
c : 4 A
d : 3 A
e : 2 A
f : 1 A

ACTIVE AIRGAP LENGTH :

g = 1 mm

For g = 0.5 mm (not shown) the excitation is halved for the same torque-speed curve.

Figure 5.3

TOTAL FLUX (ϕ_I) LEAVING THE INNER LAMINATED SECTION OF THE FIELD THROUGH SEARCH COIL 4 PLOTTED AGAINST EXCITATION (I_f) AT VARICUS SLIP SPEEDS .

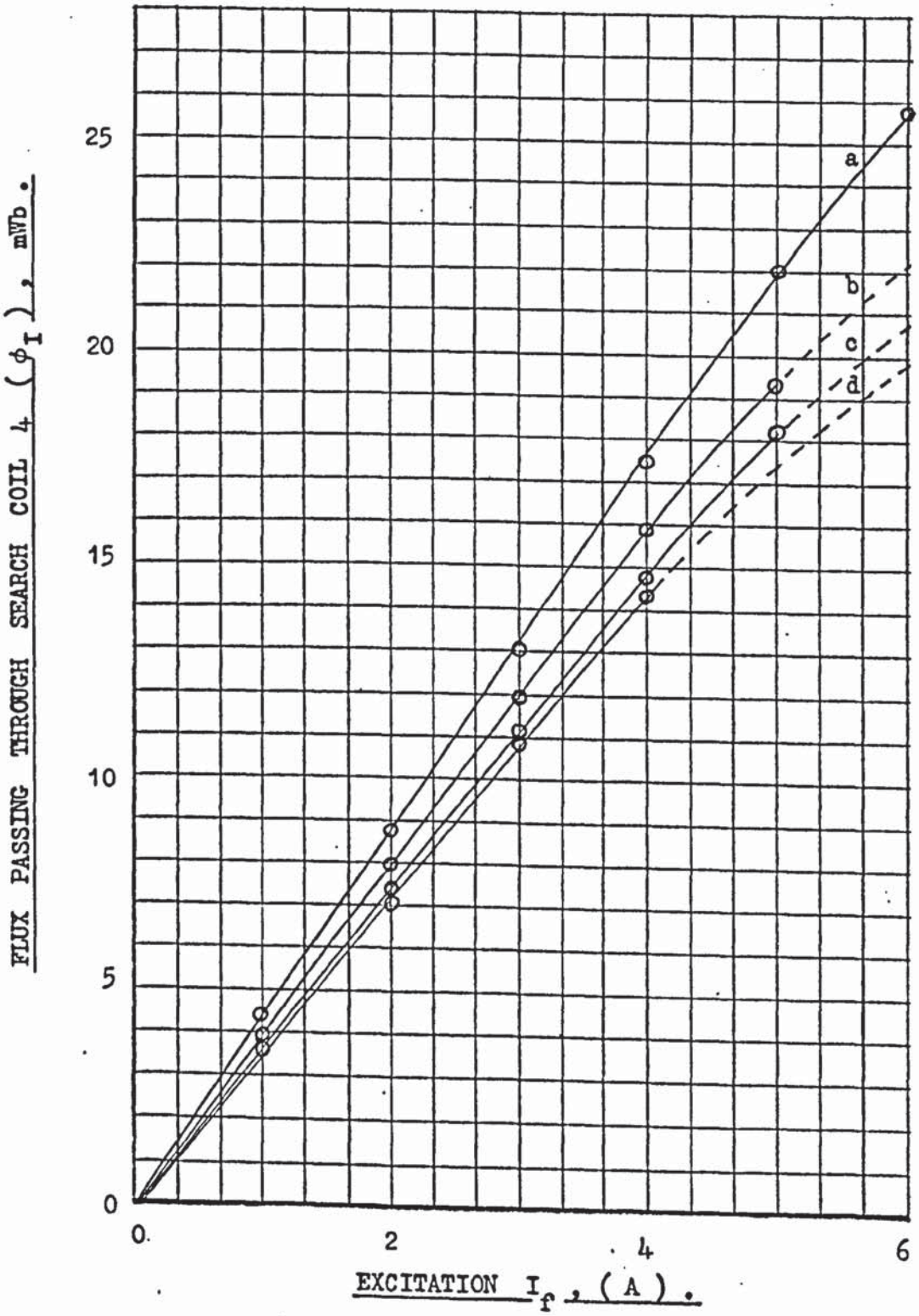

SLIP SPEEDS :

a : STANDSTILL.

b : 2000 rev/min.

c : 4000 rev/min.

d : 6000 rev/min.

Figure 5.4

FLUX (ϕ_o) ENTERING THE OUTER LAMINATED SECTION OF THE FIELD THROUGH SEARCH COIL 5 PLOTTED AGAINST EXCITATION (I_f) AT VARIOUS SLIP SPEEDS .

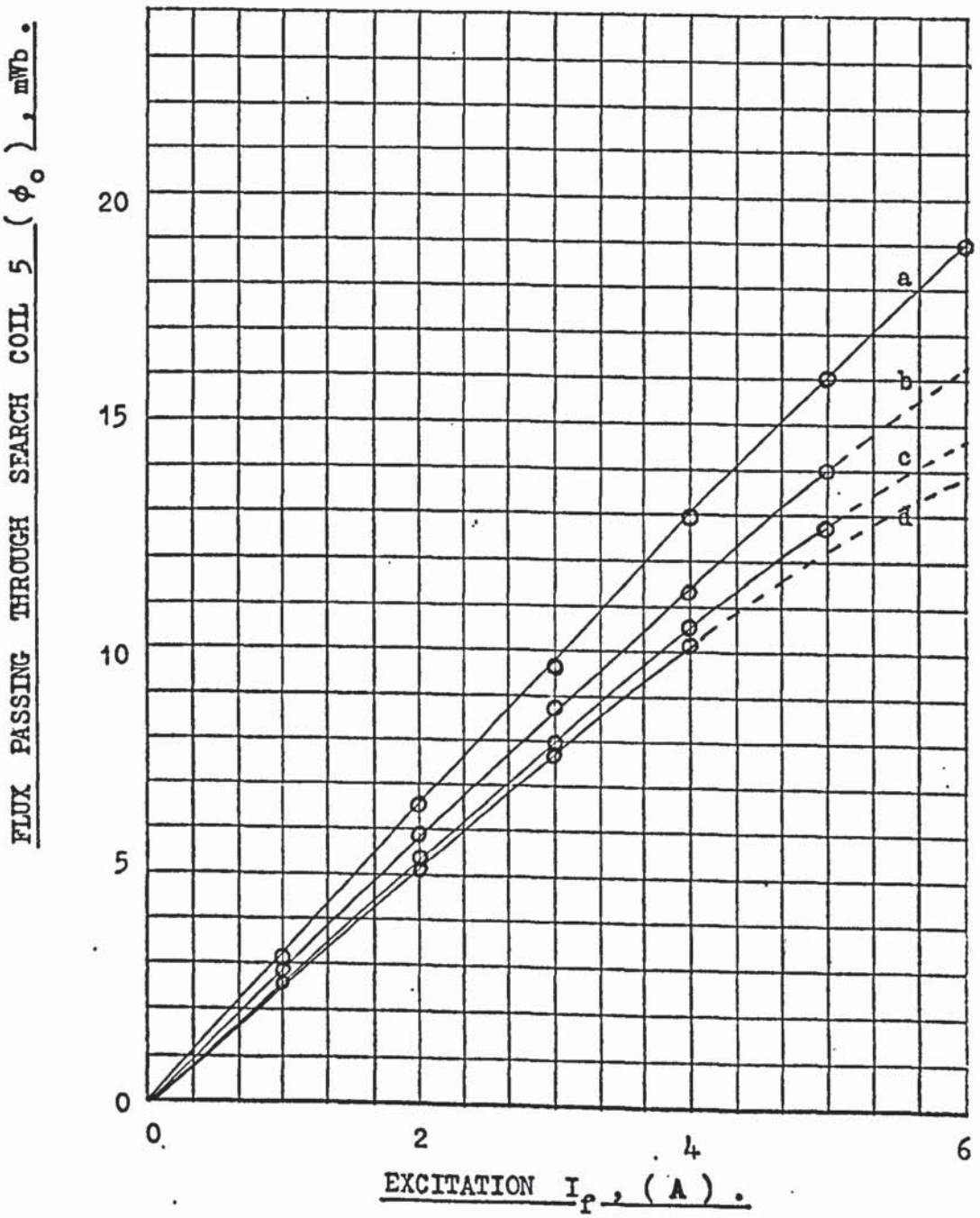

SLIP SPEEDS :

a : STANDSTILL.

b : 2000 rev/min.

c : 4000 rev/min.

d : 6000 rev/min.

Figure 5.5

LEAKAGE FLUXES (ϕ_L) THROUGH VARIOUS SECTIONS OF THE FIELD PLOTTED AGAINST EXCITATION (I_f) AT STANDSTILL.

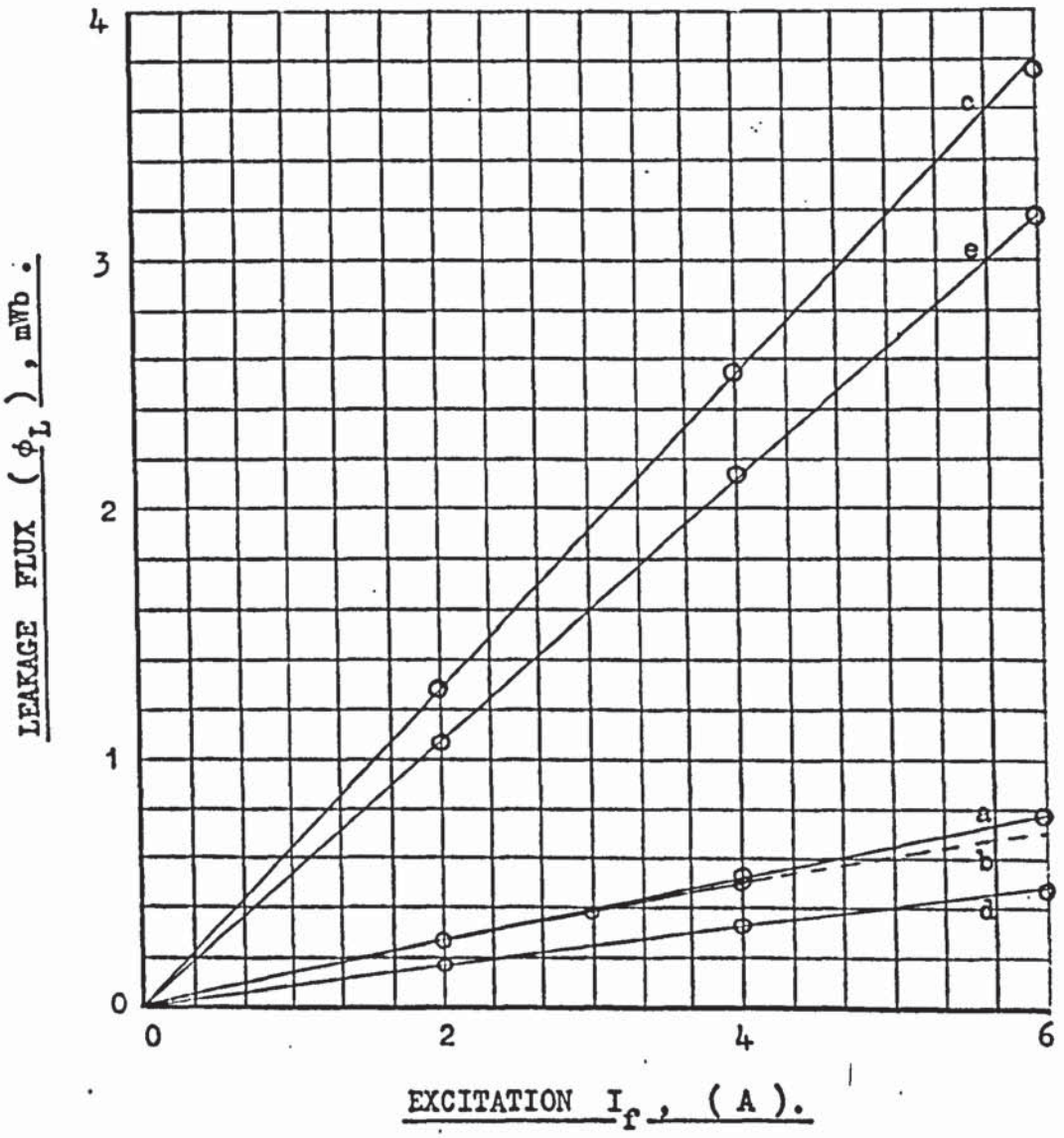

a : Shaft leakage flux through S.C. 3 at standstill.

b : Shaft leakage flux through S.C. 3 at 6000 rev/min.

c : Leakage flux through S.C. 6 at standstill.

d : Leakage flux through S.C. 7 at standstill.

e : Leakage flux through S.C. 8 at standstill.

Figure 5.6

TORQUE AGAINST EXCITATION (I_f) AND TOTAL FLUX (Φ_I) AT VARIOUS SLIP SPEEDS.

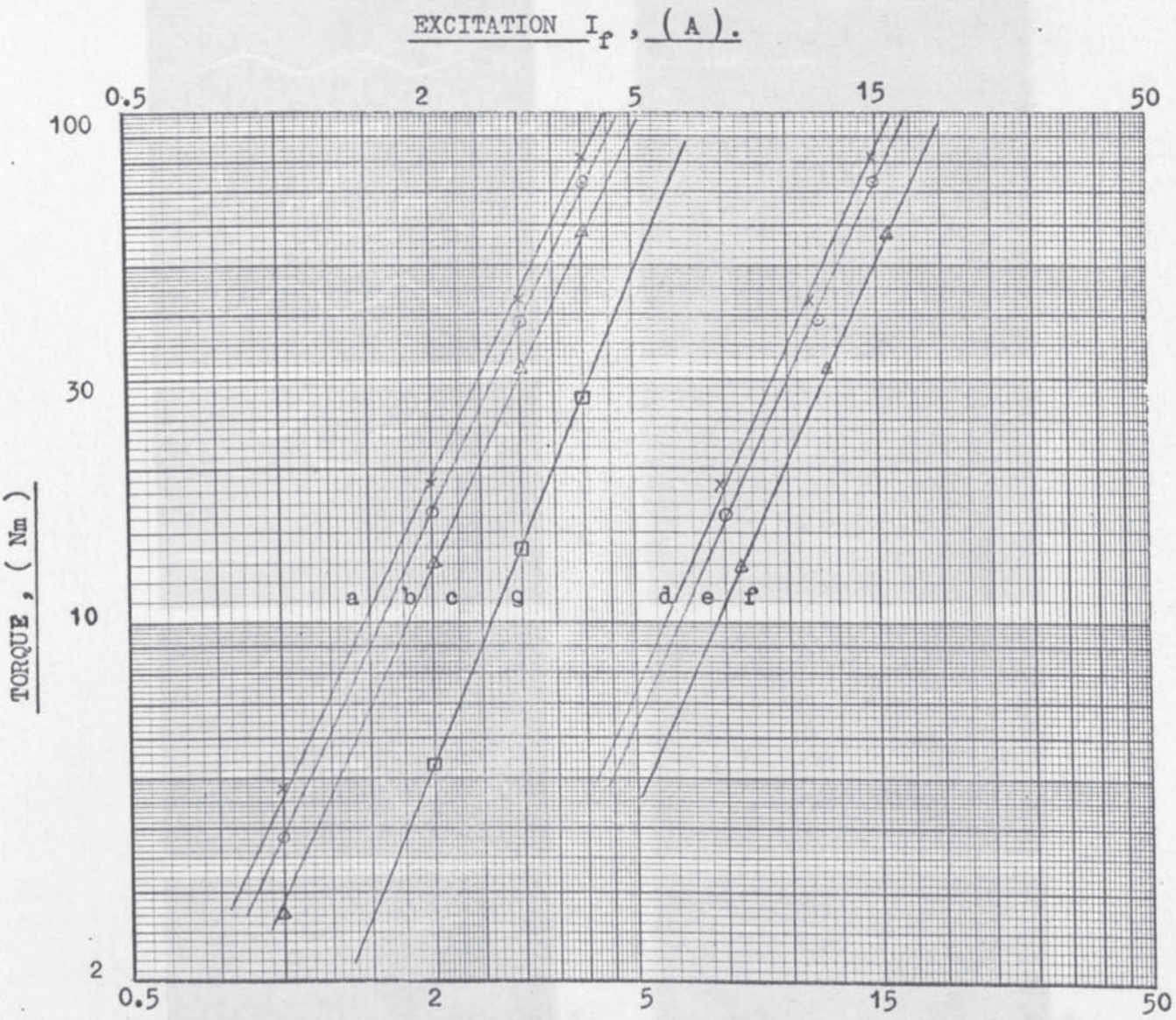

TORQUE - EXCITATION, I_f.

a : 6000 rev/min. , slope= 2.06

b : 4000 rev/min. , slope= 2.1

c : 2000 rev/min. , slope= 2.12

g : 500 rev/min. , slope= 2.36

TORQUE - TOTAL FLUX, Φ_I.

d : 6000 rev/min. , slope= 2.2

e : 4000 rev/min. , slope= 2.21

f : 2000 rev/min. , slope= 2.17

Figure 5.8

CURRENT DENSITY AMPLITUDES $f(J_z)$ AND $f(J_x)$ PLOTTED AGAINST DISTANCE ACROSS THE OUTER ACTIVE REGION AT VARIOUS SLIP SPEEDS.

EXCITATION : 2 A

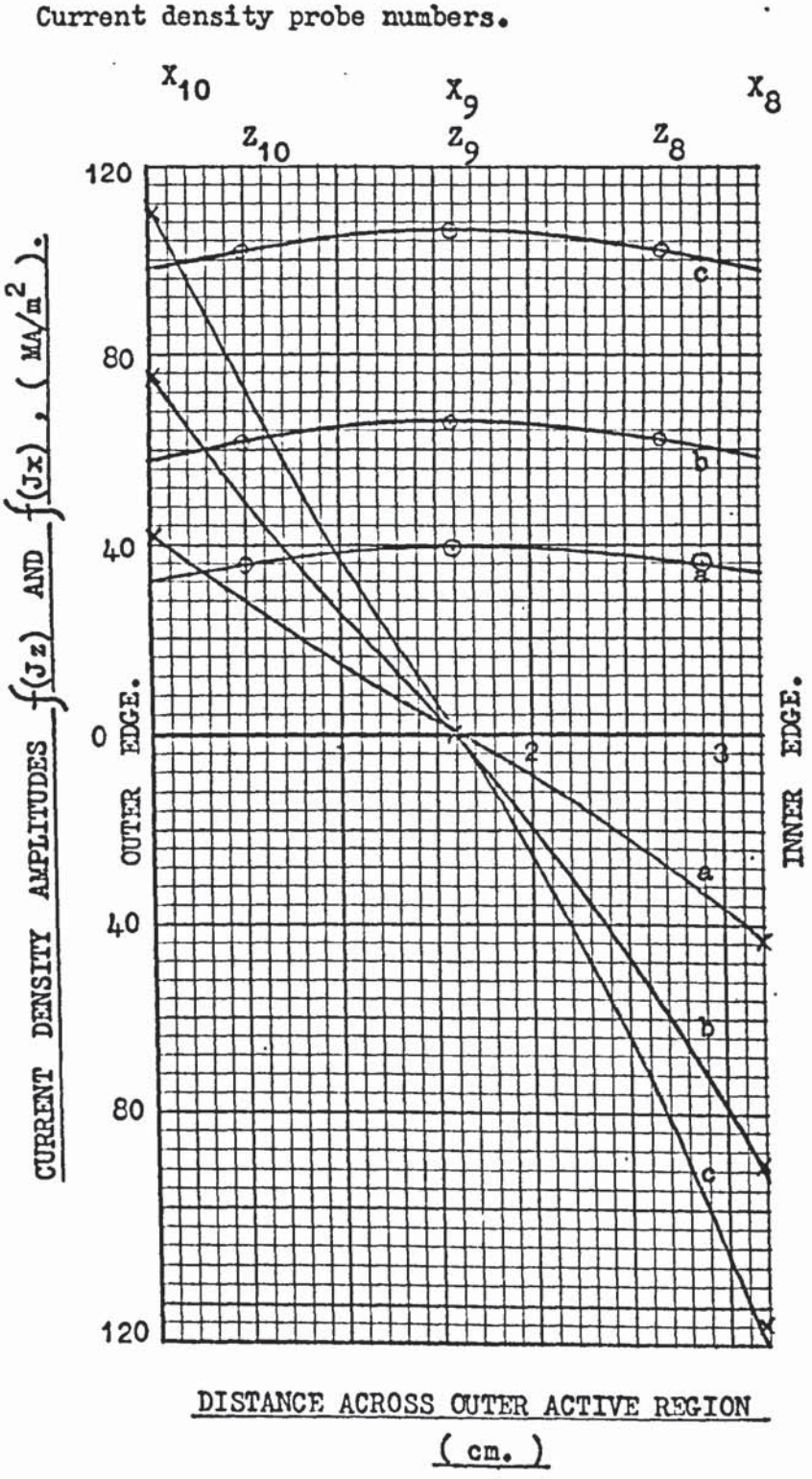

SLIP SPEEDS :

a : 2000 rev/min.

b : 4000 rev/min.

c : 6000 rev/min.

$\odot = f(J_z)$

$\times = f(J_x)$

Figure 5.16

CURRENT DENSITY AMPLITUDES $f(Jz)$ AND $f(Jx)$ PLOTTED AGAINST DISTANCE ACROSS THE INNER ACTIVE REGION AT VARIOUS SLIP SPEEDS.

EXCITATION : 2 A

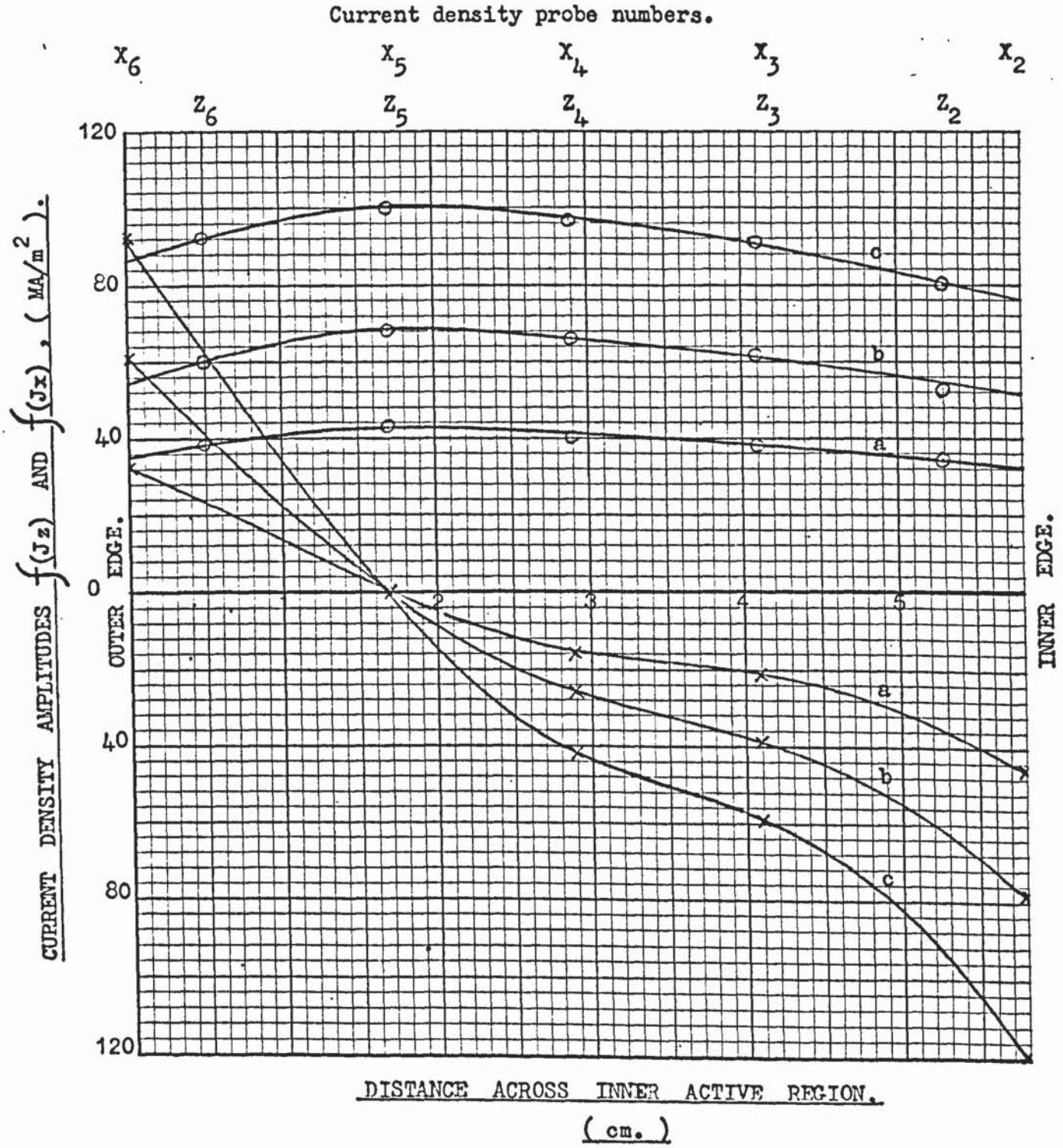

SLIP SPEEDS :

a : 2000 rev/min.

b : 4000 rev/min.

c : 6000 rev/min.

⊙ = $f(Jz)$

× = $f(Jx)$

Figure 5.17

CURRENT DENSITY AMPLITUDES $f(Jz)$ AND $f(Jx)$ PLOTTED AGAINST DISTANCE ACROSS THE OUTER ACTIVE REGION AT VARIOUS SLIP SPEEDS.

EXCITATION : 4 A

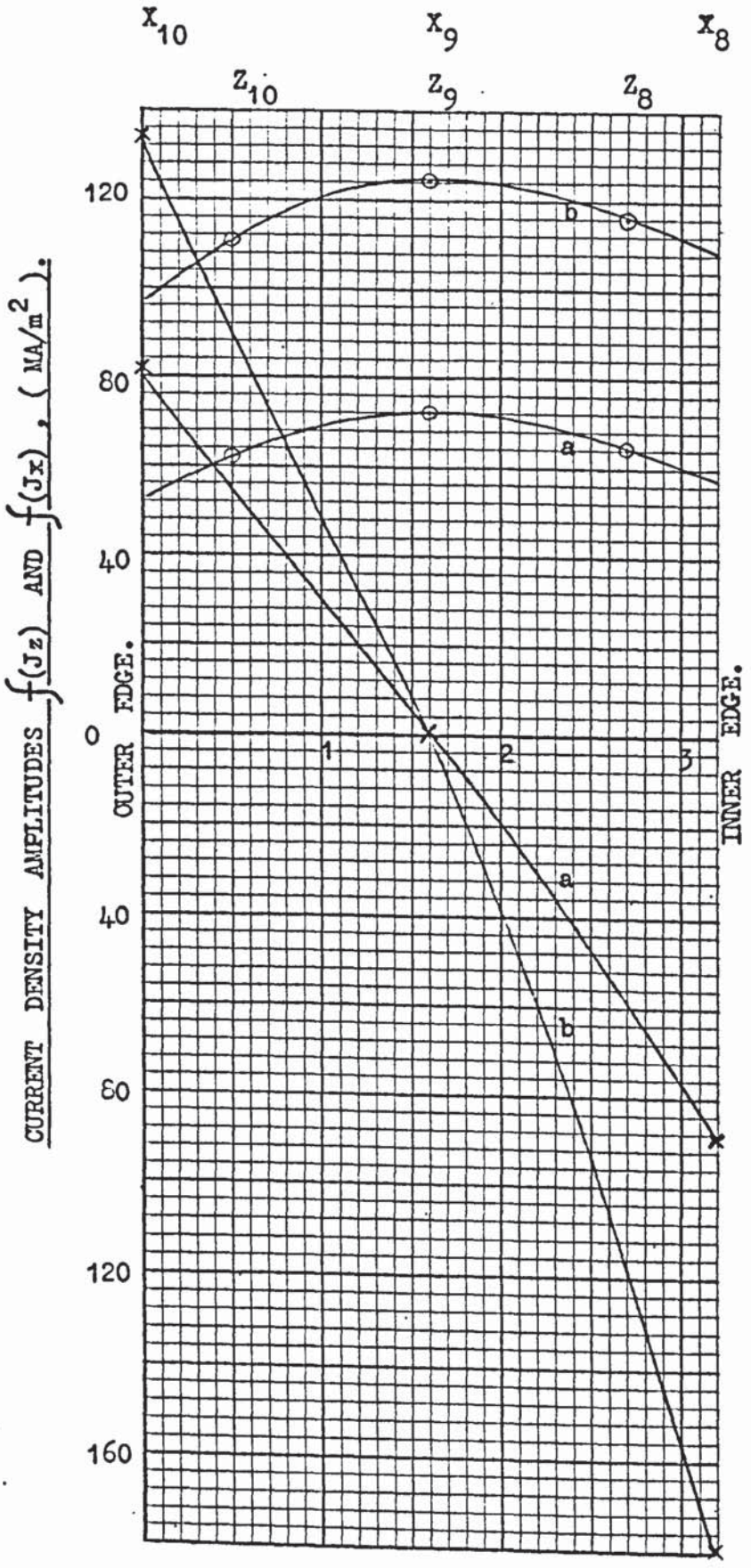

SLIP SPEEDS :

a : 2000 rev/min.

b : 4000 rev/min.

⊙ = $f(Jz)$

× = $f(Jx)$

Figure 5.18

CURRENT DENSITY AMPLITUDES $f(Jz)$ AND $f(Jx)$ PLOTTED AGAINST DISTANCE ACROSS THE INNER ACTIVE REGION AT VARIOUS SLIP SPEEDS.

EXCITATION : 4 A

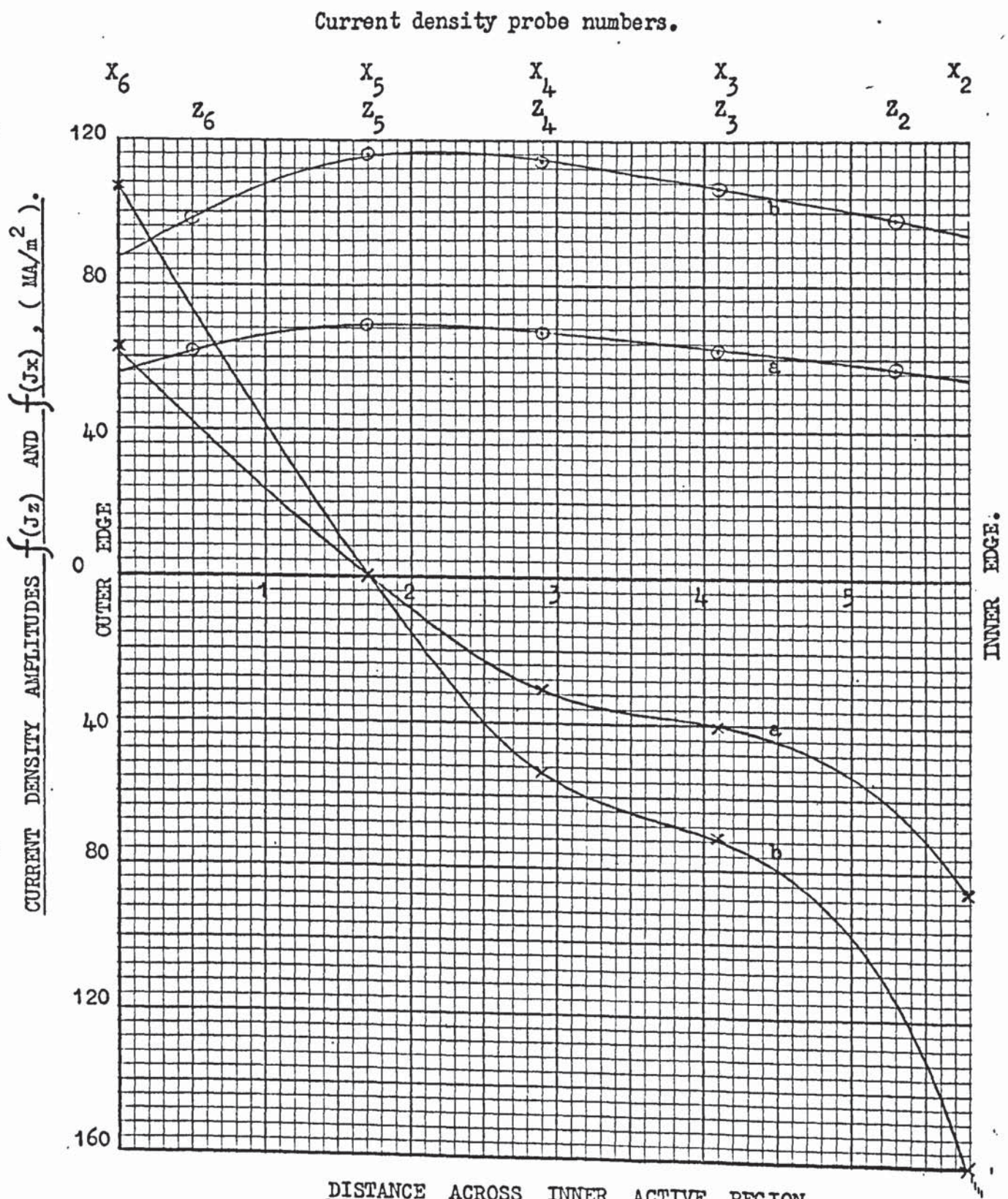

SLIP SPEEDS :

a : 2000 rev/min.

b : 4000 rev/min.

$\circ = f(Jz)$

$\times = f(Jx)$

Figure 5.19

PEAK TO PEAK VALUES OF THE END REGION CURRENT DENSITY WAVES PLOTTED AGAINST FREQUENCY AT VARIOUS EXCITATIONS.

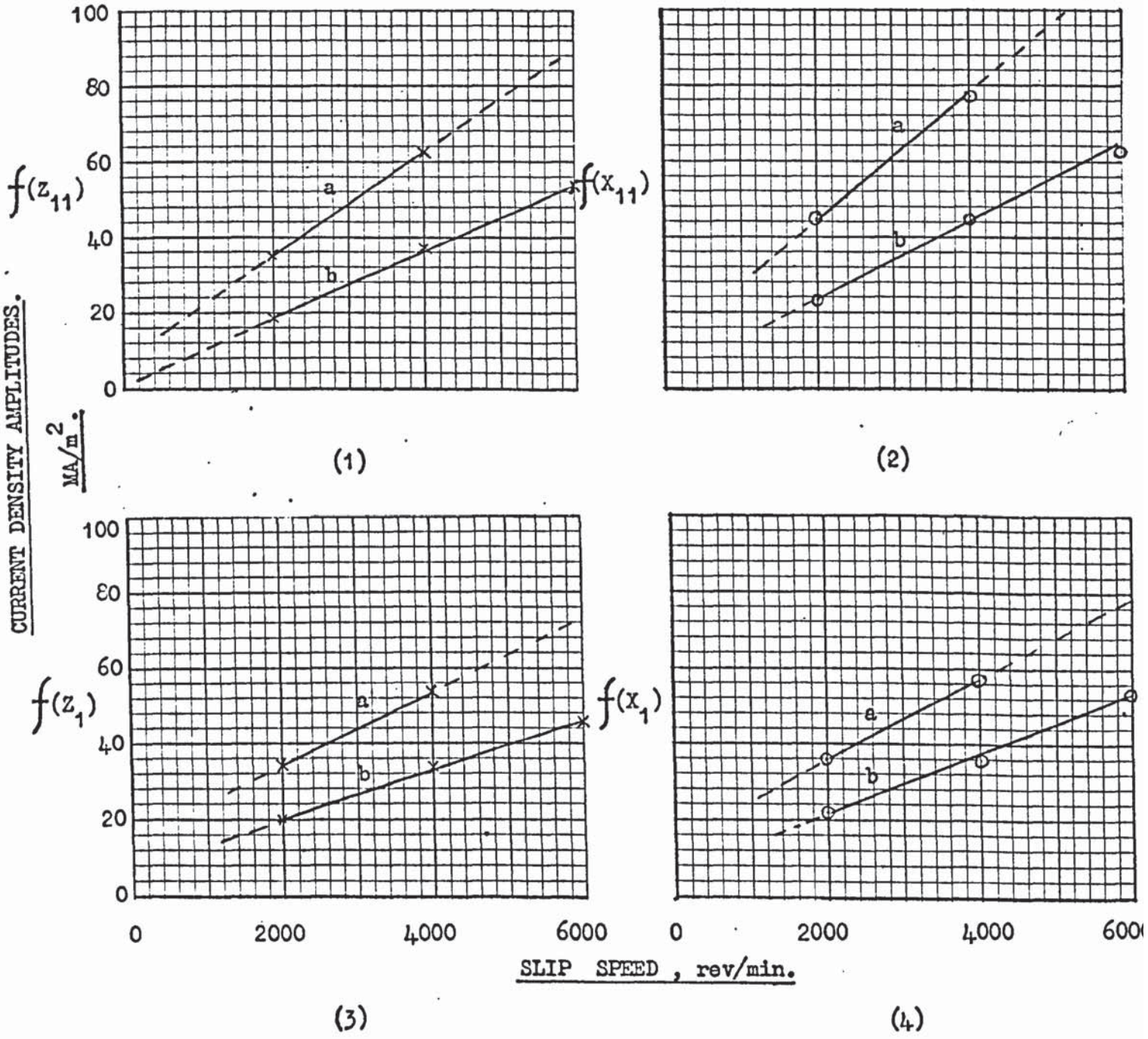

EXCITATION :

a : 2 A

b : 4 A

Figure 5.20

FLUX - DENSITY DISTRIBUTION AT THE LOSS MEMBER SURFACE AT VARIOUS SLIP SPEEDS CONSTRUCTED USING THE EXPERIMENTAL RESULTS FROM CURRENT DENSITY PROBE Z-13 AND FULL PITCH SEARCH COIL 2.

EXCITATION : 2 A (310 AT/tooth outer approx.)

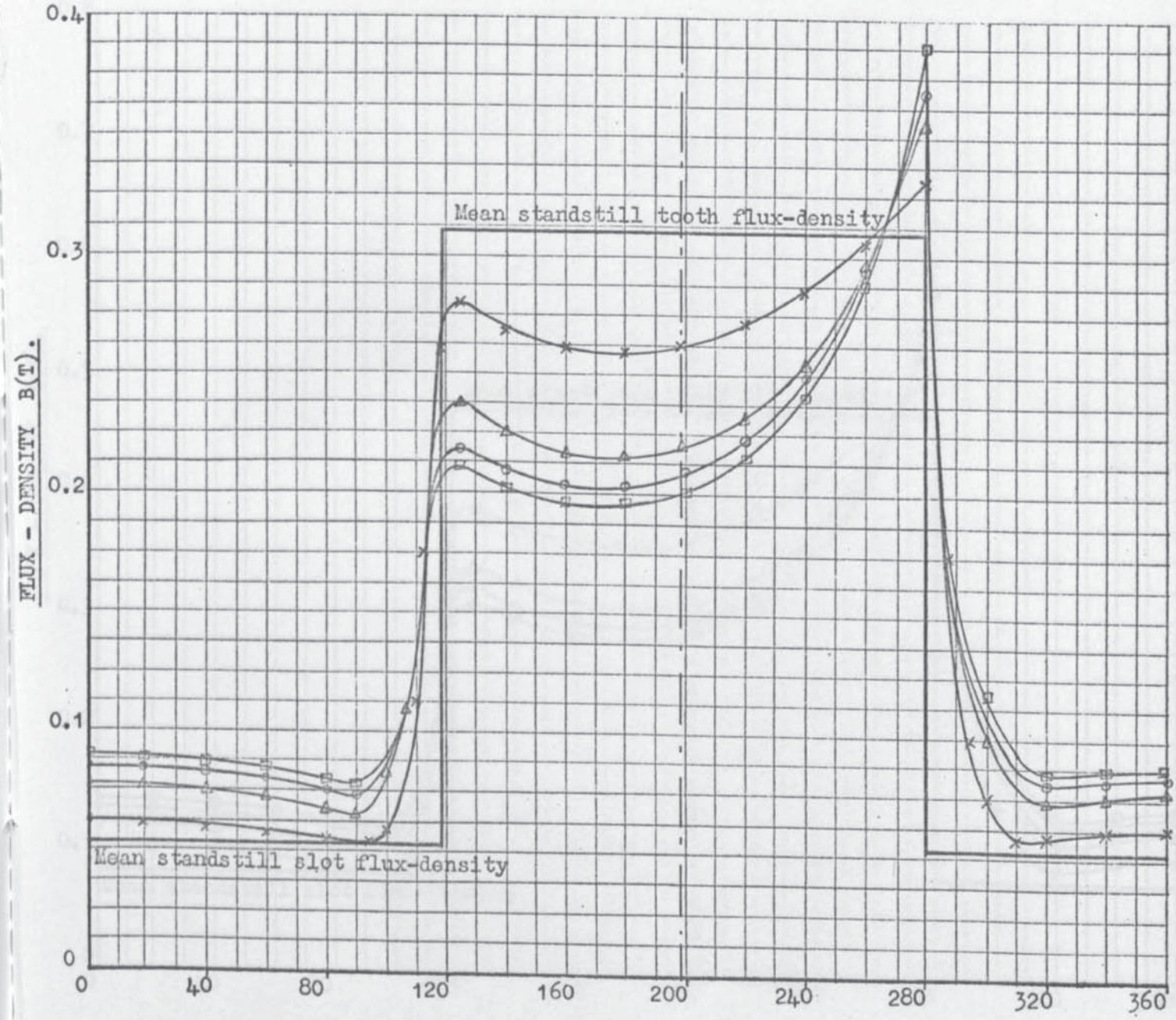

SLIP SPEEDS :

× : 500 rev/min.

△ : 2000 rev/min.

⊙ : 4000 rev/min.

⊡ : 6000 rev/min.

NOTE : Plotted points have no significance except for identification see Figures 5.21 to 5.24.

Figure 5.26

FLUX - DENSITY DISTRIBUTION AT THE LOSS MEMBER SURFACE AT VARIOUS SLIP SPEEDS CONSTRUCTED USING THE EXPERIMENTAL RESULTS FROM CURRENT DENSITY PROBE Z-13 AND FULL PITCH SEARCH COIL 2.

EXCITATION : 3 A (465 AT/tooth outer approx.)

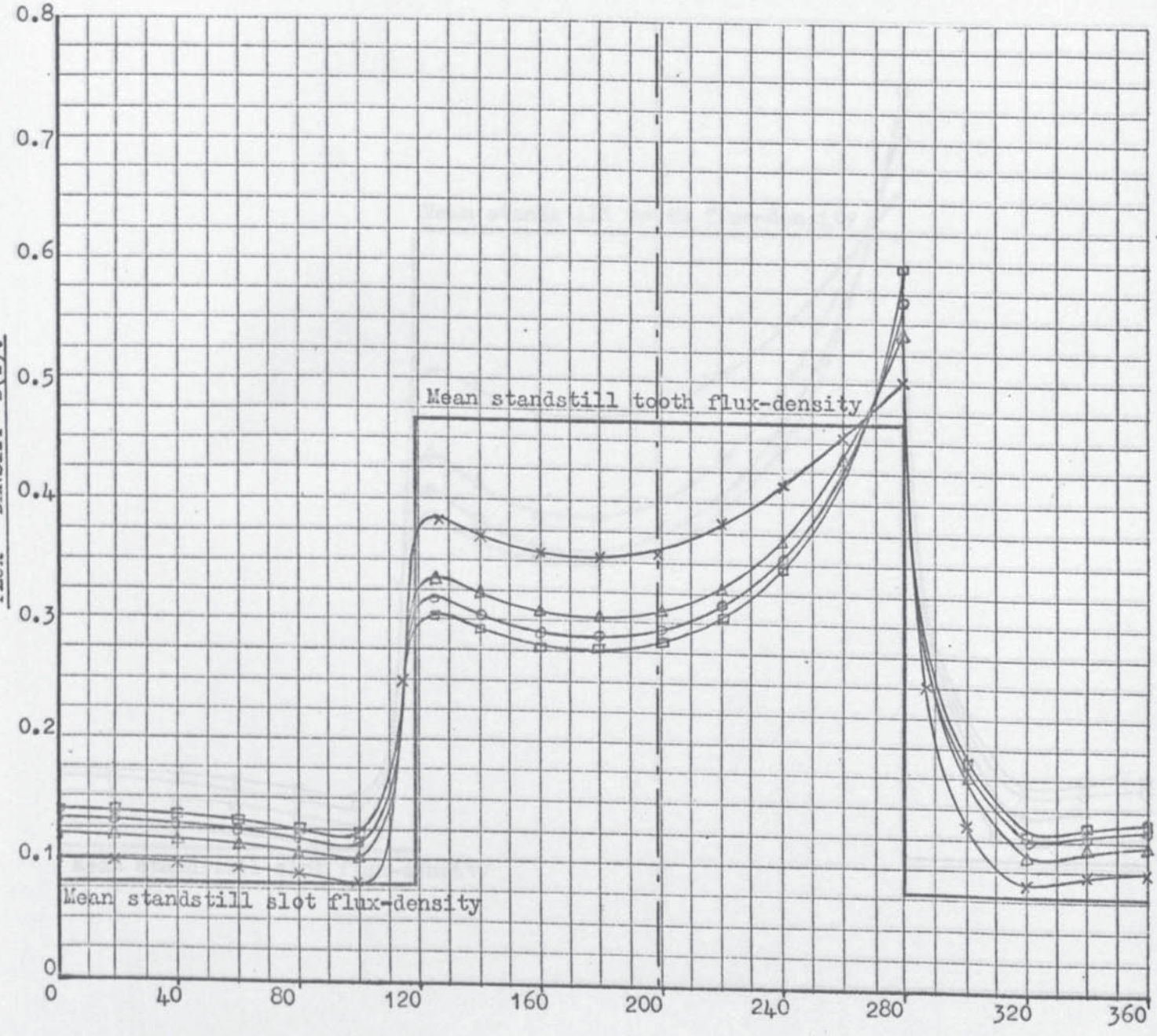

SLIP SPEEDS :

× : 500 rev/min.

△ : 2000 rev/min.

⊙ : 4000 rev/min.

⊡ : 6000 rev/min.

NOTE : Plotted points have no significance except for identification see Figures 5.21 to 5.24.

Figure 5.27

FLUX - DENSITY DISTRIBUTION AT THE LOSS MEMBER SURFACE AT VARIOUS SLIP SPEEDS CONSTRUCTED USING THE EXPERIMENTAL RESULTS FROM CURRENT DENSITY PROBE Z-13 AND FULL PITCH SEARCH COIL 2.

EXCITATION : 4 A (620 AT/tooth outer approx.)

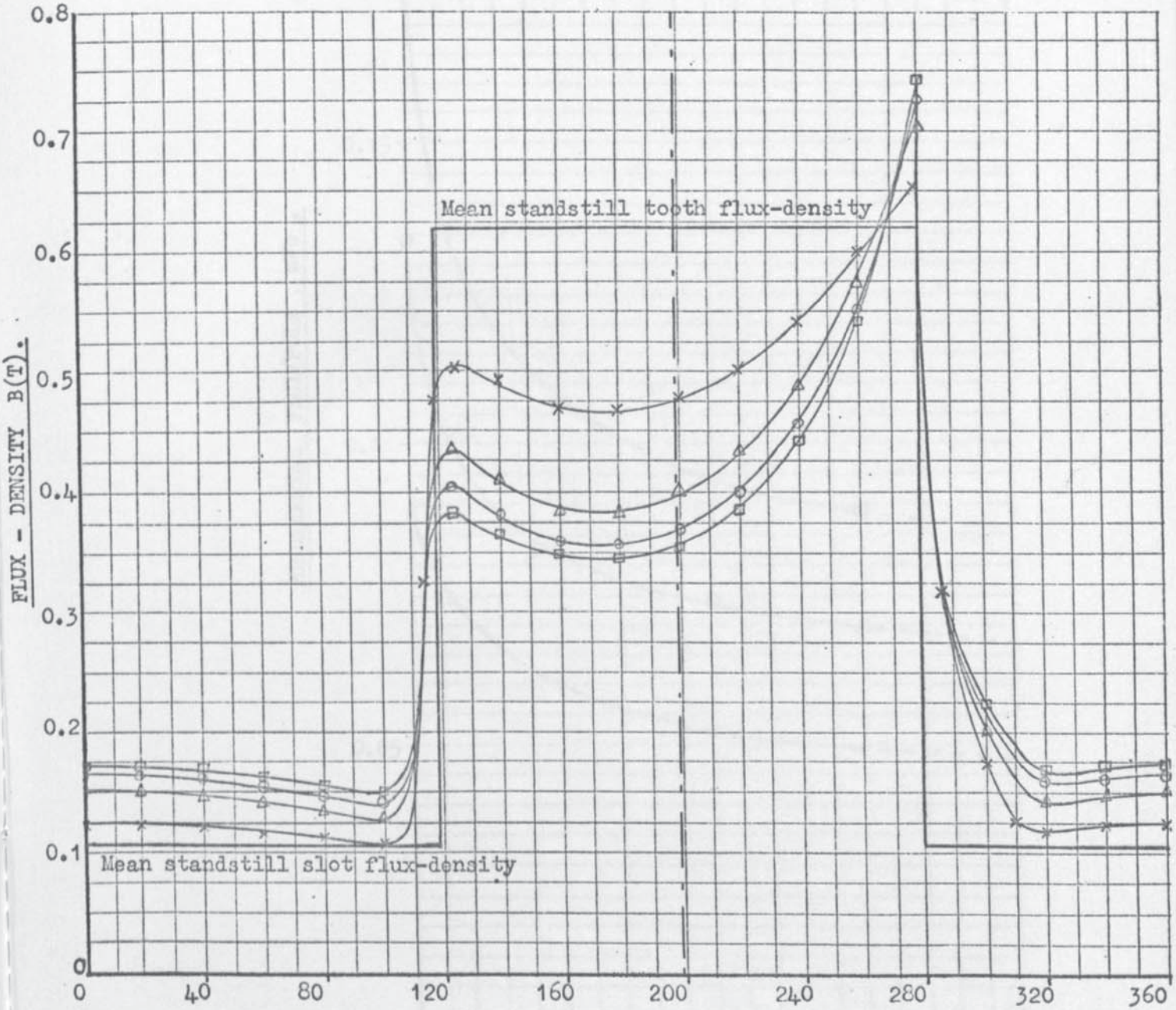

SLIP SPEEDS :

X : 500 rev/min.

△ : 2000 rev/min.

⊙ : 4000 rev/min.

⊡ : 6000 rev/min.

NOTE : Plotted points have no significance except for identification see Figures 5.21 to 5.24.

Figure 5.28

FUNDAMENTAL FLUX/POLE AGAINST SLIP SPEED AT VARIOUS EXCITATIONS.

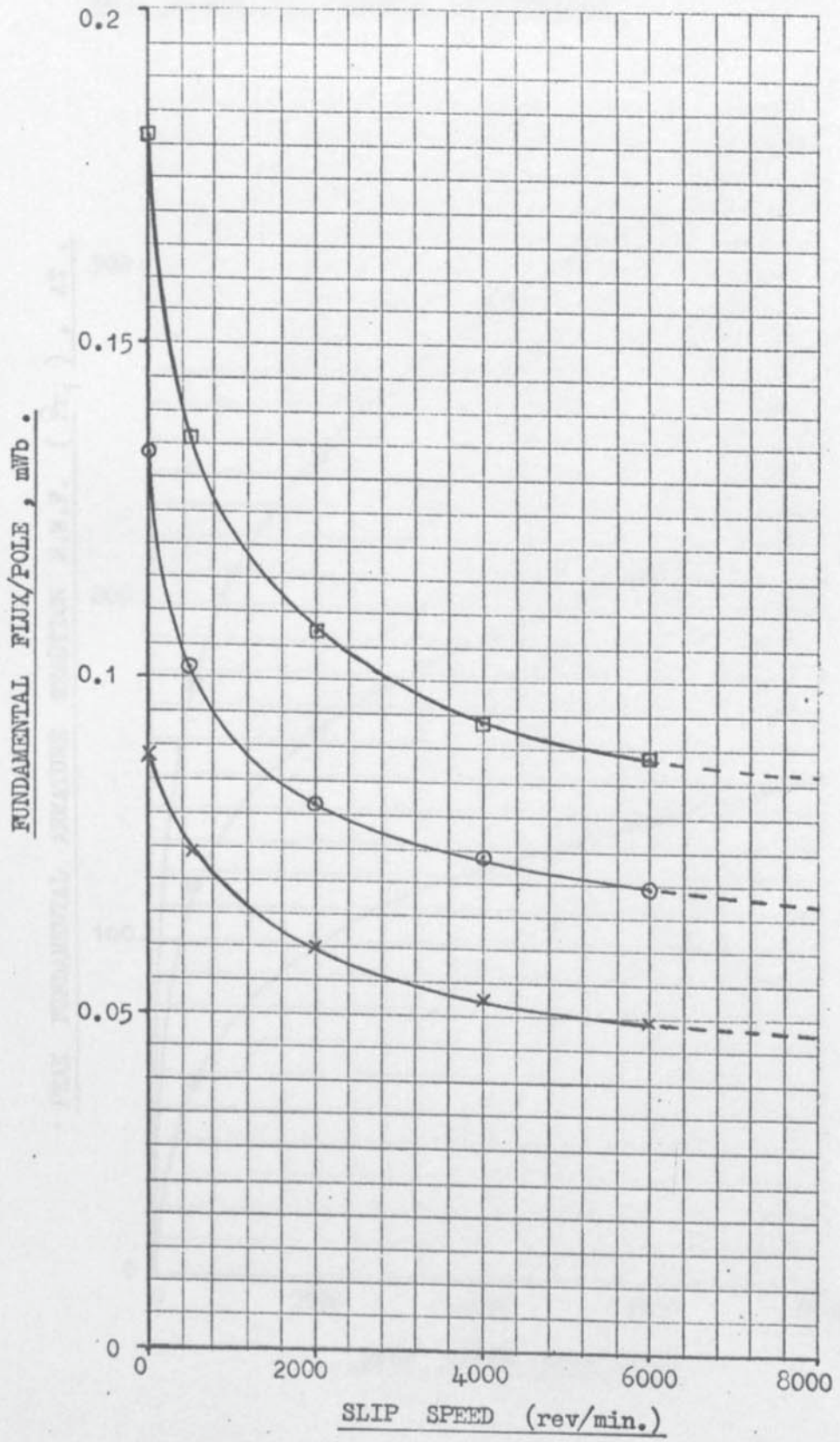

EXCITATIONS :

× : 2 A

⊙ : 3 A

⊡ : 4 A

NOTE : ϕac_1 is for the outer region only.

Figure 5.29

PEAK FUNDAMENTAL ARMATURE REACTION M.M.F. AGAINST SLIP SPEED AT VARIOUS EXCITATIONS.

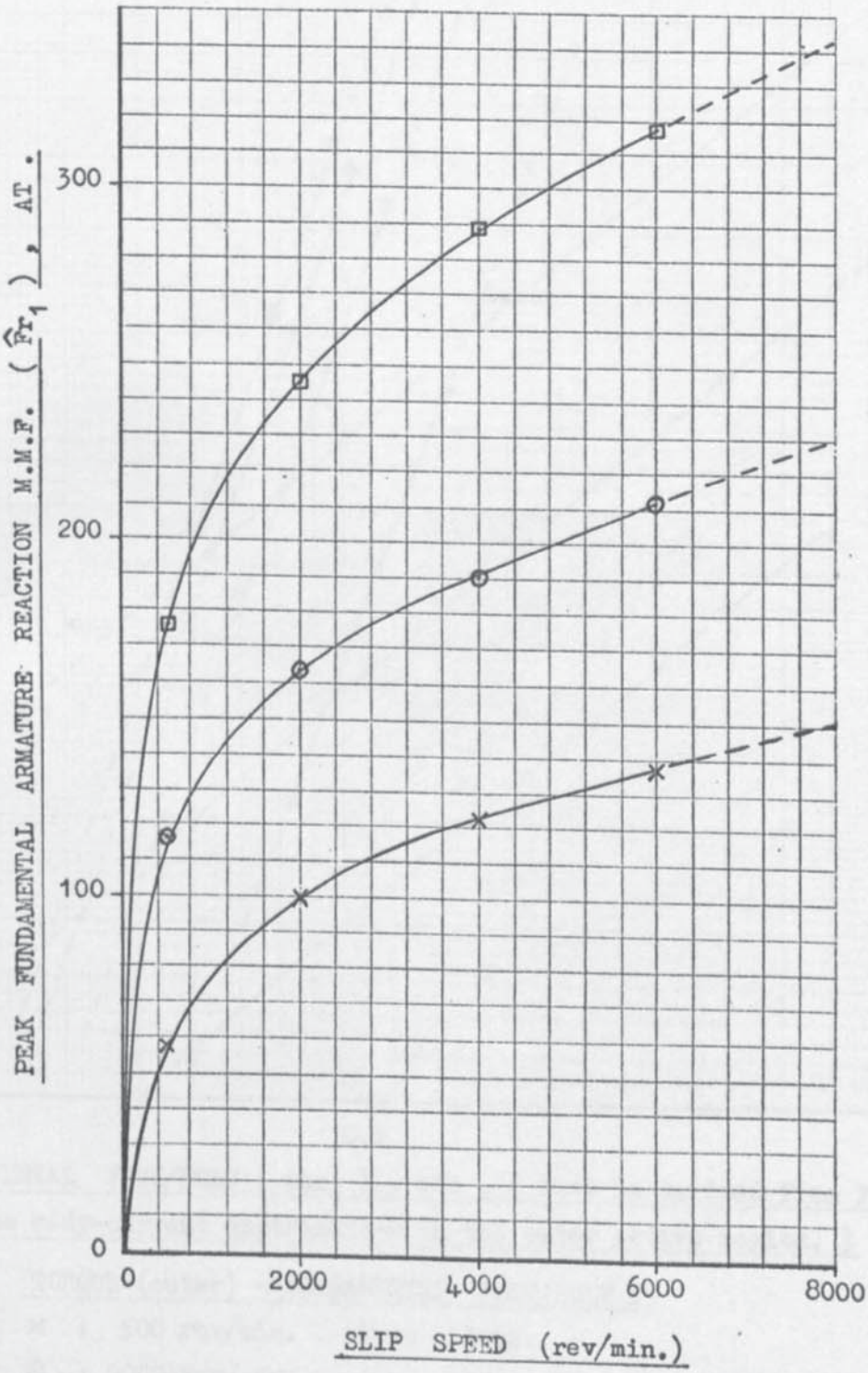

EXCITATIONS :

× : 2 A

⊙ : 3 A

⊡ : 4 A

NOTE : $\hat{F}r_1$ is for the outer region only.

Figure 5.30

VARIATION OF TORQUE (outer) WITH FLUX AT CONSTANT SLIP AND SLIP AT CONSTANT FLUX .

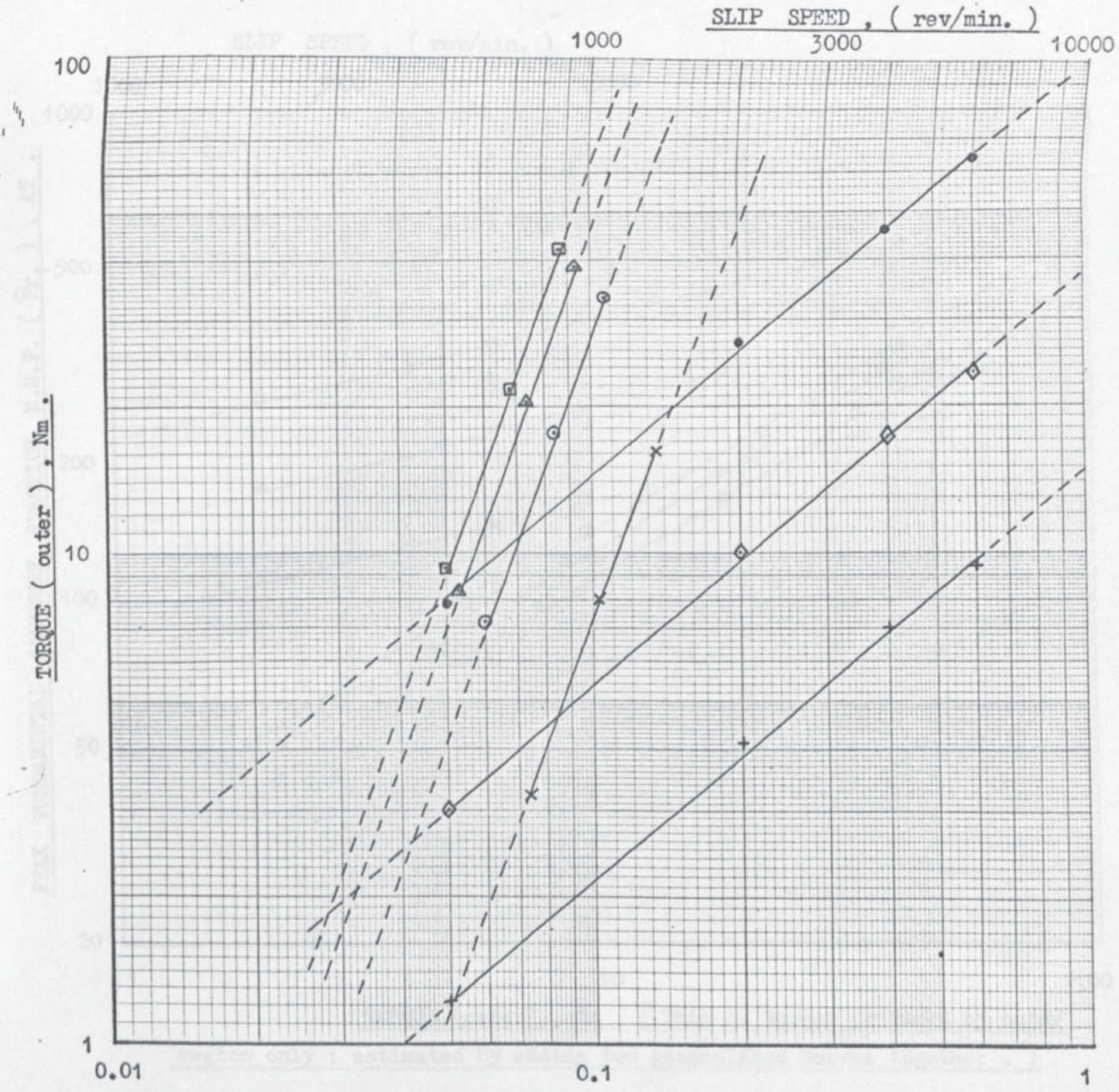

TORQUE (outer) - FUNDAMENTAL FLUX/POLE .

× : 500 rev/min. , slope = 2.64.

⊙ : 2000 rev/min. , slope = 2.71.

△ : 4000 rev/min. , slope = 2.75.

⊡ : 6000 rev/min. , slope = 2.78.

TORQUE (outer) - SLIP SPEED .

\+ : 0.05 mWb , slope = 0.83.

◈ : 0.07 mWb , slope = 0.83.

● : 0.1 mWb , slope = 0.85.

Figure 5.31

VARIATION OF MEASURED PEAK FUNDAMENTAL ARMATURE REACTION WITH TORQUE AT CONSTANT SLIP AND SLIP AT CONSTANT TORQUE .

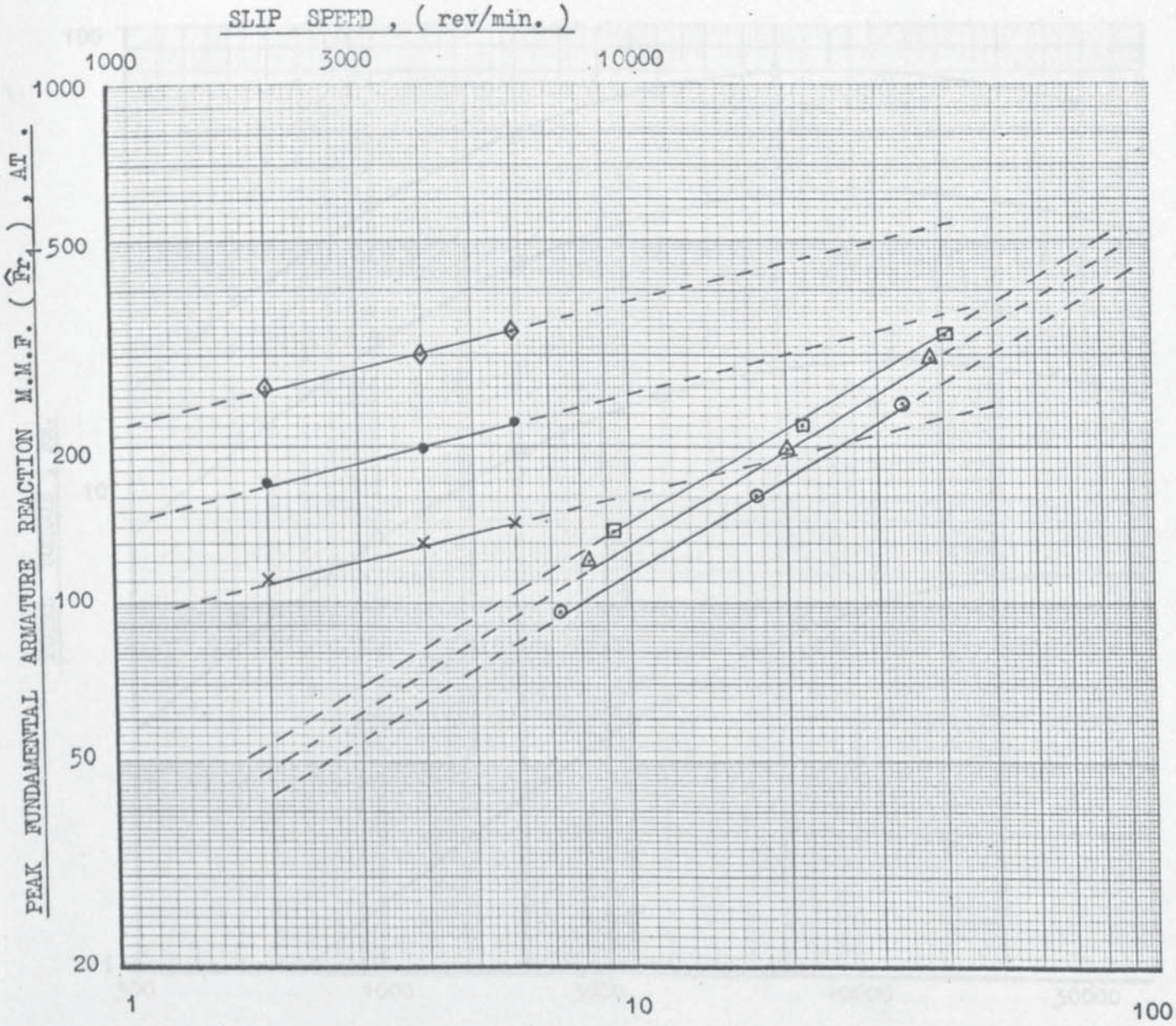

PEAK FUNDAMENTAL ARMATURE REACTION - TORQUE (outer).

⊙ : 2000 rev/min. , slope = 0.60 .

△ : 4000 rev/min. , slope = 0.61 .

⊡ : 6000 rev/min. , slope = 0.61 .

PEAK FUNDAMENTAL ARMATURE REACTION - SLIP SPEED.

× : 10 Nm , slope = 0.25 .

● : 20 Nm , slope = 0.25 .

◇ : 40 Nm , slope = 0.25 .

(NOTE : $\hat{F}r_1$ is for the outer region only.)

Figure 5.32

COMPARISON OF THE GENERALISED TORQUE - SLIP CURVE WITH THE EXPERIMENTAL CURVES.

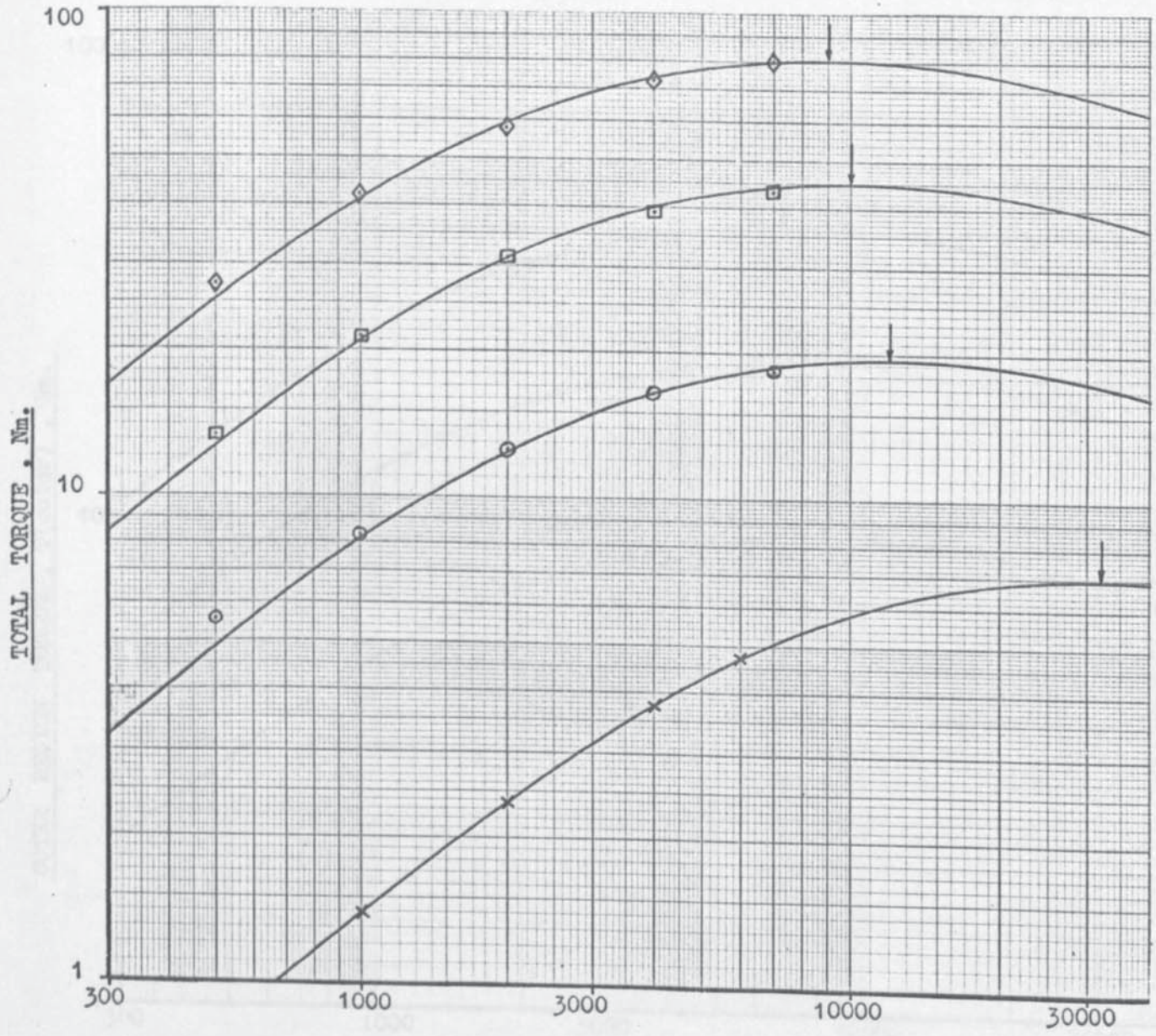

——— : DAVIES GENERALISED CURVE , m = 0.77 , $\phi = 45^{\circ}$.

EXCITATION :

× : 1 A

⊙ : 2 A

⊡ : 3 A

◇ : 4 A

Figure 5.33

COMPARISON OF THE ESTIMATED OUTER REGION TORQUE - SLIP CURVES WITH THE GENERALISED CURVE.

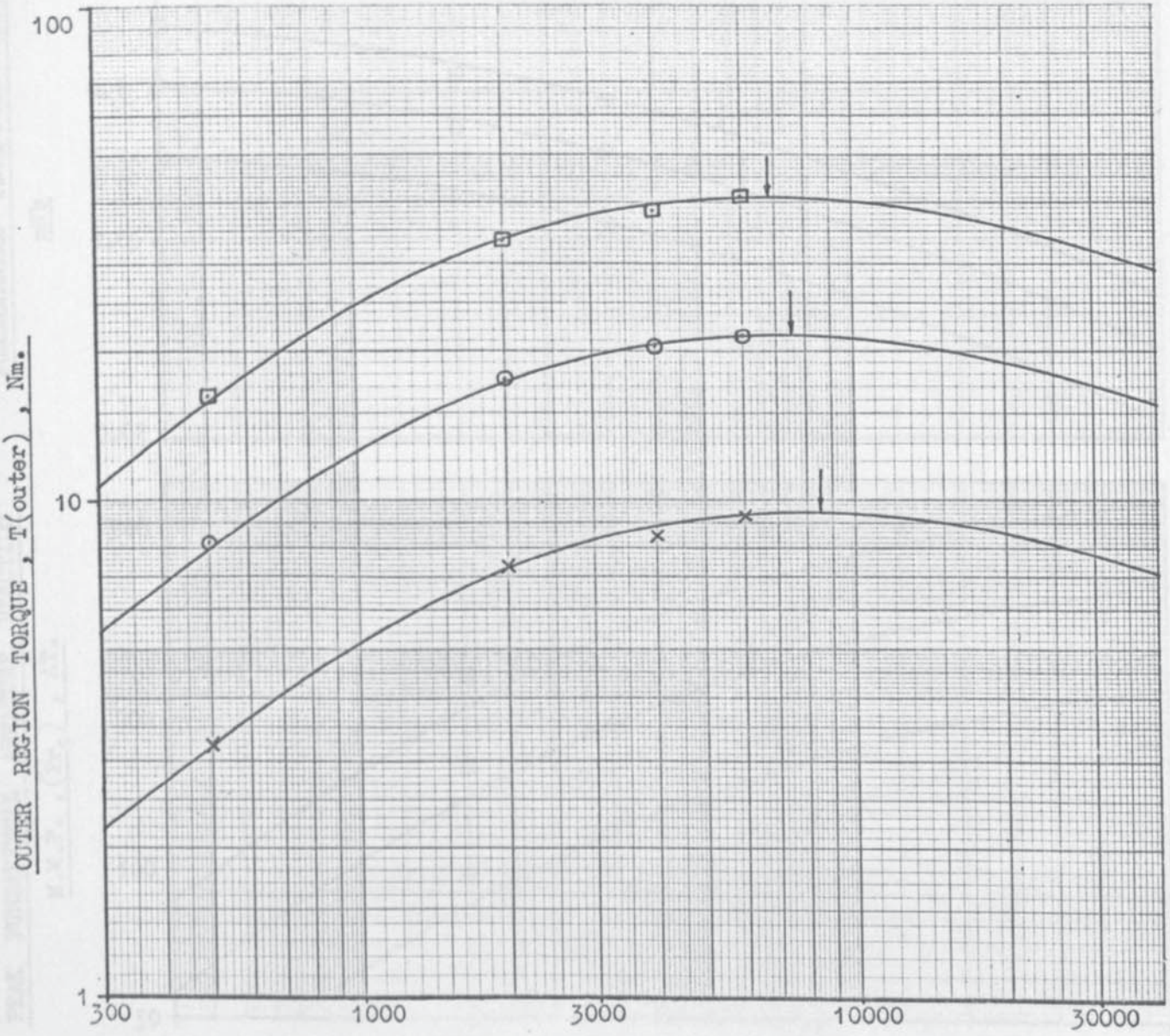

——— : DAVIES GENERALISED CURVE , m = 0.77 , $\phi = 45^{\circ}$.

EXCITATION :

× : 2 A

⊙ : 3 A

◈ : 4 A

Figure 5.34

COMPARISON OF THE PEAK FUNDAMENTAL ARMATURE REACTION M.M.F. AND FUNDAMENTAL FLUX/POLE GENERALISED CURVES WITH THE EXPERIMENTAL RESULTS.

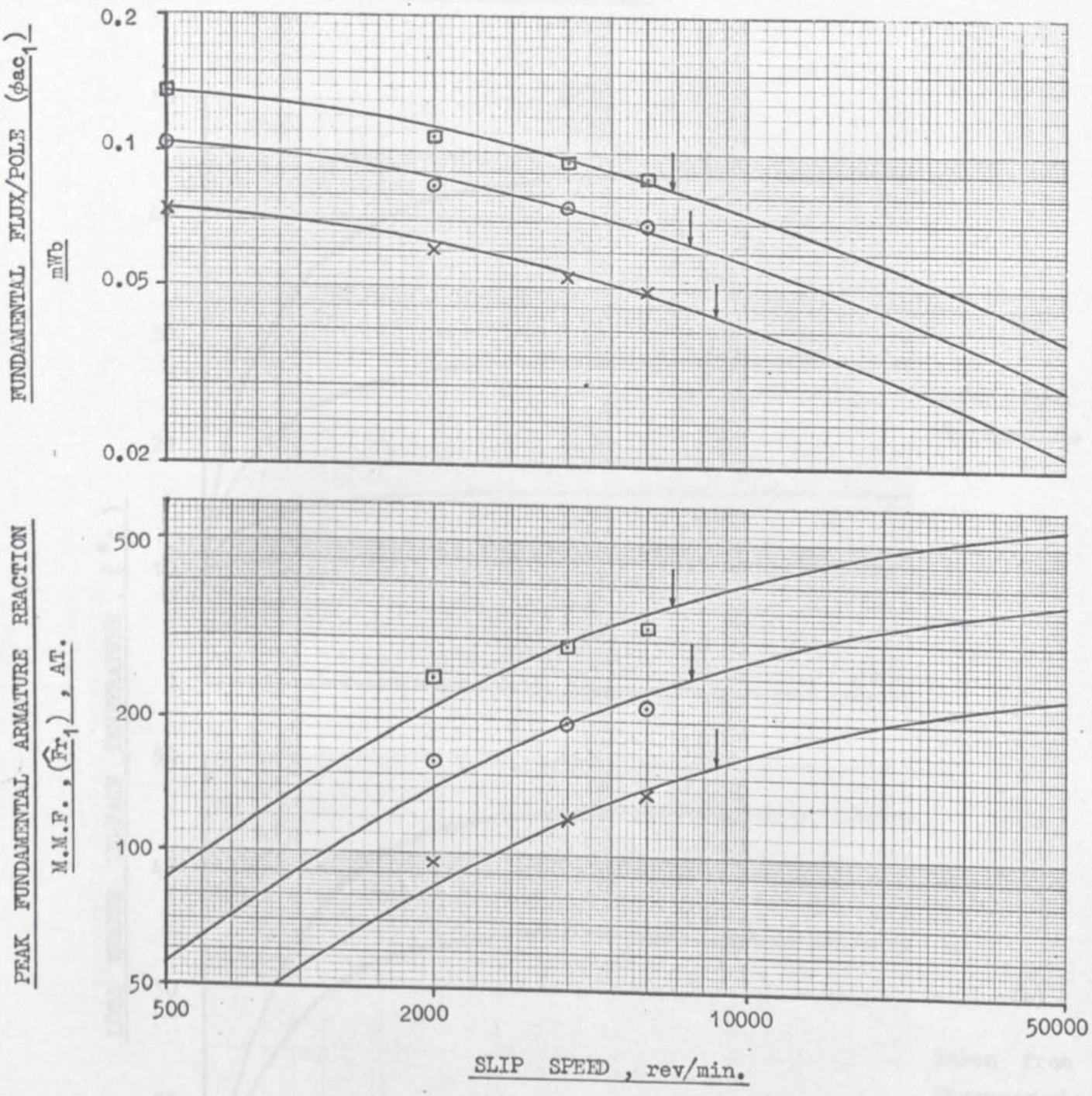

NOTE : The measured values of $\hat{F}r_1$ and ϕac_1 are from the outer region only.

——— : DAVIES GENERALISED CURVE , m = 0.77 , $\phi = 45^\circ$.

EXCITATION :

× : 2 A

⊙ : 3 A

◈ : 4 A

Figure 5.35

LOSS MEMBER SURFACE TEMPERATURE AGAINST TIME AT CONSTANT SLIP SPEED AND VARIOUS EXCITATIONS AND A COOLING WATER THROUGHPUT OF Q = 27 LITRES/MINUTE.

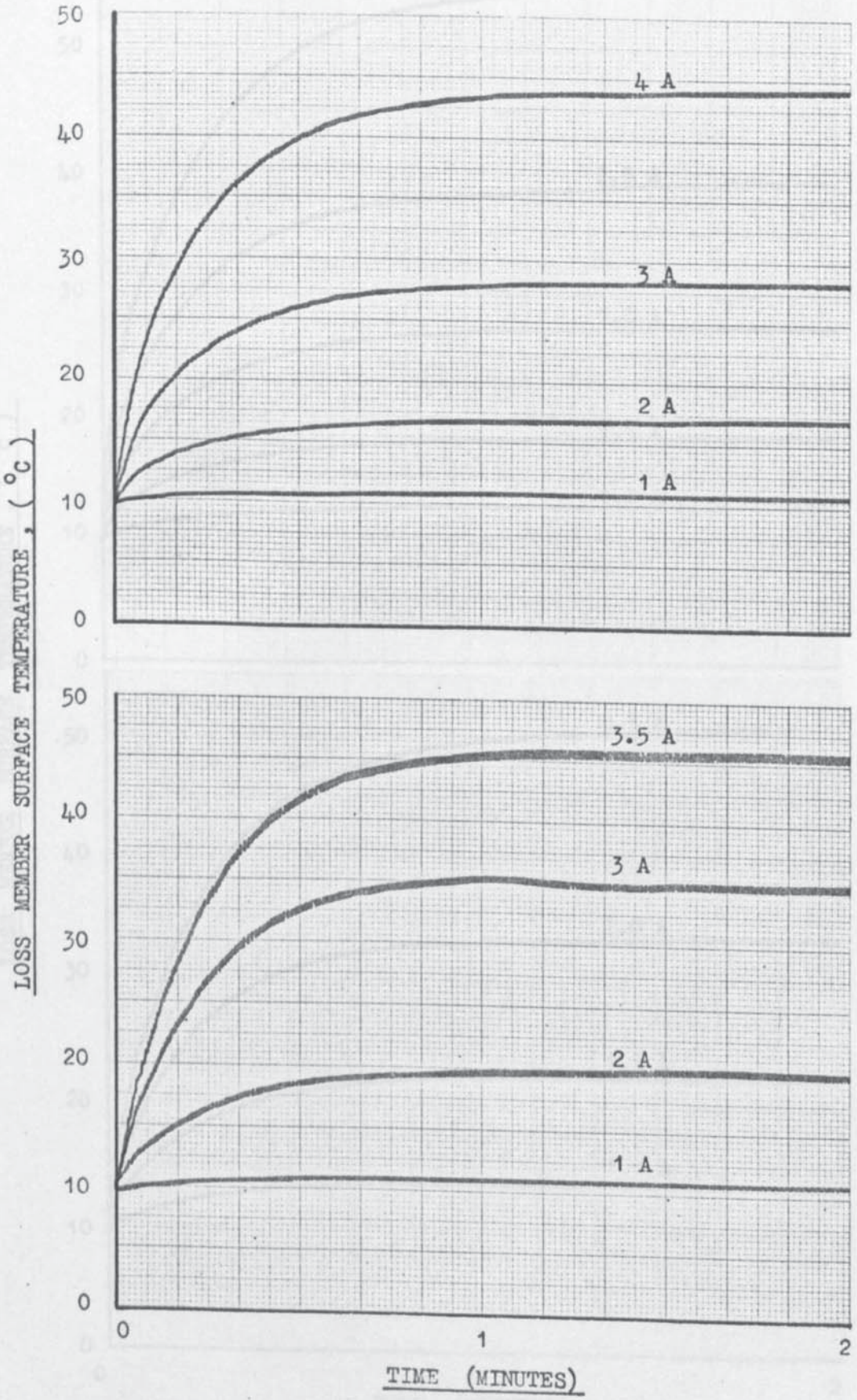

SLIP SPEED : 2000 rev/min.

Figure 5.36

LOSS MEMBER SURFACE TEMPERATURE AGAINST TIME AT CONSTANT SLIP SPEED AND VARIOUS EXCITATIONS WITH A COOLING WATER THROUGHPUT OF Q = 27 LITRES/MINUTE.

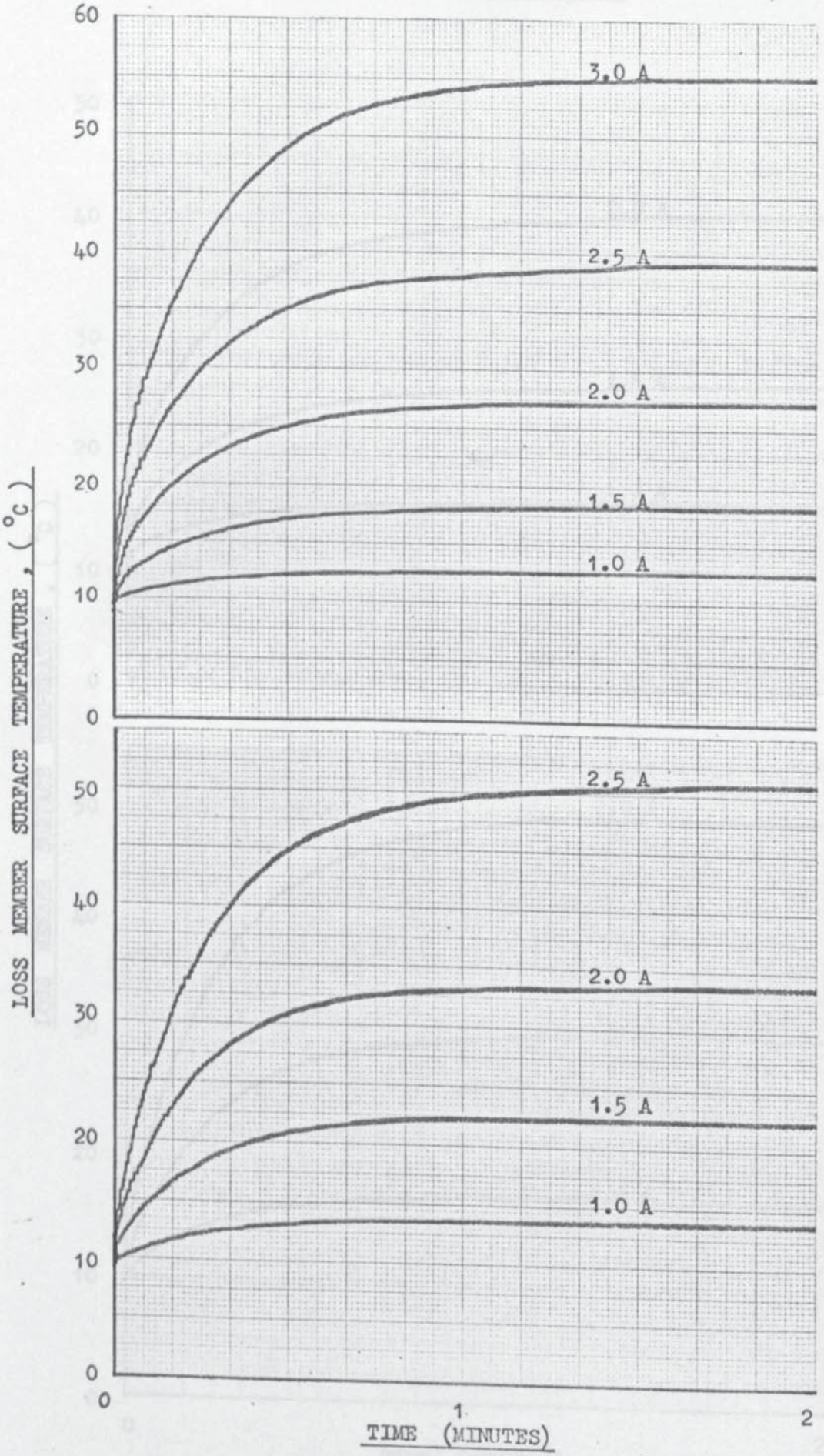

SLIP SPEED : 4000 rev/min.

Figure 5.37

LOSS MEMBER SURFACE TEMPERATURE AGAINST TIME AT CONSTANT SLIP SPEED AND VARIOUS EXCITATIONS WITH A COOLING WATER THROUGHPUT OF Q = 27 LITRES/MINUTE.

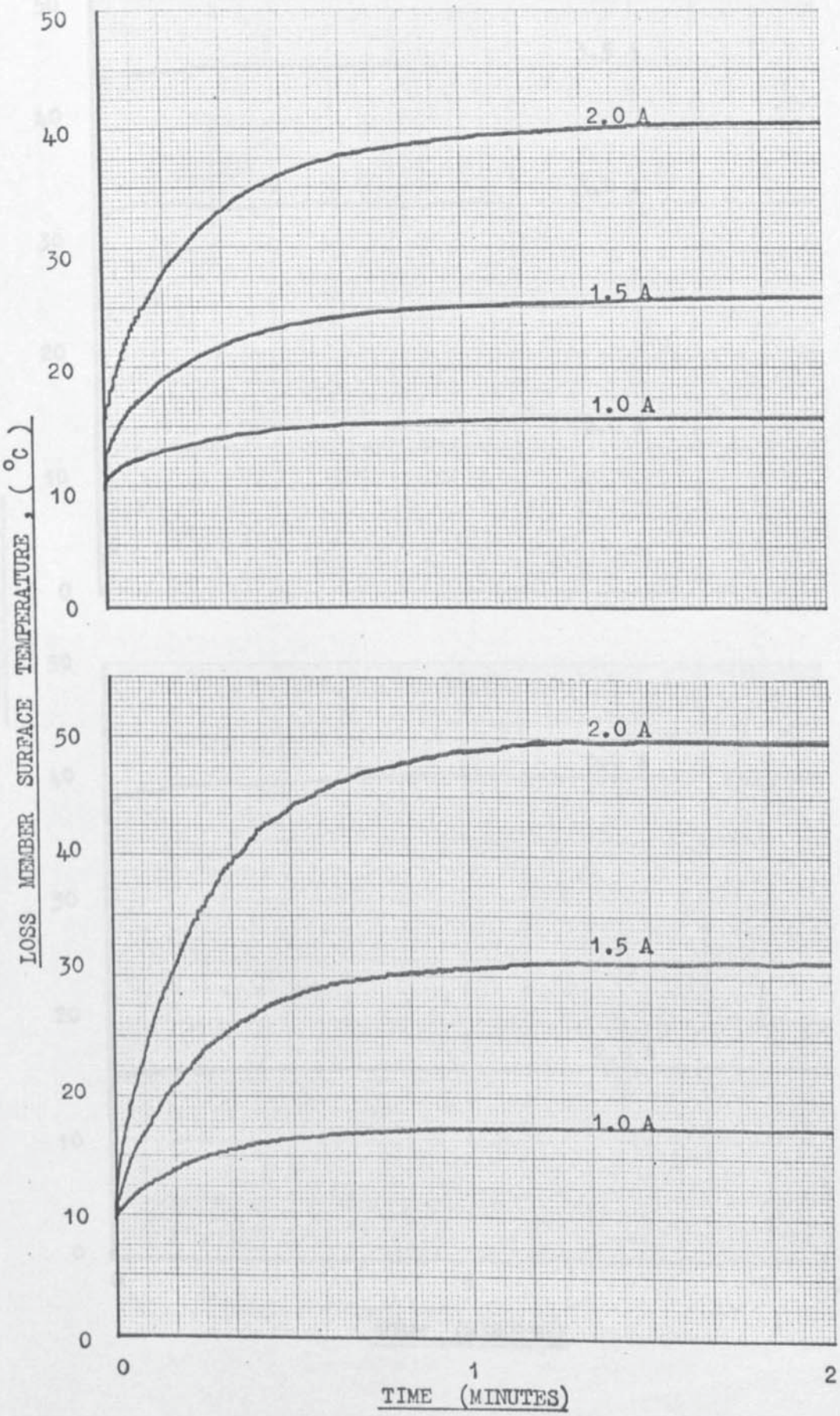

(a) Taken from Thermocouple 5

(b) Taken from Thermocouple 3

SLIP SPEED : 6000 rev/min.

TORQUE AGAINST TIME AT CONSTANT SLIP SPEED AND VARIOUS EXCITATIONS ; THESE CURVES WERE TAKEN SIMULTANEOUSLY WITH THE SURFACE TEMPERATURE AGAINST TIME CURVES.

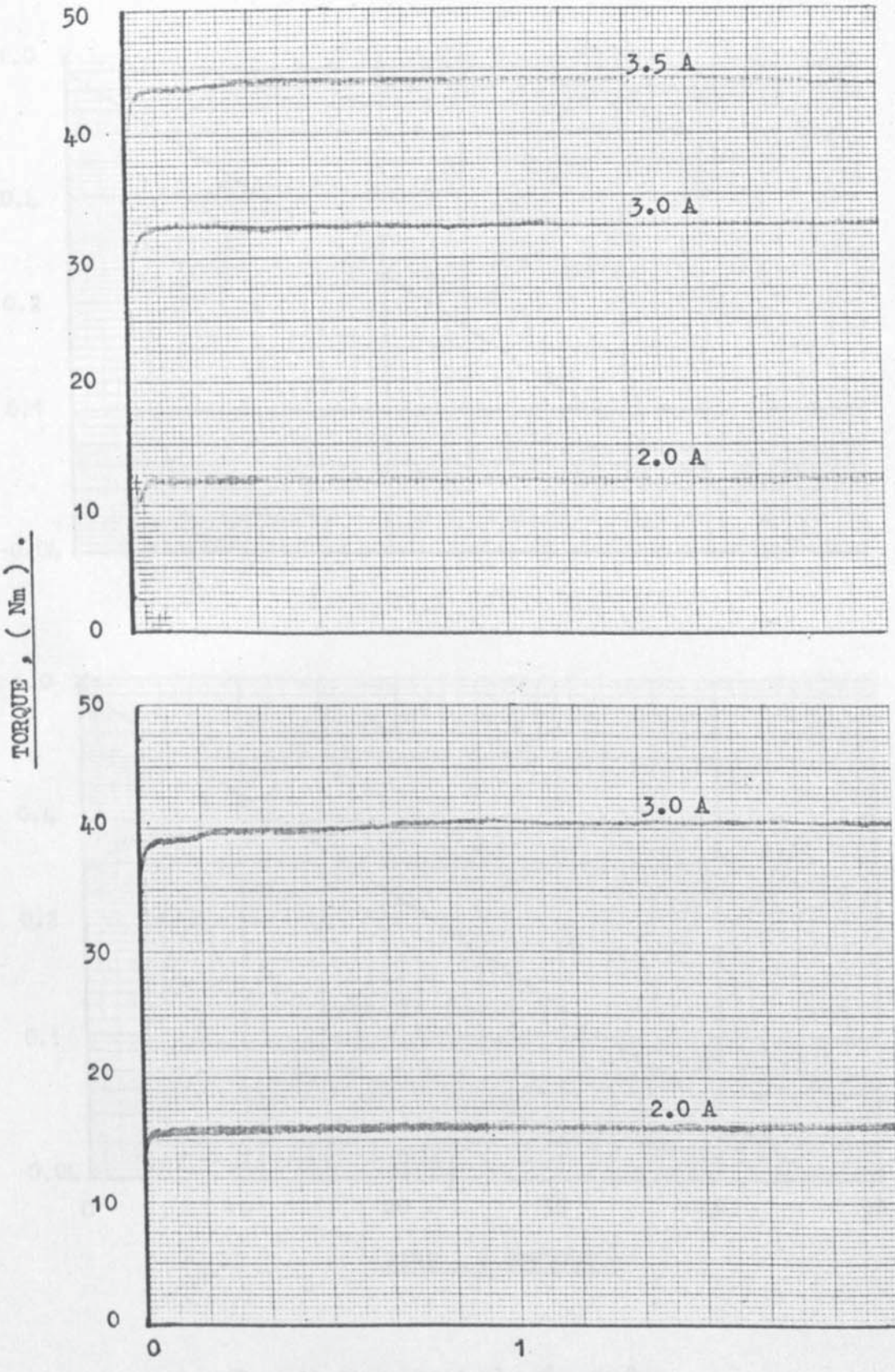

(a)

SLIP SPEED : 2000 rev/min.

(b)

SLIP SPEED : 4000 rev/min.

Figure 5.39

DERIVATION OF THE LOSS MEMBER THERMAL TIME CONSTANTS FROM THE MEASURED SURFACE TEMPERATURE RESPONSES.

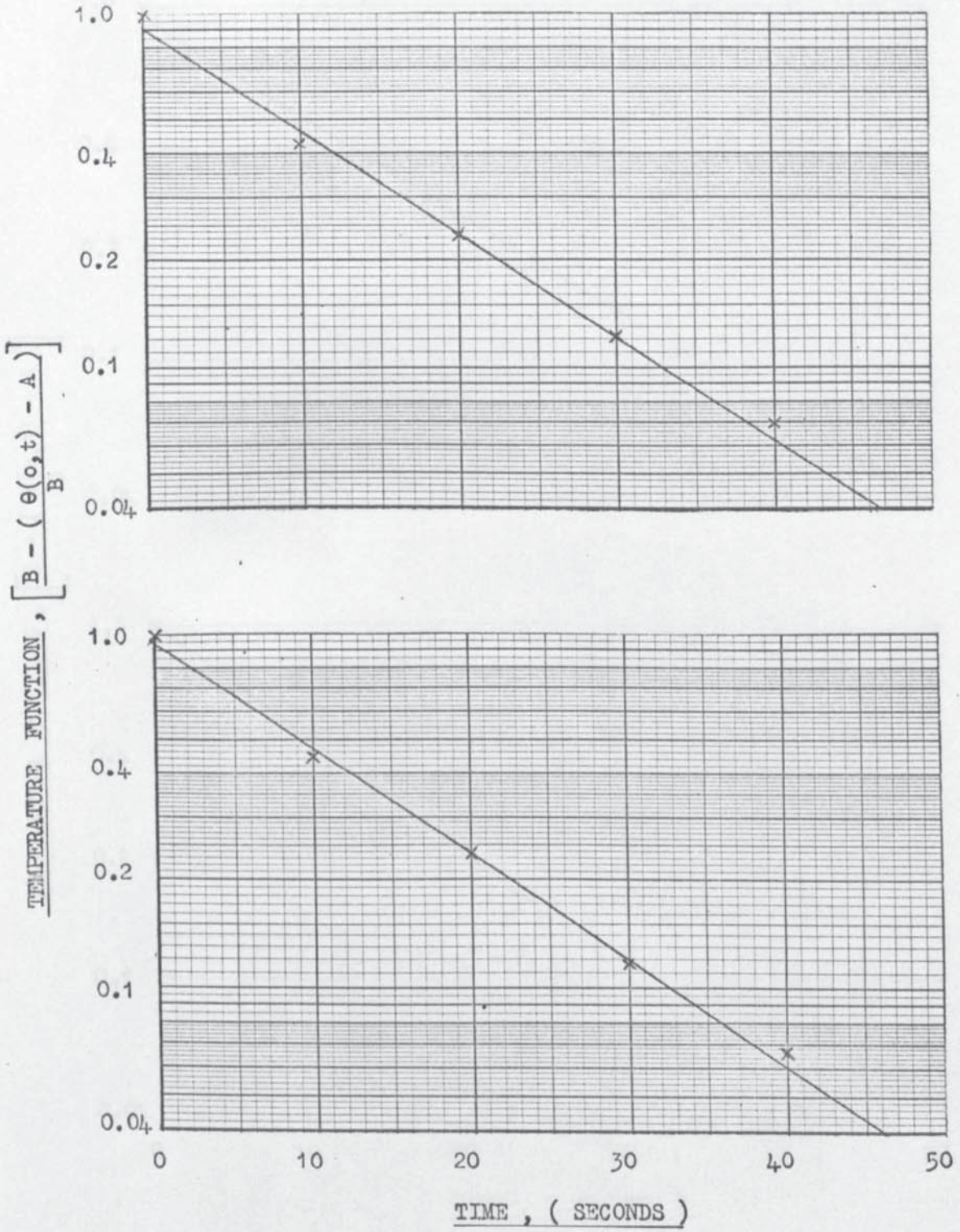

(a)
T/C 5
2000 rev/min.
Excitation : 3A

(b)
T/C 5
2000 rev/min.
Excitation : 4A

a : Thermal time constant , τ_1 = 14.8 s

b : Thermal time constant , τ_1 = 14.5 s

Figure 5.41

DERIVATION OF THE LOSS MEMBER THERMAL TIME CONSTANTS FROM THE MEASURED SURFACE TEMPERATURE RESPONSES.

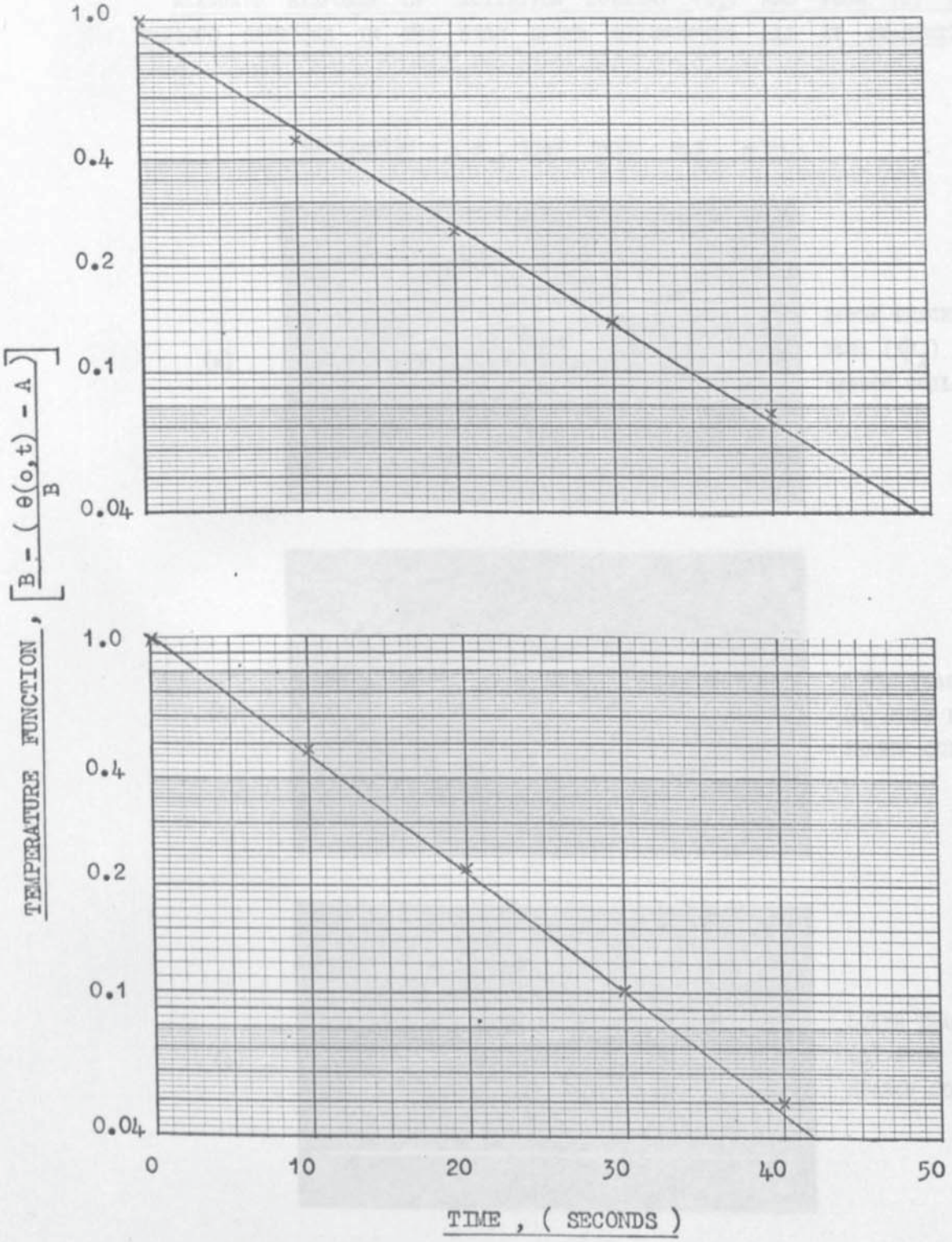

(a)
T/C 5
4000 rev/min.
Excitation : 3A

(b)
T/C 3
2000 rev/min.
Excitation : 3A

a : Thermal time constant , τ_1 = 15.4s

b : Thermal time constant , τ_1 = 12.8s

Figure 5.42

MEASURED RESPONSE OF EXCITATION CURRENT (I_f) AND FLUX (ϕ) AT VARIOUS SECTIONS IN THE HIGH SPEED DYNAMOMETER ALL AT STANDSTILL.

EXCITATION : 4 A , TIME BASE : 0.2 s/cm.

(a)

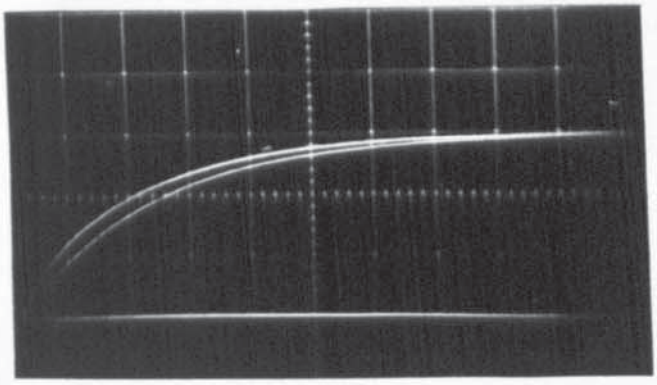

LOWER TRACE IS TOTAL FLUX (Φ_I) FROM SEARCH COIL 4 .

(b)

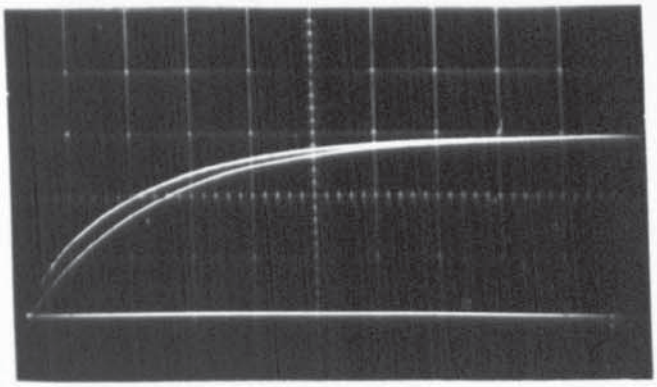

LOWER TRACE IS FLUX (ϕ_1) FROM FULL PITCH SEARCH COIL 1 .

(c)

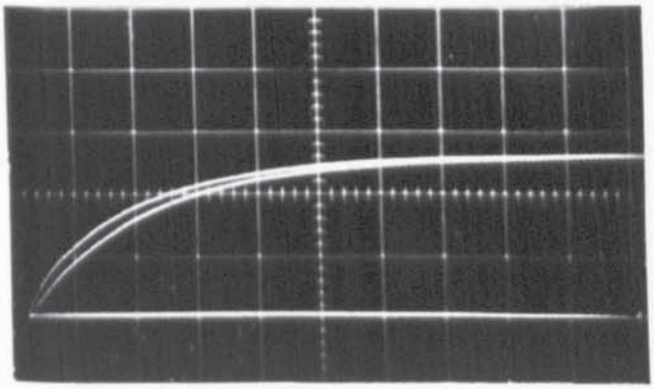

LOWER TRACE IS FLUX (ϕ_2) FROM FULL PITCH SEARCH COIL 2 .

NOTE : Full pitch search coils 1 and 2 were aligned with rotor slugs to obtain a maximum flux linkage. In trace (c) the vertical calibration of I_f (upper trace) has been reduced to correspond with the signal from full pitch search coil 2 .

Figure 5.44

MEASURED RESPONSE OF TOTAL FLUX (ϕ_I) AND EXCITATION CURRENT (I_f) AT STANDSTILL AND VARIOUS SLIP SPEEDS.

EXCITATION : 4 A , TIME BASE : 0.2 s/cm.

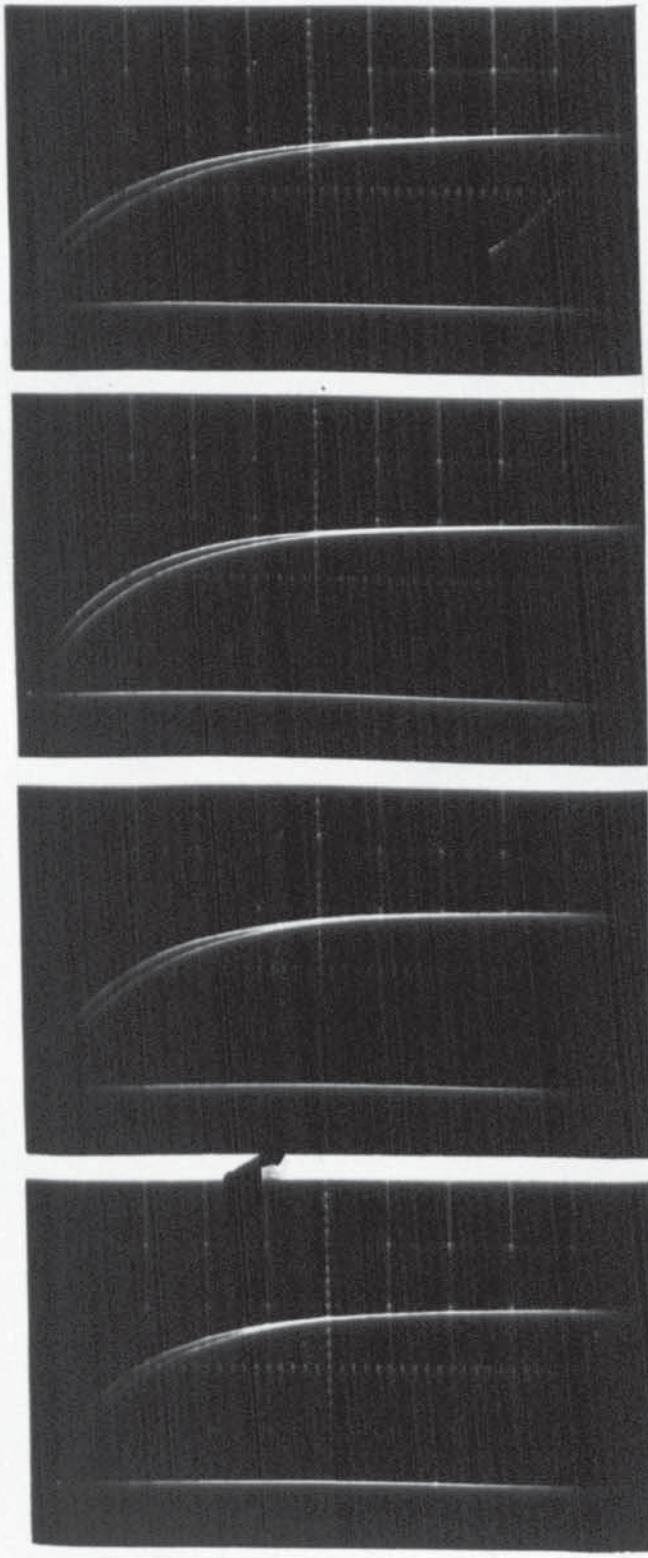

(a) STANDSTILL

τ_f = 0.34 seconds

τ_ϕ = 0.44 seconds

(b) 2000 rev/min.

τ_ϕ = 0.42 seconds

(c) 4000 rev/min.

τ_ϕ = 0.39 seconds

(d) 6000 rev/min.

τ_ϕ = 0.37 seconds

Upper trace is current response and lower trace is total flux response which is obtained by integrating the voltage induced in search coil 4.

Figure 5.45

VERIFICATION THAT TOTAL FLUX (ϕ_I) HAS AN EXPONENTIAL RESPONSE AND EVALUATION OF ITS TIME CONSTANT (τ_ϕ) AT VARIOUS SLIP SPEEDS.

EXCITATION : 4A

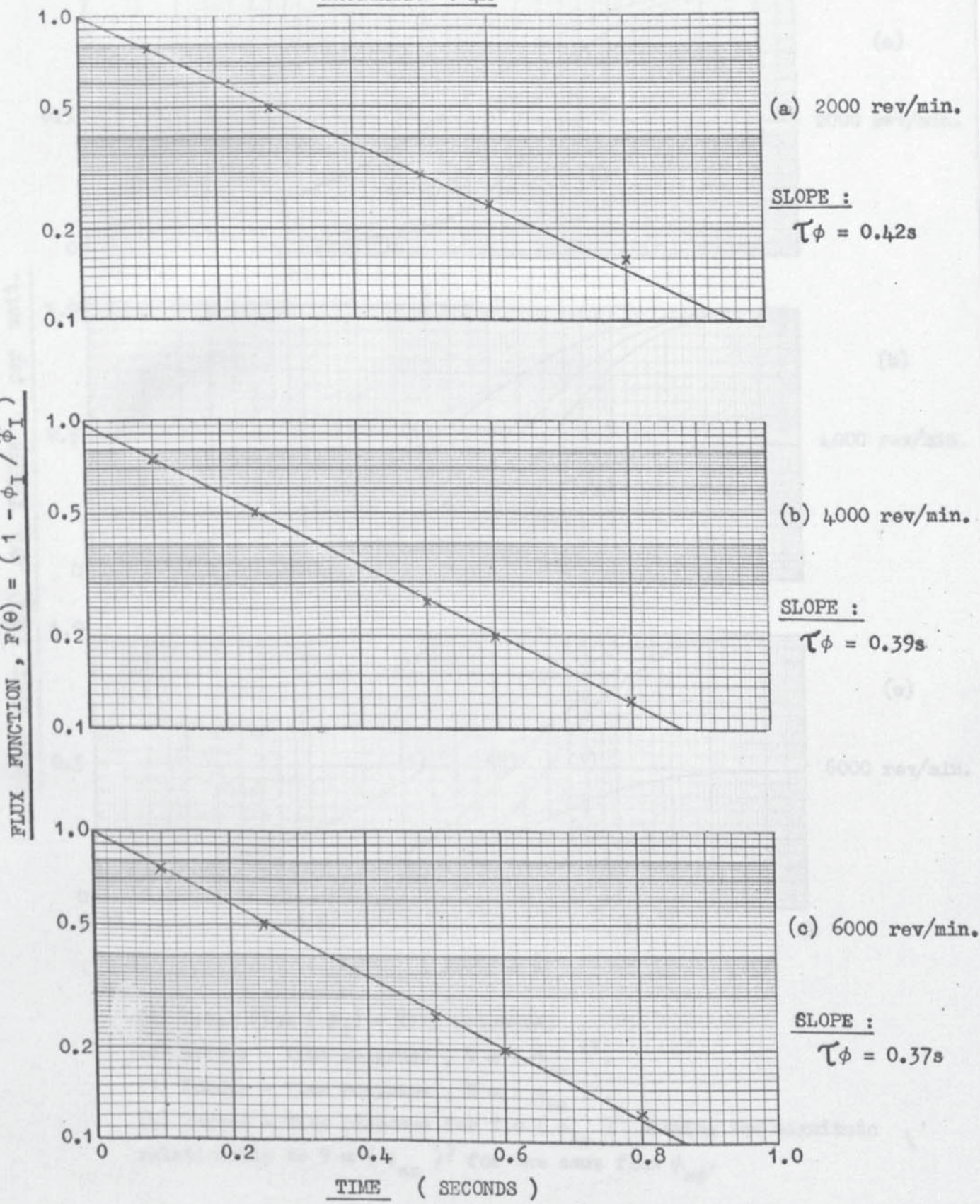

X : Experimental points taken from figures 5.44 and 5.45.

Figure 5.46

TIME RESPONSE OF TOTAL FLUX (ϕ_I) AND TORQUE AT VARIOUS SLIP SPEEDS.

EXCITATION : 4 A

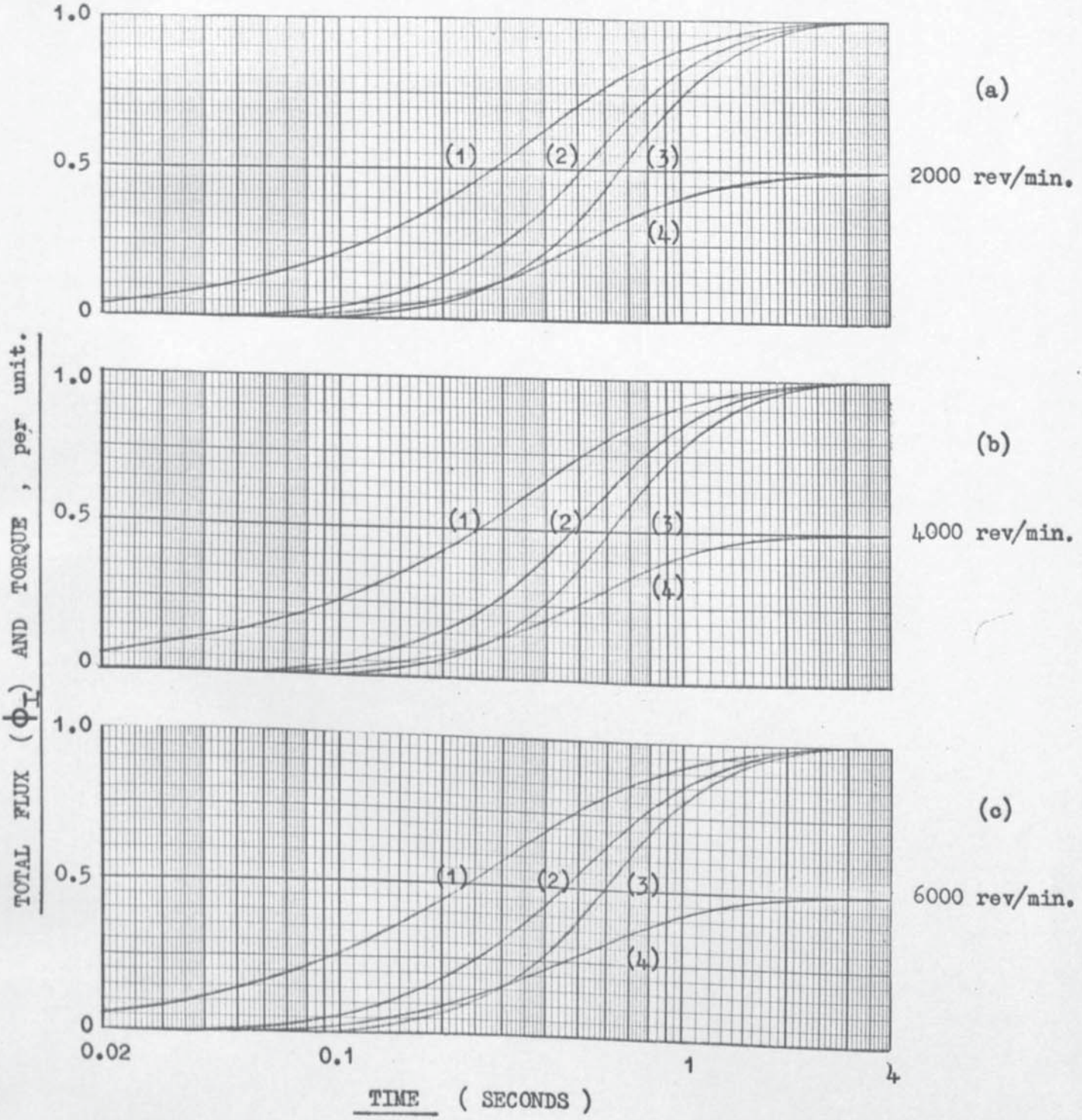

(1) Total Flux (ϕ_I) - Time response.
(2) Torque - Time response , $T \propto (\phi_{ac})^2$.
(3) Torque - Time response , $T \propto (\phi_{ac})^3$.
(4) Torque - Time response for $T \propto (\phi_{ac})^2$ showing the magnitude relationship to $T \propto (\phi_{ac})^3$ for the same flux ϕ_{ac}.

Figure 5.47